Permeability Anisotropy of Resedimented Mudrocks

by

Taylor James Nordquist

Bachelor of Science in Civil and Environmental Engineering
Brigham Young University, 2013

Submitted to the Department of Civil and Environmental Engineering in Partial Fulfillment of the requirements for the Degree of

Master of Science in Civil and Environmental Engineering

at the

MASSACHUSETTS INSTITUTE OF TECHNOLOGY

June 2015

Signature redacted

Signature of Author. . . . . .
Department of Civil and Environmental Engineering
May 21, 2015

Signature redacted

Certified by. . . . . .
John T. Germaine
Senior Research Associate and Senior Lecturer of Civil and Environmental Engineering
Thesis Supervisor

Signature redacted

Accepted by. . . . . .
Heidi M. Nepf
Donald and Martha Harleman Professor of Civil and Environmental Engineering
Chair, Departmental Committee for Graduate Students

Permeability Anisotropy of Resedimented Mudrocks

by

Taylor James Nordquist

Submitted to the Department of Civil and Environmental Engineering on May 21, 2015
in Partial Fulfillment of the Requirements for the Degree of Master of Science
in Civil and Environmental Engineering

ABSTRACT

Permeability anisotropy (ratio of horizontal to vertical permeability) is an important but uncertain parameter used in characterizing underground formations. While it is a fairly unknown parameter, it is integral for the petroleum industry, where a greater permeability anisotropy understanding can greatly aid in basin modelling, pore pressure prediction, and borehole stability. This research experimentally characterizes the permeability anisotropy of several mudrocks, which are clay-rich sedimentary formations, using resedimentation, a process of homogenization of naturally-occurring soils and recreation of the sedimentation environment in a controlled laboratory setting.

The permeability anisotropy of resedimented Boston Blue Clay (RBBC), an illitic lean clay (CL), increases from 1.5 to 3 when mechanically compressed from 0.1 to 40 MPa, corresponding to porosities ranging from 0.55 to 0.26. Resedimented Gulf of Mexico – Eugene Island mudrock (RGoM-EI), a smectitic fat clay (CH), exhibits permeability anisotropy increasing from 1 to 5 when compressed to the same stresses, corresponding to porosities ranging from 0.6 to 0.25. Not only does smectitic RGoM-EI mudrock transition to greater anisotropy with compression, but the rate of increase accelerates with compression. These measurements are made using a commercially-available Trautwein® constant rate of strain (CRS) consolidometer with vertical drainage combined with a novel radially-outward draining CRS device. The combination of the vertically and radially draining CRS devices produces permeability anisotropy data quickly, with very little scatter. For RGoM-EI, the effects of horizontal shearing to 29.5% shear strain at 0.14 MPa on permeability anisotropy are negligible.

Permeability anisotropy of the homogeneous resedimented mudrocks tested, using a cubic specimen constant head permeameter within a triaxial cell, is directly correlated to their electrical conductivity anisotropy. The permeability anisotropy values measured using this technology, however, are lower than those measured using CRS testing.

Thesis Supervisor: John T. Germaine

Title: Senior Research Associate and Senior Lecturer of Civil and Environmental Engineering

ACKNOWLEDGEMENTS

I owe much gratitude to Dr. Jack Germaine (Dr. G.), for taking me under his wing and teaching me some tricks to the trade of soil testing. He brings light-hearted creativity to lab testing that fosters creativity in those around him. He has put up with me for the last two years through many pieces of broken equipment and lots of incorrect calculations.

I would like to thank my other teachers and mentors in geotechnical engineering: Dr. Lucy Jen, who effectively connects the theoretical world with the practical one; Professor Herbert Einstein, who exemplifies passion for the art of engineering; and Professor Andrew Whittle, whose genius in accurately characterizing the world around him is unmatched. I would like to thank Dr. Peter Flemings, for teaching me presentation skills and introducing me to the world of petroleum engineering.

Stephen Rudolph, the laboratory manager and machinist, was the brains and hands behind making my new testing equipment. I would like to thank him for being willing and able to help me create new equipment and help me when old equipment stopped working, whether it be by fixing the equipment or finding something new to use.

I would like to thank Amy Adams, who was an excellent mentor to me as I started my education at MIT. Her work ethic, attitude, and intelligence made her a pleasure to work with. I would like to thank Mohammed Al-Dajani for his diligent work with me this last semester, keeping me testing during thesis writing time.

Due to many donors from the oil industry, in the form of the UT Geofluids consortium, I have benefitted from a fully-funded program. I owe much gratitude to them, as their contributions have allowed me to focus on my education and my research, and still have some time for my family, without worrying about financing. I would like to thank Peter Polito and Tessa Green for their support with UT Geofluids.

I have had many excellent classmates and friends at MIT who I have spent much time over the last two years with, including Chunwei, Amer, Jana, Brendan, Brian, Bing, Caroline, Nina, Steve, Bruno, Ivo, Wei, Yixing, Zhandos, Jialiang, Eva, Despina, Vaso, Omar, Mauro, Chin Soon, Evan, and Hao. Having good students to work with makes a great education better. I would also like to thank the students and researchers from UT Austin that I have worked with in UT Geofluids. I would like to thank Sheila Fay, Caroline Jundzilo Comer, and Jeanette Marchocki for their support and frequent sharing of a cookie.

Most of all, I would like to thank Megan and Ivy, for putting up with a husband and dad who spent so many early mornings and late nights at the lab, in Texas, or at his desk. Megan is my inspiration, and Ivy pulled me through the hard times with her daily smiles and giggles. I would like to thank my father, Jim, for allowing me to follow in his footsteps at MIT. I would like to thank my mother, Erica, as well as my in-laws, Greg and Kathy, for giving us emotional support and lots of visits during our time in Cambridge.

To Megan, Ivy, and "baby other,"

I dedicate this thesis to you.

TABLE OF CONTENTS

LIST OF TABLES

LIST OF FIGURES

LIST OF SYMBOLS

ASTM	American Society for Testing and Materials
BBC	Boston Blue Clay
BSEM	Backscattered Scanning Electron Microscope
CH	High-Plasticity (Fat) Clay
CL	Low-Plasticity (Lean) Clay
CRS	Constant Rate of Strain
DSS	Direct Simple Shear
GoM-EI	Gulf of Mexico – Eugene Island
IODP	Integrated Ocean Drilling Program
LVDT	Linear Variable Differential Transformer
MIT	Massachusetts Institute of Technology
MTC	Mass Transfer Complex
OCR	Over-Consolidation Ratio
PVA	Pressure Volume Actuator
RBBC	Resedimented Boston Blue Clay
RGoM-EI	Resedimented Gulf of Mexico – Eugene Island
RSFBM	Resedimented San Fransisco Bay Mud
SEM	Scanning Electron Microscope
SFBM	San Fransisco Bay Mud
USCS	Unified Soil Classification System
UT	University of Texas at Austin
VBA	Visual Basic for Applications

CF	calibration factor
$c_{v,r}$	coefficient of vertical consolidation with radial drainage
$c_{v,v}$	coefficient of vertical consolidation with vertical drainage
e	void ratio
F	steady state factor
g	acceleration due to gravity
G_s	specific gravity
i	electrical current
i	hydraulic gradient
K_{0NC}	normally-consolidated lateral stress ratio at rest
k_h	horizontal permeability
K_h	horizontal hydraulic conductivity
k_r	radial-horizontal permeability
K_r	radial horizontal hydraulic conductivity
k_v	vertical permeability
K_v	vertical hydraulic conductivity
m_v	coefficient of volume compressibility
n	porosity
q	volumetric flow rate
R	pore pressure ratio
r_{cv}	coefficient of vertical consolidation anisotropy
r_k	permeability anisotropy
r_σ	electrical conductivity anisotropy
S	saturation
S_u	undrained strength
S_u/ σ'_v	undrained strength ratio
u	pore water pressure
u_e	excess pore water pressure
V	voltage

wc	water content
$\dot{\varepsilon}$	strain rate
μ	dynamic viscosity
ρ	density
ρ	electrical resistivty
σ	electrical conductivity
σ'_v	vertical effective stress
σ_v	vertical total stress
ε	strain

CHAPTER 1 – INTRODUCTION

1.1 PROBLEM STATEMENT

Soil behavior is a complex field, as soil is a multi-phase, non-homogenous, anisotropic, and inelastic material. Many properties of soil formations remain unknown, leaving geotechnical, hydrological, and petroleum engineers to make educated assumptions. Permeability anisotropy, or the ratio by which fluids flow easier horizontally than vertically, is one such parameter. A better understanding of permeability anisotropy will help geotechnical engineers determine soil settlement and strength, hydrological engineers predict groundwater availability and pollution, and petroleum engineers characterize and access precious hydrocarbon reserves.

Permeability varies over orders of magnitude, depending mainly on grain size and porosity. Thus, when small grain sizes and porosities are encountered, permeability is a highly variable parameter. Mudrocks, which are sedimentary formations composed of greater than 50% siliclastic grains smaller than 0.0625 mm (Boggs, 2006), can exhibit a variability of up to 8 orders of magnitude of permeability (Neuzil, 1994; Dewhurst and Aplin, 1999; Clennel et al, 1994). Such variability can cause mudrocks to act as underground reservoirs, channels, or aquitards, depending on the magnitude of their permeabilities juxtaposed against their neighbors.

Permeability anisotropy can be caused by stratification of soil layers on the macro- or micro-scale, as well as particle rotation on micro-scale (Scholes et al, 2007; Witt and Brauns, 1983). When a formation has a combination of micro- and macro-scale permeability anisotropies, they have a multiplicative effect with each other to form a formation permeability anisotropy (Adams, 2014).

Petroleum engineers are perhaps the most interested in characterizing permeability anisotropy in underground formations, as doing so can be a great tool for them. Hydrocarbon reserve characterization is a difficult undertaking. Exploratory boreholes can be extremely expensive, and seismic imaging only gives limited information. Basin modelling is used, therefore, to try to predict how

offshore sedimentary basins might have evolved over geological time, and where current extractable reserves might be located. In these models, permeability anisotropy is an important parameter, which is often set to 1 (isotropic) or an arbitrary constant value.

Researchers have hypothesized that permeability anisotropy can be linked to electrical resistivity anisotropy; however, few experimental data have been reported to support this hypothesis. Resistivity anisotropy measurements can be performed *in-situ* with a borehole triaxial resistivity meter, and could possibly lead to *in-situ* permeability anisotropy measurement.

1.2 THESIS SCOPE AND OBJECTIVES

The objective of this research is to characterize the permeability anisotropy of clay-rich marine mudrocks compressed from low to high stresses (0.1 to 40 MPa). Experimental data are collected from uniform mechanically-compressed mudrocks, neglecting diagenetic effects from time and temperature that occur in nature. The effects of both mechanical compression and mineralogy on permeability anisotropy are assessed. The effect of horizontal shearing is also examined.

The mudrocks tested are fabricated from naturally-occurring soil powders, resedimented in a laboratory setting in attempt to mimic the mechanical aspect of *in-situ* marine sedimentation. Resedimentation is used to (1) provide homogeneous samples with known mineralogies, salinities, and stress histories that allow for cross-specimen comparison, and (2) economically obtain test specimens representing high-stress marine mudrocks.

Adams (2014) extensively studied permeability and resistivity anisotropy using cubic specimen constant head permeability and resistivity testing within a pressurized triaxial cell. She studied mostly resedimented Boston Blue Clay (RBBC), an illitic lean clay (CL), but also resedimented Gulf of Mexico – Eugene Island mudrock (RGoM-EI), a smectitic fat clay (CH), among other mudrocks. Her results show RBBC permeability anisotropy values that, while increasing from compression up to 10 MPa, decrease after further compression. She also measured lower permeability anisotropy in smectitic RGoM-EI mudrock than she did in RBBC. Both of these results are counter-intuitive, as increasing vertical compression should only increase particle alignment (Olsen, 1962; Lambe, 1958; Mitchell, 1956), and increasing smectite content should increase flowpath tortuosity (Scholes et al, 2007).

Adams' (2014) results are the main impetus for this research. We want to determine whether permeability anisotropy actually decreases at high stresses and high smectite contents, or whether these data are a result of some kind of measurement error. We approach the problem from a different

direction than the cubic specimen method used by Adams (2014): the use of constant rate of strain (CRS) consolidation testing with differing drainage regimes to determine permeability anisotropy. We take this approach because it allows for a large reduction in specimen disturbance and data can be collected much faster than with the cubic specimen constant head tests.

While vertically-draining CRS testing has been routinely used for decades (Wissa et al, 1971), radially-draining CRS testing is a fairly new concept. June and Chung (2005) theoretically developed radially-draining CRS interpretation techniques, and several experimental results are found in the literature (Yune and Jung, 2011; Seah and Juirnarongrit, 2003). Most of these data, however, are for soils at lowe stresses. The development of a robust radially-draining CRS consolidometer is needed that can test mudrocks at high stresses.

Once the radially-draining CRS consolidometer is developed, tests are run on RBBC and RGoM-EI in both vertically-draining and radially-draining CRS devices. These results allow for a comparison between the CRS and the cubic specimen permeability anisotropy measuring techniques. The results will also provide further insight into permeability anisotropy caused by particle rotation, and answer the questions of whether or not permeability anisotropy values continue to increase with compression and smectite content, or whether they reach a finite limit. The CRS technology is also used to characterize permeability anisotropy caused by mudrock shearing.

The results provide basin modelers with a model for the evolution of permeability anisotropy caused by particle rotation with burial depth, bringing them one step closer to understanding this difficult parameter. The model should be combined with the effects of micro- and macro-stratification, in order to simulate formation-scale anisotropy (Adams, 2014).

This research presents only a portion of the greater research being performed by a joint venture between Dr. Jack Germaine's geotechnical engineering group at the Massachusetts Institute of Technology and Dr. Peter Fleming's geoscience group at the University of Texas at Austin, sponsored by the UT Geofluids consortium. The overall objective of the consortium is to "study the state and evolution of pressure, stress, deformation, and fluid migration through experiments, models, and field study."

1.3 ORGANIZATION OF THE THESIS

This thesis is organized into seven chapters. These chapters include the introduction, background, materials, equipment, procedures, results and discussion, and conclusion and recommendations.

Chapter 2 gives the background of the problem statement, as well as the state of the research. We start by explaining mudrock composition, then discuss mudrock fabric, mudrock permeability, and finally mudrock permeability anisotropy.

Chapter 3 describes the mudrock materials resedimented and used for the research. It starts by describing the source materials, then gives an overview of the resedimentation procedure, and finally describes the shearing procedure used to produce horizontally-sheared specimens.

Chapter 4 presents the equipment used for the research. As much of the research is devoted to developing a radially-draining CRS consolidometer, the large first section of this chapter describes its development, design, and construction. We then describe the vertically-draining CRS and direct simple shear (DSS) devices. The cubic specimen constant head permeameter endcaps and equipment are then presented, followed by transducer calibration, the computer control systems used for the tests, and the data acquisition system.

Chapter 5 thoroughly describes the procedures used for both the vertically- and radially-draining CRS consolidometers, and summarizes the procedure for the cubic specimen constant head permeameter. The first section describes the testing procedures, while the second section describes the analysis procedures. Many of the procedures in this chapter are presented in a step-by-step format, complete with pictures, in order to foster reproducibility.

Chapter 6 presents and discusses the test results from both the CRS and cubic specimen testing programs. We start by presenting the compression results of the various materials, followed by permeability results, which are followed by resistvity results. Regressions are presented for many of the data sets, to allow for modelling of material behavior from the tests.

Chapter 7 gives a summary of the equipment development and research. It also presents recommendations for future research.

CHAPTER 2 – BACKGROUND

2.1 INTRODUCTION

This research is a continuation of work performed at the MIT geotechnical laboratory by Adams (2014). She measured the permeability anisotropy, electrical conductivity anisotropy, and particle alignment of resedimented Boston Blue Clay (RBBC), Boston Blue Clay mixed with silt (39% Clay RBBC), Gulf of Mexico – Eugene Island (RGOM-EI), and San Fransisco Bay Mud (RSFBM) mudrocks. She measured permeability anisotropy using a cubic specimen constant head permeameter setup within a triaxial cell. She measured electrical conductivity anisotropy using electrodes included in the permeameter endcaps within the traixal cell. She performed particle alignment analyses using backscattered scanning electron microscope (BSEM) imaging (Adams, 2014).

This chapter is a summary of the state of the research in mudrock permeability anisotropy both from Adams (2014) and other researchers in the literature. We will discuss Mudrock composition and fabric first, followed by mudrock permeability, and finally permeability anisotropy.

2.2 MUDROCK COMPOSITION

Fine-grained sediments have many names throughout the literature. For this work, they will be referred to as mudrocks, which we will define as earthen formations composed of greater than 50% by mass siliclastic grains which are smaller than 0.0625 mm in diameter (Boggs, 2006). These can be considered "fines" according to the USCS classification system. "Fines" are defined as the particles smaller than 0.075 mm in diameter (#200 sieve), and are sub-categorized into clays and silts.

Mudrocks are deposited in marine or lacustrine environments where water velocity is low, because that is where the fine-grained clays and silts can fall to the bottom of the water and stay there (Potter et al, 1980). The mechanical erosion of rock produces sands and silts, while clays are typically formed through a chemical erosion process called hydrolysis. Hydrolysis occurs when silicate minerals are partially dissolved by water-born acids, producing silicate clay minerals, siliceous acid, and metal cations (Boggs, 2006). Thus the siliceous materials must be located in an area where they can be saturated for an extended amount of time in order for abundant hydrolysis to occur. Once created, the fine-grained sediments can be transported to deposition beds as atmospheric dust, in rivers, and in ocean currents (Mitchell and Soga, 2005).

In mudrocks, as with most soils, the mechanical properties of the material are mostly determined by the smallest constituents, as they are the particles controlling the interaction between grains and the void networks (Terzaghi et al, 1996). The fines (< 0.075 mm) can be categorized into silts and clays, using various methods. X-ray diffraction (XRD) allows for the determination of mineralogy, where clay and silt fractions can be quantitatively determined. Atterberg limit tests are a set of inexpensive index tests used to determine whether a material behaves more like a clay or more like a silt, with the use of the Casagrande plasticity chart (see Figure 2-1). A material that plots above the "A" line is considered to have material properties dominated by clay particles, while a material that plots below the "A" line is considered to be governed by its silt particles.

Soil and mudrock fabrics of high clay fraction have always been a rich area for research. Due to the small, flake-like shapes of the clay particles and their mineralogies, the electrical forces acting on the particle surfaces govern over the gravitational forces acting on their masses (Terzaghi et al, 1996). Clay particles are made of platy tetrahedral and octahedral sheets (see Figure 2-2) (Mitchell and Soga, 2005; Terzaghi et al, 1996). The tetrahedral sheets are commonly known as silica sheets, and are made up of silicon and oxygen. They are referred to as phylosilicates (Day-Stirrat et al, 2010). The most common

octahedral sheets are gibbsite sheets, made up of aluminum and hydroxide, and brucite sheets, which are made up of magnesium and hydroxide (Lambe and Whitman, 1969).

While the term "phylosilicate" is used to describe plate-shaped silicon-based particles, "tectosilicate" refers to the rest of the silicon-based particles that make up soil solids. These tectosilicates are more equi-dimensional, and are commonly eroded from potassium feldspar (Day-Stirrat, 2010). Tectosilicates perform much more isotropically than their counterparts, as they do not orient themselves horizontally during compression and are less deformable even at the particle level (Dewhurst and Aplin, 1998; Leroueil, 1990).

2.3 MUDROCK FABRIC

Mudrocks can be further categorized into lithified and non-lithified, as well as fissile and non-fissile categories (Stow, 1981). The mudrocks looked at in this study are resedimented, and as such they are both non-lithified and non-fissile.

Mudrocks, along with other saturated soils, are composed of soil solids, water, and air. Their mechanical properties are not only functions of their composition or mineralogy, but of their spatial arrangement, or fabric (Brewer and Sleeman, 1960). Specifically, mudrock fabric relates to the distribution and geometrical orientation of the individual particles (Terzaghi et al, 1996). It is a function of the sedimentation environment, the salinity and chemistry of the pore fluid, the mineralogy of the particles, and the mudrock's stress history (Lambe and Whitman, 1969). The effect that mineralogy and stress history have on mudrock fabric will be focused on in the rest of this section.

2.3.1 Effect of Mineralogy on Mudrock Fabric

Mineralogy greatly affects the fabric of a mudrock. It plays a key role in the development of particle shapes, sizes, and surface forces. Particle shapes, sizes, and surface forces are the building blocks of mudrock fabric, which is then altered by compression and/or shear (see Section 2.2.2). When a mudrock fabric has a significant fraction of clay particles, its mechanical properties are governed by those particles, which are directed more by electrostatic forces than gravitational forces (Terzaghi et al, 1996). The interactions between the flaky clay particles and water inside and outside their double layers has everything to do with how they behave. A significant amount of research has been performed to determine how mineralogy affects mudrock fabric and mudrock fabric anisotropy.

Using backscattered SEM imaging, Day-Stirrat et al (2010) found an increasing amount of fabric anisotropy with increasing clay content from mudrock samples from Crews, Texas and Rhum, North Sea.

Figure 2-3 shows the relationship between clay content and orientation in multiples of random distribution, (m.r.d.) of pole density. Pole density will be the highest at poles representing surfaces more or less perpendicular to consolidation stress. Using relationships such as this, equations have been derived to determine fabric intensity (anisotropy) using clay or quartz content (Day-Stirrat et al, 2010).

Clennell et al (1999) looked at the effect of mineralogy on clay fabric by performing oedometric flow permeability tests in both the vertical and radial direction. They tested some kaolinite and montmorillonite and found vastly different propensities for anisotropy between the two. They found a maximum permeability anisotropy of 8 for montmorillonite, and only 1.7 for kaolinite (Clennell et al, 1999). This is likely a reflection of the large aspect ratio and surface electrictrostatic forces in montmorillonite particles compared to kaolinite.

While the presence of clay particles with large aspect ratios creates anisotropic clay fabric, the presence of sand and silt particles has the opposite effect (Daigle & Dugan, 2011). This isn't only due to the averaging effect of mixing particle alignments of both clay and silt/sand. The alignment of the clay particles themselves is likely to be affected by neighboring silt/sand particles by (a) phylosilicates bending around the surfaces of the larger particles and (b) larger particles bridging over the clay particles, shielding them from effective stress (Day-Stirrat et al, 2010). Figure 2-4 illustrates these effects.

The trends of increasing fabric anisotropy with increasing clay content from experimental data can be backed up using analytical modeling. Daigle and Dugan (2011) used particle aspect ratio as an integral input for permeability anisotropy. They showed that tortuosity caused by particle alignment of particles with an aspect ratio of 20 in a soil fabric with 40% porosity could create permeability anisotropy up to 20.

2.3.2 Effect of Stress History on Mudrock Fabric

While mineralogy creates a basis for the creation of a particular type of mudrock fabric, stress history plays a significant role in fabric development beyond a slurry state. Stress history refers primarily to the amount of stress the mudrock is or has been under in the past, as well as the directon of major and minor principle stresses. It can also refer to the rate of stress application and stress duration.

Mudrocks are created from a process called sedimentation, where the individual soil particles drop from suspension in a body of water, building up a mudrock over time. When soil particles are first

sedimented at the mudline, they occur in a slurry state. The individual soil particles are oriented more or less randomly, thus no dominant particle orientation exists. When clay particles are abundant, sediment slurries within marine environments form flocculated structures, where edge-to-face contacts are created. Clay-rich sediment slurries in lacustrine environments, however, tend towards dispersed structures, where large double layers foster more face-to-face contacts (Adams, 2014; Lambe and Whitman, 1969). The degree of flocculation versus dispersion has a significant impact on mudrock fabric (Terzaghi et al, 1996; Lambe and Whitman, 1969). As compression occurs, mudrock fabric evolves from more randomly-oriented particles to particles oriented with their long axes oriented more perpendicular to the major principle stress (Delage and Lefebvre, 1984; Ladd, 1996; Terzaghi et al, 1996). This compression can occur due to progressing sedimentation, glaciation, or tectonics.

Compression changes the mudrock from a flocculated or dispersed fabric to a solidified mudrock fabric. Vertical compression is accompanied by a vertical effective stress increase, causing the particles to slowly change from a random orientation to a more ordered, anisotropic orientation. Figure 2-5 shows three backscattered electron microscope (BSEM) images at the same scale from a clay core out of the Gulf of Mexico. Compared to image A (σ'_v=0.25 MPa), the particles shown in image C (σ'_v=3.98 MPa) are more sandwiched together, with the particles' long axes perpendicular to the direction of the major principal stress. This illustrates how clay fabric in general changes with depth, or effective stress (Day-Stirrat et al, 2012). At increasing depths (effective stresses) the slender clay particles become more horizontally aligned, creating permeability anisotropy. Emmanuel and Day-Stirrat (2012) imaged resedimented Boston Blue Clay (RBBC) at 0.1, 1, and 10 MPa effective stresses using BSEM imaging. Their images, shown in Figure 2-6, are a very nice illustration of the development of anisotropic mudrock fabric with compression for RBBC. Adams et al (2013) quantified the orientation of RBBC particles from 9 images from their study, and measured a change in average particle orientation from 50° to 28° from horizontal as the mudrock is compressed from 0.1 to 10 MPa (see Figure 2-7). Day-Stirrat et al (2012) used X-ray goniometry to measure particle alignment as a function of burial depth, or vertical effective stress, of intact core from the Integrated Ocean Drilling Program (IODP) Expediiton 308 in the Ursa Basin within the Gulf of Mexico. They found a general increase in particle alignment with depth (see Figure 2-8). This shows that fabric anisotropy not only develops from mechanical compression in the lab, but from natural compression due to sedimentation under the seafloor.

Early on in the sedimentation process, soil fabric is formed predominantly by cluster rearrangement, as the dense clusters move into the open space (Olsen, 1962; Delage and Lefebvre, 1984). The largest

pores, which govern the permeability, are created by the bridging of the largest particle clusters. These bridges collapse during compression, allowing the largest voids to be filled, rearranging the mudrock fabric (Delage and Lefebvre, 1984; Dewhurst and Aplin, 1999).

Once the clusters have optimized their use of the free space, clayey mudrock fabric development is governed by the rotation of individual soil particles (Olsen, 1962; Lambe, 1958; Mitchell, 1956). This mechanism is believed to be the main cause of mudrock fabric anisotropy. It tends to occur in mudrocks before the vertical effective stress reaches 0.1 to 0.3 MPa (Adams et al, 2013, Day-Stirrat, 2010; Clennel et al, 1999; Martin & Ladd, 1975). However, this number is very dependent on material type – mineralogy, chemistry, and environment.

The research done on mudrock fabric at the MIT geotechnical laboratory is focused primarily on resedimented specimens. These specimens are created out of trimming, core, or excavation material that can be highly disturbed. The disturbed materials are air-dried and ground into a fine powder. The powder is mixed with water and salt, and loaded over time. The process is intended to mimic *in-situ* sedimentation conditions and fabric. This is done not only for economy, but to create homogenous mudrocks with controlled stress histories, from which separate specimens can be fabricated and compared with each other (Ladd, 1996; Germaine, 2009).

2.4 MUDROCK PERMEABILITY

Mudrock permeability is closely linked to its fabric. Permeability is an inverse measure of the amount of interference that a soil skeleton gives to a fluid. Specifically, it is affected by "particle size, shape, aspect ratio, mineralogy, particle packing, pore fluid chemistry and salinity, and bound water layers surrounding charged particles." (Adams, 2014)

Permeability can be thought of as the "flowability" of a fluid through a porous medium. The coefficient of permeability, or hydraulic conductivity, can measured by flowing water through the medium and using Darcy's law, as shown in Equation 2-1 (Terzaghi et al, 1996). Hydraulic conductivity is a property of the porous medium and the fluid.

$$v = K\left(\frac{\Delta h}{L}\right) \tag{2-1}$$

where:
v = discharge velocity
K = hydraulic conductivity
Δh/L = hydraulic gradient

Permeability, which is an intrinsic property of the porous medium, can be calculated from hydraulic conductivity using Equation 2-2. This removes the effect of fluid properties.

$$k = \frac{K\mu}{\rho g} \tag{2-2}$$

where:
k = permeability
μ = dynamic viscosity of fluid
ρ = density of fluid
g = acceleration due to gravity

Mudrock permeability is an important parameter in oil and gas reservoir characterization. It determines how far pore fluid (water, oil, or gas) will migrate in response to pressure gradients. Consequently, combining a knowledge of subsurface geology, bore log data, and seismic data, petroleum engineers can estimate where oil or gas is coming from and where it is going. These estimations lead to the ability to model where oil and gas reservoirs are located, as well as estimate which ones are economically extractable (Gluyas and Swarbrick, 2004). Mudrock permeability is also an important parameter to aid in pore pressure prediction in overpressured (sedimenting) basins.

While permeability is such a crucial parameter, it is highly variable and hard to predict. As the porosity of a mudrock decreases from 0.9 to 0.05, in fact, the permeability of a mudrock can decrease by up to 8 orders of magnitude (Neuzil, 1994; Dewhurst and Aplin, 1999; Clennel et al, 1994).

Permeability has long been modelled using the Kozeny-Carman equation (Equation 2-3). This equation mechanistically predicts permeability as a function of particle shape, particle specific surface area, flow path tortuosity, and porosity (or void ratio) (Scholes et al, 2007).

$$k = \left(\frac{1}{C_k}\right)\left(\frac{1}{\tau^2}\right)\left(\frac{1}{{S_S}^2}\right)\left(\frac{e^3}{1+e}\right) \quad (2\text{-}3)$$

where:
k = permeability
C_k = shape factor
τ = tortuosity
S_S = specific surface area
e = void ratio

Yang and Aplin (1998) modeled how mudrock permeability behaves as a function of pore-size distribution and lithology, or mudrock composition. They provide a framework for estimating mudrock permeability by inputting pore throat size distribution, pore shape, and pore alignment.

Adams (2014) extensively measured the permeability of RBBC and took a few measurements on other mudrocks and mudrock mixtures, namely RGoM-EI, RSFBM, and 39% clay RBBC. For RBBC, she measured a horizontal permeability trending from 7E-17 to 2E-18 m^2 as the mudrock compresses from a porosity of 0.49 to 0.30, respectively. For vertical RBBC permeability, she measured 6E-17 to 8E-19 m^2 along the same range of porosities. Figure 2-9 shows a summary of her permeability measurements.

2.5 MECHANISMS FOR PERMEABILITY ANISOTROPY

Permeability anisotropy is defined as the ratio between horizontal and vertical permeability (Scholes et al, 2007; Bolton et al, 2000). As horizontal permeability is typically higher than vertical, permeability anisotropy is usually a value greater than one.

There are three main causes for permeability anisotropy: (1) macro-stratification, or layering of different materials, (2) micro-stratification, or miniature layering in which individual layers cannot be easily characterized, and (3) individual particle rotation due to flatness (Scholes et al, 2007; Witt and Brauns, 1983). Particle rotation can be caused by mechanisms such as compaction, shearing, bioturbation, or the formation of stress cracks. When homogeneous mudrock layers exhibit permeability anisotropy due to particle orientation within a stratified formation, the anisotropies from particle rotation and from layering have a multiplicative effect on the overall anisotropy (Adams, 2014).

While mudrock permeability is hard to accurately predict, permeability anisotropy is even harder. Since permeability varies by orders of magnitude depending on material type, homogeneity, porosity, and

everything else listed in Section 2.1, finding a small difference between different directions is very sensitive to experimental noise.

2.5.1 Macro-Stratification

Macro-stratification and is very common in mudrocks. It is caused by changes in deposition materials and conditions over geological time, creating different layers. Conceptually, the higher-permeability layers will carry most of the flow in a parallel-to-bedding flow regime while the lower-permeability layers will govern the perpendicular-to-bedding flow regime, creating anisotropy. Mathematically, the formation permeability parallel to the layering can be represented by the weighted mean of the individual layer permeabilities (see Equation 2-4), while the permeability perpendicular to the layering is represented by the weighted harmonic mean of the individual layer permeabilities (see Equation 2-5).

$$k_{\parallel} = \frac{\sum_{i=1}^{n}(k_i L_i)}{\sum_{i=1}^{n} L_i} \tag{2-4}$$

$$k_{\perp} = \frac{\sum_{i=1}^{n} L_i}{\sum_{i=1}^{n}\left({}^{L_i}/_{k_i}\right)} \tag{2-5}$$

where:
$k_{\parallel}$ = formation permeability parallel to layering
$k_{\perp}$ = formation permeability perpendicular to layering
k_i = permeability of i_{th} layer
L_i = thickness of i_{th} layer
n = total number of layers

2.5.2 Micro-Stratification

Micro-stratification causes permeability anisotropy the same way that macro-stratification does, and is just as common. However, micro-stratification can be distinguished from macro-stratification in that individual layer parameters cannot be practically characterized because the layers are too thin (Witt and Brauns, 1983). Micro-stratification can be created within a mudrock due to seasonal variations in deposition materials and conditions, as well as geological variations in a sedimentation bed with a very slow deposition rate. An good example of micro-stratification is a varved clay (Mitchell and Soga, 2005).

2.5.3 Particle Orientation from Compression

Although macro- and micro-layering typically have the greatest impact on permeability anisotropy at the formation scale, particle orientation within homogenous layers causes permeability anisotropy at the small scale. Particle orientation is most commonly a result of compression, where particles align themselves perpendicular to the major principle stress, much like papers on a cluttered desk. The development of particle orientation with compression is discussed in Section 2.2.2.

At the particle scale, permeability anisotropy is developed due to flowpath tortuosity within the mudrock (see Figure 2-10). Scholes et al (2007) found a direct relationship between tortuosity anisotropy and permeability anisotropy. Meegoda (1989) produced an equation, similar to Kozeny-Carman, which mechanistically calculates permeability in multiple directions (see Equation 2-6).

$$K_\theta = \left(\frac{1}{3}\right)\left(\frac{A}{T}\right)\left(\frac{1}{S_S{}^2}\right)\left(\frac{e^3}{1+e}\right) \tag{2-6}$$

where:
k_Θ = *permeability in direction* Θ *to particle alignment*
$A = (K_\vartheta / K_{\vartheta+90°})^{2/3}$
$T = [(r+r_0)/r']^{-0.5}$
r = *radius of large sphere*
r_0 = *radius of small sphere*
r' = *radius of sphere volumetrically equivalent to large and small spheres r and* r_0
S_S = *specific surface area*
e = *void ratio*

Permeability anisotropy through particle orientation due to compression was the main characterization objective of Adams' (2014) research. She extensively measured permeability anisotropy of resedimented mudrocks using cubic specimen constant head testing in a triaxial cell. She measured a permeability anisotropy for RBBC of 1.1 at a porosity of 0.49, increasing to 1.9 at a porosity of 0.36. She attributed this increasing anisotropy with decreasing porosity trend to particle orientation from compression.

At porosities lower than 0.36, she measured a permeability anisotropy decreasing to as low as 1.4 (see Figure 2-11). The cause of this decreasing anisotropy was hypothesized to be either material behavior

controlled by the collapsing of horizontal flowpaths at low porosities (Adams, 2014), handling disturbance on the specimens, or experimental error.

Adams (2014) also measured permeability anisotropy on RSFBM and RGoM-EI mudrocks (see Figure 2-12). Some of these mudrocks were mixed with silt or leached prior resedimentation to explore the effects of clay fraction and flocculation, respectively. In all materials, however, permeability anisotropy increased as a function of compression.

2.5.4 Particle Orientation and Cracking from Mudrock Shearing

Mudrock shearing can cause permeability anisotropy, through particle orientation and cracking parallel to the shear plane. This can also occur in faults, landslide scarps, or within mass-transport complexes (MTCs). Microscopically, this shearing is believed to arrange particles in the direction of the shearing, which can then alter fabric even with ensuing compression (Dewhurst et al, 1996; Terzaghi et al, 1996). Macroscopically, shearing creates anastomosing flow paths in a direction parallel to shearing, which are then likely to be closed with ensuing compression (Dewhurst et al, 1996; Arch and Maltman, 1990). Whether particle orientation or cracking are the predominating shearing mechanism is a function of the stiffness and strength of the material, as well as the strain rate.

2.5.5 Other Considerations

As was stated previously, horizontal permeability is typically greater than vertical permeability (anisotropy greater than one), due to layering particle orientation, and cracking. However, vertical permeability greater than horizontal permeability (anisotropy less than one) has been found at shallow depths. This phenomenon is hypothesized to stem from bioturbation, where topical roots and wormholes create vertical holes. Stress micro-cracks can also create preferential vertical permeability (Chapuis and Gill, 1989; Bolton et al, 2000).

2.6 ELECTRICAL CONDUCTIVITY ANISOTROPY

Electrical resistivity has long been used in borings to estimate lithology and engineering parameters. It is also frequently measured in a laboratory setting to better understand soil behavior, as resistivity is a function of particle size, shape, orientation, degree of pore saturation, porosity, and pore fluid salinity (McCarter et al, 2005). To decouple the effect of pore fluid salinity on a specimen's resistivity, the formation resistivity factor is used, which describes the resistivity of the formation itself, normalized to the pore fluid salinity (Archie, 1942). This means that if engineering parameters are to be estimated

from a borehole using resistivity, the formations' pore fluid salinity must be known. The correlations between resistivity and engineering properties are highly empirical, and are dependent on resistivity probe seating, pore fluid salinity and chemistry, and formation resistivity factor (Archie, 1942).

While estimating engineering properties from resistivity is highly coupled, estimating fabric anisotropy from electrical resistivity, or conductivity, anisotropy, normalizes the coupling effect away. McCarter et al (2005) measured electrical anisotropy of resedimented kaolin in a laboratory using an electrode-equipped oedometer and calculated anisotropy between 1.4 and 1.5 when compressed from 0.01 to 0.3 MPa. Mousseau and Trump (1967) measured electrical anisotropy in a similar way, testing shale, kaolinite, and bentonite. They measured anisotropy around 5 for the shale and 4 for the kaolinite. They measured incredible anisotropy development with compression for bentonite, changing from 1 to 25 when compressed to 384 and 1130 psi, respectively.

Adams (2014) measured electrical conductivity anisotropy and compared it to permeability anisotropy (see Figure 2-13). She started by measuring conductivity outside the triaxial cell on the same specimens that she measured permeability inside the triaxial cell. She later developed the technology to measure both conductivity and permeability on the same specimen within the triaxial cell. She found an approximate "one to one" correlation between the two parameters on most of her tests, apart from her RGoM-EI measurements (this is discussed in Section 6.2.4). This relation goes to show that electrical conduction path tortuosity within a uniform mudrock is directly proportional to fluid flow path tortuosity. Using such a relation could cater to using downhole triaxial resistivity meters to infer permeability anisotropy of uniform formations *in-situ*.

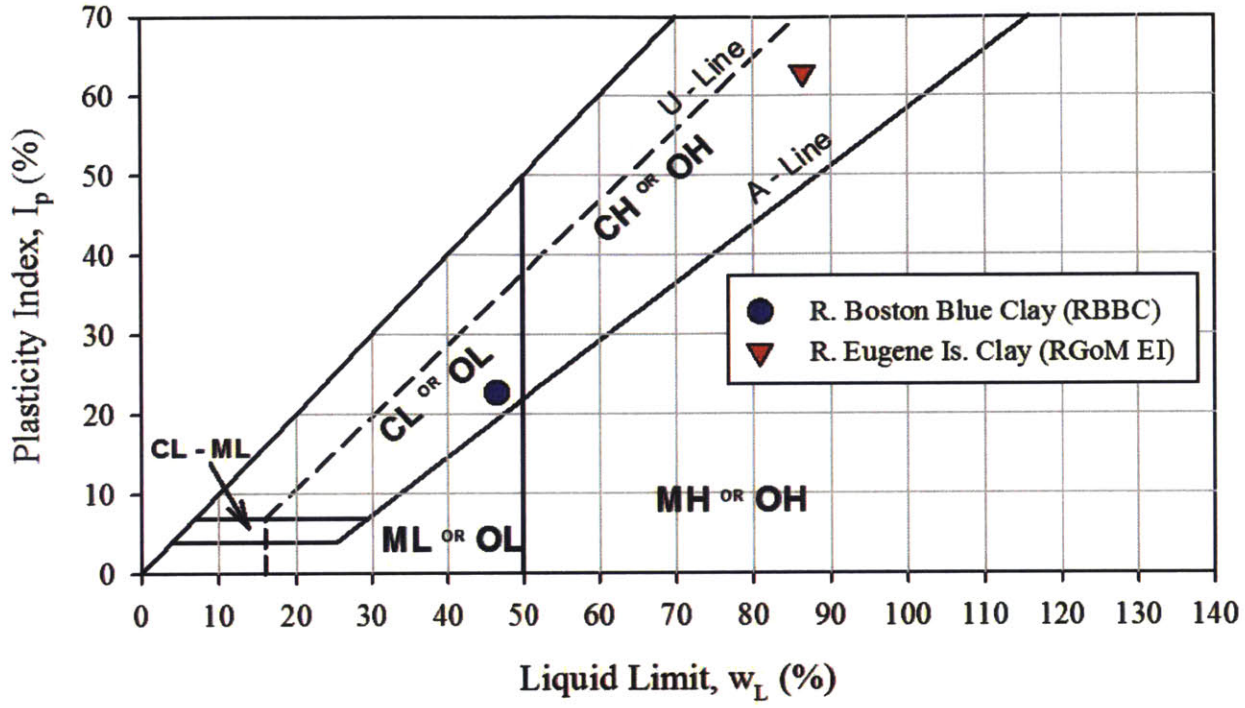

Figure 2-1: The Casagrande plasticity chart indicates that the behavior of both RBBC and RGoM-EI is dominated by their clay particles, as they plot above the "A" line.

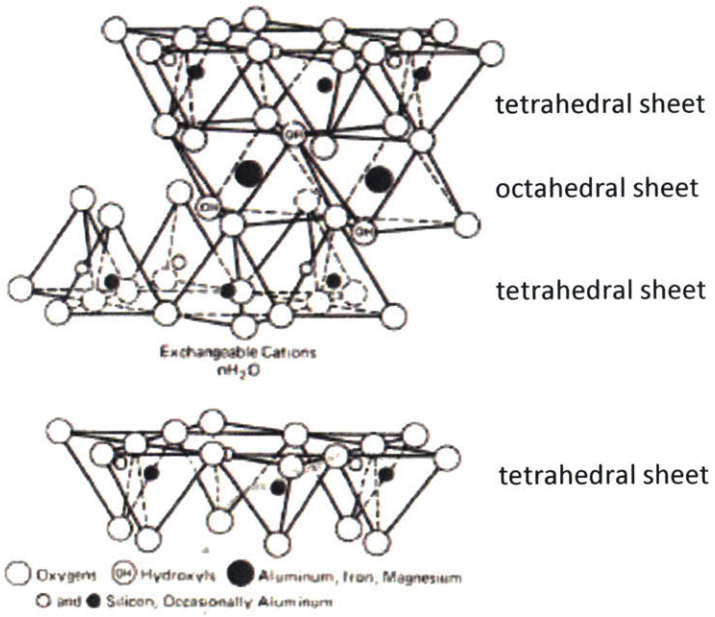

Figure 2-2: Diagrammatic sketch of montmorillonite structure shows tetrahedral and octahedral sheets, the building blocks of clay structure (Mitchell and Soga, 2005).

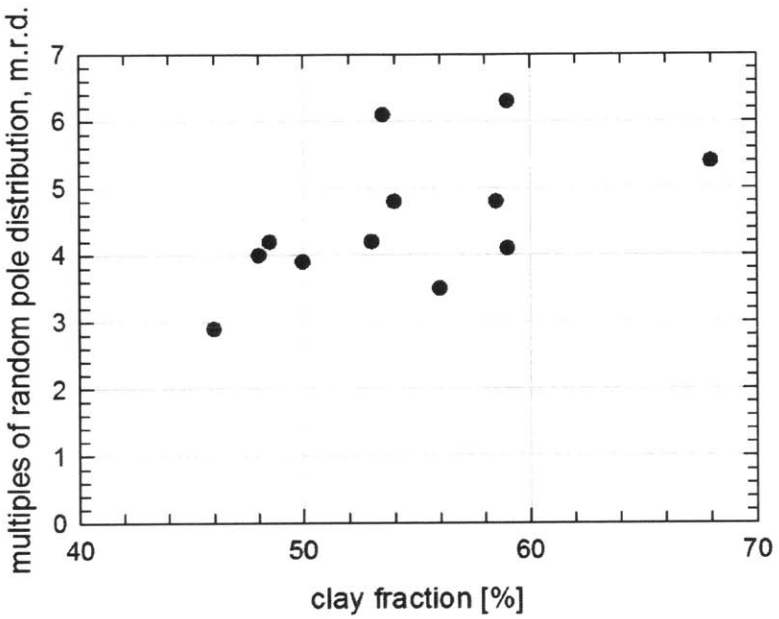

Figure 2-3: Illite-smectite particle orientation from the Crews and Rhum wells becomes more aligned with increasing clay fraction (Day-Stirrat et al, 2010).

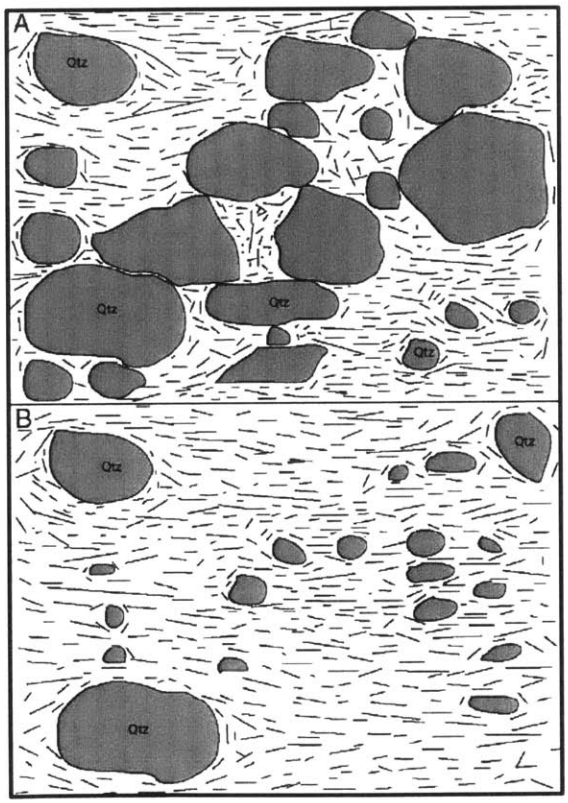

Figure 2-4: Clay particle orientation is greatly affected by large amounts of silt/sand (A) when compared to particle orientation with low amounts of silt/sand (B) (Day-Stirrat et al, 2010).

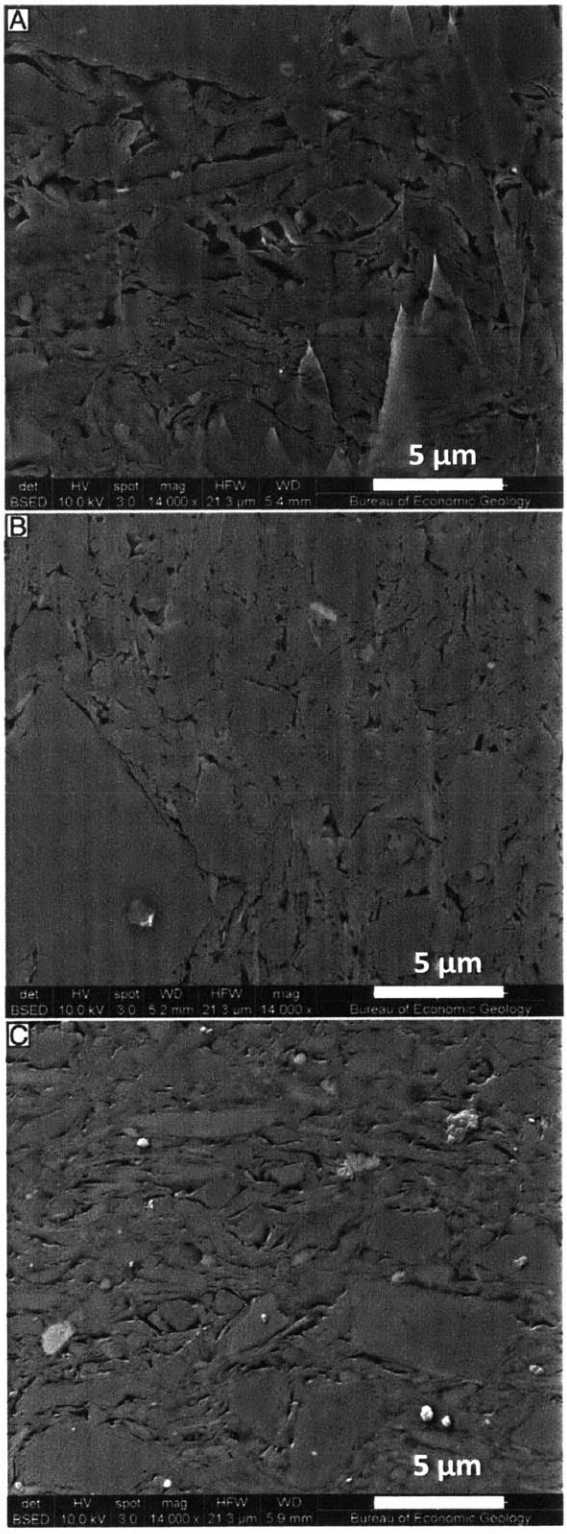

Figure 2-5: Backscattered scanning electron microscope (BSEM) images from IODP (International Ocean Discovery Program) expedition 308 show mudrock fabric development with increasing depth. A - 74.5 mbsf & σ'v = 0.25 MPa, B - 178.6 mbsf & σ'v = 0.90 MPa, C - 570.0 mbsf & σ'v = 3.98 MPa. (Day-Stirrat et al, 2012)

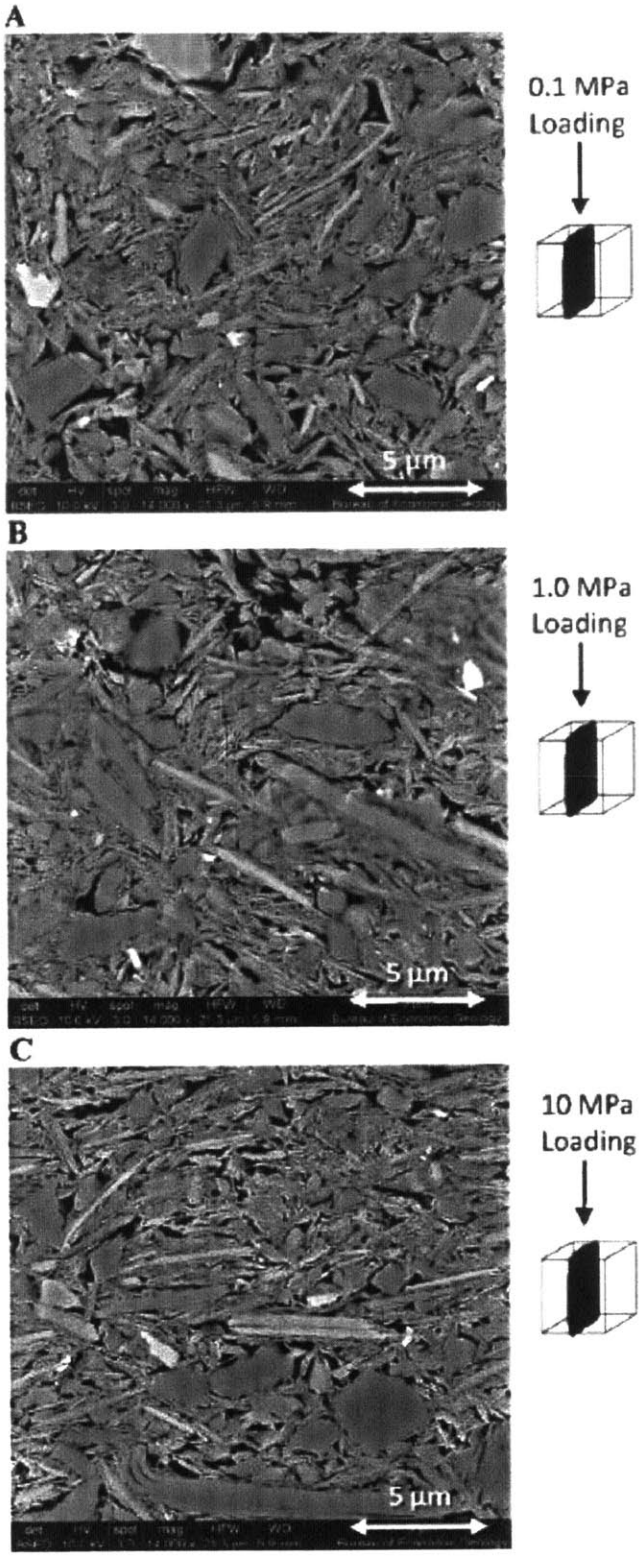

Figure 2-6: BSEM images of RBBC at (a) 0.1 MPa, (b) 1.0 MPa, and (c) 10 MPa (Emmanuel and Day-Stirrat, 2012) show anisotropic fabric development with compression.

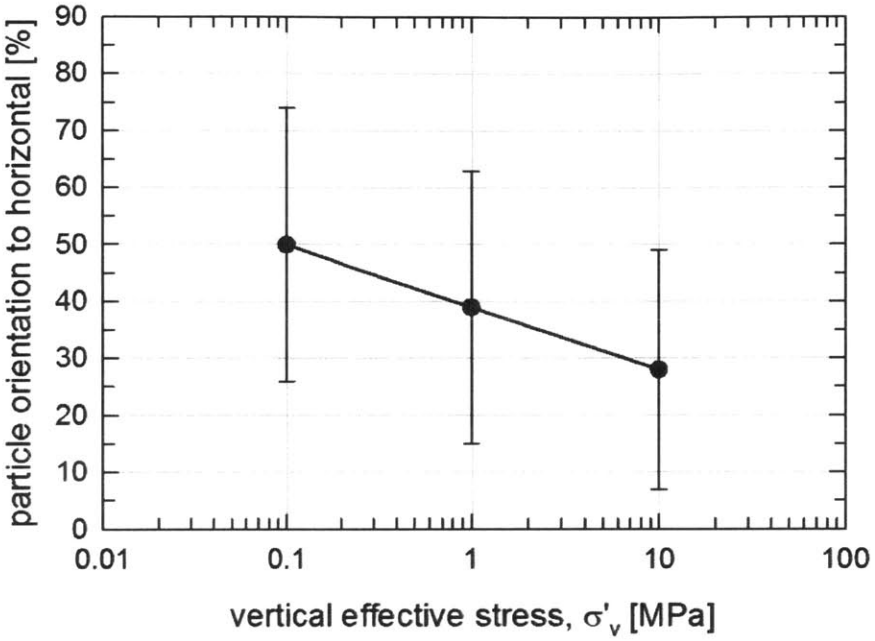

Figure 2-7: Particle orientation with compression from BSEM images (Emmanuel and Day-Stirrat, 2012) of RBBC (Adams et al, 2013) shows the development of fabric anisotropy.

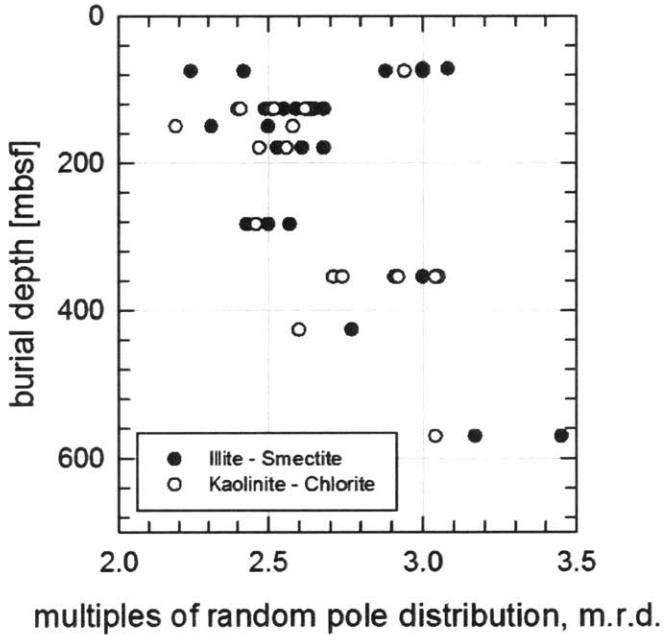

Figure 2-8: Clay mineral particle alignment with depth data from IODP Expedition 308 in the Ursa Basin (Day-Stirrat et al, 2012) show that fabric anisotropy occurs from natural sedimentation.

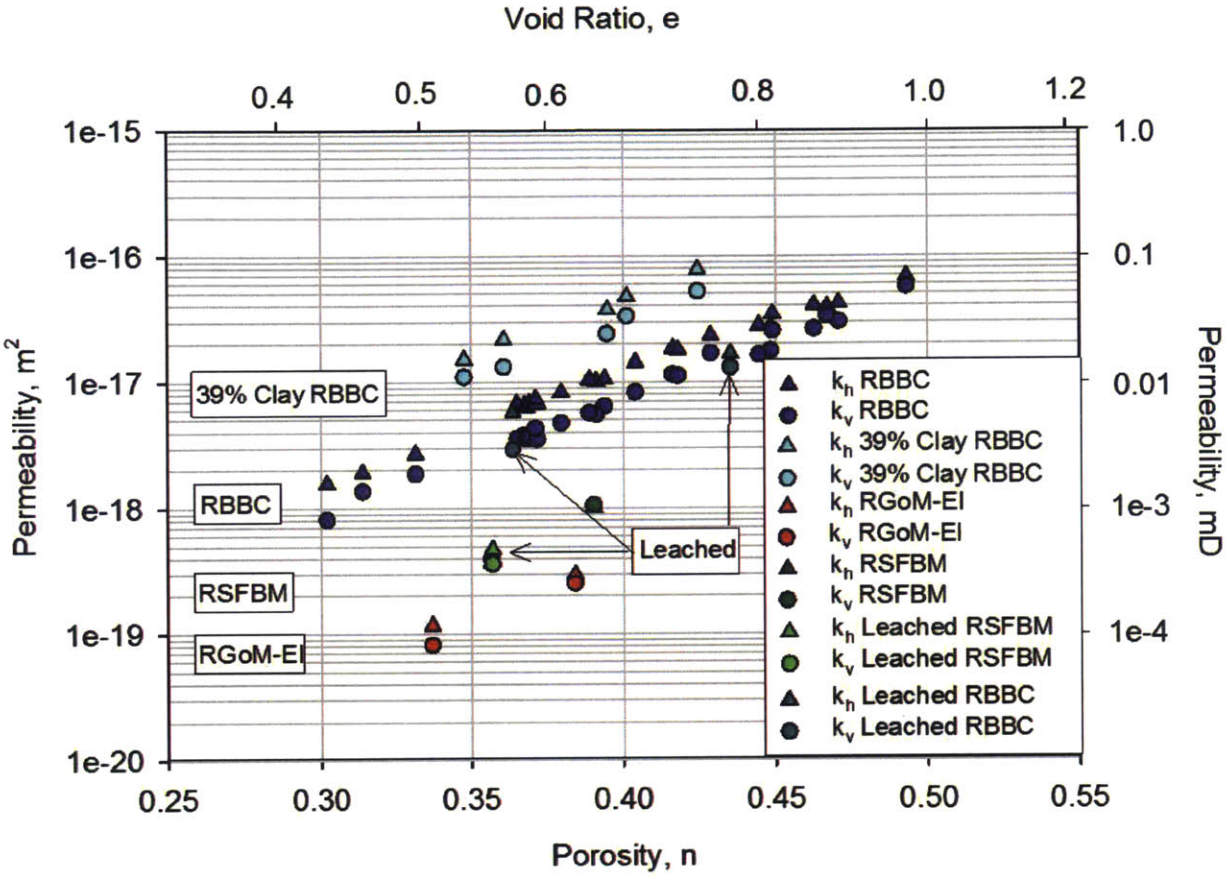

Figure 2-9: Vertical and horizontal permeability measurements taken using cubic specimen constant head testing in a triaxial cell from Adams (2014) show a general decrease in permeability as porosity decreases.

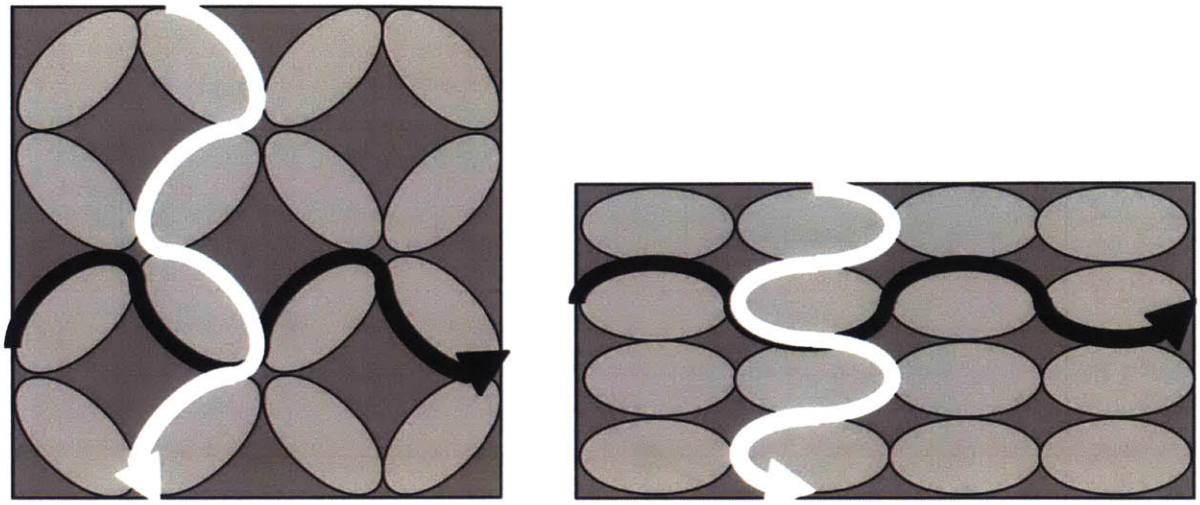

Figure 2-10: A schematic representation of flow in vertical and horizontal directions through an array of ellipses illustrates how flowpath tortuosity affects permeability anisotropy (Scholes et al, 2007).

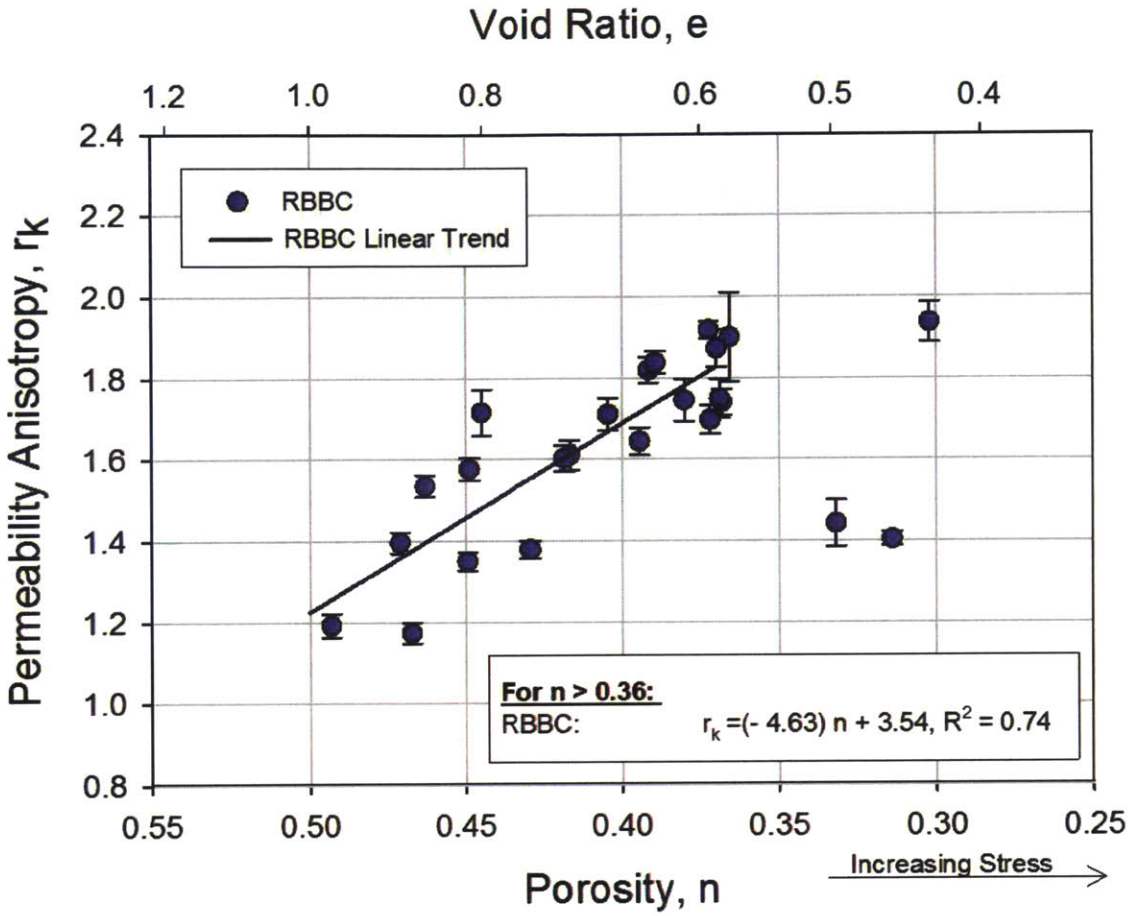

Figure 2-11: Permeability anisotropy measurements taken on RBBC using cubic specimen constant head testing in a triaxial cell from Adams (2014) show anisotropy increases as porosity decreases to about 0.36.

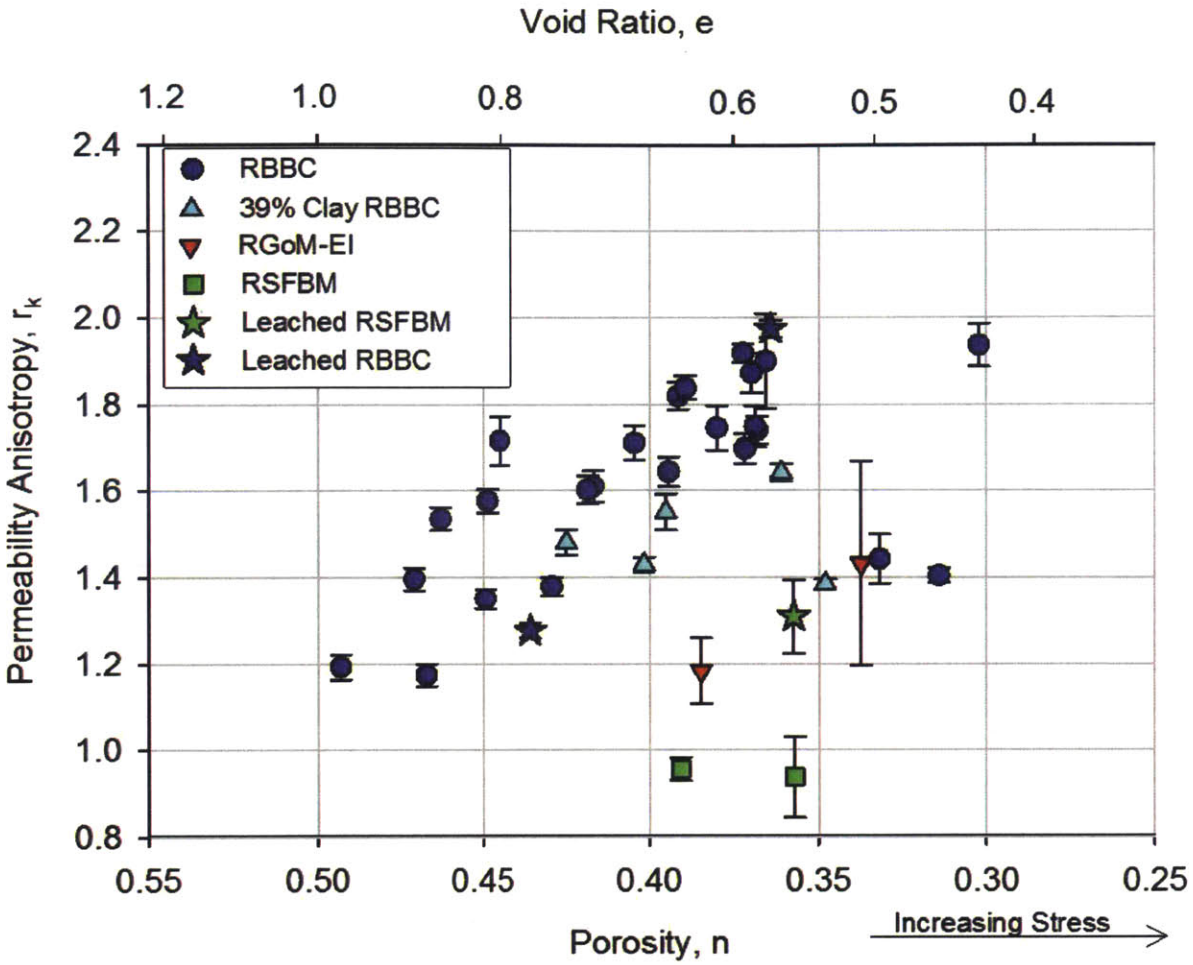

Figure 2-12: Permeability anisotropy measurements taken on various mudrocks and mudrock mixtures using cubic specimen constant head testing in a triaxial cell from Adams (2014) show anisotropy stays below 2.

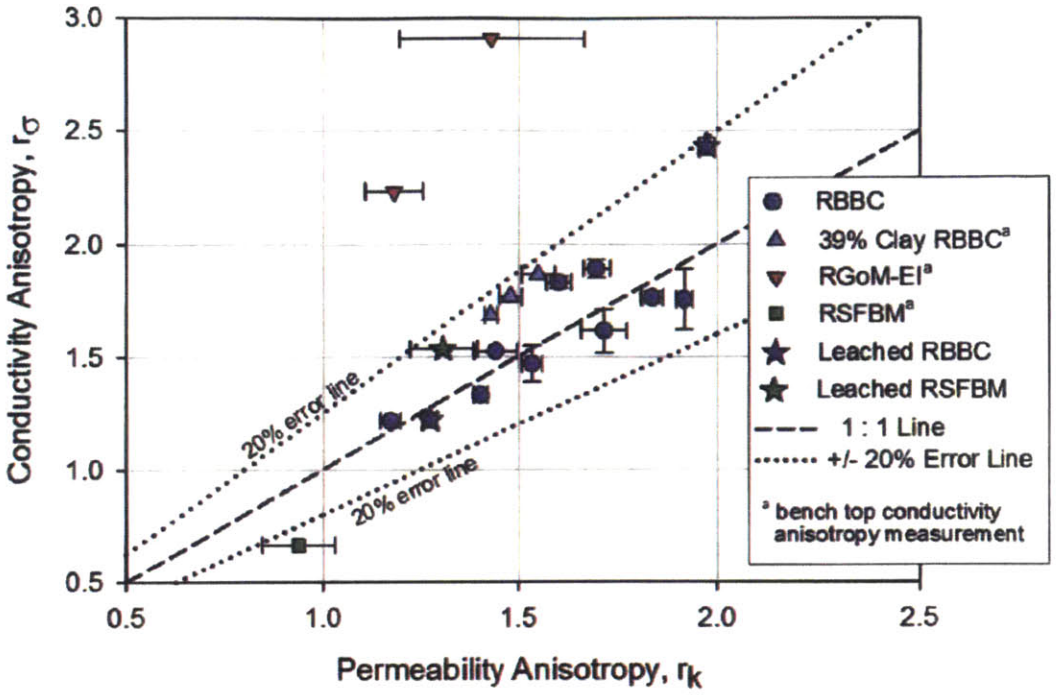

Figure 2-13: Adams (2014) measured a 1:1 correlation between permeability anisotropy and conductivity anisotropy with most mudrocks studied.

CHAPTER 3 - MATERIALS

3.1 INTRODUCTION

The purpose of this research is to identify trends in permeability anisotropy due to particle orientation in naturally-occurring mudrocks. Homogenized resedimented mudrocks are used in order to easily determine trends. Boston Blue Clay (BBC) and Gulf of Mexico – Eugene Island (GoM-EI) mudrocks are both used, in order to look at anisotropy trends in illite-rich and smectite-rich materials. The resedimented samples were compressed to a predetermined vertical stress and unloaded to an over-consolidation ratio (OCR) of 4. A pair of samples is loaded to virgin compression, then sheared horizontally in the direct simple shear (DSS) apparatus to determine the effect of shearing on permeability anisotropy.

This chapter starts by describing the origins, processing, and properties of the mudrock samples tested. It then describes the resedimentation procedure. At the end, we explain the horizontal shearing technique.

3.2 MUDROCK SAMPLES

Two naturally-occurring mudrock samples and one mudrock mixture were tested in this research: Boston Blue Clay (BBC), Boston Blue Clay mixed with 9% Montmorillonite (BBC + 9% Mont.), and Gulf of Mexico – Eugene Island (GoM-EI).

3.2.1 Boston Blue Clay (BBC)

Boston Blue Clay (BBC) is an illitic marine clay that underlies the greater Boston area in thicknesses from 20 to 40 m (Abdulhadi, 2009). It was deposited as a great submarine delta, as regional glaciers melted and sea levels rose during the Holocene Epoch (last 10,000 years). It is characterized by a greenish-gray color with occasional shells. Due to desiccation and oxidation, the top 15 feet or so of the deposit exhibits over-consolidated behavior and can be identified by a more yellowish color (Barosh and Woodhouse, 2012).

The sample of BBC used in this research is from Series IV, meaning that it is the fourth large homogenized sample of BBC collected for testing at MIT. It was collected in 1992 from the bottom of the excavation for the MIT Koch Biology Building, #68 (GPS Coordinates 42° 21.706', -71° 5.317') in Cambridge, MA (see Figure 3-1). The 2500 kg sample was taken from an approximate depth of 12 m (Abdulhadi, 2009). The sample was processed in two units. Each unit was mixed with tap water and passed through a #10 sieve to remove large sands, gravels, and shells. The slurry was then oven dried at 60° C and ground in a roller mill press to make a powder to achieve 95% passing the #100 sieve. The two units were then blended and stored in 40 gallon drums (Cauble, 1997) (see Figure 3-2).

BBC is classified by the Unified Soil Classification System (USCS) as a "lean," or low-plasticity, clay (CL) (see Figure 3-3), derived from its plasticity index of 23 and liquid limit of 47. It is a mixture of silt and illitic clay (see Figure 3-4 and Figure 3-5). It has an external specific surface area, measured by nitrogen adsorption, of 24 m^2/g, and a total (internal + external) specific surface area, measured by methylene blue titration, of 49 m^2/g. These properties and more are summarized in Table 3-1.

BBC is used in this research due to its availability, the extent of research previously performed on it, and its high illite content. Most of the greater Boston area is underlain with BBC, making it very economically available. Furthermore, the Series IV BBC held in the MIT Geotechnical Laboratory is an abundant source. Due to its availability and proximity to MIT and other research institutions, its mechanical properties have been studied extensively since 1961 (Bailey, 1961). An overview of previous RBBC studies at MIT is shown in Table 3-2, adapted from Horan (2012). The permeability anisotropy of RBBC has been extensively studied recently by Adams (2014). Due to the large extent of previous research on RBBC, the testing of it allows a researcher a vast amount of data for comparison with his/her own results. Finally, RBBC provides a good bench mark for how an illitic mudrock will behave, allowing for comparison with more smectitic materials.

3.2.2 Boston Blue Clay w/ 9% Montmorillonite (BBC + 9% Mont.)

In order to investigate how smectite content affects permeability anisotropy, selective BBC samples were resedimented from a mixture of 91% BBC Series IV and 9% montmorillonite by weight (RBBC + 9% Mont.). This mixing process was performed during the resedimentation mixing process (see Section 3.2.1). The montmorillonite used was manufactured Puregold® Gel powder, which is industrially produced for use in drilling fluid (Bentonite CAS# 1302-78-9) (see Figure 3-6).

3.2.3 Gulf of Mexico – Eugene Island (GoM-EI)

The Gulf of Mexico – Eugene Island mudrock (GoM-EI) comes from Eugene Island blocks 330 and 316 (see Figure 3-7). Core was collected from about 8,000 ft below the seafloor from one boring in each block. The core was removed using hand tools, the sandy portions were discarded, and the clayey core was broken into fist-sized chunks using a sledge hammer. The chunks were laid out to air dry for 18 days. The material was then shipped to an industrial processor, where the material was ground to achieve 99% passing the #100 sieve and homogenized (Betts, 2014). It is now stored in 5-gallon buckets (see Figure 3-8).

GoM-EI is classified by the USCS as a "fat," or high-plasticity, clay (CH) (see Figure 3-3). This classification is derived from its plasticity index of 63 and liquid limit of 87. It is a mixture of silt and clay, with a clay fraction mineralogy of both smectite and illite (see Figure 3-4 and Figure 3-5). It has an external specific surface area, measured by nitrogen adsorption, of 43 m^2/g, and a total (internal + external) specific surface area, measured by methylene blue titration, of 267 m^2/g. These properties and more are summarized in Table 3-1.

GoM-EI was selected as a test material for two main reasons. Firstly, its high smectite content is believed to foster high permeability anisotropy, due to the high aspect ratios of smectite particles. Secondly, it is a marine deposit from an area of high petroleum exploration interest, so its behavior is immediately beneficial to our UT Geofluids sponsors.

3.3 RESEDIMENTATION

The samples used for this study, along with most studies performed at the MIT Geotechnical Lab, are resedimented. Resedimentation is a process where a homogenous soil slurry is K_0 (one-dimensional) consolidated in the lab. This technique is performed in order to control homogeneity and stress history in test specimens, while "replicating the stress state and structure found in nature" (Germaine and

Germaine, 2009). Such control overcomes a major obstacle in investigating trends in soil behavior - sample heterogeneity. In soil testing for site characterization, sample heterogeneity is recognized in a testing program, and a factor of safety is implemented in design to account for measured and expected further heterogeneity. When tests are being compared for soil behavior, however, heterogeneity noise can crowd out soil behavior trends. This problem is especially pronounced when taking sensitive measurements, such as permeability anisotropy.

Resedimentation was initially performed at MIT by creating large soil cakes, partially saturated and compressed up to no more than 200 kPa, out of which individual specimens were cut for testing (Ladd and Varallyay, 1965). Germaine (1982) later modified the technique to create better saturation within the samples. Seah (1990) modified the technique more by extruding resedimented specimens from their confining tubes and monitoring their consolidation on a remote data acquisition system. Abdulhadi (2009) introduced the technique of preparing individual resedimented specimens for each test, reducing the amount of trimming needed and allowing much greater stresses to be achieved by virtue of stress being the product of load and area. The samples resedimented in this research use all of the aforementioned techniques. When possible, multiple test specimens are taken along the vertical profile of individual resedimented samples.

The mixing and loading procedures are described further in this section.

3.3.1 Mixing Procedures

To start resedimentation, a soil slurry is mixed using various proportions of soil powder, sea salt, and distilled water. The soil powder is prepared as described in Section 3.1. Sea salt is used to mimic natural conditions, and is mixed with distilled water to create a desired salinity. The salinity may be selected to represent *in-situ* salinity or to meet other criteria.

Salt water density changes as a function of salinity. The density change cannot be calculated using phase relations assuming constant salt and distilled water densities. This is due to a coupling effect between salt density and saltwater salinity. To account for this coupling, a "salt mixing guide" is used at the MIT Geotechnical Laboratory that uses empirical saltwater density measurements from Sharqawy et al (2010). The density of pure water is calculated as a function of temperature using Equation 3-1:

$$\rho = (-4.95 * 10^{-6})T^2 + (-7.77 * 10^{-6})T + 1.00034 \quad (3\text{-}1)$$

where:
ρ = density of pure water [g/cm^3]
T = temperature [°C]

The effective sea salt density, which is a theoretical number that can be added to pure water density using phase relations to calculate sea salt water density, is calculated as a function of salinity using Equation 3-2:

$$\rho = (1.06 * 10^{-5})c^2 + (-0.0075)c + 4.17 \quad (3\text{-}2)$$

where:
ρ = effective density of sea salt [g/cm^3]
c = salinity of sea salt water [g/L]

The proper amounts of soil powder, sea salt and distilled water are determined to achieve the desired pore fluid salinity and to produce a flowable slurry without allowing particle sedimentation during mixing. The water content needed to make a flowable slurry varies by material and batching salinity, but is typically close to twice the liquid limit (Germaine and Germaine, 2009).

The soil powder, distilled water, and salt are mixed with a Kitchen Aid® mixer (see Figure 3-9). The salt is first added to the water and allowed to dissolve. The soil powder is then slowly added to the salt water to prevent excessive powder from blowing into the air as dust.

After mixing, the slurry is sealed to prevent moisture loss and allowed to equilibrate for 24 hours, so that the clay particles' double layers can absorb water to equilibrium. The slurry is then remixed to undo any particle sorting that might have occurred during equilibration time. Finally, the slurry is placed under about 1 atmosphere of vacuum pressure for 20-30 minutes and agitated to remove the majority of the entrapped air bubbles. To create the vacuum pressure, the Kitchen Aid mixing bowl is placed inside a large vacuum chamber, which is connected to a vacuum pump (see Figure 3-10). The chamber includes a valve that allows for the vacuum pressure to be maintained while the pump can be shut off and a clear lid that allows the user to observe the evacuation process and prevent the slurry from "boiling over." This process creates a uniform slurry of soil solids, salts, and water, ready to compress to a desired stress.

The effect of salts dissolving into the pore water from the soil powder is not taken into account during mixing. However, pore fluid salinity measurements are made on all test samples after resedimentation to obtain test condition pore fluid salinities. These measured salinities are the salinities used in calculations.

3.3.2 Loading Precedures

Once the slurry is mixed, equilibrated, and evacuated, it is ready to be poured into a sedimentation column and loaded.

The sedimentation columns used are clear acrylic tubes varying from 9" to 18" long and from 1.7" to 3" in diameter (see Figure 3-11). They are pre-coated with a thin layer of silicon oil to minimize the effect of sidewall friction on the specimen. The tubes are placed in sea salt water baths of the same salinity as the batching pore water salinity. A PVC spacer is placed at the bottom of the tube with a porous stone and two pieces of oversized nylon filter paper. The filter paper used is 05/15 nylon Sefar Nitrex®. The stone and filter papers should be close enough to the inner diameter of the acryilic tube to not allow leaking of soil slurry into the bath water, but far enough from the acrylic that they don't create unnecessary sidewall friction. The PVC spacer needs to have clearance between the inner diameter of the acrylic tube to allow water drainage from the soil specimen, through the filter papers and porous stone, past the PVC spacer and into the water bath.

The soil slurry is resedimented similar to the standard oedometer one-dimensional consolidation test frequently used in Geotechnical Engineering (ASTM D2435). The soil slurry is carefully placed inside the sedimentation column to avoid the creation of air bubbles within the slurry. This is done with the use of a tremie made out of a plastic funnel connected to a plastic tube (see Figure 3-12). The slurry is tremmied from the bottom of the column to the top. Care is taken not to create a plug-flow within the funnel or tube, as this will entrap air bubbles and force them down into the soil matrix. Once the sedimentation column is filled with the desired amount of slurry, a porous stone and two filter papers are placed on top of the slurry. If the top of the slurry doesn't reach the top of the sedimentation column, a Shop-Vac® can be used to hold the top stone during placement. Again, this stone-and-paper setup must have enough clearance from the acrylic tube to not transfer undue load into the sidewall, yet close enough to the tube to prevent extrusion of excessive soil slurry. The water bath is filled, with sea salt water of the same salinity as the batched pore fluid, to above the bottom of the specimen, and the water height is marked. This water height is maintained during resedimentation despite evaporation by adding distilled water to the water bath.

With the top porous stone and filter papers placed on the slurry, the loading process has begun. The stone and filter paper are left in place for several days as the first load. Next a small PVC spacer, identical to the spacer placed at the base of the sedimentation column, is placed and left for a couple days. Subsequent loads are placed by approximately doubling the existing load, creating a load-increment-ratio (LIR) of about 1. The loads are initially placed on top of the top PVC spacer. When the loads get bigger (on the order of kilograms), they are placed beneath the specimen on a hanger, as shown in Figure 3-13. When using the hanger, PVC spacers, and/or porous stones, their masses are included in the load calculation. If stresses higher than about 0.1 MPa are desired (the stress capacity depends on the consolidation tube diameter), the specimens are quickly transferred to a consolidometer with a 100:1 lever arm (see Figure 3-15). During this process, the bottom PVC spacer is replaced with a longer one, to create a floating cylinder wall and reduce sidewall friction. If stresses higher than 1.5 MPa are desired, the specimen is again moved to an air-pressure load frame, where they can be consolidated to about 10 MPa (see Figure 3-16). For each load, displacements are measured using a linear variable differential transducer (LVDT) (see Figure 3-14). New loads are only placed after the previous load reaches 90% consolidation according to the Taylor (1948) square root of time method (see Figure 3-17).

When the maximum desired consolidation stress is achieved, the load is maintained on the specimen for a log cycle of time beyond the time for end of primary consolidation as determined by the Casagrande logarithm of time method (see Figure 3-18). This makes sure that the excess pore pressures are dissipated to a degree that any excess pressures are negligible. It also allows for the determination of the coefficient of secondary consolidation or creep, c_α.

The specimen is finally unloaded to an over-consolidation ratio (OCR) of 2, and then to an OCR of 4, meaning the final load is ¼ of the maximum load. This is done for several reasons. An OCR of 4 brings most soils close to an isotropic stress state, meaning the K_0 value, or lateral stress ratio, is close to 1. An over-consolidated mudrock exhibits stiffer behavior at low stresses, minimizing strains from extrusion, handling, and trimming (Santagata, 1994). The final over-consolidated stress is also maintained on the specimen for at least a log cycle of time beyond the time to end of primary consolidation.

When the sample is ready to be trimmed and tested, it is completely unloaded and extruded from the consolidometer. It is immediately removed from the water bath and the water in the sedimentation tube above the specimen is drained, to minimize specimen swelling. For the low-stress specimens (i.e. the specimens loaded to 0.1 MPa for CRS testing) the resedimented specimens can be extruded by

hand. For the medium and high stress specimens (i.e. the specimens used for cubic specimen constant head testing), a hydraulic jack is used to for extrusion (see Figure 3-19). When the specimen is unloaded and extruded, the OCR 4 stress state is maintained, as the process is undrained. In other words, negative pore pressures develop that are equal in magnitude to the effective stress of the soil matrix. This negative pore pressure is often called apparent cohesion, as it is what holds the soil together in a zero stress statae.

The resedimentation process provides homogeneous, reproducible specimens with known stress histories, which can then be used in research to determine material trends. It allows for incredibly repeatable results in CRS permeability anisotropy testing.

3.3.3 Resedimentation Results

Sixteen resedimented specimens, consisting of RBBC, RBBC + 9% Mont., or RGoM-EI are fabricated and used for this testing program. Table 3-3 lists the resedimented specimens, along with their diameters, maximum effective stresses applied, sampling effective stresses, and test(s) they are used for.

Specimen pore fluid salinities are measured using a conductivity meter, calibrated for sea salt water. For the cubic specimens, salinity is measured on specimen trimmings before testing and on a portion of the cubic specimen after testing. Salinity test results for the cubic specimens are shown in Table 3-4. The average of the two salinities is used for phase relation and permeability calculations. No conclusive trend is observed indicating an increase or decrease in pore fluid salinity during testing. For the CRS specimens, one salinity measurement is performed on a portion of the resedimented sample that is not being used for CRS testing. Salinity test results for the CRS specimens are shown in Table 3-5. This salinity is used for phase relations and permeability calculations for all CRS tests performed on portions of that resedimented sample.

3.4 SAMPLE SHEARING

In order to explore the effect of horizontal shearing on permeability anisotropy, a few resedimented samples are sheared in a Geonor® direct simple shear (DSS) device prior to permeability anisotropy measurement (see Figure 3-20). Permeability anisotropy is then measured on the sheared samples using constant rate of strain (CRS) consolidation testing (see Chapter 4).

Samples of RGoM-EI are resedimented to 0.1 MPa and unloaded to 0.025 MPa, before being trimmed and placed into the DSS device. Once in the DSS device, they are reloaded to 0.14 MPa, in order to get the specimen to virgin compression.

In the normally-consolidated state, the samples are sheared to 29.5% shear strain. In a DSS device, the shear strain is distributed over the height of the sample, through the use of a rubber membrane supported by a wire coil, or "slinky." In other words, when the side view of the sample is a rectangle prior to shearing, it turns into a parallelogram with non-right angles after shearing (see Figure 3-22). The stiff membrane, combined with zero axial displacement creates an undrained, or constant volume, shear. As horizontal shear happens through the specimen, horizontal fabric alignment is expected, along with horizontal micro-cracks, creating more permeability anisotropy (Daigle and Dugan, 2011; Dewhurst et al, 1996; Arch and Maltman, 1990). The mechanism of fabric alignment is illustrated in Figure 3-21.

Once the samples are sheared, they are removed from the DSS apparatus and prepared to be placed into the CRS apparatus for permeability anisotropy testing. This is done by coring smaller CRS specimens from larger sheared DSS specimens using piano wire and two acrylic cylinders as guides (see Figure 3-23). The 0.5 mm steel piano wire is inserted through the sheared specimen using a hollow 1 mm diameter rigid steel tube, clamped at the front end. This procedure is derived from the procedure described in Germaine and Germaine (2009) for removing intact samples from Shelby tubes. The smaller cored sample is then ready for trimming and testing in the CRS apparatus (see Chapter 5).

Table 3-1: The properties of the materials used were intended to vary by smectite content, which directly controls the Atterberg limits and specific surface area.

	Mineralogy < 2 μm fraction				Atterberg Limits				Specific Surface Area [m^2/g]	
	Clay Fraction [%]	Illite [%]	Smectite [%]	USCS Classification	Liquid Limit [%]	Plastic Limit [%]	Plasticity Index [%]	Specific Gravity	External	Internal & External
BBC	56	92	1	CL	47	24	23	2.778	24	49
39% Clay BBC*	-	-	-	-	-	-	-	2.750	-	43
BBC + 9% Mont.	-	-	-	CH	76	22	54	2.78	-	-
GoM-EI	63	30	65	CH	87	24	63	2.775	43	267
SFBM*	52	47	45	CH	60	32	29	2.690	21	121

*These mudrocks are not used for testing in this study

Table 3-2: Overview of previous studies performed using RBBC (after Horan, 2012)

Series	Year	Researcher	Topic	Testing Performed
1	1961	Bailey	Effect of salt concentration on undrained shear strength	-
	1963	Jackson	Thixotropy	Triaxial
	1964	Varallyay	Influence of stress system on undrained strength	Triaxial
	1965	Ladd	Use of pressure transducers to measure soil pressure	-
	1965	Preston	Sample Disturbance	Triaxial
	1966	Braathen	Disturbance effects on undrained strength	Triaxial
	1967	Dickey	Development of plane strain device	Plane strain device
	1967	Rixner	Behavior in plane strain at OCR 1, 2, & 4	Plane strain device
	1968	Bovee	Behavior in plane strain at OCR 1, 2, & 4	Plane strain device
	1970	Kinner	Behavior of strip footings during undrained loading	Model footing tests
II	1982	Germaine	Cross-anisotropic behavior at OCR 4	DSC, Triaxial
	1984	Bensari	Stress-strain and yielding behavior	Triaxial
	1985	O'Neill	Anisotropy of thixotropic clay	DSC, Triaxial
	1986	Fayad	Volumetric and undrained behavior	Triaxial
	1987	Malek	Behavior under cyclic loading	DSS
III	1988	Walbaum	Investigation of sample disturbance	DSS
	1988	Sheahan	Modification of computer controlled triaxial apparatus	Triaxial
	1989	DeGroot	Behavior in undrained multidirectional DSS at OCR 1	DSS
	1990	Ahmed	Normalized behavior in DSS	DSS
	1990	Seah	Anisotropy at OCR 1	DSC
	1991	Ting	Performance of sand drains	Model Testing
	1991	Sheahan	Time dependent materials	Triaxial
	1992	Ortega	Computer automation of DSS	DSS
	1993	Cauble	Cyclic and post cyclic behavior in simple shear	DSS
	1994	Santagata	Simulation of sampling disturbance in soft clays using triaxial tests	Triaxial
IV	1994	Sinfield	Simulation of sampling and effects on compression and shear	CRS, Triaxial
	1996	Cauble	Behavior of model suction caisson	Model Caisson
	1998	Santagata	Pre-failure behavior	Triaxial
	1998	Force	Strain rate selection in triaxial tests	CRS
	2000	Gonzalez	Investigation of CRS consolidation	CRS
	2009	Abdulhadi	Stability of boreholes	Triaxial, Model BH
	2009	Moniz	Normalized behavior in triaxial extension	Triaxial
	2011	Casey	Significance of end restraint in triaxial testing	Triaxial
	2011	Adams	Measurement of hydraulic conductivity in CRS	CRS
	2012	Horan	Effect of salt on normally consolidated behavior	CRS, Triaxial
	2014	Casey	Consolidation and strength behavior	Triaxial
	2014	Adams	Permeability and resistivity anisotropy	cubic specimen permeameter
	2015	Dierieh	SEM image analysis	SEM
	2015	Marjanovic	P and S Wave Velocity	Triaxial
	2015	Nordquist	Permeability anisotropy	CRS

Table 3-3: Resedimented specimens used in testing program

Test ID	Test(s) Run	Mudrock	σ'_{max} [Mpa]	σ'_s [Mpa]	Diameter [cm]
RS307	HC 058	RGoM-EI	0.1	.025	7.6
RS371	HC 054	RBBC + 9% Mont.	9.51	2.40	7.6
RS384	HC 055	RBBC + 9% Mont.	3.12	0.81	7.6
RS416	HC 057	RBBC + 9% Mont.	0.78	0.20	7.6
RS417	HC 056	RBBC + 9% Mont.	6.27	1.55	7.6
RS418	HC 059	RGoM-EI	9.68	2.37	7.6
RS419	HC 060	RGoM-EI	6.27	1.55	7.6
RS421	CRS 1415, 1416, 1417	RBBC	0.1	0.025	4.3
RS422	CRS 1412, 1413, 1414	RBBC	0.1	0.025	4.3
RS425	CRS 1422, 1423, 1424, 1425	RBBC	0.1	0.025	4.3
RS426	CRS 1418, 1419, 1420, 1421	RBBC	0.1	0.025	4.3
RS431	CRS 1426, 1427, 1428, 1429	RGoM-EI	0.1	0.025	4.3
RS432	CRS 1430, 1431, 1432, 1433	RGoM-EI	0.1	0.025	4.3
RS433	CRS 1437, 1438, 1439, 1440	RGoM-EI	0.1	0.025	4.3
RS434	CRS 1441, 1442, 1443, 1444	RGoM-EI	0.1	0.025	4.3
RS436	DSS 835,836 to CRS 1435,1436	RGoM-EI	0.1	0.025	7.6

Table 3-4: Batched and measured pore fluid salinity values for resedimented specimens used for cubic specimen constant head testing.

Test ID	Test Run	Mudrock	Batched Salinity* [g/L]	Measured Salinity [g/L]			
				Before Test		After Test	
				Average	St.Dev.	Average	St.Dev.
RS307	HC 058	RGoM-EI	80	50.96	0.5	60.32	0.5
RS371	HC 054	RBBC + 9% Mont.	16	27.35	0.97	20.59	0.97
RS384	HC 055	RBBC + 9% Mont.	16	22.58	0.71	17.9	0.18
RS416	HC 057	RBBC + 9% Mont.	16	24.02	0.39	18.8	0.34
RS417	HC 056	RBBC + 9% Mont.	16	19.25	1.45	18	0.25
RS418	HC 059	RGoM-EI	80	82.31	3.8	87.5	4.6
RS419	HC 060	RGoM-EI	80	81.71	2.34	73.22	1.04

*Batched salinity refers to salinity of saltwater added to the slurry at the beginning of resedimentation.

Table 3-5: Batched and measured pore fluid salinity values for resedimented specimens used for CRS testing.

Test ID	Tests Run	Mudrock	Batched Salinity* [g/L]	Measured Salinity [g/L]	
				Average	St. Dev.
RS421	CRS 1415, 1416, 1417	RBBC	16	20.85	1.39
RS422	CRS 1412, 1413, 1414	RBBC	16	20.12	0.32
RS425	CRS 1422, 1423, 1424, 1425	RBBC	16	25.21	0.56
RS426	CRS 1418, 1419, 1420, 1421	RBBC	16	29.74	0.36
RS431	CRS 1426, 1427, 1428, 1429	RGoM-EI	80	74	3.5
RS432	CRS 1430, 1431, 1432, 1433	RGoM-EI	80	67.2	1.79
RS433	CRS 1437, 1438, 1439, 1440	RGoM-EI	80	83.94	4.75
RS434	CRS 1441, 1442, 1443, 1444	RGoM-EI	80	74.91	1.88
RS436	DSS 835,836 to CRS 1435,1436	RGoM-EI	80	78.82	4.91

*Batched salinity refers to salinity of saltwater added to the slurry at the beginning of resedimentation.

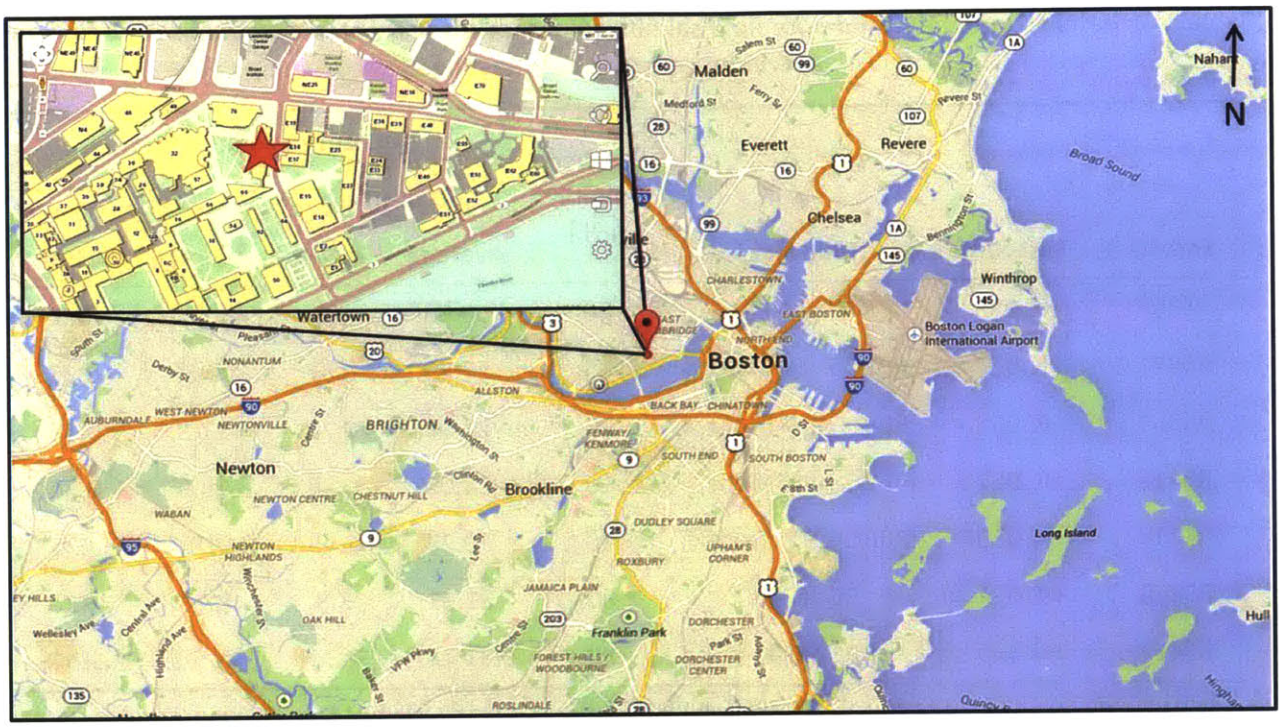

Figure 3-1: BBC Series IV was collected from the excavation of the MIT Koch Biology Building (#68) in 1992.

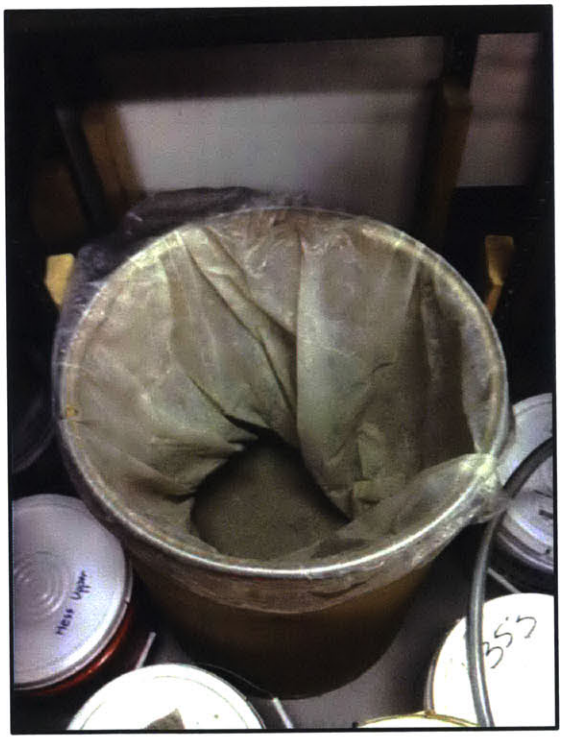

Figure 3-2: The BBC Series IV powder used has a grayish color and is stored in 40-gallon drums.

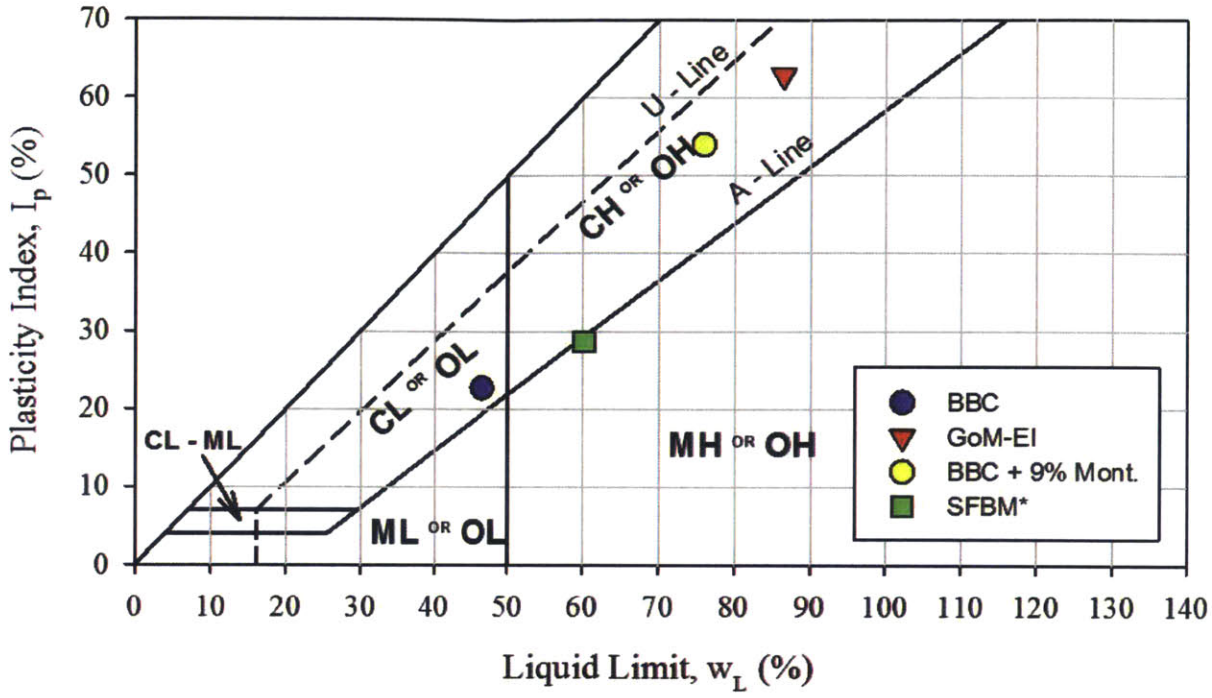

Figure 3-3: The Casagrande chart shows the range in plasticity of the mudrocks tested. (*SFBM mudrocks are not tested in this study)

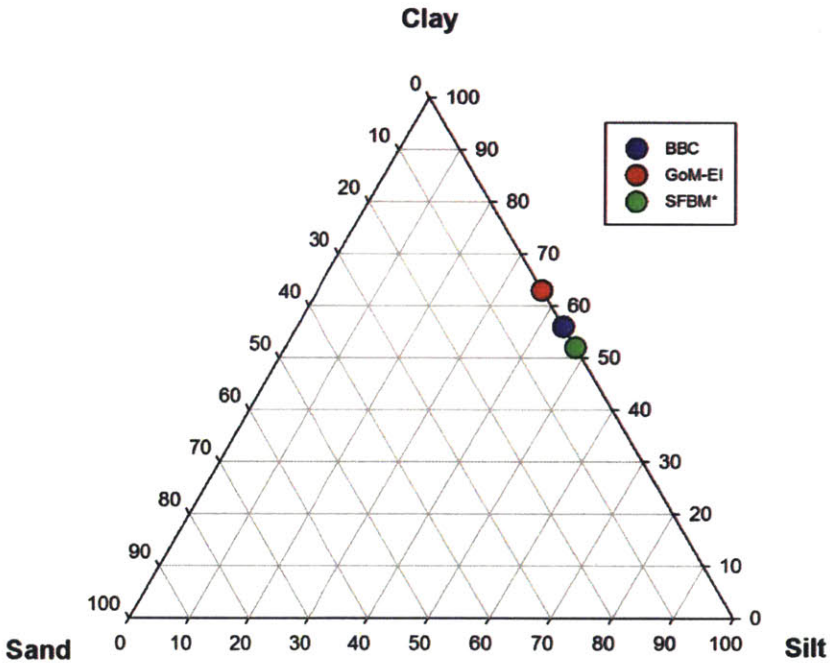

Figure 3-4: The bulk mineralogy of the materials, measured using X-ray diffraction, shows they have similar clay fractions with no sand. (*SFBM mudrocks are not tested in this study)

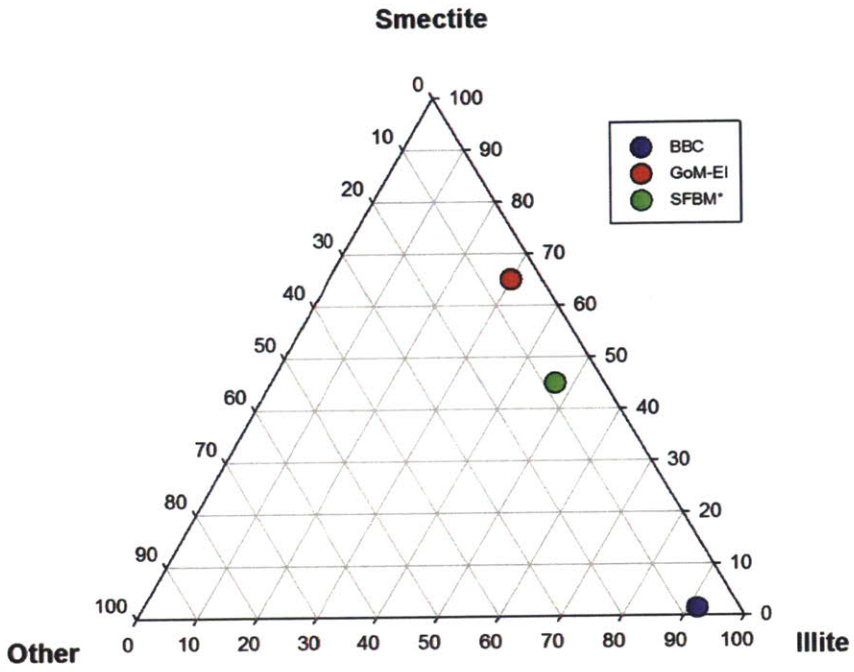

Figure 3-5: The clay fraction (< 2 μm) mineralogy of the materials, measured from X-ray diffraction, shows the range in smectite content between BBC, GoM-EI, and SFBM. (*SFBM mudrocks are not tested in this study)

Figure 3-6: Puregold® Gel bentonite powder for drilling fluid is mixed with BBC to make BBC + 9% Mont. This is done in order to look at the effect of smectite (bentonite) content on mudrock permeability anisotropy.

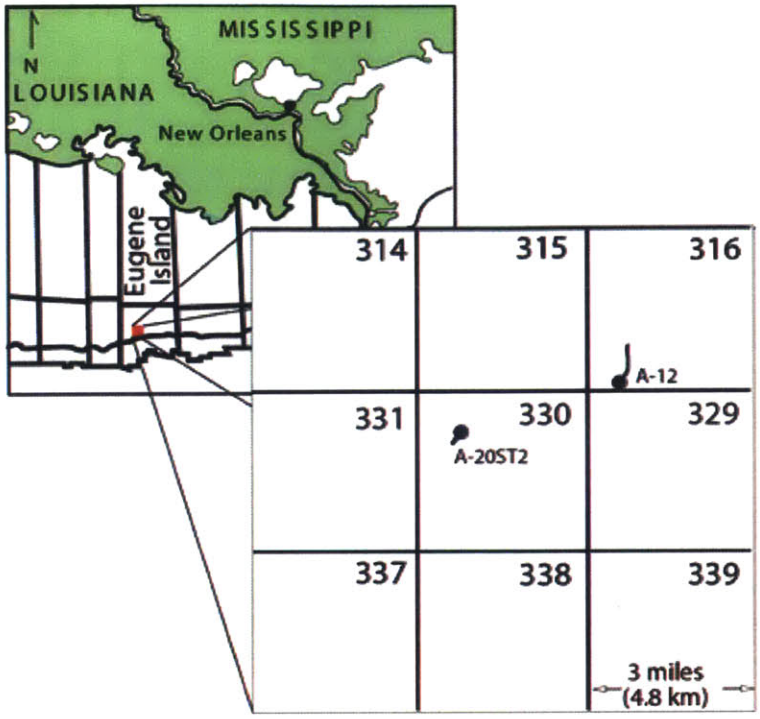

Figure 3-7: Two cores from Eugene Island Blocks 316 and 330 are the source of RGoM-EI.

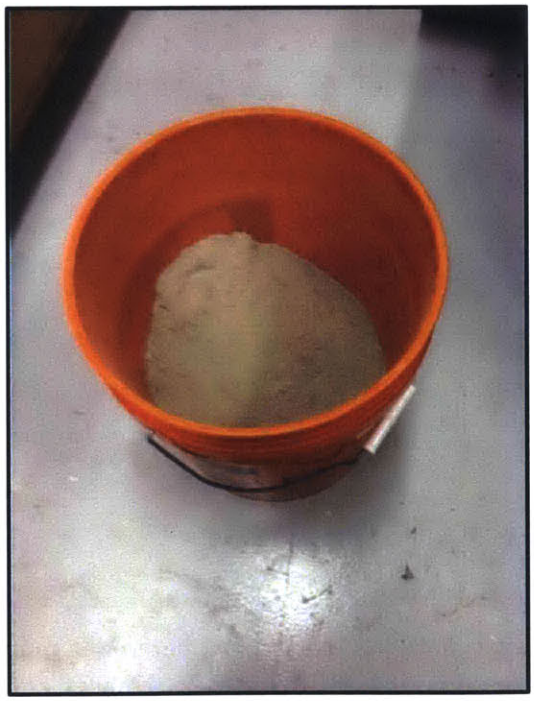

Figure 3-8: The GoM-EI powder used has a brownish color and is stored in 5-gallon buckets.

Figure 3-9: Soil powder is mixed into sea salt water using a Kitchen Aid® mixer (Casey, 2014).

Figure 3-10: Soil slurry is evacuated in vacuum chamber under approximately 1 atmosphere of vacuum pressure for 20-30 minutes to removed entrapped air.

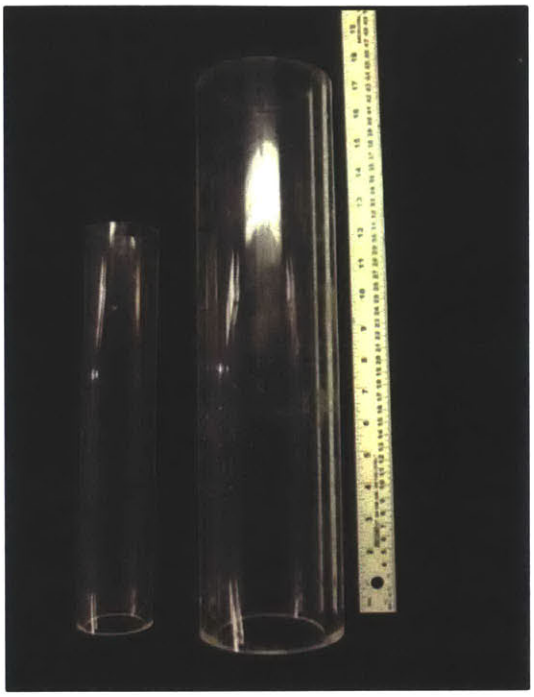

Figure 3-11: Acrylic sedimentation columns are used as consolidometers. The 1.7" diameter columns are used for CRS testing and the 3" diameter columns are used for cubic specimen constant head and DSS testing.

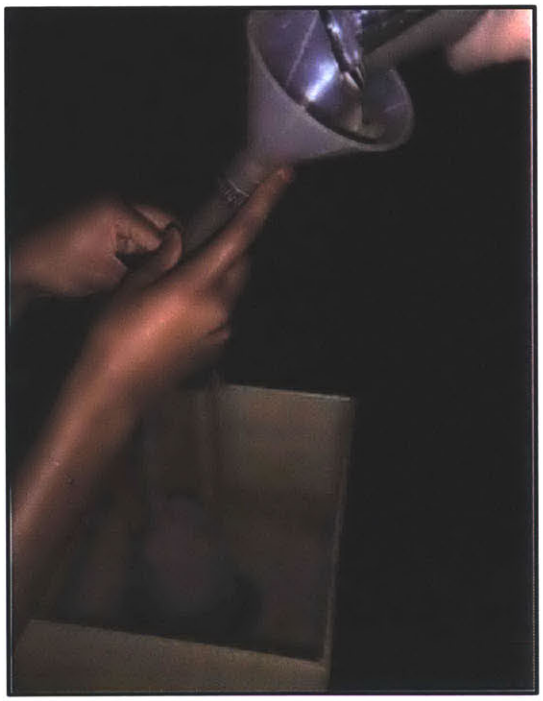

Figure 3-12: Soil slurry is carefully tremmied into acrylic sedimentation column prior to loading (Adams, 2014).

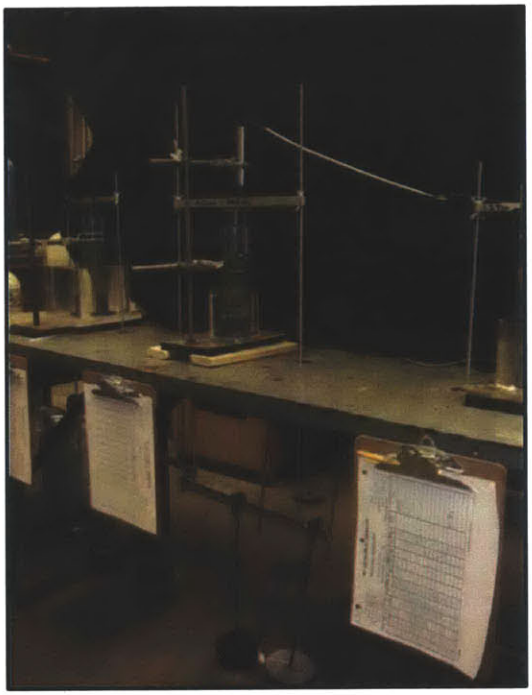

Figure 3-13: The "bench" setup transfers load from dead weights (below table) onto specimen (on table) using a metal hanger.

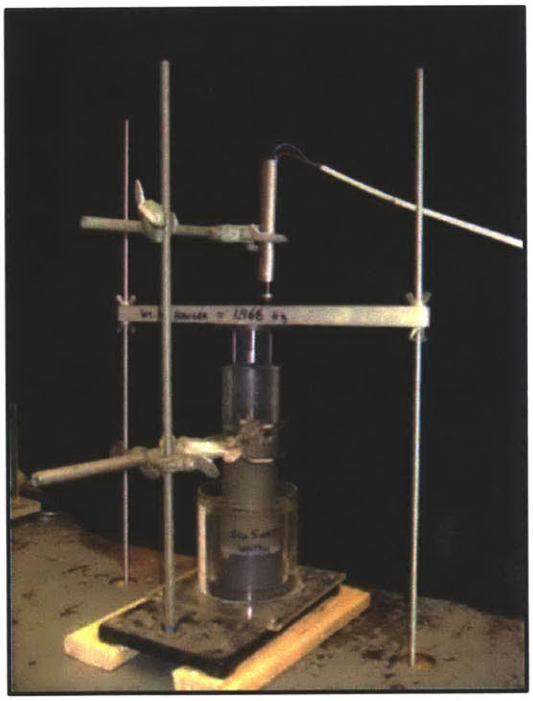

Figure 3-14: An LVDT is connected to the consolidometer to measure vertical settlement.

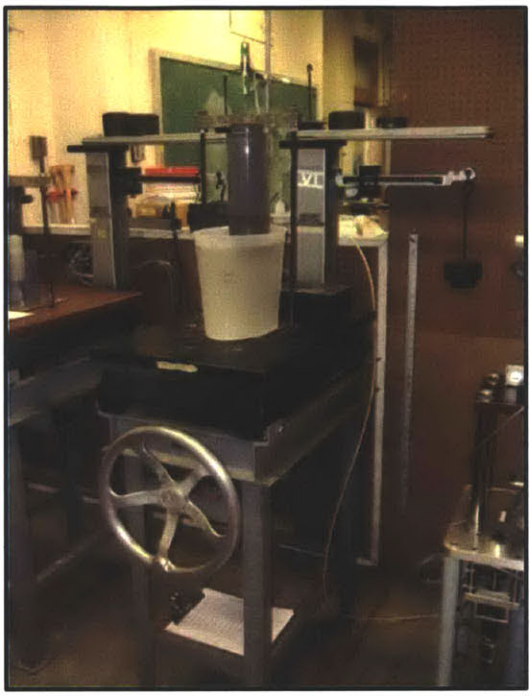

Figure 3-15: A consolidometer with a 100:1 lever arm is used to compress specimens from about 0.1 to 1.5 MPa. The lever arm magnifies the load provided by the weights.

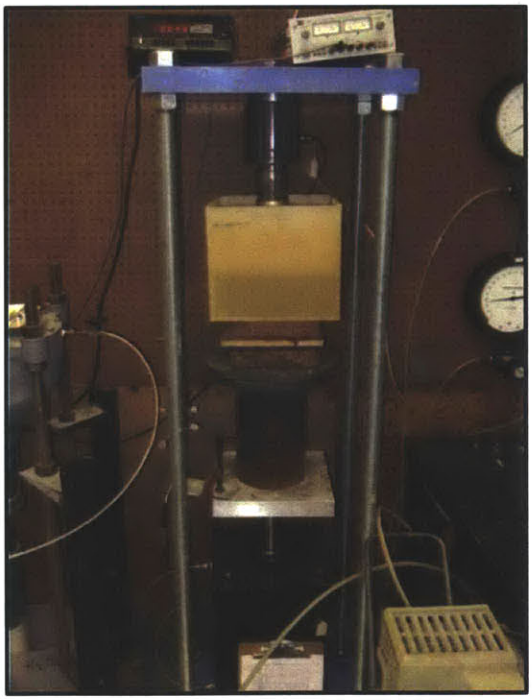

Figure 3-16: An air-pressure controlled load frame is used to compress specimens up to about 10 MPa. An air-pressure actuator at the base applies a load and a load cell at the top measures it.

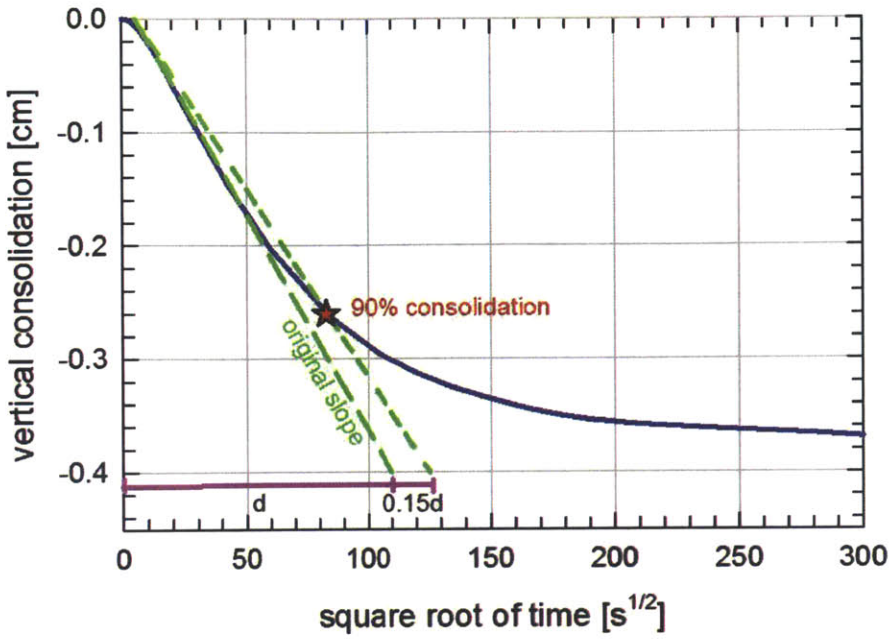

Figure 3-17: New loading increments are placed only after the sample reaches 90% of primary consolidation according to the square root of time method (Taylor, 1948). This example is from the maximum load of RS431.

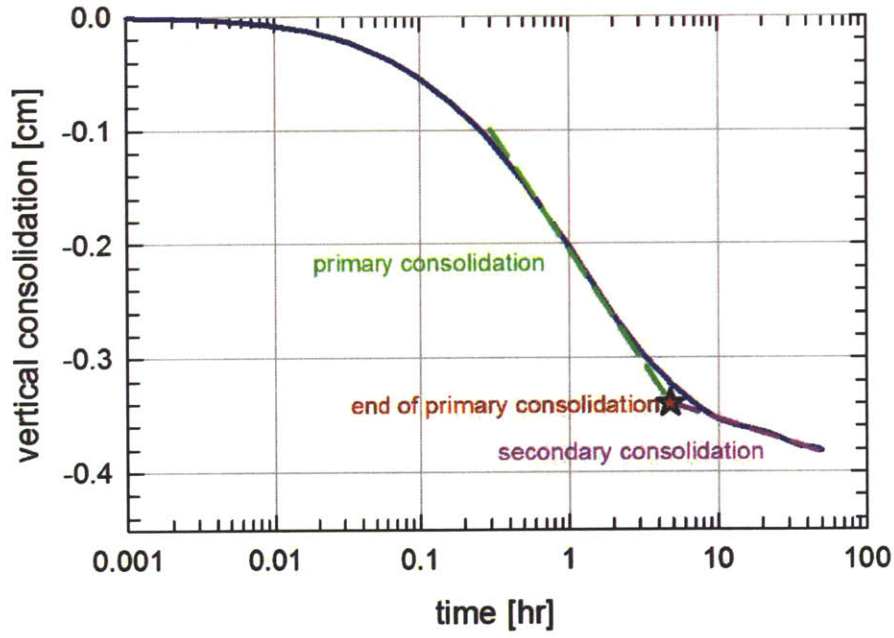

Figure 3-18: The maximum consolidation stress, as well as the final unloading stress, are left on the specimen for one log cycle of time beyond the end of primary consolidation, as determined by the Casagrande logarithm of time method. This example is from the maximum load of RS431.

Figure 3-19: Medium and high stress resedimented specimens (> 0.1 MPa) are extruded using a hydraulic jack (Fahy, 2014).

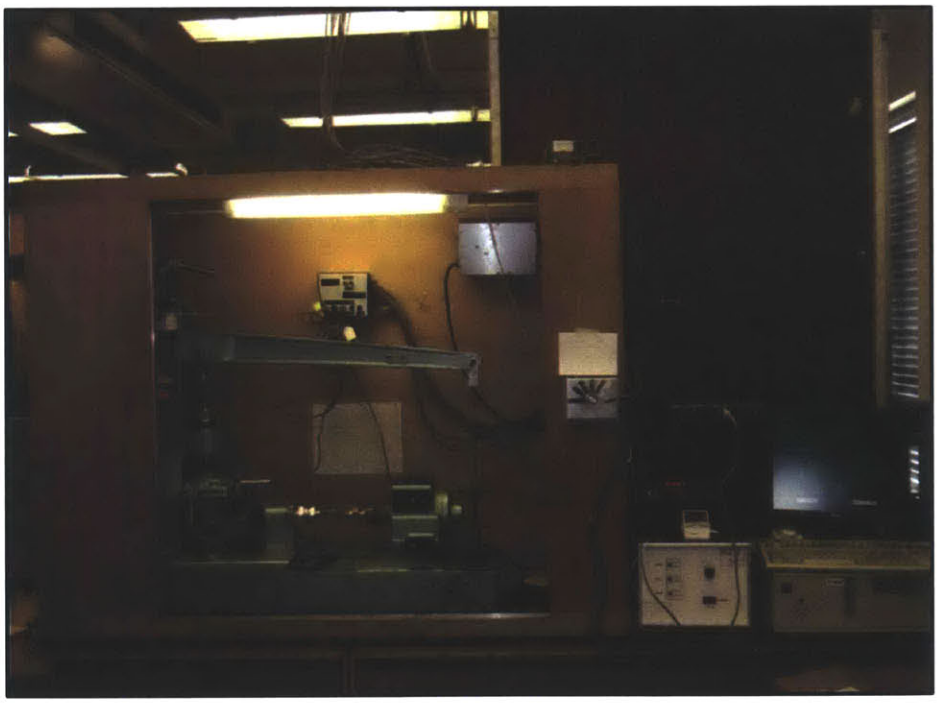

Figure 3-20: A DSS device is used to shear the samples in uniform horizontal simple shear. This is thought to create more fabric anisotropy than vertical compression alone.

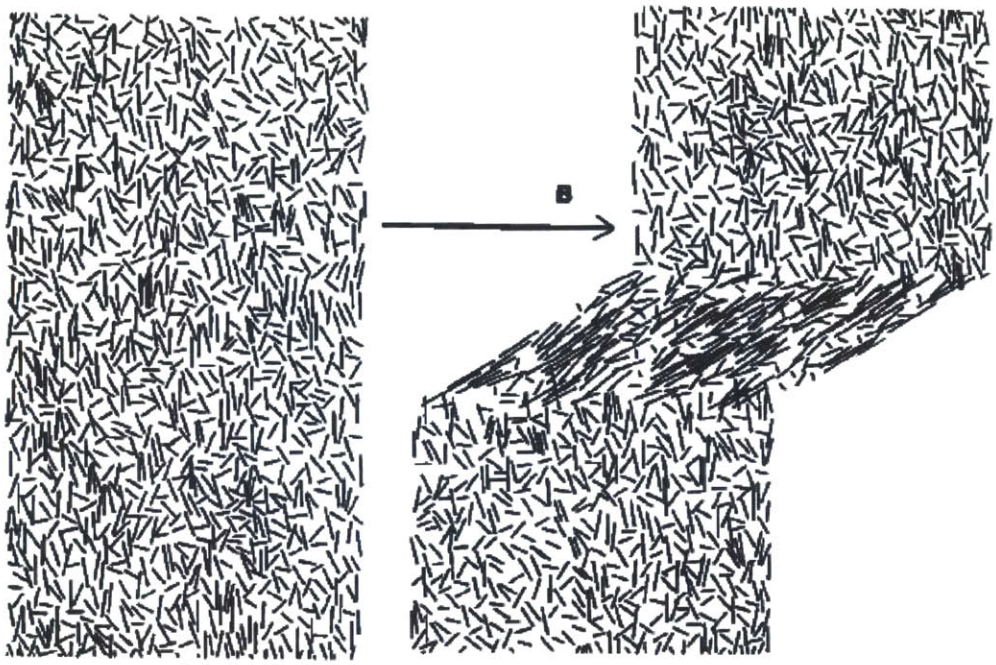

Figure 3-21: Simple shear is likely to orient elongated particles in the direction of shear (Arch and Maltman, 1990).

Figure 3-22: The coil-reinforced rubber membrane in concert with endcaps set to zero axial displacement create undrained horizontal simple shear in a DSS device. The profile of this sheared specimen (within the membrane) shows a parallelogram with non-right-angle corners.

Figure 3-23: A smaller specimen is cored out of the larger specimen sheared in the DSS device using piano wire and acrylic cylinders as guides.

CHAPTER 4 – EQUIPMENT

4.1 INTRODUCTION

Various types of geotechnical testing equipment are used for the study of permeability anisotropy which is included in this thesis. Most of the data are collected using an internally-developed radially-draining constant-rate-of-strain (CRS) consolidometer, run simultaneously with a commercially-available Trautwein® vertically-draining CRS consolidometer. The radially-draining CRS device, developed by the author, is an adaptation to the conventional vertically-draining device. While most of the data collected come from consolidated resedimented mudrocks, some were collected from resedimented mudrocks sheared in a direct simple shear (DSS) device prior to testing within the radially-draining and vertically-draining CRS devices. For comparison, permeability anisotropy is also measured using cubic specimen constant head permeability testing within a triaxial cell, technology recently developed at MIT (Adams, 2014). All test data are collected using in-house calibrated electronic transducers. The tests are controlled using feedback loops connecting the transducers to pressure-volume actuators (PVA) and mechanical drives via computer control systems. The transducer data are collected for analysis using a centralized data acquisition system.

4.2 RADIALLY-DRAINING CRS

Vertical permeability is routinely measured in conventional vertically-draining CRS equipment (Wissa, 1971). It is computed from measuring the buildup of an excess pore pressure gradient between the top and bottom of the specimen during one-dimensional compression. Thus the vertical permeability of a normally-consolidated mudrock can be characterized as a continuous function of vertical effective stress or porosity. A radially-draining CRS device is desirable, as it can characterize the horizontal (radial) permeability of a normally-consolidated mudrock as a continuous function of effective stress, or porosity, as well.

Radially-draining CRS equipment has infrequently been used prior to this study, and the soils tested have been compressed to relatively low stresses (Seah & Juirnarongrit, 2003; Yune & Chung, 2005; Yune & Jung, 2012). As such, equipment is not commercially available, and we are have not seen radially-draining CRS equipment made that can test mudrocks compressed to high stresses (40 MPa). Therefore, to obtain equipment, we modified a commercially-available vertically-draining Trautwein CRS consolidometer. We designed the modified parts and fabricated them both in the MIT central machine shop and in the MIT Civil & Environmental Engineering machine shop, with the help of Mr. Stephen Rudolph.

Before investing in the construction of this equipment, a numerical model was created to predict how excess pore pressures will develop within a radially-draining CRS specimen. This model provided confidence in the applicability of the radially-draining CRS concept, and the design was commenced.

Relatively few parts needed to be redesigned for the modified CRS device. A modified confining ring with an inset tubular-shaped porous stone allows for radially-outward drainage during specimen compression. A cell base exhibits two .005" diameter pinholes drilled into the steel, allowing for the measurement of pore pressure within the specimen at very specific points. A cutting shoe, top cap, trimming tool, and LVDT holder are also designed and fabricated to work with the modified cell.

Once the modified CRS device is designed and built, the CRS cell is calibrated for the weight and area of the piston, and apparatus compressibility. The LVDTs (linear variable displacement transformers) are also calibrated to determine an absolute zero specimen height, allowing them to read specimen heights rather than simply displacements.

4.2.1 Numerical Model

In order to determine the distribution of excess pore pressures within a vertically-compressed radially-draining CRS specimen, a finite difference simulation is performed in Microsoft Excel®. The model uses a cylindrical specimen with a diameter of 3.8 cm and a height of 1.3 cm. A no-flow boundary is imposed on the top and bottom of the specimen, and a drainage boundary is used around the circumference of the specimen. A strain rate of 0.1 %/hr of engineering strain is used. Time is represented in the model by using a single 5-second time step, so it is not a variable. A small strain assumption is used, as the only deformation is that which is associated with the 5-second time step. The model assumes a hydraulic conductivity of 1.0 x 10^{-8} cm/sec, typical of Resedimented Boston Blue clay at a consolidation stress of about 3 MPa.

The model compresses the specimen vertically. Assuming 100% saturation, the volume compressed out of the specimen must equal the volume of water extruded from the specimen in any time increment. The model slices the specimen into cylindrical rings of 0.1 cm thickness. For a time increment of 5 seconds, the water pressures and soil skeleton effective stresses are calculated in each ring. The flow radially outward from each cylindrical ring must equal the compressed volume of the ring from vertical compression plus the flow from the cylindrical ring neighboring the ring on the inside.

The incremental displacement, δ, is calculated as follows:

$$\delta = H_i * \dot{\varepsilon} * \mathrm{t} \qquad \textbf{(4-1)}$$

where:
H_i = initial specimen height
$\dot{\varepsilon}$ = strain rate (decimal)
t = time

The outflow from each cylindrical ring, q_{oi}, is calculated as follows:

$$q_{o,i} = q_{o,i-1} + \frac{\delta * ring\ area}{\Delta t} \quad \textbf{(4-2)}$$

where:
$q_{o,i-1}$ *= flow from inner adjacent cylindrical ring*
ring area = cross-sectional area of cylindrical ring in horizontal plane
Δt *= time increment*

The area of flow at the outside of each cylindrical ring, A_i, is calculated as follows:

$$A_i = 2 * \pi * r_i * H_0 \quad \textbf{(4-3)}$$

where:
r_i *= outside radius of cylindrical ring*

The hydraulic gradient for each cylindrical ring, i_i, is calculated using Darcy's law as follows:

$$i_i = \frac{(q_{o,i} + q_{0,i-1})/2}{k * (A_i + A_{i-1})/2} \quad \textbf{(4-4)}$$

where:
k=hydraulic conductivity

The change in excess pore water pressure between each cylindrical ring, $\Delta u_{e,i}$, is then calculated as follows:

$$\Delta u_{e,i} = i_i * (r_i - r_{i-1}) * \rho_w \quad \textbf{(4-5)}$$

where:
P_w*=density of water*

Because the drainage occurs radially outward and no vertical flow or sidewall friction is assumed, any vertical profile in the specimen is assumed to be at an identical stress state. It follows that any point along a vertical profile has the same porosity.

We assume that the specimen is compressed at a constant rate throughout the horizontal cross-section of the specimen and that no soil particles move horizontally. Therefore, the specimen has a unique porosity at any given time, not only along the vertical profile, but in a horizontal plane. It is also assumed that the specimen is normally consolidated, and normally consolidated materials have a unique effective stress for any given porosity. It follows that the specimen must have a constant effective stress across a horizontal plane, since it must have a constant porosity.

Applying Terzaghi's effective stress principle, we can explore the stresses throughout the specimen. The finite difference model shows that the excess pore pressures vary parabolically across the specimen. Since the effective stresses remain constant throughout the specimen, the total stress follows the pattern of the excess pore pressure, parabolically increasing towards the specimen's center (see Figure 4-1).

4.2.2 Porous Confinement Ring Design

With the concept of a radially-draining CRS device proven viable using numerical finite difference, we designed modified parts to transform a conventional vertically-draining CRS device into a radially-draining device. The initial design effort went into finding a material that was porous but strong enough to withstand the lateral stresses from the soil, and discovering a way to attach it to the stainless steel confinement ring.

Constant rate of strain tests with both radially-outward and radially-inward drainage have been performed prior to this study, but at stresses less than 1 MPa. The radially-outward draining tests used porous plastic around the circumference of the specimen, making a drainage path in-between the specimen and the confinement ring. The maximum excess pore pressure, assumed to be along the center vertical profile of the cylindrical specimen, was measured using a small porous stone at the bottom center of the specimen, connected to a pressure transducer. The radially-inward draining tests used the above-mentioned porous plastic around the specimen's circumference, connected to a pressure transducer, to measure the maximum excess pore pressure, assumed to be at the specimen's circumference. A cylindrical porous stone, allowing drainage and measurement of minimum pore

pressure, was placed inside a cylindrical hole at the center of the cylindrical specimen (Seah & Juirnarongrit, 2003; Yune & Chung, 2005; Yune & Jung, 2012).

The experimental program of this study is to determine permeability anisotropy of mudrocks compressed to effective stresses up to 40 MPa. Therefore, porous plastic does not have the stiffness to prevent significant lateral specimen extension, or even remain porous at the desired effective stresses. Only radially-outward drainage was considered.

A high-strength porous stone material is used, cut into a hollow cylinder, and placed inside a stainless steel confinement ring. The material is Allundum® P280 made by Saint-Gobain Ceramics, and is composed of fused alumina grains held together by porcelain bonds. An in-house unconfined compressive strength test is performed on the material to determine its stiffness and strength. The resulting stress-strain plot is shown in Figure 4-2, and the properties of the material can be seen in Table 4-1. The placement of the Allundum® material within the confining ring requires some creative engineering.

Placement of porous stone inside confining ring

The confinement ring in a CRS device needs to be able to withhold high hoop stresses and exhibit minimal radial expansion through the duration of the test. The maximum loading stress is 5.8 ksi (40 MPa), governed by the capacity of the load cells. The lateral active pressure against the sides of the ring can therefore be as high as 5.8 ksi (40 MPa), assuming a lateral stress ratio, K, of 1 during compression. The steel confinement ring used in the vertically-draining CRS device is very capable of holding such stresses. With an outer diameter of 3" and an inner diameter of 1.5", the maximum hoop stress, σ_1, can be calculated as follows:

$$\sigma_1 = \frac{pressure * inner\ radius}{wall\ thickness} = \frac{(5.8\ ksi)(0.75\ in)}{(0.75\ in)} = 5.8\ ksi \qquad \textbf{(4-6)}$$

The 5.8 ksi hoop stress is well below the tensile strength of steel of 100 ksi (see Table 4-1), therefore the stainless steel ring can easily hold the compressing specimen's lateral pressure in response to loading. The diametric strain corresponding to this maximum stress is 0.02%, which is below the 0.04% limit specified for oedometer tests by ASTM D2435.

For the radially-draining device, the circumferential drainage boundary must also hold this kind of hoop stress and have similar stiffness. The porous stone would be unlikely to be able to hold the stress by itself. Although it has high compressive strength, siliceous materials are not known for having large tensile strengths, which would be needed to hold large hoop stresses. The Alundum® P280 material also has a lower modulus than steel, and would diametrically strain 0.07%, above the 0.04% ASTM D2435 limit. Thus the design of a porous stone inset within a steel confining ring is implemented.

In order to transfer the load from the stone to the steel, however, a tight fit needs to be made between the two materials. We went through two iterations to fabricate the stone/steel confinement ring configuration.

First iteration: epoxied stone

The first iteration was to cut a steel confining ring with an inner diameter equal to the outer diameter of a tubular-shaped porous stone, with a tolerance large enough to easily fit the porous stone within the confinement ring. The 0.2" thick porous stone was then epoxied into the steel confining ring, and the epoxy was allowed to cure. We were alarmed by two observations of the cured porous stone/ring assembly. First, a large, uneven, epoxy-filled gap was observed between the porous stone and the steel ring. Second, the epoxy appeared to have penetrated into the porous stone, taking away its porosity in affected areas (see Figure 4-3). Using the composite ring, a trial CRS test was run to a vertical effective stress of 6.5 ksi (45 MPa) with an intact Presumscot Clay specimen. After the test, several large cracks appeared in the cylindrical porous stone, with the gap between the stone and the ring observed before the test made much smaller (see Figure 4-4). The stress at which the stone failed was easily identified from the loading curve shown in Figure 4-5. The vertical effective stress at failure was 1.9 ksi. The hoop stress at failure within the stone can be calculated, assuming a lateral stress ratio, K, value of 0.5. The stone's tensile strength can be estimated as this value, which is shown in the following equation:

$$\sigma_1 = \frac{(0.5)(1.9\ ksi)(0.75\ in)}{(0.2\ in)} = 3.6\ ksi \qquad \textbf{(4-7)}$$

The calculation assumes that no stress is transferred to the steel, giving an upper-bound estimate of strength. In the trial run, the stone had expanded towards the steel and failed. The tolerance between the outer diameter of the stone and the inner diameter of the steel was large enough that the tubular porous stone was able to expand enough to cause failure. After failure, the test continued to run, as the

hoop stress was then held in the steel confining ring. From this observation, we decided to reduce the tolerance between the two materials enough that the stone would transfer the lateral load onto the steel, and not deform enough to break. The clearance between the two pieces needed to be small in order to transfer enough lateral load from the porous stone to the confinement ring to keep the porous stone from cracking. However, the clearance also needed to be large enough that the porous stone could physically fit into the confinement ring, within the tolerances for error expected in machining the individual parts. Rather than optimizing this process and machining parts to painstaking and impractical clearances and tolerances, a thermal press-fit procedure was adopted, taking advantage of the expansive thermal properties of stainless steel.

Second iteration: press-fit of porous stone

The second and final iteration was to press-fit the tubular-shaped porous stone into the steel confining ring, meaning the ring holds the stone in place without the use of any cement. The stainless steel ring is heated and expanded, allowing enough clearance that the stone can be physically dropped inside of it. It is then cooled in order to make a tight fit between the porous stone and the confinement ring, with no epoxy needed. The first benefit to this system is that the lateral stress from loading is transferred from the porous stone to the confining ring, mobilizing the high strength and stiffness of the stainless steel. The second benefit is that the stone is pre-stressed with compressive hoop stress, allowing for the soil loading process to relive some of the compressive stress already on the stone. The final benefit is that no epoxy is needed, keeping the porous stone free from clogging effects. The following steps describe how the ring is fabricated.

Step 1: Machine ring and stone

The design diameter for the inside of the steel confining ring and the outside of the tubular-shaped porous stone is 1.9". In order to keep the steel/stone interface tight, the outside diameter of the stone is machined to be 1.902", while the inside diameter of the steel confining ring is machined to be 1.901". These dimensions are achieved using a mill, in order to keep the pieces as uniform, concentric, and exact as possible. Thus a negative clearance between the two parts is created, facilitating a solid contact and pre-stress between them during operation.

Step 2: Heat ring ~100° C

The steel confining ring is heated on a hot plate from room temperature to 130° C. The thermal expansion of the steel increases the inner ring diameter from 1.901" to 1.905", using a thermal expansion coefficient of 1.7×10^{-5} decimal strain/°C (see Table 4-1), creating a temporary clearance large enough to fit the tubular-shaped porous stone inside the steel ring (see Figure 4-6).

Step 3: Press-fit stone into heated shoe

The steel confining ring is kept on the hot plate at 130° C, expanded to an inner diameter of 1.905". The tubular-shaped porous stone of outer diameter 1.902", at room temperature, is carefully lowered into the confining ring. The stone is placed as perfectly in line as possible, avoiding contact between the two pieces as much as possible. If part of the stone touches the steel before it is properly in place, either from skewness or incomplete penetration, the stone will start to heat and expand, while the steel will start to cool and contract. This will lock the pieces together, and could make it impossible to separate them again after they are in contact.

Step 4: Let steel cool

Once the tubular porous stone completely penetrates the steel confining ring and the two parts are properly aligned, the hot plate is shut off, and the setup is allowed to cool to room temperature. As the setup cools, the steel confining ring shrinks onto the tubular porous stone, pre-stressing the stone with a compressive hoop stress (see Figure 4-6 and Figure 4-7). The final diameter of the interface between the porous stone and the steel is somewhere in-between 1.901" and 1.902".

Loading

During specimen loading from a CRS test, a radial strain is applied on the composite tubular porous stone – steel confinement ring. This radial strain decreases the hoop stress in the porous stone, because the porous stone has a radially-inward pre-stress. The applied radial strain increases the hoop stress on the steel ring. Due to the higher stiffness of the steel, it takes on much of the tensile hoop stress, lowering the hoop stress felt in the stone. The high strength and stiffness of the stainless steel confinement ring is sufficient to hold the total stress placed on it. A conceptual stress-displacement plot is shown for the confinement ring – porous stone setup in Figure 4-7, assuming a maximum axial stress of 40 MPa and a loading K value of 0.6.

Several CRS tests on intact Presumscot clay and RBBC are performed with the press-fit radially-draining confinement ring and the traditional vertically-draining base, in order to proof the confinement ring before the base s created to match the ring. The tests verify that the mudrocks can be loaded to 40 MPa without confinement ring failure.

The press-fit confinement ring construction provides a robust load-bearing cylindrical drainage boundary for specimens being loaded in the CRS cell. The confinement ring creates a cylindrically-shaped drainage boundary forcing a flow regime essential for the measurement of horizontal permeability. The shop CAD drawing for the ring is included in Appendix A.

4.2.3 Cell Base Design

The cell base needs to create a no-flow boundary at the bottom of a 1.5" diameter soil specimen, while measuring the maximum excess pore pressure at its center axis. The Trautwein® CRS cell base design is modified for the radially-draining CRS device, in order to provide this no-flow drainage boundary at the bottom of the cylindrical specimen and characterize the buildup of excess pore pressure along its radial profile. The base includes a 0.13" inch pedestal that sits inside the tubular porous stone at the base of the stone, directly beneath the specimen.

The pedestal has two 0.005" diameter pinholes to measure excess pore pressure at the base of the specimen at two separate, precise locations. One location is directly at the center of the pedestal, corresponding to the center of the porous stone and specimen, assumed to be the location of maximum excess pore pressure. The second pinhole is located at a radial distance of 0.685" from the pedestal's center, used to check the distribution of pore pressure in-between the maximum at the center and the minimum at the edges. The precise excess pore pressure measurements made from these pinholes are accompanied with a number of challenges. Among these are the likelihood of the magnitude of the pore pressure line volumes to lower the pore pressure readings and the tendency of the pore pressure lines to clog. A check is performed to determine the effect that pore pressure volume has on pore pressure readings.

Appendix A shows the CAD drawing used to manufacture the base.

Pore Pressure Line Volume Check

When pore pressures are measured at the base of a specimen within a traditional vertically-draining CRS consolidometer, the pore pressure line is connected to the specimen base through a porous stone and filter paper along the specimen's entire base. The excess pore pressure is then easily transferred from the pore fluid within the specimen to the water in the porous stone, the pore pressure lines, and the pressure transducer housing. With the radially-draining CRS consolidometer, the pore pressure at the center of the specimen is connected to the pore pressure monitoring system only through a single 0.005" pinhole. Therefore, less pore water volume is available to transfer the pore pressure in the specimen to the pore pressure line. It is possible that a local hydraulic gradient is induced near the pinhole, and the pore pressure line has slightly less pressure than the maximum excess pore pressure within the specimen. This phenomenon will happen if there is sufficient compressibility in the pore pressure system. Therefore, the effect of changing pore pressure line volume, hence pore pressure line compressibility, is studied.

The effect of pore pressure line volume on the buildup of pore pressures and permeability measurements is analyzed to determine acceptability of pore pressure line water volumes. Two radially-draining CRS tests are performed on two resedimented Boston blue clay (RBBC) specimens from the same resedimentation tube, with different pore pressure volumes. CRS 1212 is performed with approximately 1.56 cm^3 of pore pressure line volume, while CRS 1214 is performed with approximately 1.18 cm^3 of pore pressure line volume. The decrease in volume between the two tests is created by reducing the volume of the largest portion (73%) of the pore pressure monitoring system – the transducer housing. This is done by placing small stainless steel rods that have a combined volume of 0.38 cm^3 inside two large diameter holes within the pore pressure transducer housing. If a decrease in pore pressure line volume were to significantly increase the magnitude of pore pressure response from compression, further design iteration would be needed to minimize the effect of water compressibility in the pore pressure lines.

The changes in pore pressure values between a porosity of 0.350 and 0.300 for CRS 1212 and CRS 1214 are shown in Table 4-2. Only a 0.2 kPa increase in the pore pressure response is seen with the lower pore pressure line volume. Similarly, only a minor difference in permeability results between the two tests is seen, as shown in Figure 4-8. The pressures within the excess pore pressure lines, and consequently the permeability values, do not significantly change between the two tests. It is concluded, therefore, that for RBBC tested at a 1.4%/hr strain rate with small pore pressure line volumes, the compressibility of water does not significantly alter the results.

4.2.4 Design of Other CRS Tools

Other CRS tools are fabricated to aid in the radially-draining CRS testing program. These objects include a cutting shoe, a non-porous steel top cap, an acrylic trimming spacer, and a dual LVDT holder.

Cutting Shoe

A stainless steel cutting shoe is designed to allow specimen trimming with minimum specimen disturbance and maximum specimen – tubular porous stone contact before loading. The cutting shoe is designed to slide into a 3" diameter turntable mount during trimming, then slide onto the top of the confining ring – porous stone assembly for specimen placement into the confining ring – porous stone assembly. The tip of the cutting shoe has a 30° cutting edge, allowing for easy shoe advancement onto a soil sample, with the aid of a small bevel trimmed into the soil sample by a small blade or spatula. Appendix A shows the CAD drawing used to manufacture the cutting shoe.

Top Cap

A stainless steel top cap is designed to load the specimen and to create a no-flow boundary along its top. The top cap incorporates a 5° bevel, to minimize the risk of top cap binding due to skewed placement within the confining ring – porous stone assembly. Appendix A shows the CAD drawing used to manufacture the top cap.

Trimming Spacer

An acrylic trimming spacer is designed to trim each specimen to a repeatable initial height close to 0.5". The trimming spacer fits nicely through the cutting shoe and confining ring – porous stone assembly, with an oversized shoulder at one end to limit the tool's advancement through the other parts. This way, after the specimen is trimmed into the cutting shoe and the cutting shoe is placed onto the confining ring – porous stone assembly, the specimen can be easily advanced into the confining ring – porous stone assembly. Once the oversized shoulder of the trimming tool meets the cutting edge of the cutting shoe, the specimen can be trimmed at the base of the confining ring – porous stone to a consistent initial height of 0.5". Section 5.1.2 gives step-by-step instructions of how to use the trimming spacer, and its CAD drawing is shown in Appendix A.

Dual LVDT Holder

A dual LVDT holder is designed in order to allow vertical displacements to be measured from two points on opposite sides of the same plane, perpendicular to and equidistant from the axis of the loading piston. This allows the average of the two displacements away from the piston to equal the displacement at the piston. Appendix A shows the CAD drawing used to manufacture the dual LVDT holder.

4.2.5 Apparatus Compressibility and LVDT Zeros

To collect precise data, the LVDTs need to be accurately zeroed to the location where the base of the specimen sits, which is at the top of the cell base. The CRS cell also needs to be corrected for the compressibility of the piston due to vertical loading, and the uplift force on the piston due to back-pressuring in the cell needs to be accounted for.

LVDT Zeroing

Any error in specimen height measurement directly affects the void ratio and porosity of the test specimens. This complicates the process of matching data from separate specimens according to their

porosities. In order to minimize error in porosity measurements, the LVDTs are zeroed to a reference steel dummy specimen. As long as the LVDTs are never removed from their hanger or from the cell piston, the zero value can be reused from test to test.

To do this, the cell is set up with a steel dummy specimen of height 12.46 mm in place of a soil specimen. The cell is back-pressured to 0.4 MPa (the same pressure that is used in testing). The piston is placed just above the top of the specimen, so that any displacement in the piston results in no change in load cell reading. The piston is then loaded onto and unloaded from the dummy specimen twice. The load-LVDT reading curve for the blue LVDT of CRS consolidometer TR5 is shown in Figure 4-9. The normalized LVDT voltage at dummy specimen contact for each loading/unloading curve is determined as the intersection of the linear portions of the curves before and after the point of contact. The average LVDT contact normalized voltage is then associated as voltage representing a specimen of the dummy specimen's height, 12.46 mm. The calculation of this zero voltage is illustrated in Figure 4-10. The normalized zero voltages for the LVDTs used can be seen in Table 4-3.

Apparatus Compressibility

As the specimen is loaded vertically during a typical test, part of the deformation measured by the LVDT's outside the cell is due to the compressibility of the piston and setup. This compressibility needs to be measured and subtracted from the measured displacement as follows:

$$\Delta H_{LVDT} = \Delta H_{specimen} + \delta_{apparatus\ compressibility} \quad \textbf{(4-8)}$$

In order to measure the piston compressibility, a steel dummy specimen is placed in the cell in place of a soil specimen. The cell is assembled and back-pressured to 0.4 MPa, and the dummy specimen is loaded to 4,500 kg (load cell capacity) and unloaded two times. An example of the loading and unloading curves can be seen in Figure 4-11. A power-law regression is fit to the average of the loading curves for each cell, in the following form:

$$\delta_{apparatus\ compressibility} = a * (load\ [kg])^b \quad \textbf{(4-9)}$$

The apparatus compressibility parameters a and b for each cell used are presented in Table 4-3.

Correction for Back-pressure Piston Uplift

The effect of the cell pressure on the specimen's vertical stress needs to be corrected for, as the force vertically loading the specimen is not the same as the force being measure by the external load cell. To make this correction, the cell is back-pressured with no specimen or with the dummy specimen. A gap is left in-between the dummy specimen or the base and the piston, in order to let the cell pressure alone push on the piston. The cell pressure is incrementally increased to 0.5 MPa and reduced close to atmospheric twice. The load is plotted against the cell pressure (see Figure 4-12). The area of piston, A_p, and weight of piston, w_p, are calculated as the slope and y-intercept of the line, respectively. These two parameters are used to calculate the vertical stress within the specimen as follows:

$$\sigma_a = \frac{f_a + w_p}{A} + \sigma_c \left(\frac{1 - A_p}{A}\right) \quad \textbf{(4-10)}$$

where:
f_a = *vertical force measured from load cell*
w_p = *weight of piston*
A = *specimen horizontal area*
A_p = *area of piston*
σ_c = *cell pressure*

The area and weight of pistons for each individual cell can be seen in Table 4-3.

4.3 VERTICALLY-DRAINING CRS

Vertically-draining constant-rate-of-strain (CRS) consolidation testing has been routinely performed for decades (Wissa et al, 1971). It is a time-efficient, automated way to produce compression curves for soft soils, allowing greater precision and reduced creep effects when compared to oedometer consolidation testing. Traditional CRS testing also allows for the characterization of the coeffiecient of consolidation, c_v, and vertical permeability, k_v, as a function of porosity, n, or effective stress, σ'_v. Adams (2011) compared CRS vertical permeability results with constant head results in the CRS cell, and found agreement between the two procedures.

The MIT Geotechnical lab uses Trautwein® CRS cells, placed under gear-driven load frames within temperature control boxes. The cells are equipped with load cells for measuring vertical load, linear variable displacement transformers (LVDT's) for measuring axial displacement, and pressure transducers

for measuring cell and pore pressures. Each of the transducers are recently calibrated (see section 4.6 and Table 4-4). The cell itself is calibrated for apparatus compressibility due to loading and backpressuring, and the LVDT's are zeroed to a steel dummy placed inside the backpressured cell.

4.3.1 Apparatus Compressibility and LVDT Zeros

The vertically-draining CRS consolidometer is calibrated the exact same way as the radially-draining consolidometer. The LVDTs are zeroed against the location where the base of the specimen sits, which is the bottom filter paper. The cell is corrected for the compressibility of the piston due to vertical loading, and the uplift force on the piston due to back-pressuring in the cell is accounted for. The apparatus compressibility, LVDT zero, and cell calibration factors are listed in Table 4-3. For details on how these values are calculated, see Section 4.2.5 and Figure 4-10.

4.4 DIRECT SIMPLE SHEAR

Anisotropy in a clay-rich mudrock fabric is typically developed from one-dimensional consolidation. It is also possible that anisotropy is enhanced if a mudrock is sheared horizontally (Dewhurst et al, 1996; Terzaghi et al, 1996). To determine whether this is the case, a set of resedimented test specimens were horizontally sheared using a direct simple shear (DSS) device before permeability anisotropy was measured in a radially-draining and vertically-draining CRS device.

DSS testing is thoroughly described in a research report by Ladd and Edgers (1972). It imposes a plane strain shear condition, where the principle stress planes rotate to an orientation typical of in situ horizontal failure conditions (Ladd and Edgers, 1972). DSS tests are performed in this research in order to analyze the effects of this horizontal failure on permeability anisotropy. When fine-grained soils shear, they can shear within the soil matrix, rather than with the development of macroscopic shearing planes. Thus the individual plate-shaped clay particles are likely to align themselves horizontally due to horizontal shear.

DSS equipment uses a "slinky," or steel wire coil, coated in rubber for a cylindrical membrane, with top and bottom porous end caps. The top and bottom end caps translate horizontally with respect to each other, creating horizontal shearing in the specimen. The vertical height of the specimen is maintained constant. Due to the assumed non-expansion of the membrane and the constant vertical height during shearing, the specimen is sheared under constant volume, or undrained, conditions (Ladd and Edgers, 1972).

A Geonor® DSS device is used for shearing. It was originally manufactured for manual control of normal stress (to maintain no vertical strain) and manual measurements. However, it has been renovated to allow computer-feedback control to suppress vertical strain by varying the normal stress through a mechanical loading system. It is also set up with electronic load cells and LVDTs to measure horizontal and vertical loads and displacements. These transducers are fed into the central data acquisition system, where the transducer readings can be recorded and archived. (see Section 4.8).

4.5 CUBIC SPECIMEN CONSTANT HEAD IN TRIAXIAL CELL

CRS testing isn't the first method used at the MIT geotechnical laboratory to measure permeability anisotropy. It has been measured for the last several years using constant head tests within a triaxial cell (Adams, 2014). Multiple flow directions are measured using specimens trimmed into cubes. The cubes are set up in a triaxial cell, under hydrostatic conditions and at an OCR of 4, to measure the permeability in one direction, then the setup is taken down and the cube is rotated 90° to measure the permeability in a perpendicular direction.

A correction is made for permeability measurements taken subsequent to the initial permeability measurement made, in order to account for specimen disturbance during unloading, specimen rotating, and reloading of the specimen. When taking permeability measurements for the two horizontal directions, a decrease in permeability can be seen, despite the cross-anisotropy of the specimens. This decrease in permeability between theoretically-equal permeability directions is extrapolated to estimate the permeabilities that would be measured in each direction, had the measurements in that direction been the first to be taken. This correction is made either globally (a correction calculated for all the specimens of the same material) or specifically (a correction calculated for each individual specimen). For more details on cubic specimen constant head testing see Amy Adams' Ph.D. thesis (2014).

This method of permeability measurement is a very mathematically-robust way of measuring permeability, as it simply uses Darcy's law. It also removes uncertainty in comparison between vertical and horizontal permeability due to heterogeneity between specimens, as the same specimen is used for permeability measurements in both directions. Substantial specimen disturbance likely occurs, however, during initial specimen trimming into a cube and subsequent cube rotation within the triaxial cell.

4.6 TRANSDUCER CALIBRATION

All measurements of engineering values during the course of the tests are collected using electronic transducers. These transducers convert an input voltage to an output voltage that is representative of a displacement, force, or pressure. The analog voltages are converted to digital data, and recorded in a central data acquisition system (see Section 4.8). In order to assure accurate and precise measurements, each transducer is calibrated before the commencement of testing. The results of the calibrations can be seen in Table 4-4.

To calibrate a transducer, the normalized voltage (output voltage divided by input voltage) is plotted against the reference engineering measurement. The calibration factor, CF, is taken as the slope of a linear fit through the data. An example transducer calibration is shown in Figure 4-13.

Each type of transducer has its own range and resolution. A summary of the average range, resolution, and stability values is shown in Table 4-5. The range is the range of values that the transducer can accurately measure without causing plastic deformation on the transducer. The resolution is the minimum value that can be read by the transducer. The stability is the amount of noise that is picked up by the transducer and data acquisition system.

4.7 COMPUTER CONTROL SYSTEM

The tests are performed using computer feedback controls to obtain desired stress/strain states within the soil specimens. The CRS and DSS tests include single-axial computer feedback controls, while the cubic specimen constant head tests use tri-axial feedback controls.

For CRS tests, a computer can be used to maintain a constant cell pressure around the specimen during loading. The pressure transducer connected to the cell fluid sends a voltage signal to the computer. The computer uses a given calibration factor and zero voltage reading to calculate the value of the cell pressure. If this value is above or below the desired value, the computer sends a voltage signal to a pressure-volume actuator (PVA) connected to the cell fluid in order to correct the pressure. In this research, the vertically-draining CRS device is controlled using a computer system, while the horizontally-draining CRS device is controlled using an air-pressure-controlled PVA.

For DSS tests, a computer is used to maintain a constant volume within the specimen during shearing, simulating undrained shearing. While the specimen is being sheared laterally, a displacement transducer (LVDT) aligned vertically sends a voltage reading to the computer. The computer uses a

given calibration factor and initial specimen height voltage reading to calculate the vertical strain of the specimen. The computer then sends a voltage signal to the vertical displacement motor, allowing the vertical strain to stay close to zero.

For cubic specimen constant head tests within a triaxial cell, three axes of control are performed via computer – cell, top pore, and base pore pressures. Each pressure is predetermined in order to create a desired isotropic stress state (cell pressure) and hydraulic gradient (top and base pore pressures). Each transducer sends a voltage signal to the computer, which converts the signal into a pressure using the respective calibration factor and zero voltage value. The computer then sends a signal to each respective pressure-volume actuator (PVA) connected to the cell, base pore, and top pore fluid lines to keep them all at the desired pressures. This is especially important for the top and base pore pressures. As pore water flows through the sample, the fluid volumes in the PVAs will change over time. The PVAs adjust to maintain pressures, consequently adjusting volumes.

4.8 DATA ACQUISITION

The engineering measurements during the tests are recorded as digital voltage values through a central data acquisition system. This system is in place for simultaneously reading and collecting data from all the transducers in the MIT geotechnical laboratory. It allows for data to be collected at pre-selected time intervals, with high precision and no human resources needed. A data acquisition system requires four components (see Figure 4-14, Germaine & Germaine, 2009).

A. **Electronic transducers** are needed to convert engineering values (displacements, forces, pressures, and volume changes) into analog voltage differentials. These transducers are connected to the testing device (such as a triaxial or consolidation cell).
B. **A multiplexer** or switching mechanism is needed to allow a computer to select which transducer to read at any given time.
C. **An analog to digital (A/D) converter** converts the analog voltage signals from the electronic transducers into digital "words" for a computer to read. This can occur before or after the multiplexer switching mechanism.
D. **A computer** is required to orchestrate when to collect digital readings of the analog transducer voltages. It then collects the digital readings for engineering analysis.

The MIT geotechnical lab data acquisition system consists of 140 separate channels connected to a Hewlett Packard HP3497A data acquisition unit with 17 ½ bit resolution. The unit uses autoranging

voltage amplification to maximize data precision for each transducer individually, according to its output voltage magnitude. The unit is connected to a PC with an Intel 486 microprocessor. A Windows interface allows for data files to be collected for any combination of the 140 channels at preselected time intervals. This system provides precision, reliability, and extreme flexibility.

Table 4-1: Engineering properties of materials used for confinement ring of radially-draining CRS device

	Compressive Strength [ksi (MPa)]	Tensile Strength [ksi (MPa)]	Modulus [ksi (MPa)]	Permeability [m^2]	Thermal Expansion Coeffcient [$°C^{-1}$]
Allundum® P280 porous stone	20 (138)*	7.1*	7,790 (53,700)*	3 to 4 x $10^{-10‡}$	-
stainless steel	-	100 (689)†	29,000 (200,000)†	-	1.7 x 10^{-5}

*MIT lab
†Gere & Goodno (2009)
‡Saint Gobain (2003)

Table 4-2: Pore pressure and dimension change data from porosity, n, = 0.350 to 0.300 for tests run with different pore pressure housing volumes show minimal housing volume effect on pore pressure.

Test ID	Pore Pressure Housing Volume [cm^3]	Δu_{max} [kPa]	H_i [cm]	ΔH [cm]	ΔV [cm^3]
CRS 1412	1.56	46.2	0.541	0.062	0.708
CRS 1414	1.18	46.4	0.569	0.066	0.754

Table 4-3: CRS cell LVDT zero, apparatus compressibility, and cell calibration values

		TR2 – Radial Drainage	TR2 – Vertical Drainage	TR4 – Radial Drainage	TR5 – Vertical Drainage
LVDT normalized zero [V/V]	blue	-	+0.4635	-0.4484	+0.3897
	black	-	-0.4542	-0.4472	-0.3728
apparatus compressibility parameter, a*		9.991×10^{-4}	2.033×10^{-5}	3.774×10^{-5}	5.191×10^{-5}
apparatus compressibility parameter, b*		0.4140	0.8581	0.7513	0.7670
area of piston, A_p [cm2]		-	-	2.96	3.37
weight of piston, w_p [kg]		-	-	1.30	5.20

*a & b parameters are used in conjunction with Equation 4-9

Table 4-4: Electronic transducer information

Transducer I.D.	Type	Equipment	Capacity (Range)	Calibration Factor, CF	R^2	Date	Calibrated by
D10342	pressure transducer	CRS TR5	14 kgf/cm^2	-703.158760 kgf/cm^2/(V/V)	0.999986	8/27/2014	TJN
D10343	pressure transducer	CRS TR5	14 kgf/cm^2	-700.821961 kgf/cm^2/(V/V)	0.99998	8/27/2014	TJN
0243-0000 G-90	LVDT	CRS TR5	(1 cm)*	2.521938 cm/(V/V)	0.999997	8/27/2014	TJN
0243-0000 D-94	LVDT	CRS TR5	(1 cm)*	2.572132 cm/(V/V)	0.999993	8/27/2014	TJN
FID1M3	load cell	CRS TR5	4,500 kgf	1,508,993.93 kgf/(V/V)	0.9999985	3/2/2009	JTG
A80012	pressure transducer	CRS TR4	14 kgf/cm^2	-701.135551 kgf/cm^2/(V/V)	0.999995	5/27/2014	TJN
A53551	pressure transducer	CRS TR4	14 kgf/cm^2	-702.328383 kgf/cm^2/(V/V)	0.999998	5/23/2014	TJN
-	pressure transducer	CRS TR4	14 kgf/cm^2	-706.675163 kgf/cm^2/(V/V)	0.99998	5/27/2014	TJN
0243-0000 G-90	LVDT	CRS TR4	(1 cm)*	2.624379 cm/(V/V)	0.999990	3/5/2014	TJN
0243-0000 H-90	LVDT	CRS TR4	(1 cm)*	2.647994 cm/(V/V)	0.999995	3/5/2014	TJN
-	load cell	CRS TR4	4,500 kgf	143,628.441 kgf/(V/V)	0.999998	2008	NAH
0243-0000 H-90	LVDT	DSS 2	(2 cm)	2.475528 cm/(V/V)	0.99997	1/12/2015	MAD
0243-0000 H-90	LVDT	DSS 2	(2 cm)	2.508556 cm/(V/V)	0.99996	1/12/2015	MAD
91144	load cell	DSS 2	225 kgf	6,798.18 kgf/(V/V)	.999992	1/22/2015	MAD
2894-0001	load cell	DSS 2	900 kgf	28,966.04 kgf/(V/V)	.99991	1/22/2015	MAD

*calibrated at ± 1 V

Table 4-5: Average resolution and stability of transducers used in testing

Device	Range	Resolution		Stability	
Stringpot PVAs	48 cm^3	0.00018 cm^3	(0.01 mV)	0.00018 cm^3	(0.01 mV)
LVDTs	2 cm	0.000005 cm	(0.01 mV)	.000031 cm	(0.07 mV)
Load Cells	44,000 N	1.5 N	(0.001 mV)	3.0 N	(0.002 mV)
Pressure Transducers	14,000 kPa	0.14 kPa	(0.001 mV)	4.2 kPa	(0.033 mV)
Pressure Transducers	1,400 kPa	.014 kPa	(0.001 mV)	0.18 kPa	(0.014 mV)
Pressure Transducers	700 kPa	0.007 kPa	(0.001 mV)	0.09 kPa	(0.014 mV)
Pressure Transducers	350 kPa	0.003 kPa	(0.001 mV)	0.02 kPa	(0.008 mV)

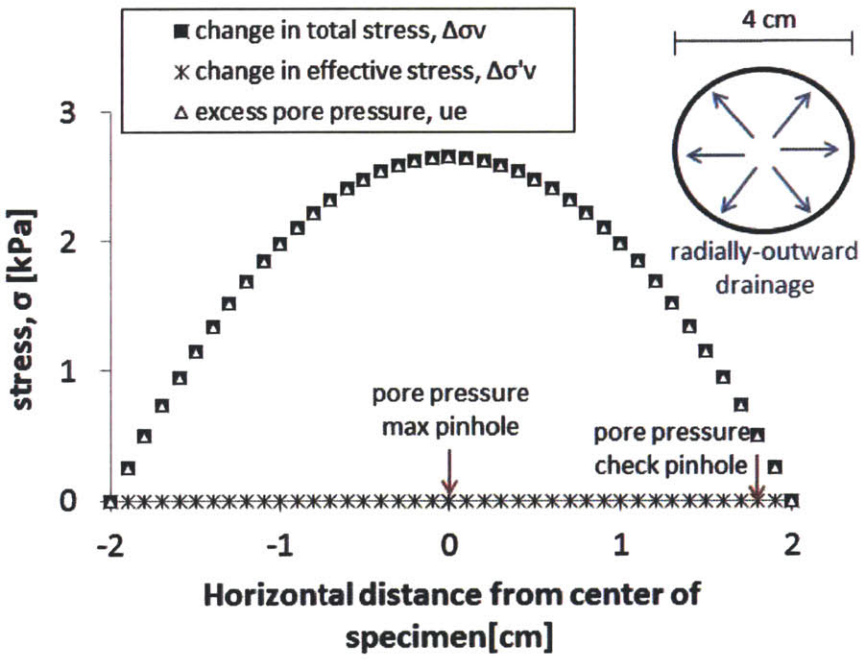

Figure 4-1: The distribution of soil stresses and water pressures throughout the diametric profile of the finite difference model specimen show a parabolic pore pressure and total stress distribution.

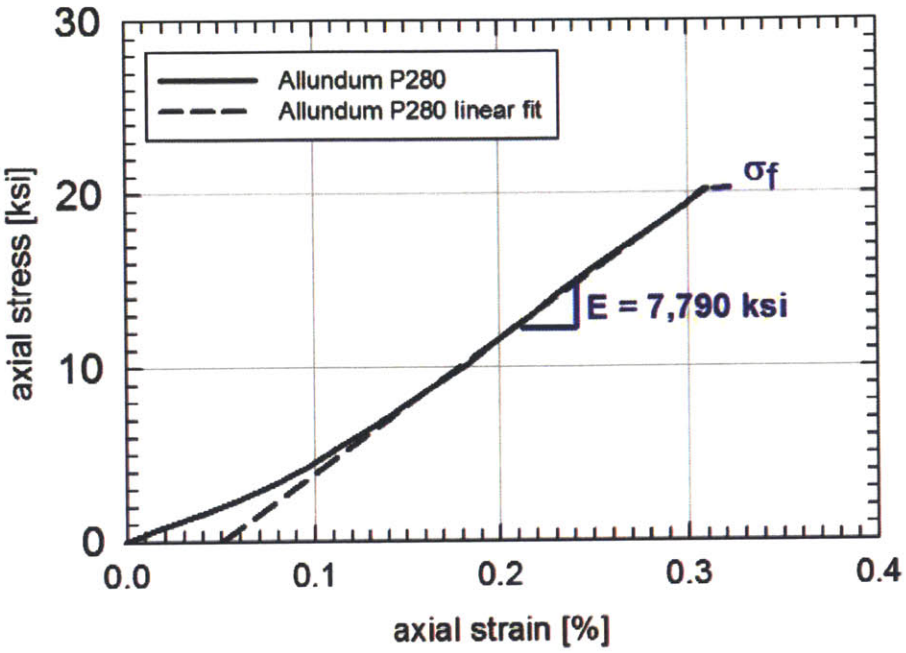

Figure 4-2: The stress-strain curve from an unconfined compression test characterizes the Allundum® P280 porous stone material.

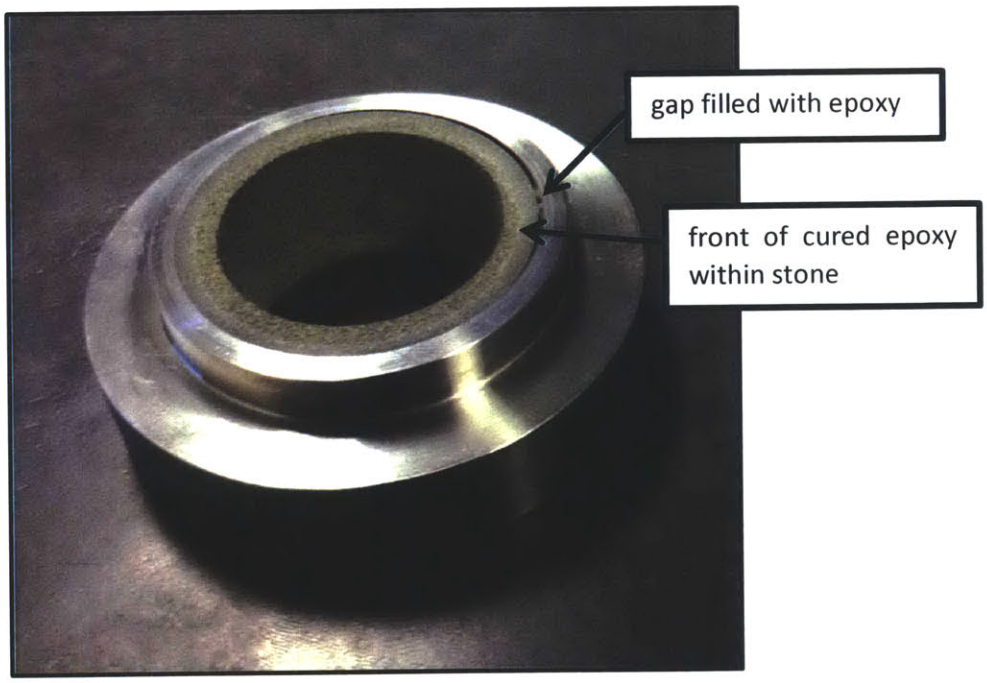

Figure 4-3: The epoxied porous stone within the steel confining ring was partially penetrated with epoxy and exhibited a discontinuous gap between the stone and ring.

Figure 4-4: The epoxied porous stone cracked during trial loading.

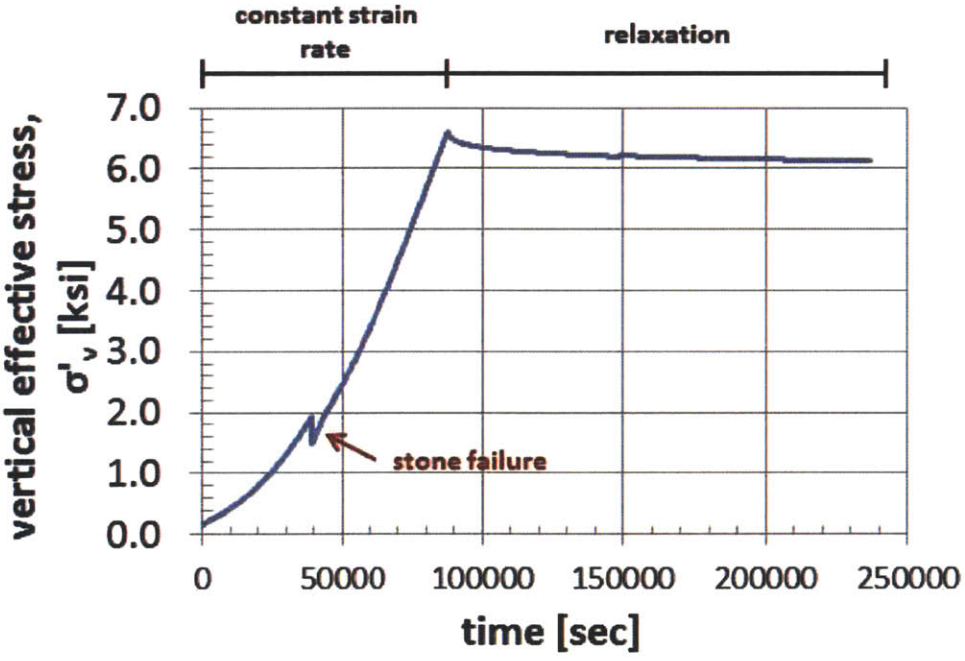

Figure 4-5: The loading of Presumscot clay inside epoxied trial radially-draining confinement ring shows the stress of stone failure.

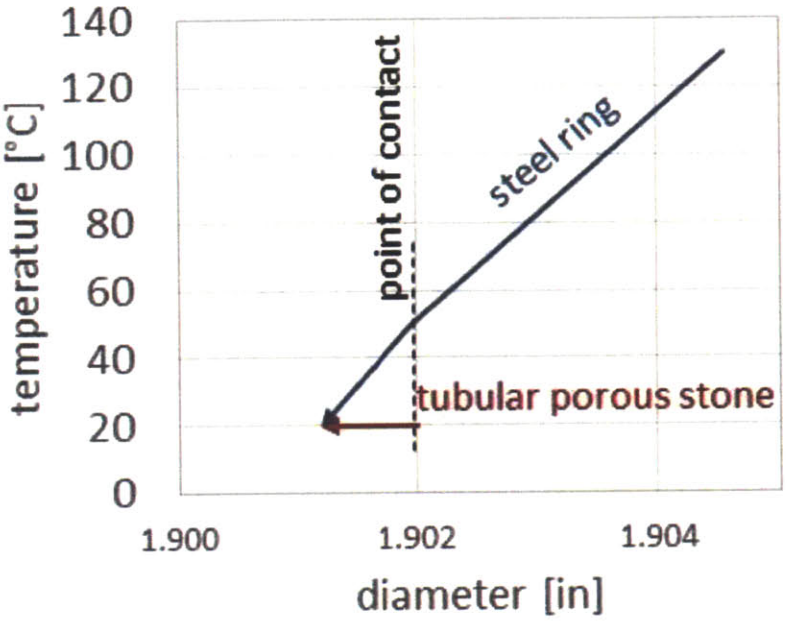

Figure 4-6: The change in interface diameter of confinement ring components due to cooling in thermal press-fit process creates an inward pre-strain on the tubular porous stone.

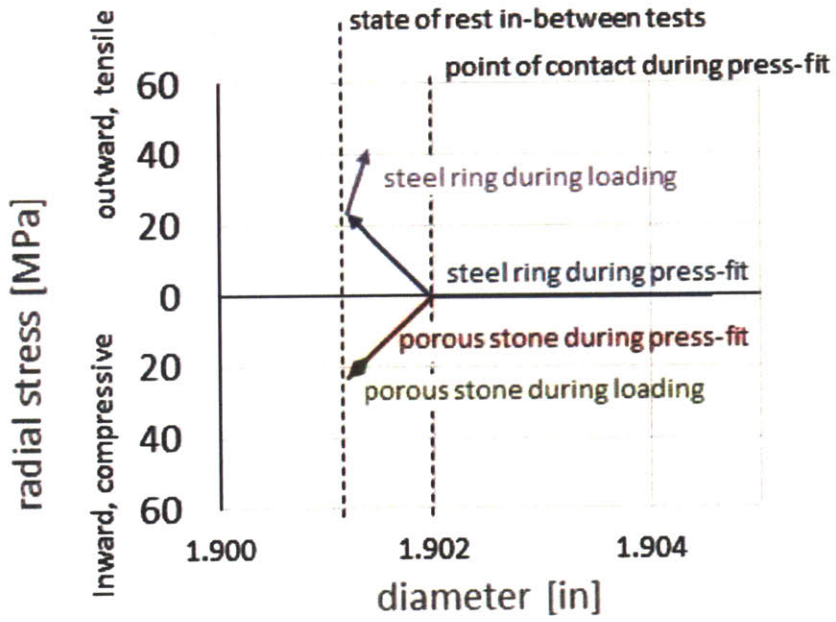

Figure 4-7: The thermal press-fit of the tubular-shaped porous stone creates an inward, compressive stress. Only the steel ring experiences outward, tensile stress during the loading process.

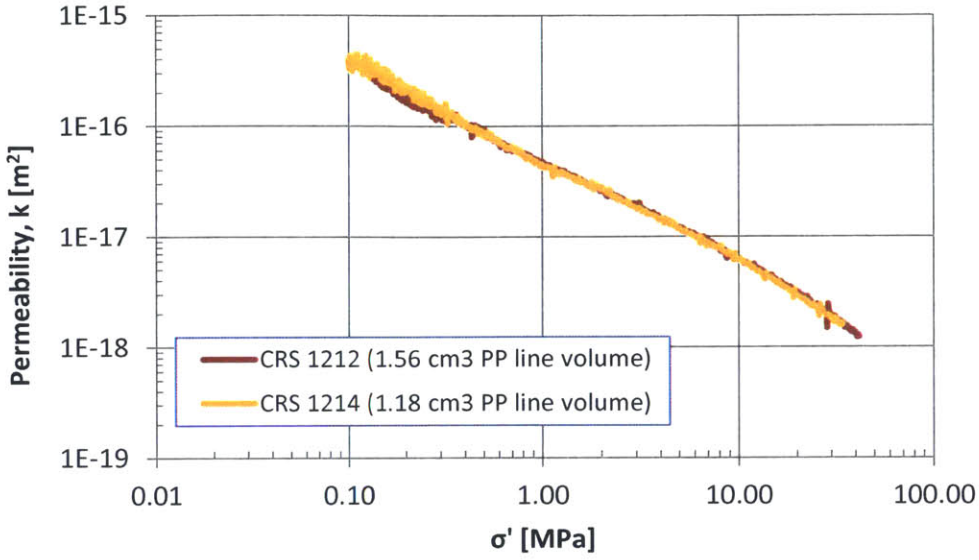

Figure 4-8: The comparison of permeability between CRS 1212 and CRS 1214 show minimal change in results as a function of pore pressure line volume.

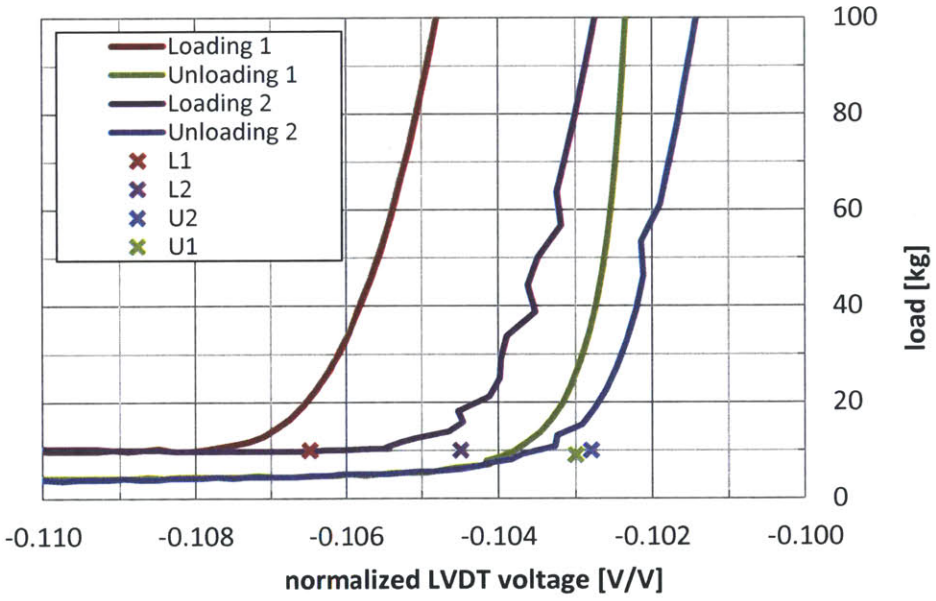

Figure 4-9: LVDT zero voltages were recorded as the voltage at the threshold of contact between the piston and the steel dummy specimen during constant-rate-of-strain loading. This example is from the LVDT zeroing of the blue LVDT from CRS TR5.

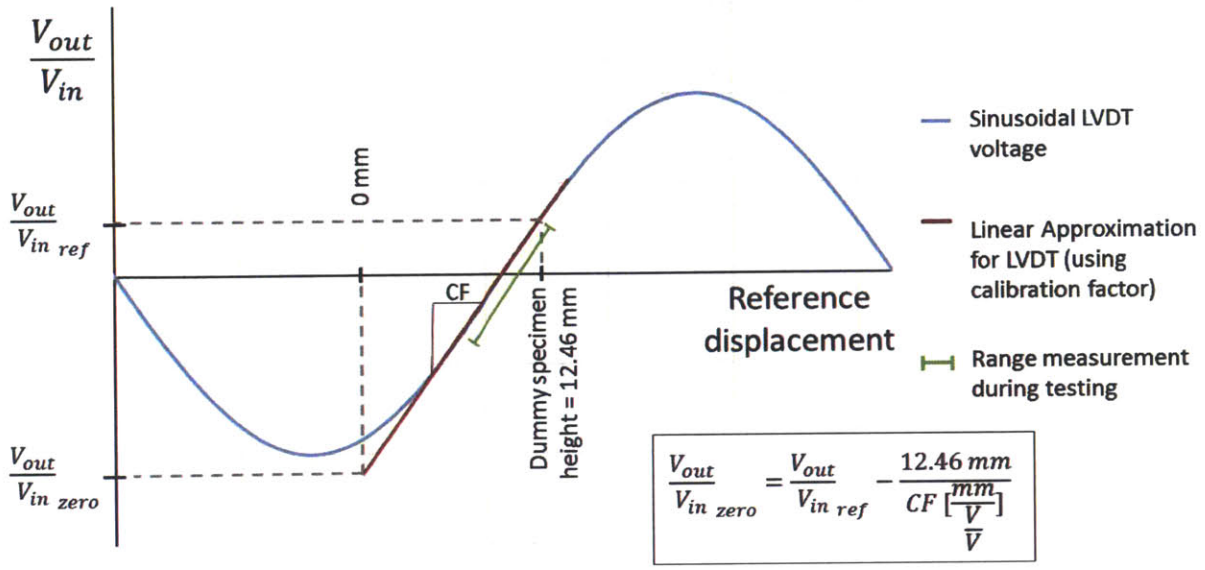

Figure 4-10: The calculation of the LVDT normalized zero voltages is represented conceptually. This method allows for accuracy, precision, and reproducibility in porosity measurements.

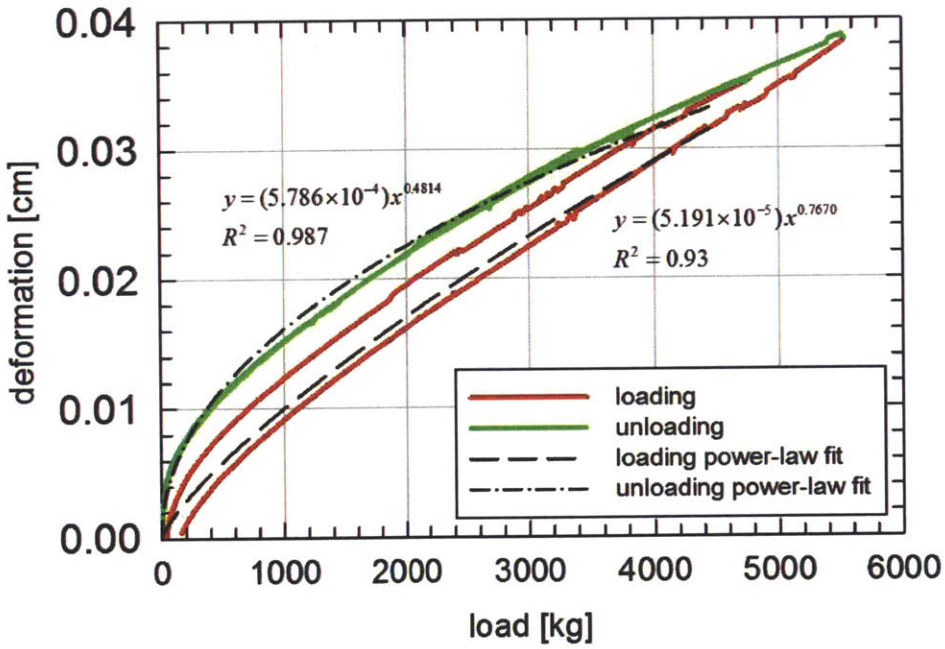

Figure 4-11: The apparatus compressibility curve for the TR5 – vertically draining CRS consolidometer is reproduced and used to correct the deflection data during testing using a power law function.

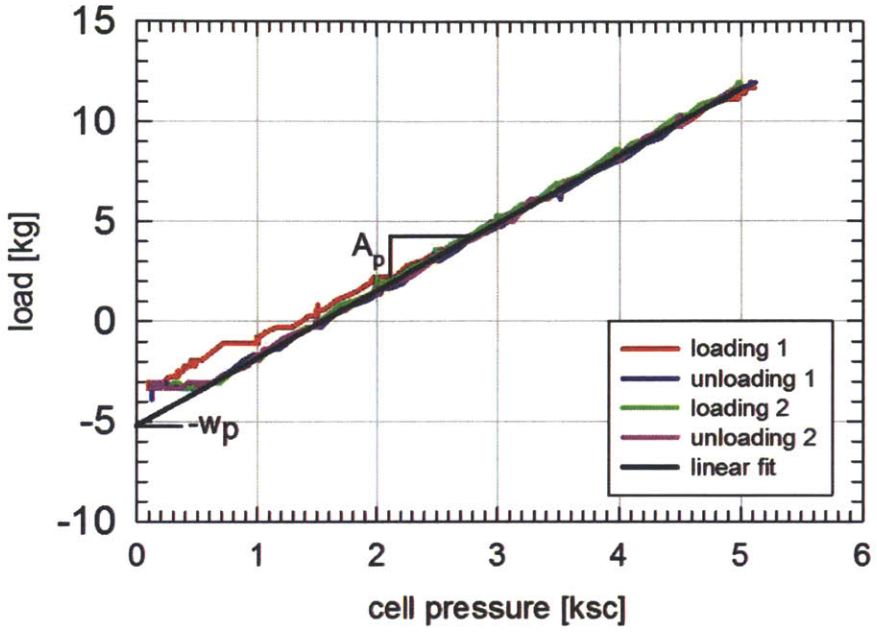

Figure 4-12: The calibration of CRS consolidometer TR5 was performed to determine the area (A_p) and weight of the piston (w_p) parameters.

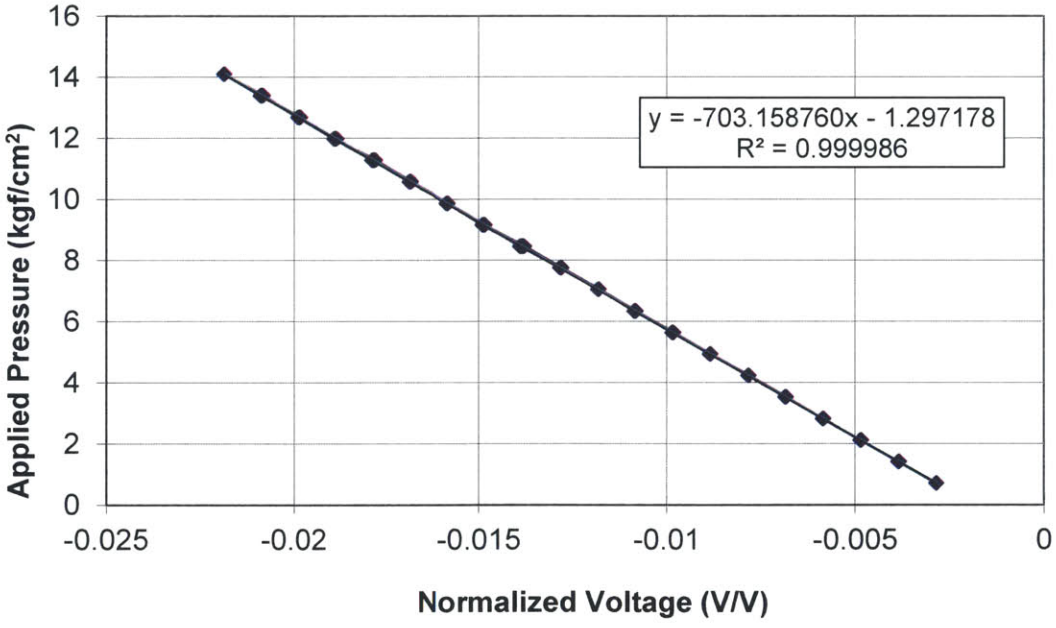

Figure 4-13: Engineering values are correlated to normalized voltage readings using a calibration factor. The calibration factor of pressure transducer D10342 is equal to the slope of a linear fit through the data.

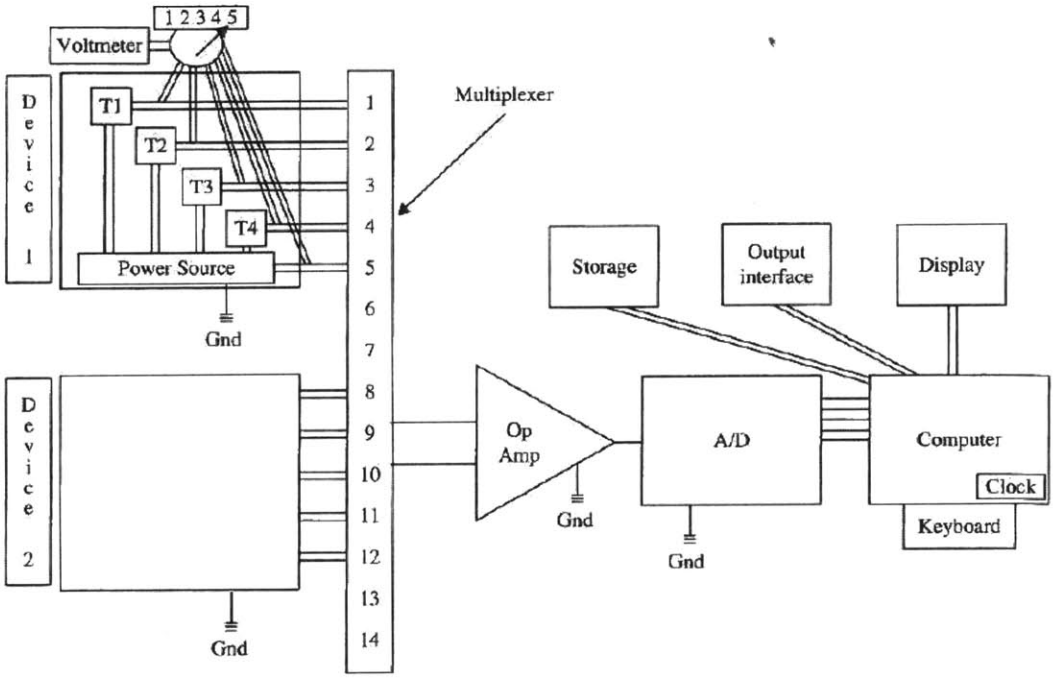

Figure 4-14: Test data are collected through a centralized data acquisition system, which can be represented in this schematic diagram. (Germaine & Germaine, 2009)

CHAPTER 5 – PROCEDURES

5.1 INTRODUCTION

This chapter explains the testing and analysis procedures used to measure permeability anisotropy. Vertically- and radially-draining CRS testing and analysis is described in great detail, in the form of instructions, as this permeability anisotropy measurement method is developed by the author. Cubic specimen constant head permeability and resistivity anisotropy measurement testing and analysis is only summarized, as a more detailed description can be found in Adams' PhD thesis (2014).

5.2 TESTING PROCEDURES

This section describes specimen testing procedures, from resedimentation tube extrusion to data processing. Vertically- and radially-draining CRS testing procedures are first described in the form of instructions. We then summarize the cubic specimen constant head permeability and resistivity testing procedures.

5.2.1 Vertically-Draining Constant Rate of Strain (CRS) Testing

This sub-section gives detailed instructions for testing a mudrock specimen in a conventional Trautwein® vertically-draining CRS device. The procedures are sub-divided into the following steps: preparations for testing, specimen trimming, cell set-up, backpressuring, saturation check, re-zeroing transducers,

leak check, loading, and disassembly. The procedures are listed in the form of a checklist on the testing data sheet, shown in Appendix B, to foster consistent procedures between tests.

Preparations

Prepare to set up the vertically-draining CRS device using the following procedure:

1. Be sure the LVDTs have previously been zeroed to the point where the top cap comes into contact with the base (see Section 4.3.1).
2. Disassemble the CRS apparatus (see Figure 5-1).
3. Set the gears to the desired strain rate (see Figure 5-2).
4. Obtain the following (see Figure 5-3):
    a. trimming turntable w/ wax paper at the base
    b. trimming tool(s)
    c. wire saw
    d. plastic discs
    e. calipers
    f. large Ziploc® bag
    g. top porous stone and filter paper (1.4" diameter)
    h. bottom porous stone and filter paper (2.5" diameter)
5. Obtain the mass of the following:
    a. 3 tares to measure the water content of trimmings
    b. confinement ring
    c. acrylic spacer
    d. top porous stone, SSD (saturated surface dry)
    e. top filter paper, SSD
6. Obtain the following dimensions:
    a. confinement ring inner diameter
    b. confinement ring height
    c. top porous stone w/ filter paper thickness
    d. bottom porous stone w/ filter paper thickness

Specimen Trimming

The resedimented soil specimen is trimmed into the confinement ring using the following procedure:

1. Extrude approximately 1" of at least 1.7" diameter resedimented mudrock from a resedimentation tube (see Figure 5-4).
2. Place the sample on the trimming turntable pedestal, with a piece of wax paper in-between the soil and the pedestal to prevent adhesion.
3. Attach the confinement ring, with the cutting edge towards the sample, into the top of the trimming turntable.
4. Align the specimen to be concentric with the confinement ring, in order to create a specimen that has minimal disturbance due to consolidation and extrusion sleeve friction.
5. Using a trimming blade, create a taper at the top of the sample, gradually reducing the sample diameter from the resedimentation tube diameter to the cutting edge diameter (see Figure 5-5).
6. Once the top of the taper almost meets the cutting edge, gently advance the cutting shoe downward. Clean away cut soil from the cutting shoe.
7. Collect some soil trimmings in the pre-massed tares and store them in a Ziploc® bag to prevent moisture loss.
8. Repeat steps 5-7 until the sample has advanced nearly the whole way into the cutting shoe.
9. Carefully remove the confinement ring (containing the soil) from the trimming turntable.
10. Secure the confinement ring (containing the soil) with a bench-mounted vice, and trim the top of the sample using a wire saw. The wax paper can be used to help remove the trimmings. Clean the confinement ring (see Figure 5-6).
11. Place the top filter paper on top of the specimen.
12. Place the acrylic spacer on the counter with the small diameter facing up, and place the confinement ring, soil specimen, and filter paper on top of the acrylic spacer (see Figure 5-7).
13. Use the spacer to advance the soil specimen through the confinement ring until the confinement ring stops on the shoulder of the acrylic spacer (see Figure 5-8).
14. Place the confinement ring, specimen, top filter paper, and acrylic spacer setup on its side in a table-mounted vice. Use a wire saw to carefully trim the bottom of the specimen at the base of the confinement ring. In order to catch the trimming before it adheres back onto the trimmed specimen, place a plastic disc onto the face to be trimmed. This disc can be used to remove the soil trimming while it is trimmed with the wire saw (see Figure 5-9).
15. Clean the bottom of the confinement ring.

16. Obtain the mass of the confinement ring, specimen, top filter paper, and acrylic spacer setup.
17. Obtain the mass of the tares with the wet cuttings, and place them in an oven for moisture content measurements.
18. Save portions of the sample for pore fluid salinity measurements and/or SEM imaging.

Cell Set-up

Set up the vertically-draining CRS cell using the following procedure:

1. Run water out of the pore pressure line to ensure saturation. Thoroughly clean and dry the cell base.
2. Place the bottom porous stone and filter paper into the depression in the base (SSD to prevent specimen swelling).
3. Concentrically place the confinement ring, specimen, top filter paper, and acrylic spacer setup onto the base (see Figure 5-10).
4. Carefully remove the acrylic spacer.
5. Place the top porous stone (SSD) on top of the specimen and top filter paper. The acrylic spacer can be used to help place the porous stone horizontally.
6. Measure the height difference between the top of the confinement ring and the top of the top porous stone with calipers (see Figure 5-11).
7. Lightly grease a square O-ring and place it around the base of the confinement ring.
8. Place the cell on top of the base, with the confinement ring, specimen, and top porous stone inside. Be sure that the top piston is raised high enough that it does not touch the top cap of the specimen during bolt tightening.
9. With the top cell drainage line open, tightly bolt the cell down to the base, alternatively tightening each bolt in increments to ensure level placement (see Figure 5-12).
10. Place the cell into the load frame enclosed in a temperature control box.
11. Secure the pre-zeroed LVDTs onto the top piston via a dual LVDT holder (see Figure 5-13).
12. Unlock the piston and lower in onto the top porous stone. The piston should remain unlocked beyond this point.
13. Record the "zero" voltage reading from the load cell.
14. Insert a moment/shear break in-between the piston and the load cell (see Figure 5-14).

15. Lower the load frame to contact the piston through the moment/shear break, ensuring the cell is placed concentrically within the load frame. Place a small seating load, roughly equal to 10% of the sampling effective stress (ASTM D4186, Note 15).
16. Record the "seated zero" voltage reading from the load cell.
17. Fill the cell with de-aired water that is at the same salinity as the specimen pore fluid. Flush any entrapped air through the top cell drainage line, and then close it.
18. Attach the pore pressure transducer after pore pressure line is fully saturated. Be sure the line is open to atmosphere at time of installation.
19. Hydraulically connect the cell to atmosphere through the burette above the PVA. Open the pore pressure line valve to connect pore pressure transducer to atmosphere.
20. Record LVDT, pressure transducer, and input "zero" voltage readings.

Backpressure the specimen

Although the water used is de-aired and care is taken to minimize entrapped air during set-up, it is impossible to keep the system air-free. In order to force the inevitable entrapped air into solution, the specimen is backpressured to 0.4 MPa. The pressure is applied incrementally to avoid specimen consolidation or shearing. The pressure is started at the seating load, then doubled until the cell pressure of 0.4 MPa is reached (ASTM D4186, Note 18). Backpressuring is performed using the following procedure:

1. Turn on the temperature control system within the temperature control box.
2. Input the correct transducer "zero" voltage readings and calibration factors into the computer feedback control system. Use the backpressure program to specify the desired cell pressure increments at intervals of 10 minutes.
3. Start a 4 minute data file, recording transducer readings on all channels.
4. Start the backpressure program on the computer feedback control system.
5. Monitor the backpressuring process on the data acquisition system.
6. Allow at least 8 hours after full backpressure is reached for pressure and temperature equilibration.

Check specimen saturation

CRS tests cannot be checked for saturation the same way triaxial tests can with a "B" value check, due to a lack of boundary condition control between the specimen and the cell. However, saturation can be hinted at by doing a "quasi-B" value check, with the following procedure:

1. Monitor saturation check using 3 second time intervals on the data acquisition system.
2. Close the pore pressure valve to isolate the pore pressure system from the cell pressure.
3. Use the computer feedback control to increase and hold the cell pressure at 0.5 MPa.
4. Monitor the increase in pore pressure for 60 seconds. According to ASTM D4186, if the pore pressure increases rapidly within 15 seconds, the specimen is sufficiently backpressured. An example of satisfactory performance is shown as Figure 5-15.
5. Reduce the cell pressure back to 0.4 MPa, and allow the pore pressure system to respond.
6. Open the pore pressure valve to hydraulically connect it to the cell pressure.

Re-Zero Transducers

Vertical permeability is calculated using the pressure gradient within the specimen. Therefore, it is critical to re-zero the pressure transducers so they read the same pressures at the 0.4 MPa backpressure. The following procedure outlines how to do this:

1. With the two pressure transducers hydraulically connected, record the output and input voltages at 0.4 MPa cell pressure.
2. Calculate the adjusted zero values for the pore pressure transducer, so that it gives similar pressure readings at 0.4 MPa as the cell pressure transducer. This can be done using the spreadsheet "vertical CRS calculation.xlsm."

Leak Check

Before the specimen is loaded, it is prudent to check for leaks in the pore pressure line. This is done using the following procedure:

1. Set the data acquisition system to take readings every 20 seconds.
2. Close the pore pressure line valve to isolate the pore pressure system so that it is connected only to the specimen.
3. Check for a substantial leak after 10 minutes. A substantial leak would be characterized by a substantial pressure drop in the pore pressure system. An example leak check is shown as Figure 5-16.
4. Open the pore pressure line valve to allow the pore pressures to re-equilibrate.

Loading

To calculate permeability as a function of compression, the specimen is loaded and pore pressure gradients are monitored. Specimen loading is conducted using the following procedure:

1. Set the gears and transmission to the desired strain rate. The strain rate should be high enough to develop excess pore pressures that are readable within the resolution of the pore pressure transducers, but low enough that the induced flow doesn't disturb the soil fabric. This study used a strain rate of 1.4% per hour for RBBC and 0.3% per hour for RGoM-EI. The pore pressure ratio (ratio between maximum excess pore pressure and vertical total stress) should be between 3% and 15% with a target of 5% (ASTM D4186). Calculations have been successful with pore pressure ratios as low as 0.5%, however (Fahy, 2014). Further suggestions on strain rate can be found in ASTM D4186 Notes 20 and 21.
2. Set the data acquisition system to take readings every 3 to 4 minutes.
3. Close the pore pressure line valve.
4. Engage the transmission and start the motor to begin vertical compression.
5. Load the specimen to the desired stress, without exceeding the load cell or pore pressure transducer capacities.
6. Shut off the motor.

Disassembly

The vertical CRS setup is disassembled using the following procedure:

1. Obtain the mass of two tares for the measurement of water content.
2. Obtain a knife, calipers, a beaker of water, and a water bottle
3. Prepare a hydraulic jack for specimen extrusion.
4. Record the transducer readings just before disassembly.
5. Lock the piston to minimize swelling during unloading.
6. Open the pore pressure system valve, to hydraulically connect the pore pressure line to the cell pressure line and the PVA.
7. Reduce the cell and pore pressure systems to atmospheric pressure at the burette above the PVA.
8. Record the final LVDT, pore pressure, and cell pressure "zero" voltage readings.
9. Unload the piston.
10. Record the final load cell "zero" voltage reading.

11. Remove the LVDT hanger (connected to the LVDTs) from the piston.
12. Remove the cell from the load frame / temperature control box and place it on a paper-towel-covered tray (see Figure 5-29).
13. Close the valve connecting the manifold to the cell, open the top drainage line on the cell, and remove the cell from the base, allowing the cell water to flow out.
14. Carefully drain the water trapped above the specimen, and measure the distance between the top of the confinement ring and the top porous stone using calipers (see Figure 5-30).
15. Remove the square O-ring.
16. Remove the confinement ring, specimen, and top porous stone from the base pedestal.
17. Dry off any excess water from the confinement ring, and obtain final mass of specimen, ring, top porous stone, and top filter paper.
18. Remove the specimen from the confinement ring. A hydraulic jack might be needed to overcome the friction between the stone and the soil (see Figure 5-32).
19. Measure the height of the specimen using calipers.
20. Obtain the wet mass of specimen within a tare and dry it in an oven for 24 hours to obtain the dry mass.
21. Collect any extraneous soil from the confinement ring, top porous stone, and top filter paper in a tare. A water bottle can be used to wash the soil solids off of the equipment. Oven dry the extraneous soil and tare to add extraneous soil solids to the specimen's dry mass.

5.2.2 Radially-Draining Constant Rate of Strain (CRS) Testing

The following procedures are used to test a mudrock specimen in a radially-draining CRS device. The procedures are sub-divided into the following steps: preparations for testing, specimen trimming, cell set-up, backpressuring, saturation check, re-zeroing transducers, leak check, loading, and disassembly. The procedures are listed in the form of a checklist on the testing data sheet, shown in Appendix B, to foster consistent procedures between tests.

Preparations

Prepare to set up the radially-draining CRS device using the following procedure:

1. Be sure the LVDTs have previously been zeroed to the point where the top cap comes into contact with the base (see Section 4.2.5).
2. Disassemble the CRS apparatus (see Figure 5-17).
3. Run water through the pore pressure pinholes in the base to be sure there are no clogs (see Figure 5-18). See "Pore Pressure Pinhole Un-clogging" section for help with clogs.
4. Set the gears to the desired strain rate (see Figure 5-2).
5. Obtain the following (see Figure 5-19):
    a. trimming turntable w/ wax paper at the base
    b. trimming tool(s)
    c. wire saw
    d. plastic discs
    e. calipers
    f. large Ziploc® bag
6. Obtain the mass of the following:
    a. 3 tares to measure the water content of trimmings
    b. cutting shoe
    c. acrylic spacer
    d. stainless steel top cap
7. Obtain the following dimensions:
    a. confinement ring inner diameter
    b. confinement ring height
    c. top cap thickness
    d. base pedestal height

Specimen Trimming

The resedimented soil specimen is trimmed into the confinement ring using the following procedure:

1. Extrude approximately 1" of at least 1.7" diameter resedimented specimen from its resedimentation tube (see Figure 5-4).
2. Place the specimen on the trimming turntable pedestal, with a piece of wax paper in-between the soil and the pedestal to prevent adhesion.

3. Attach the cutting shoe to the top of the trimming turntable.
4. Align the specimen to be concentric with the cutting shoe, in order to create a specimen that has minimal disturbance due to consolidation and extrusion sleeve friction.
5. Using a trimming blade, create a taper at the top of the sample, gradually reducing the sample diameter from the resedimentation tube diameter to the cutting edge diameter (see Figure 5-5).
6. Once the top of the taper almost meets the cutting edge, gently advance the cutting shoe downward. Clean away the cut soil from the cutting shoe.
7. Collect some soil trimmings in the pre-massed tares and place them in a Ziploc® bag to prevent moisture loss.
8. Repeat steps 5-7 until the specimen has advanced nearly the whole way into the cutting shoe.
9. Mass the confinement ring at saturated surface dry (SSD) condition. Do not return it to its water bath.
10. Carefully remove the cutting shoe (containing the soil) from the trimming turntable.
11. Place the cutting shoe (containing the soil) into a bench-mounted vice, and trim the top of the sample using a wire saw. Clean the cutting shoe (see Figure 5-6).
12. Place the cutting shoe (containing the soil) on top of the confinement ring (see Figure 5-20).
13. Place the stainless steel top cap on top of the specimen, with the large diameter against the specimen, and gently push down to start advancing the specimen towards the confinement ring.
14. Place the acrylic spacer on the counter with the small diameter facing up, and place the confinement ring, cutting shoe, soil specimen and top cap on top of the acrylic spacer. Be sure to hold the cutting shoe and confinement ring together during this process to minimize sample disturbance (see Figure 5-21).
15. Use the spacer to advance the soil specimen into the confinement ring until the shoulder on the acrylic spacer stops on the cutting shoe's cutting edge (see Figure 5-22).
16. Place the confinement ring, cutting shoe, specimen, top cap, and acrylic spacer setup on its side in a table-mounted vice. Use a wire saw to carefully trim the bottom of the specimen at the base of the confinement ring. In order to catch the trimming before it adheres back onto the trimmed specimen, place a plastic disc onto the face to be trimmed. This disc can be used to remove the soil trimming while it is trimmed with the wire saw. This surface is extremely important, as it is where excess pore pressures are measured from (see Figure 5-23).
17. Clean the bottom of the confinement ring.

18. Obtain the mass of the confinement ring, cutting shoe, specimen, top cap, and acrylic spacer setup.
19. Obtain the mass of the tares with wet cuttings from the Ziploc® bag, and oven dry them for 24 hours for moisture content measurements.
20. Save portions of the sample for pore fluid salinity measurements and/or SEM imaging.

Cell Set-up

Set up the radially-draining CRS cell using the following procedure:

1. Run water out through the pore pressure pinholes on the base pedestal to ensure line saturation, check for, and prevent clogging (see Figure 5-18).
2. Close the pore pressure valves and dry the pedestal thoroughly to prevent specimen swelling.
3. Concentrically place the confinement ring, cutting shoe, specimen, top cap, and acrylic spacer setup onto the base. When it is aligned, gently push down to allow the pedestal to contact the soil specimen, and push it back up into the confinement ring. Push the confinement ring all the way down so that it rests firmly on the base (see Figure 5-24).
4. Carefully remove the acrylic spacer and cutting shoe (see Figure 5-25).
5. Measure the height difference between the top of the confinement ring and the top of the top cap with calipers (see Figure 5-26).
6. Lightly grease a square O-ring and place it around the base of the confinement ring.
7. Place the cell on top of the base, with the confinement ring, specimen, and top cap inside. Be sure that the top piston is raised high enough that it does not touch the top cap of the specimen during bolt tightening.
8. With the top cell drainage line open, tightly bolt the cell down to the base, alternatively tightening each bolt in increments to ensure level placement (see Figure 5-12).
9. Place the cell into the load frame within a temperature control box.
10. Record the "zero" voltage reading from the load cell.
11. Insert a moment/shear break in-between the piston and the load cell (Figure 5-14).
12. Release the piston and lower it onto the top cap. The piston should remain unlocked beyond this point.
13. Lower the load frame to contact the piston, ensuring the cell is placed concentrically within the load frame. Place a small seating load, roughly equal to 10% of the sampling effective stress (ASTM D4186, Note 15).

14. Record the "seated zero" voltage reading from the load cell.
15. Fill the cell with de-aired water that is at the same salinity as the specimen pore fluid. Flush any entrapped air through the top cell drainage line, and then close it.
16. Hydraulically connect the cell to atmosphere through a burette on the manifold. Open the pore pressure line valves to connect all three pressure transducers to atmosphere.
17. Record the LVDT, pressure transducer, and input "zero" voltage readings.

Backpressure the specimen

Although the water used is de-aired and care is taken to minimize entrapped air during set-up, it is impossible to keep the system air-free. In order to force the inevitable entrapped air into solution, the specimen is backpressured to 0.4 MPa. The pressure is applied incrementally to avoid specimen consolidation or shearing. The pressure is started at the seating load, then doubled until the cell pressure of 0.4 MPa is reached (ASTM D4186, Note 18). Backpressuring is performed using the following procedure:

1. Turn on the temperature control system inside the temperature control box.
2. Calculate the voltage output readings expected from the cell pressure transducer during the backpressure process. This can be done by inputting the transducer zero readings and calibration factors into the "Transducers" tab of the spreadsheet "radial CRS calculation.xlsm," and converting the desired pressures into voltage readings in the "BP" tab.
3. Start a 4 minute data file, recording transducer readings on all channels.
4. Backpressure the cell to 0.4 MPa, waiting at least 10 minutes between adding each increment, using an air pressure regulator connected to the cell pressure via a pressure-volume actuator. The desired pressures can be achieved by matching the cell pressure transducer output readings to the calculated backpressuring schedule output readings.
5. Monitor the backpressuring process on the data acquisition system.
6. Allow at least 8 hours after full backpressure is reached for pressure and temperature equilibration.

Check specimen saturation

CRS tests cannot be checked for saturation the same way triaxial tests can with a "B" value check, due to a lack of boundary condition control between the specimen and the cell. However, saturation can be hinted at by doing a "quasi-B" value check, with the following procedure:

1. Monitor the saturation check using 3-second time intervals on the data acquisition system.

2. Close the pore pressure monitor valves to isolate the pore pressure monitors from the cell pressure lines.
3. Calculate the voltage output reading required from the cell pressure transducer to read 0.5 MPa.
4. Close the cell pressure valve, and increase the pressure in the manifold to 0.5 MPa using the air pressure regulator. Open the cell pressure line to expose the cell and specimen to an instantaneous increase to 0.5 MPa of pressure.
5. Monitor the increase in pressure in the pore pressure monitor lines for 60 seconds. According to ASTM D4186, if the pore pressure increases rapidly within 15 seconds, the specimen is sufficiently backpressured. An example of satisfactory performance is shown as Figure 5-27.
6. Reduce the cell pressure back to 0.4 MPa, and allow the pore pressure monitor lines to respond.
7. Open the pore pressure valves to hydraulically connect them to the cell pressure lines.

Re-Zero Transducers

Radial permeability is calculated using the pressure gradient within a specimen. Therefore, it is critical to re-zero the pressure transducers so they read the same pressures at the 0.4 MPa backpressure. The following procedure outlines how to do this:

1. With the three pressure transducers hydraulically connected, record the output and input voltages at 0.4 MPa of cell pressure.
2. Calculate the adjusted zero values for both the maximum pore pressure and the pore pressure check transducers, so that they give similar pressure readings at 0.4 MPa. This can be done using the "transducers" tab of the spreadsheet "radial CRS calculation.xlsm."

Leak Check

Before the specimen is loaded, it is prudent to check for leaks in the pore pressure lines. This is done using the following procedure:

1. Set the data acquisition system to take readings every 20 seconds.
2. Close the pore pressure line valves to isolate the pore pressure lines to be connected only to the specimen.
3. Check for substantial leaks after 10 minutes. A substantial leak would be characterized by a substantial drop in pressure in the pore pressure lines. An example satisfactory leak check is shown as Figure 5-28.
4. Open the pore pressure line valves to let the pore pressure lines re-equilibrate.

Loading

To calculate permeability as a function of compression, the specimen is loaded and pore pressure gradients are monitored. Specimen loading is conducted using the following procedure:

1. Set the gears and transmission to the desired strain rate. The strain rate should be high enough to develop excess pore pressures that are readable within the resolution of the pore pressure transducers, but low enough that the induced flow doesn't disturb the soil solid fabric. This study used a strain rate of 1.4% per hour for RBBC and 0.3% per hour for RGoM-EI. The pore pressure ratio (ratio between maximum excess pore pressure and vertical total stress) should be between 3% and 15% with a target of 5% (ASTM D4186). Calculations have been successful with pore pressure ratios as low as 0.5%, however (Fahy, 2014). Further suggestions on strain rate can be found in ASTM D4186 Notes 20 and 21.
2. Set the data acquisition system to take readings every 3 to 4 minutes.
3. Close the pore pressure line valves.
4. Engage the transmission and start the motor to begin vertical compression.
5. Load the specimen to the desired stress, without exceeding the load cell or pore pressure transducer capacities.
6. Shut off the motor.

Disassembly

1. Obtain the mass of two tares for the measurement of water content.
2. Obtain a knife, calipers, a beaker of water, and a water squirt bottle.
3. Prepare a hydraulic jack for specimen extrusion.
4. Record the LVDT, load, and cell pressure voltage readings just before disassembly.
5. Lock the piston to minimize swelling during unloading.
6. Open the pore pressure monitor valves, to hydraulically connect the pore pressure monitors to the cell pressure and the manifold.
7. Reduce the cell pressure to atmospheric pressure using the air pressure regulator at first, and the manifold burette at the end.
8. Record the final LVDT, pore pressure, and cell pressure zero readings.
9. Unload the piston.
10. Record the final load cell "zero" voltage reading.

11. Remove the cell from the load frame within the temperature control box and set it on a tray covered in paper towels. The paper towels are used to absorb the water from the cell when the cell is taken apart (see Figure 5-29).
12. Close the valve connecting the manifold to the cell, open the top drainage line on the cell, and remove the cell from the base, allowing the cell water to flow out and soak into the paper towels.
13. Carefully drain the water trapped above the specimen, and measure the distance between the top of the confinement ring and the top of the top cap using calipers (see Figure 5-30).
14. Carefully remove the confinement ring, specimen, and top cap from the base pedestal. This can be a tough process as the bottom of the specimen tends to adhere to the stainless steel pedestal after exposure to high stresses. The use of a razor blade can help in separating the confinement ring from the base (see Figure 5-31).
15. Dry off any excess water from the confinement ring, and obtain the final mass of the specimen, ring, and top cap setup.
16. Remove the specimen from the confinement ring. A hydraulic jack might be needed to overcome the friction between the stone and the soil (see Figure 5-32).
17. Measure the height of the specimen using calipers.
18. Obtain the wet mass of the specimen inside a tare and place it in an oven for 24 hours to obtain its dry weight.
19. Collect any extraneous soil from the ring, pedestal, and top cap in a tare. A water bottle can be used to wash the soil solids off of the equipment. Oven dry the extraneous soil, which will be added to the mass of the dry specimen for the total dry mass (see Figure 5-33 and Figure 5-34).
20. Obtain the mass of the composite porous stone - steel confinement ring (SSD) after extrusion and collection of extraneous soil.
21. Repeatedly place confinement ring in an ultrasonic bath, rub the surface of the porous stone, and change the bath water, until no soil is seen exiting stone in the bath.
22. Obtain the mass (SSD) of the composite porous stone - steel confinement ring after ultrasonic cleaning. The mass should reach close to the original saturated surface dry mass, to prevent clogging of the stone over repeated usage.

Pore Pressure Pinhole Un-clogging

The 0.005" diameter pore pressure pinholes tend to clog frequently, especially when high salinity pore fluid is used. The best practice to keep them from becoming completely clogged is to check and clean them in-between each use. The following tricks can be used to clean and un-clog the pinholes:

- Increase the pressure gradient within the hole, by increasing the pressure in the pore pressure line when the pinholes vent to atmosphere. If no water flows, a very small wire can be used to penetrate the surface of the pinhole and loosen any surface obstacles. Once flowing, allow a large volume of water to flow through (see Figure 5-18).
- The 0.005" pinholes only penetrate 0.040" into the base before they open up into 1/16" diameter holes, which are drilled from the underside of the base to meet the 0.005" holes. Remove the plugs on the underside of the base to access the pinholes from the bottom. Penetrate the underside of the pinhole by hand using a small (~1/64") drill bit. This can loosen precipitates and soils stuck at the bottom of the pinhole.
- Place the base in an ultrasonic bath in distilled water.
- Pressurize the system using distilled water without a specimen.

5.2.3 Cubic Specimen Constant Head Permeability and Resistivity Testing

Constant head permeability tests are performed using a flexible wall permeameter within a triaxial cell (ASTM D5084). Permeability and electrical resistivity are measured in orthogonal directions by testing cubic specimens at different orientations. Measurements are collected on separate specimens with varying stress histories. The specimens have theoretically identical mineralogies and pore fluid salinities through the resedimentation technique.

The testing equipment and procedure used were developed by Adams (2014). The resedimented sample is first trimmed into a cube. It is then placed inside the permeameter setup within a triaxial cell and an initial cell pressure is induced under undrained conditions. The specimen is then backpressured to force entrapped air into solution. The sample is then reconsolidated to the OCR = 4 hydrostatic stress state. Under that hydrostatic stress, we measure the permeability and electrical resistivity of the specimen. The setup is tested for leaks before it is taken down, and quantified leaks are corrected for in the analysis. After each measurement is complete, the setup is taken down and these steps are repeated on the same specimen in two more orthogonal directions. This allows one to determine

anisotropy and correct for disturbance effects that occur during take down and setup. For a more detailed description of the cubic specimen constant head permeability and resistivity testing procedures used, see Adams' (2014) thesis.

Specimen Trimming

To perform a cubic specimen constant head test, we start by obtaining a 3-inch diameter resedimented mudrock. A miter box is used to trim the mudrock orthogonally. First the height of the specimen is trimmed to 5 cm. The cylindrical specimen is then positioned in the miter box with the flat surfaces on top and bottom. A 3 inch spacer block is placed behind the specimen, and another block is placed on the side of the specimen. A clamp is then used to hold the specimen in place while the first side of the specimen is cut. The opposite side is then cut after flipping the specimen around, creating the second 5 cm dimension. The final two sides are then cut in a similar fashion, with a 5 cm spacer block behind the specimen instead of a 3 inch spacer. The exact dimension measurements are obtained and moisture contents of the trimmings are determined. The faces are lightly marked as V, H1, or H2, in order to keep track of the setup geometry and correctly match geometries with measured data.

For high porosity mudrocks, trimming can be done using a wire saw. For medium porosity mudrocks, a razor blade can be used as a knife. For low porosity mudrocks, a coarse-toothed bow saw is used. In low and medium porosity mudrock specimens, small holes are drilled on the specimen's faces which will come in contact with the porous stones and electrodes, in order for the resistivity pin to penetrate the specimen without shearing it. This is best done with a Dremel® drilling tool.

Permeameter Setup

After the specimen is trimmed into a cube, it is placed inside a triaxial cell with special square endcaps. If resistivity measurements are also desired, endcaps including electrodes need to be used. The bottom endcap is placed over the existing cylindrical triaxial endcap. A square specimen is placed on the endcap, with a square porous stone and filter paper placed in-between them. Another square filter paper and porous stone are placed on top of the specimen, with the top endcap placed on top. The specimen/endcap setup is encased by two 2.5 inch diameter, 9 inch long, 0.025 inch thick rubber membranes. They are placed onto the setup using a membrane stretcher. The ends of the membranes are sealed to the endcaps using the signature MIT 3 O-ring configuration on each end. Two of the O-rings are placed in-between the membranes, while one of the O-rings is placed outside both membranes and rests in-between the other two.

Once the specimen, endcaps, and membranes are in place, the top cap drainage line is connected to the base drainage line. The setup is then placed under vacuum from both the top and the bottom, stiffening the setup. The connections for the resistivity probes are then made. The triaxial cell is then assembled and filled with silicon oil.

While the specimen is still under vacuum, the cell is pressurized to just above the expected sampling effective stress. Once that pressure is achieved, the vacuum on the specimen is released and the specimen is given brief access to saltwater (the salt water used in the lines has the same salinity as the specimen's batched pore water salinity). The drainage lines are then closed, with a pressure transducer left to monitor the pore pressure within the specimen. The specimen is left for at least 8 hours, in order to temperature and pressure equilibrate. Subtracting the equilibrated pore pressure from the cell pressure gives the sampling effective stress.

Backpressuring

The specimen is backpressured to force entrapped air into solution and create a more incompressible fluid. The backpressure is introduced in 0.05 to 0.1 MPa increments, up to at least 0.6 MPa. The triaxial "B" parameter is calculated as the ratio of the change in undrained pore pressure as a response an increase in cell pressure, over the change in cell pressure. If the "B" value is high and the pore pressure response is fast, the specimen is considered sufficiently saturated. If the specimen is not sufficiently saturated, further increasing the backpressure should force more air into solution and increase the saturation, thus increasing the "B" value. It should be kept in mind, however, that the "B" value is not only a function of the system saturation, but also of the stiffness of the mudrock. A stiff mudrock, for example, will take on a good portion of the increase in cell pressure as effective stress, decreasing the increase in pore pressure during a "B" value check. Some stiff mudrocks cannot exceed "B" values of 0.75, without exceeding the capacity of the pore pressure transducers. When saturation is deemed acceptable, the final backpressure is maintained for at least 8 hours for pressure equilibration.

Recompression

It is likely that the sampling effective stress is different from the desired effective stress, thus the porosity is also slightly different. However, it is critical that the permeability measurements in the different directions are performed at the same effective stress and porosity. If the difference in stress is significant, the specimen is recompressed to the desired effective stress. This is done by adjusting the

cell pressure while holding the pore pressure constant. The specimen is left to consolidate for at least 12 hours or until the rate of secondary compression can be determined.

Permeability Measurement

With the specimen set up, backpressured, and consolidated to the desired effective stress, permeability measurements are ready to be made. A hydraulic gradient is induced within the sample, by increasing the pressure at the base of the specimen and decreasing the pressure at the top of the specimen. By increasing the pressure at the base by the same increment as decreasing the pressure at the top of the specimen, the average effective stress within the specimen stays the same. Permeability is calculated by measuring the volume of water expelled from the PVA connected to the base of the specimen and the volume of water admitted into the PVA connected to the top of the specimen over a given time.

For each set up direction, at least three different gradients are measured, to uncouple permeability from induced gradient. Each gradient is left on the specimen for at least 12 to 24 hours, ensuring that a sufficient amount of data has been collected after the specimen has reached equilibrium (a small amount of swelling occurs at the base of the specimen due to the increase in pore water pressure, causing a decrease in effective stress; a small amount of consolidation occurs at the top of the specimen due to the decrease in pore water pressure, causing an increase in effective stress).

Leak Check

Before taking the setup down, a leak check is performed by inducing a "zero" gradient within the specimen. This is performed by holding the top PVA and the bottom PVA at the same pressure, while keeping them hydraulically separated. The PVAs are only hydraulically connected through the specimen, allowing them to exhibit individual leakage characteristics. The volume of water expelled by each PVA during 12 to 24 hours allows for leak calculation for each PVA and its associated plumbing.

In geotechnical testing, leaks cannot be completely avoided. Great precision can be gained, however, by quantifying them. This check is performed, and the leak rates are quantified, so that the leaks can be subtracted from the measured flow rate through the specimen.

Resistivity Measurement

While the setup is confined within the triaxial cell, the electrical resistivity is measured. An electrical current is induced through the specimen through square-shaped plate electrodes located on each endcap. The voltage is measured between two pin electrodes which protrude into the specimen, which are electrically separate from the current-inducing electrodes. The resistivity is calculated from the

voltage and current using several different currents. This allows for detection of any current – resistivity trend, similar to the decoupling of hydraulic gradient and conductivity in the permeability measurement.

Take Down

Following permeability and resistivity measurement, the cell is disassembled and the specimen is removed. Small holes are left on the cube's faces where the resistivity pin probe penetrated, and these holes can cause puncturing in the rubber membranes. Small pieces of rubber O-ring are placed inside holes to prevent such puncturing. The specimen is rotated 90° and the permeameter is set up again.

This process is repeated until permeability has been measured in all three orthogonal directions, typically in the following order: vertical, horizontal 1, and horizontal 2. After the final direction is measured and the permeameter is taken down, the specimen is allowed to equilibrate at atmospheric pressure within a double zip-lock bag. The final dimensions, mass, and moisture content are determined.

5.3 ANALYSIS PROCEDURES

The procedures used to analyze data for each individual test are described in this section. The procedures used to account for the presence of salt in phase relations calculations are first discussed. The methods for vertically and radially draining CRS data analysis are then described in the form of instructions, as these procedures were developed by the author (in accordance with ASTM D4186). Cubic specimen constant head permeability and resistivity data analysis procedures are then summarized (for further detail, see Adams, 2014).

5.3.1 Salt Mixing Guide

In order to correctly determine the phase relations of the specimens tested, a salt mixing guide, developed in the MIT Geotechnical Laboratory, is used for all calculations. Salt water density changes as a function of salinity and temperature. The density change cannot be calculated using phase relations assuming constant salt and distilled water densities. This is due to a coupling effect between salt density and saltwater salinity. The mixing guide incorporates the fact that salts behave like solids when dry, but dissolve into ions intermixed with water molecules when wet. Thus they change the density of the water, and can artificially increase the measured density of a specimen if not corrected for.

In order to account for the saltwater density coupling effect, an effective salt density is used. The dissolved density of the salt, which changes as a function of ion concentration, is calculated using

Equation 5-1. It is obtained in the form of Matlab® code derived from empirical measurements of saltwater density at various salinities (Sharqawy et al, 2012).

$$G_{s,sea\ salt} = (1.06\ x\ 10^{-5}) * salinity^2 + (-0.0075) * salinity + 4.17 \quad (5\text{-}1)$$

where:
$G_{s,sea\ salt}$ = effective specific gravity of salt
salinity = pore fluid salinity (g/L)

The density of water also changes as a function of temperature. The density of distilled water as a function of temperature is obtained from a curve-fit, developed from empirical standard water tables, given in ASTM D854. The density, ρ_w (g/cm^3) is calculated using Equation 5-2:

$$\rho_w = (-4.95\ x\ 10^{-6}) * T^2 + (-7.77\ x\ 10^{-6}) * T + 1.00034 \quad (5\text{-}2)$$

where:
T = temperature of water (°C)

The density of saltwater at a given temperature and salinity, ρ_{sw} (g/cm^3) can then be calculated using phase relations as shown in Equation 5-3:

$$\rho_{sw} = \rho_w + \left(1 - \frac{\rho_w}{G_{s,sea\ salt} * \rho_{w,20°C}}\right) * salinity * \left(\frac{1\ L}{1000\ cm^3}\right) \quad (5\text{-}3)$$

where:
$\rho_{w,20°C}$ = density of pure water at 20°C = 0.99821 g/cm^3

The dynamic viscosity of water, which is needed to calculate the permeability of a soil, is also dependent on both temperature and salinity. Sharqawy et al (2012) also provides Matlab® code for determining dynamic viscosity as a function of temperature and salinity, taken from fitting equations to measured water viscosities at various temperatures and salinities. The dynamic viscosity, μ [kg/(m-s)], for water at 24°C is calculated using Equation 5-4:

$$\mu = (5.0\ x\ 10^{-8}) * salinity^2 + (2.0\ x\ 10^{-5}) * salinity + 9.2\ x\ 10^{-3} \quad (5\text{-}4)$$

5.3.2 Vertically-Draining Constant Rate of Strain (CRS) Analysis

The vertically-draining constant rate of strain (CRS) consolidation test is analyzed in order to determine the compression and permeability behavior of a mudrock. This section gives instructions and equations for the analysis, subdivided into the following sections: (a) initial phase relations, (b) engineering values during test, (c) final phase relations, and (d) noise reduction. The methods follow the general procedure outlined in ASTM D4186, but are modified for greater precision and reproducibility.

Initial Phase Relations

The initial specimen properties are calculated for reference during the testing process and comparison with the final specimen properties. The initial measurements are not used for the final analysis, as they are not the most reliable.

The initial wet mass of the specimen, $m_{w,i}$ (g), is calculated by determining the mass of the trimmed specimen inside the confinement ring, with the acrylic spacer still attached. The individual masses of the confinement ring and acrylic spacer are then subtracted from the total mass.

The initial moisture content, wc_i (decimal), is calculated by averaging the moisture contents from various tares of specimen trimmings.

The initial dry mass of the specimen, $m_{d,i}$ (g), is calculated from the trimmed specimen and the averaged water content before the test using Equation 5-5:

$$m_{d,i} = \frac{m_{w,i}}{1 + wc_i} \quad (5\text{-}5)$$

The initial volume of the specimen, V_i (cm^3), is calculated using Equation 5-6:

$$V_i = h_i * A \tag{5-6}$$

where:
h_i = initial caliper-measured height of specimen inside ring (cm)
A = cross-sectional area of specimen/confinement ring (cm^2)

The initial dry density of the specimen, ρ_{di} (g/cm^3), is calculated using Equation 5-7:

$$\rho_{d,i} = {}^{m_{d,i}}/_{V_i} \tag{5-7}$$

The initial mass of water, $m_{water,i}$ (g), is calculated using Equation 5-8:

$$m_{water,i} = m_{d,i} * wc_i \tag{5-8}$$

The initial mass of salts, $m_{salt,i}$ (g), is calculated using Equation 5-9:

$$m_{salt,i} = \frac{salinity}{1000\ cm^3/L} * \left[\frac{m_{d,i} * wc_i}{\rho_w}\right] \tag{5-9}$$

where:
salinity = measured pore fluid salinity (g/L)
ρ_w = density of pure water at test temperature (g/cm^3)

The initial mass of soil grains, $m_{grains,i}$ (g), is calculated using Equation 5-10:

$$m_{grains,i} = m_{d,i} - m_{salt,i} \tag{5-10}$$

The initial volume of soil grains, $V_{grains,i}$ (cm^3), is calculated using Equation 5-11:

$$V_{grains,i} = \frac{m_{grains,i}}{G_s * \rho_{w\,@\,20°C}} \tag{5-11}$$

where:
G_s = specific gravity of soil solids
$\rho_{w\,@\,20°C}$ = density of pure water at 20° C (g/cm^3)

The initial equivalent height of soil solids, $H_{grains,i}$ (cm), is calculated using Equation 5-12:

$$H_{grains,i} = {}^{V_{grains,i}}/_{A} \tag{5-12}$$

The initial mass of fluid, $m_{fluid,i}$ (g), is calculated using Equation 5-13:

$$m_{fluid,i} = m_{w,i} - m_{grains,i} \tag{5-13}$$

The initial volume of fluid, V_{fluid} (cm^3), is calculated using Equation 5-14:

$$V_{fluid,i} = {}^{m_{fluid,i}}/_{\rho_{sw}} \tag{5-14}$$

where:
ρ_{sw} = density of water at pore fluid salinity and test temperature (g/cm^3)

The initial void ratio, e_i, is calculated using Equation 5-15:

$$e_i = \frac{V_i - V_{grains,i}}{V_{grains,i}} \tag{5-15}$$

The initial porosity, n_i, is calculated using Equation 5-16:

$$n_i = \frac{V_i - V_{grains,i}}{V_i} \tag{5-16}$$

The initial saturation, S_i, is calculated using Equation 5-17:

$$S_i = \frac{V_{fluid,i}}{V_i - V_{grains,i}} \tag{5-17}$$

Engineering Values during Test

The engineering values of the test specimen are calculated for each line of data, corresponding to each time the data acquisition system records the transducer readings. The frequency of these data is set to every 3 or 4 minutes, depending on the material being tested. The calculations leading to the engineering values are subdivided in this section into the following categories: (a) transducer readings, (b) apparatus compressibility, (c) physical properties, (d) stresses/pressures, (e) permeability & compressibility, and (f) checks. The "Loading Input" tab of the "Vertical CRS Calculation.xlsm" spreadsheet follows the calculations given in this section in order.

Transducer Readings

For accuracy, and to correct for any skewness in the LVDT holders, two LVDT's are used to measure displacements at opposite sides of the cell. The average of the two displacements is reported and used for subsequent calculations. An absolute zero voltage, representing a specimen height of zero, is computed for each LVDT. To find this absolute zero, the cell is first backpressured to 0.4 MPa to eliminate any errors due to cell expansion. With the LVDT's in place, the piston is loaded and unloaded twice onto a steel dummy specimen of known height, with porous stones and filter papers in place. The point of contact is graphically identified and the normalized LVDT reading (V/V) is recorded for each loading/unloading cycle. These readings are averaged, and the theoretical normalized zero LVDT reading is calculated by extrapolating from the known dummy height to a height of zero, using the LVDT's conversion factor (cm/(V/V)). This value is theoretical, because the LVDTs' ranges are too small to physically measure this value without the use of a dummy specimen. A detailed description of this process is given in Section 4.3.1 and shown in Figure 4-10.

The uncorrected height of the specimen, $h_{u,n}$ (cm), is calculated for each LVDT using Equation 5-18:

$$h_{u,n} = CF * \left(\frac{V_{out}}{V_{in}} - \frac{V_{out,zero}}{V_{in,zero}} \right) \quad (5\text{-}18)$$

where:
CF = LVDT calibration factor (cm/(V/V))
V_{out} = output voltage from LVDT
V_{in} = input voltage to LVDT
$V_{out,zero}/V_{in,zero}$ = normalized output voltage from LVDT at zero height

The cell pressure, $\sigma_{c,n}$ (kgf/cm^2), is calculated using Equation 5-19:

$$\sigma_{c,n} = CF * \left(\frac{V_{out}}{V_{in}} - \frac{V_{out,zero}}{V_{in,zero}} \right) \quad (5\text{-}19)$$

where:
CF = pressure transducer calibration factor ((kgf/cm^2)/(V/V))
$V_{out,zero}/V_{in,zero}$ = normalized output voltage from transducer at atmospheric pressure

The pore pressure at the bottom of the specimen, assumed to be the maximum pore pressure during loading, $u_{max,n}$ (kgf/cm^2), is calculated using Equation 5-20:

$$u_{max,n} = CF * \left(\frac{V_{out}}{V_{in}} - \frac{V_{out,zero}}{V_{in,zero}} \right) \quad (5\text{-}20)$$

where:
CF = pressure transducer calibration factor ((kgf/cm^2)/(V/V))
$V_{out,zero}/V_{in,zero}$ = normalized output voltage from transducer at atmospheric pressure

The vertical force, $f_{a,n}$ (kgf), is calculated using Equation 5-21:

$$f_{a,n} = CF * \left(\frac{V_{out}}{V_{in}} - \frac{V_{out,zero}}{V_{in,zero}} \right) \quad (5\text{-}21)$$

where:
CF = force transducer calibration factor (kgf/(V/V))
$V_{out,zero}/V_{in,zero}$ = normalized output voltage from load cell at zero load

Apparatus Compressibility

As the specimen is loaded, the apparatus compresses slightly, giving a higher displacement than the specimen's actual displacement. Thus, the calculated deformation of the specimen is slightly reduced with increasing stress, through the use of increasing the specimen height with an apparatus compressibility correction equation. The apparatus compressibility equation is derived by running two loading cycles on a steel dummy specimen. The displacement for each is recorded as a function of vertical force, and a power law regression is fit for both loading cycles. This allows one to reduce the magnitude of vertical displacement of the specimen, or increase the height of the specimen, as a function of vertical stress. For a more detailed description of the apparatus compressibility measurement, see Section 4.3.1. The reduction in magnitude of vertical displacement, or increase in specimen height, due to apparatus compressibility, Δh_{ac} (cm), is calculated using Equation 5-22:

$$\Delta h_{ac,n} = a * ({f_{a,u,n}}^{b} - {f_{a,initial}}^{b}) \quad (5\text{-}22)$$

where:
a,b = apparatus compressibility factors given in Table 4.2
$f_{a,initial}$ = vertical force of first line of data

The corrected height of the specimen, h_n (cm), is calculated using Equation 5-23:

$$h_n = h_{u,n} + \Delta h_{ac,n} \quad (5\text{-}23)$$

Physical Properties

The deformation of the specimen, δ_n (cm), is calculated using Equation 5-24. h_1 is taken at the first line of LVDT data. This measures the LVDT initial height after cell set up and swelling (see Figure 5-35).

$$\delta_n = h_1 - h_n \tag{5-24}$$

The void ratio during the test, e_n, is calculated using Equation 5-25:

$$e_n = \frac{(h_n - h_{grains,f})}{h_{grains,f}} \tag{5-25}$$

where:
$h_{grains,f}$ *= final equivalent height of soil solids*

The porosity during the test, n_n, is calculated using Equation 5-26:

$$n_n = \frac{(h_n - h_{grains,f})}{h_n} \tag{5-26}$$

where:
$h_{grains,f}$ *= final equivalent height of soil solids*

The vertical strain, $\varepsilon_{a,n}$ (%), is calculated using Equation 5-27:

$$\varepsilon_{a,n} = \frac{(h_1 - h_n)}{h_1} * 100 \tag{5-27}$$

The strain rate, $\dot{\varepsilon}_n$ (hr^{-1}), is calculated using Equation 5-28:

$$\dot{\varepsilon}_n = \left(\frac{\delta_{n+1} - \delta_{n-1}}{h_1}\right) * \left(\frac{1}{t_{n+1} - t_{n-1}}\right) * \left(\frac{3600\ sec}{1\ hr}\right) \tag{5-28}$$

where:
t_n *= time reading was taken (seconds)*

Stresses/pressures

The excess pore pressure at the bottom of the specimen, assumed to be the maximum pore pressure during loading, $u_{e\,max,n}$ (kgf/cm^2), is calculated using Equation 5-29:

$$u_{e\,max,n} = u_{max,n} - \sigma_{c,n} \tag{5-29}$$

The vertical stress, $\sigma_{a,n}$ (kgf/cm^2), is calculated using Equation 5-30:

$$\sigma_{a,n} = \frac{f_{a,n} + w_p}{A} + \sigma_{c,n} * \left(1 - {}^{A_p}/_{A}\right) \tag{5-30}$$

where:
w_p = weight of piston (kgf)
A_p = cross-sectional area of piston (cm^2)
A = cross-sectional area of specimen (cm^2)

The vertical effective stress at the top of the specimen, $\sigma'_{a,b,n}$ (kgf/cm^2), is calculated using Equation 5-31:

$$\sigma'_{a,b,n} = \sigma_{a,n} - \sigma_{c,n} \tag{5-31}$$

The average vertical effective stress, $\sigma'_{a,n}$ (kgf/cm^2), is calculated using Wissa's linear theory (Wissa et al, 1971) using Equation 5-32:

$$\sigma'_{a,n} = \sigma'_{a,b,n} - \frac{2}{3} * \left(u_{e\,max,n}\right) \tag{5-32}$$

Permeability & Compressibility

The hydraulic conductivity in the vertical direction, $K_{v,n}$ (cm/s) is calculated using Equation 5-33 (ASTM D4186, 2012):

$$K_{v,n} = \left(\frac{\dot{\varepsilon}_n * h_n * h_i * \rho_{sw}}{2 * u_{e\,max,n}}\right) * \left(\frac{1\ kg}{1000\ g}\right) \tag{5-33}$$

where:
h_i = initial height of specimen (cm)
ρ_{sw} = density of salt water at test temperature (g/cm^3)

The hydraulic conductivity is converted to permeability, $k_{v,n}$ (m^2), using Equation 5-34:

$$k_{v,n} = \frac{\left\{K_{v,n} * \left(\frac{1\ m}{100\ cm}\right)\right\} * \mu}{\left\{\rho_{sw} * \left(\frac{100\ cm}{1\ m}\right)^3 * \left(\frac{1\ kg}{1000\ g}\right)\right\} * g} \tag{5-34}$$

where:
μ = dynamic viscosity of salt water at test temperature (kg/m-s)
ρ_{sw} = density of salt water at test temperature (g/cm^3)
g = acceleration due to gravity (9.81 m/s^2)

The volume compressibility, $m_{v,n}$ (cm^2/kg), is calculated using Equation 5-35 (ASTM D4186, 2012):

$$m_{v,n} = \left(\frac{\varepsilon_{n+1} - \varepsilon_{n-1}}{\sigma'_{a,n+1} - \sigma'_{a,n-1}}\right) * \left(\frac{1.0}{100\%}\right) \tag{5-35}$$

The coefficient of consolidation, $c_{v,n}$ (m^2/s), is calculated using Equation 5-36 (ASTM D4186, 2012):

$$c_{v,n} = \frac{K_{v,n}}{m_{v,n} * \rho_{sw}} \tag{5-36}$$

where:
ρ_{sw} = density of salt water at test temperature (g/cm^3)

Checks

A steady state factor is used in CRS testing to determine whether, during a loading stage of the test, the specimen is in a steady state. If the factor is above 0.4, the hydraulic conductivity can be calculated (ASTM D4186, 2012). The steady state factor, F_n, is calculated using Equation 5-37:

$$F_n = \frac{(\sigma_{a,n} - \sigma_{a,1}) - (u_{e\,max,n} - u_{e\,max,1})}{(\sigma_{a,n} - \sigma_{a,1})} \tag{5-37}$$

A pore pressure ratio is used to determine if the pore pressure gradient is large enough to produce excess pore pressures above the pressure transducer resolutions and prevent the effects of secondary consolidation, and should therefore be greater than 0.5% (Fahy, 2014). The pore pressure ratio should also be less than 15%, to control the effects of strain rate sensitivity (ASTM D4186, 2012). The pore pressure ratio, $R_{u,n}$, is calculated using Equation 5-38:

$$R_{u,n} = \frac{u_{e\,max,n}}{\sigma_{a,n}} \tag{5-38}$$

Final Phase Relations

The final phase relations are computed for the specimen after it has been extruded from the confinement ring at the end of the test. There is considerable error between the porosity of the specimen inside the consolidometer at the end of loading and the extruded specimen, mainly due to the swelling that occurs in the specimen as it has access to free water during the unloading and disassembly of the apparatus. Figure 5-35 illustrates this phenomenon. Therefore, the final volume calculated on the extruded specimen is used simply as a comparison with the test data.

The final dry mass, $m_{d,f}$ (g), is the mass of the oven-dried extruded specimen plus the extraneous soil left on the equipment after extrusion. This final dry mass is used as the dry mass throughout the test. It is compared against the specimen volume calculated using the properly-zeroed LVDTs to accurately determine specimen porosity. This method of porosity calculation has proven to provide repeatable results.

The final water content, wc_f (decimal), is calculated by obtaining the mass of the extruded specimen before and after oven-drying.

The final wet mass, $m_{w,f}$ (g), is calculated using Equation 5-39:

$$m_{w,f} = m_{d,f} * (1 + wc_f) \tag{5-39}$$

The rest of the final phase relations, which are only used as comparisons to the phase relations calculated during the test using the LVDT heights and final dry mass, are calculated the exact same way as is shown in the "Initial Phase Relations" section.

Noise Reduction

CRS tests are prone to both testing and electronic noise, as they can be long tests with frequent data collection. Noise can be seen in the raw permeability data for CRS 1429, as seen in Figure 5-36. In order to reduce this noise and make the test data more readable, the test data are run through numerical and manual smoothing processes.

The numerical smoothing process is first performed to smooth out the minor noise in the permeability data. After the test is completed, the cell pressure and pore pressure transducer output voltages are smoothed using a 5-point moving average. The smoothing is performed using a visual basic (VBA) code in Microsoft® Excel, which can be found in Appendix C.

The numerical smoothing process is not powerful enough to smooth over occasional large voltage jumps, which are likely due to electrical interference or grounding issues with the transducer circuits. These voltage jumps are manually removed. The final smoothed permeability data for CRS 1429 is shown as Figure 5-37. Comparing this with Figure 5-36 shows how the noise is reduced in the permeability curve from the smoothing processes without affecting the fundamental trend.

The data are also trimmed at high porosities so that permeability data are only being reported after the specimen reaches the normally consolidated state.

5.3.3 Radially-Draining Constant Rate of Strain (CRS) Analysis

The radially-draining constant rate of strain (CRS) consolidation test is analyzed in order to determine the radial horizontal permeability behavior of a mudrock. This section reflects the vertically-draining CRS analysis section, as it subdivides the analysis into the following sections: (a) initial phase relations, (b) engineering values during the test, (c) final phase relations, and (d) noise reduction. The methods follow the general procedure outlined in ASTM D4186, but are modified for radial flow and greater precision and reproducibility. Yune and Chung's (2005) equations are used to calculate the radial permeability and to estimate the effective stress.

Initial Phase Relations

The initial porosity of the specimen is calculated using volume, mass, and water content measurements. This porosity is not very accurate, as the volume measurement is made using calipers and the water content of the trimmings is used rather than the water content of the actual specimen. These initial values are therefore used only for porosity calculations during the duration of the test and as a check against the porosity reported in the final data.

The initial wet mass of the specimen, $m_{w,i}$ (g), is calculated by obtaining the mass of the trimmed specimen inside the confinement ring, with the top cap, cutting shoe, and acrylic spacer attached. The individual masses of the confinement ring (saturated surface dry), top cap, cutting shoe, and acrylic spacer are then subtracted from the total mass to estimate the wet mass of the specimen.

The initial moisture content, wc_i (decimal), is calculated by averaging the moisture contents from various tares of specimen trimmings.

The initial dry mass of the specimen, $m_{d,i}$ (g), is calculated from the trimmed specimen before the test using Equation 5-40:

$$m_{d,i} = \frac{m_{w,i}}{1 + wc_i} \tag{5-40}$$

The initial volume of the specimen, V_i (cm^3), is calculated using Equation 5-41:

$$V_i = h_i * A \tag{5-41}$$

where:
h_i = initial caliper-measured height of specimen in ring(cm)
A = cross-sectional area of specimen/confinement ring (cm^2)

The initial dry density of the specimen, ρ_{di} (g/cm^3), is calculated using Equation 5-42:

$$\rho_{d,i} = {}^{m_{d,i}}/_{V_i} \tag{5-42}$$

The initial mass of water, $m_{water,i}$ (g), is calculated using Equation 5-43:

$$m_{water,i} = m_{d,i} * wc_i \tag{5-43}$$

The initial mass of salts, $m_{salt,i}$ (g), is calculated using Equation 5-44:

$$m_{salt,i} = \frac{salinity}{1000\ cm^3/L} * \left[\frac{m_{d,i} * wc_i}{\rho_w}\right] \tag{5-44}$$

where:
salinity = measured pore fluid salinity (g/L)
ρ_w = density of pure water at test temperature (g/cm^3)

The initial mass of soil grains, $m_{grains,i}$ (g), is calculated using Equation 5-45:

$$m_{grains,i} = m_{d,i} - m_{salt,i} \tag{5-45}$$

The initial volume of soil grains, $V_{grains,i}$ (cm^3), is calculated using Equation 5-46:

$$V_{grains,i} = \frac{m_{grains,i}}{G_s * \rho_{w\,@\,20°C}} \tag{5-46}$$

where:
G_s = specific gravity of soil solids
$\rho_{w\,@\,20°C}$ = density of pure water at 20° C (g/cm^3)

The initial equivalent height of soil solids, $H_{grains,i}$ (cm), is calculated using Equation 5-47:

$$H_{grains,i} = {}^{V_{grains,i}}/_{A} \tag{5-47}$$

The initial mass of fluid, $m_{fluid,i}$ (g), is calculated using Equation 5-48:

$$m_{fluid,i} = m_{w,i} - m_{grains,i} \tag{5-48}$$

The initial volume of fluid, V_{fluid} (cm^3), is calculated using Equation 5-49:

$$V_{fluid,i} = {}^{m_{fluid,i}}/_{\rho_{sw}} \tag{5-49}$$

where:
ρ_{sw} = density of water at pore fluid salinity and test temperature (g/cm^3)

The initial void ratio, e_i, is calculated using Equation 5-50:

$$e_i = \frac{V_i - V_{grains,i}}{V_{grains,i}} \tag{5-50}$$

The initial porosity, n_i, is calculated using Equation 5-51:

$$n_i = \frac{V_i - V_{grains,i}}{V_i} \tag{5-51}$$

The initial saturation, S_i, is calculated using Equation 5-52:

$$S_i = \frac{V_{fluid,i}}{V_i - V_{grains,i}} \tag{5-52}$$

Engineering Values during Test

The engineering values of the test specimen are calculated for each line of data, corresponding to each time the data acquisition system records the transducer readings. The frequency of these data is set to every 3 or 4 minutes, depending on the material being tested. The calculations leading to the engineering values are subdivided in this section into the following categories: (a) transducer readings, (b) apparatus compressibility, (c) physical properties, (d) stresses/pressures, (e) permeability & compressibility, and (f) checks. The "Loading Input" tab of the "Radial CRS Calculation.xlsm" spreadsheet follows the calculations given in this section in order.

Transducer Readings

For accuracy, and to correct for any skewness in the LVDT holders, two LVDTs are used to measure displacements at opposite sides of the cell. The average of the two displacements is reported and used for subsequent calculations. An absolute zero voltage, representing a specimen height of zero, is computed for each LVDT. To find this absolute zero, the cell is first backpressured to 0.4 MPa to eliminate any errors due to cell expansion. With the LVDTs in place, the piston is loaded and unloaded twice onto a steel dummy specimen of known height. The point of contact is graphically identified and the corresponding normalized LVDT reading (V/V) is recorded for each loading/unloading cycle. These readings are averaged, and the theoretical normalized zero LVDT reading is calculated by extrapolating from the known dummy height to a height of zero, using the LVDTs' conversion factors (in cm/(V/V)). This value is theoretical, because the LVDTs' ranges are too small to physically measure this value without the use of a dummy specimen. A detailed description of this process is given in Section 4.2.5 and shown in Figure 4-10.

The uncorrected height of the specimen, $h_{u,n}$ (cm), is calculated for each LVDT using Equation 5-53:

$$h_{u,n} = CF * \left(\frac{V_{out}}{V_{in}} - \frac{V_{out,zero}}{V_{in,zero}} \right) \quad (5\text{-}53)$$

where:
CF = LVDT calibration factor (cm/(V/V))
V_{out} = output voltage from LVDT
V_{in} = input voltage to LVDT
$V_{out,zero}/V_{in,zero}$ = normalized output voltage from LVDT at zero height

The cell pressure, $\sigma_{c,n}$ (kgf/cm^2), is calculated using Equation 5-54:

$$\sigma_{c,n} = CF * \left(\frac{V_{out}}{V_{in}} - \frac{V_{out,zero}}{V_{in,zero}} \right) \quad (5\text{-}54)$$

where:
CF = pressure transducer calibration factor ((kgf/cm^2)/(V/V))
$V_{out,zero}/V_{in,zero}$ = normalized output voltage from transducer at atmospheric pressure

The pore pressure at the center of the specimen, assumed to be the maximum pore pressure during loading, $u_{max,n}$ (kgf/cm^2), is calculated using Equation 5-55:

$$u_{max,n} = CF * \left(\frac{V_{out}}{V_{in}} - \frac{V_{out,zero}}{V_{in,zero}} \right) \quad (5\text{-}55)$$

where:
CF = pressure transducer calibration factor ((kgf/cm^2)/(V/V))
$V_{out,zero}/V_{in,zero}$ = normalized output voltage from transducer at atmospheric pressure

The pore pressure at the check point in-between the center and the perimeter of the specimen, $u_{check,n}$ (kgf/cm^2), is calculated as follows:

$$u_{check,n} = CF * \left(\frac{V_{out}}{V_{in}} - \frac{V_{out,zero}}{V_{in,zero}} \right) \quad (5\text{-}56)$$

where:
CF = pressure transducer calibration factor ((kgf/cm^2)/(V/V))
$V_{out,zero}/V_{in,zero}$ = normalized output voltage from transducer at atmospheric pressure

The uncorrected vertical force, $f_{a,u,n}$ (kgf), is calculated as follows:

$$f_{a,u,n} = CF * \left(\frac{V_{out}}{V_{in}} - \frac{V_{out,zero}}{V_{in,zero}}\right) \quad (5\text{-}57)$$

where:
CF = force transducer calibration factor (kgf/(V/V))
$V_{out,zero}/V_{inczero}$ = normalized output voltage from load cell at zero load

Apparatus Compressibility

As the specimen is loaded, the apparatus compresses slightly, giving a higher displacement than the specimen's actual displacement. Thus, the calculated deformation of the specimen is slightly reduced with increasing stress, through the use of increasing the specimen height with an apparatus compressibility correction equation. The apparatus compressibility equation is derived by running two loading cycles on a steel dummy specimen. The displacement for each is recorded as a function of vertical force, and a power law regression is fit for both loading cycles. This calculates a reduction in the magnitude of vertical displacement of the specimen, or an increase in the height of the specimen, as a function of vertical stress. The reduction in magnitude of vertical displacement, or increase in specimen height, due to apparatus compressibility, Δh_{ac} (cm), is calculated using Equation 5-58:

$$\Delta h_{ac,n} = a * ({f_{a,u,n}}^b - {f_{a,initial}}^b) \quad (5\text{-}58)$$

where:
a,b = apparatus compressibility factors given in Table 4.2

The corrected height of the specimen, h_n (cm), is calculated using Equaton 5-59:

$$h_n = h_{u,n} + \Delta h_{ac,n} \quad (5\text{-}59)$$

Physical Properties

The deformation of the specimen, δ_n (cm), is calculated using Equation 5-60. h_1 is taken at the first line of the LVDT data. This measures the LVDT initial height after set up and swelling (see Figure 5-38).

$$\delta_n = h_1 - h_n \tag{5-60}$$

The void ratio during the test, e_n, is calculated using Equation 5-61:

$$e_n = \frac{(h_n - h_{grains,f})}{h_{grains,f}} \tag{5-61}$$

The porosity during the test, n_n, is calculated using Equation 5-62:

$$n_n = \frac{(h_n - h_{grains,f})}{h_n} \tag{5-62}$$

The vertical strain, $\varepsilon_{a,n}$ (%), is calculated using Equation 5-63:

$$\varepsilon_{a,n} = \frac{(h_1 - h_n)}{h_1} * 100 \tag{5-63}$$

The strain rate, $\dot{\varepsilon}_n$ (hr^{-1}), is calculated using Equation 5-64:

$$\dot{\varepsilon}_n = \left(\frac{\delta_{n+1} - \delta_{n-1}}{h_1}\right) * \left(\frac{1}{t_{n+1} - t_{n-1}}\right) * \left(\frac{3600\ sec}{1\ hr}\right) \tag{5-64}$$

where:
t_n = time reading was taken (seconds)

Stresses/Pressures

The excess pore pressure at the center of the specimen, assumed to be the maximum excess pore pressure during loading, $u_{e\,max,n}$ (kgf/cm^2), is calculated using Equation 5-65:

$$u_{e\,max,n} = u_{max,n} - \sigma_{c,n} \tag{5-65}$$

The excess pore pressure at a point in between the center and the perimeter of the specimen, $u_{e\,check,n}$ (kgf/cm^2), is calculated using Equation 5-66:

$$u_{e\,check,n} = u_{check,n} - \sigma_{c,n} \tag{5-66}$$

The uncorrected vertical stress, $\sigma_{a,u,n}$ (kgf/cm^2), is computed taking the cell pressure and weight of the piston beneath the load cell into account. It is calculated using Equation 5-67:

$$\sigma_{a,u,n} = \frac{f_{a,u,n} + w_p}{A} + \sigma_{c,n} * \left(1 - {}^{A_p}/_{A}\right) \tag{5-67}$$

where:
A_p = cross-sectional area of piston (cm^2)
w_p = weight of piston (kgf)
A = cross-sectional area of specimen (cm^2)

The uncorrected vertical effective stress without considering excess pore pressures, $\sigma'_{a,b,u,n}$ (kgf/cm^2), is calculated using Equation 5-68:

$$\sigma'_{a,b,u,n} = \sigma_{a,u,n} - \sigma_{c,n} \tag{5-68}$$

The uncorrected average vertical effective stress, $\sigma'_{a,u,n}$ (kgf/cm^2), is calculated using Yune and Chung's (2005) excess pore pressure solution as shown in Equation 5-69:

$$\sigma'_{a,u,n} = \sigma'_{a,b,u,n} - \frac{1}{2} * \left(u_{e\,max,n}\right) \tag{5-69}$$

Sidewall Friction Correction

While conventional vertically-draining CRS calculations assume a frictionless sidewall, the sidewall in the radially-draining CRS device is far from frictionless, as it is made of a siliceous porous stone. In order to more accurately report the effective stress within the sample, the sidewall friction is estimated. It is assumed that the interface strength between the porous stone and the clay is greater than the undrained strength of the clay itself, causing a cylindrical shear plane within the mudrock specimen just inside of the porous stone. The sidewall friction is subsequently assumed to be equal to the undrained shear strength of the material.

The undrained strength ratio (s_u/σ'_{vc}), is calculated as a function of consolidation stress. For RBBC, a logarithmic function is fit to test data from direct simple shear (DSS) tests as shown in Figure 5-41 (Ahmed, 1990). While the database compiled by Ahmed (1990) only includes specimens consolidated up to 1.2 MPa, the testing regime of this study tests specimens up to 40 MPa consolidation stress. Thus, the undrained strengths used in the sidewall friction correction of this study are highly extrapolated. However, the effect that sidewall friction has on the effective stress/permeability relation is small, therefore the extrapolation is justified. The undrained strength ratio for RBBC, (s_u/σ'_{vc}), is calculated using Equation 5-70:

$$RBBC: \quad \frac{s_u}{\sigma'_{vc_n}} = -0.003 * \ln(\sigma'_{a,u,n}) + 0.2016 \tag{5-70}$$

where:
$\sigma'_{a,u,n}$ *= vertical consolidation effective stress (kgf/cm²)*

For RGoM-EI, no DSS data set is available, so triaxial test data from Casey (2014) are used to determine the undrained strength ratio as a function of normal effective stress. The undrained strength ratio for RGoM-EI, (su/σ'vc), is calculated using Equation 5-71:

$$RGoM - EI: \quad \frac{S_u}{\sigma'_{vc_n}} = 0.60 * (1{,}000 * \sigma'_{a,u,n})^{-0.148} \tag{5-71}$$

where:
$\sigma'_{a,u,n}$ *= vertical consolidation effective stress (MPa)*

In order to estimate the effective stress normal to the failure plane (that which determines undrained strength), the lateral stresses at rest, or K_0 stresses, are estimated. A series of K_0-consolidated triaxial tests performed on various clays by Casey (2014) allows one to estimate K_0 values for homogenous normally-consolidated clays as a function of liquid limit and consolidation stress. With a liquid limit of 46.5% for RBBC (Casey, 2014), the K_0 value for normally-consolidated RBBC, K_{0NC}, is calculated using Equation 5-72:

$$RBBC: \quad K_{0NC,n} = 0.59 * (0.1 * \sigma'_{a,u,n})^{0.0305} \tag{5-72}$$

where:
$\sigma'_{a,u,n}$ = vertical consolidation (effective) stress (MPa)

With a liquid limit of 85.8% for RGoM-EI (Casey, 2014), the K_0 value for normally-consolidated RGoM-EI, K_{0NC}, is calculated using Equation 5-73:

$$RGoM - EI: \quad K_{0NC,n} = 0.81 * (0.1 * \sigma'_{a,u,n})^{0.0989} \tag{5-73}$$

where:
$\sigma'_{a,u,n}$ = vertical consolidation (effective) stress (MPa)

The undrained strength, $S_{u,n}$ (kgf/cm^2), is therefore calculated using Equation 5-74:

$$S_{u,n} = \left(K_{0NC} * \sigma'_{a,u,n}\right) * \frac{S_u}{\sigma'_{vc_n}} \tag{5-74}$$

where:
$\sigma'_{a,u,n}$ = uncorrected vertical effective stress (kgf/cm^2)

The friction force, $f_{f,n}$ (kgf), is calculated using Equation 5-75:

$$f_{f,n} = S_{u,n} * (diameter * \pi * h_n) \tag{5-75}$$

where:
diameter = diameter of specimen (cm)

The vertical force, $f_{a,n}$ (kgf), is calculated using Equation 5-76:

$$f_{a,n} = f_{a,u,n} - {}^{f_{f,n}}/_{2} \tag{5-76}$$

The vertical stress, $\sigma_{a,n}$ (kgf/cm^2), is calculated using Equation 5-77:

$$\sigma_{a,n} = \frac{f_{a,n} + w_p}{A} + \sigma_{c,n} * \left(1 - {}^{A_p}/_{A}\right) \tag{5-77}$$

where:
A = cross-sectional area of specimen (cm^2)

The vertical effective stress without considering excess pore pressures, $\sigma'_{a,b,n}$ (kgf/cm^2), is calculated using Equation 5-78:

$$\sigma'_{a,b,n} = \sigma_{a,n} - \sigma_{c,n} \tag{5-78}$$

The average vertical effective stress, $\sigma'_{a,n}$ (kgf/cm^2), is calculated using Yune and Chung's (2005) excess pore pressure solution shown in Equation 5-79:

$$\sigma'_{a,n} = \sigma'_{a,b,n} - \frac{1}{2} * \left(u_{e\,max,n}\right) \tag{5-79}$$

Permeability & Compressibility

The hydraulic conductivity in a radially-outward direction, $K_{r,n}$ (cm/s), is calculated using Equation 5-80 (Yune & Chung, 2005):

$$K_{r,n} = \frac{\rho_{sw} * r^2 * \left(\frac{\dot{\varepsilon}_n * h_1 * A}{V_{grains,f}}\right)}{4 * u_{e\,max,n} * \left\{1 + e_1 - \left(\frac{\dot{\varepsilon}_n * h_1 * A}{V_{grains,f}}\right) * t\right\}} \quad (5\text{-}80)$$

where:
ρ_{sw} = density of salt water at test temperature (g/cm^3)
r = radius of specimen (drainage distance) (cm)
A = cross-sectional area of specimen (cm^2)
$V_{grains,f}$ = volume of soil solids determined after the test (cm^3)
t = time since beginning of loading portion of test (sec)

The hydraulic conductivity is converted to permeability, $k_{r,n}$ (m^2), using Equation 5-81:

$$k_{r,n} = \frac{\left\{K_{r,n} * \left(\frac{1\,m}{100\,cm}\right)\right\} * \mu}{\left\{\rho_{sw} * \left(\frac{100\,cm}{1\,m}\right)^3 * \left(\frac{1\,kg}{1000\,g}\right)\right\} * g} \quad (5\text{-}81)$$

where:
μ = dynamic viscosity of salt water at test temperature (kg/m-s)
ρ_{sw} = density of salt water at test temperature (g/cm^3)
g = acceleration due to gravity (9.81 m/s^2)

The volume compressibility, $m_{v,n}$ (cm^2/kg), is calculated using Equation 5-82 (ASTM D4186, 2012), assuming the effective stress is constant throughout the radial profile of the specimen (see Figure 4-1):

$$m_{v,n} = \left(\frac{\varepsilon_{n+1} - \varepsilon_{n-1}}{\sigma'_{a,n+1} - \sigma'_{a,n-1}}\right) * \left(\frac{1.0}{100\%}\right) \quad (5\text{-}82)$$

The coefficient of vertical consolidation with radial drainage, $c_{vr,n}$ (m^2/s), is calculated using Equation 5-83 (ASTM D4186, 2012):

$$c_{vr,n} = \frac{K_{r,n}}{m_{v,n} * \rho_{sw}} \tag{5-83}$$

where:
ρ_{sw} = *density of salt water at test temperature* (g/cm^3)

Checks

A steady state factor is used in CRS testing to determine whether, during a loading stage of the test, the specimen is in a steady state. If the factor is above 0.4, the hydraulic conductivity can be calculated (ASTM D4186, 2012). The steady state factor, F_n, is calculated using Equation 5-84:

$$F_n = \frac{(\sigma_{a,n} - \sigma_{a,1}) - (u_{e\ max,n} - u_{e\ max,1})}{(\sigma_{a,n} - \sigma_{a,1})} \tag{5-84}$$

A pore pressure ratio is used to determine if the pore pressure gradient is large enough to produce excess pore pressures above the pressure transducer resolutions and prevent the effects of secondary consolidation, and should therefore be greater than 0.5% (Fahy, 2014). The pore pressure ratio should also be less than 15%, to control the effects of strain rate sensitivity (ASTM D4186, 2012). The pore pressure ratio, $R_{u,n}$, is calculated using Equation 5-85:

$$R_{u,n} = \frac{u_{e\ max,n}}{\sigma_{a,n}} \tag{5-85}$$

Final Phase Relations

The final phase relations are computed after the specimen has been extruded from the confinement ring after the test. There is considerable error between the properties of the specimen inside the consolidometer at the end of loading and the extruded specimen, mainly due to the swelling that occurs in the specimen as it has access to free water during the unloading and disassembly of the apparatus.

Figure 5-38 illustrates this phenomenon. Therefore, the values for the final specimen are used simply as a check, or reference, on the test data.

The final dry mass, $m_{d,f}$ (g), is calculated by adding the oven-dried mass of the extruded specimen plus the extraneous soil held onto the ring, top cap, and base after extrusion. This final dry mass is the mass used for the reported porosity calculations throughout the test, as it is a direct measurement of the soil solids being compressed.

The final water content, wc_f (decimal), is calculated obtaining the mass of the extruded specimen before and after oven-drying.

The final wet mass, $m_{w,f}$ (g), is calculated using Equation 5-86:

$$m_{w,f} = m_{d,f} * (1 + wc_f) \tag{5-86}$$

The rest of the final phase relations, which are only used as comparisons to the phase relations calculated during the test using the LVDT-measured heights and final dry mass, are calculated the exact same way as is shown in the "Initial Phase Relations" section.

Noise Reduction

Using the exact same procedure that is described in the "Noise Reduction" sub-section of the "Vertically-Draining CRS" section, electronic and testing noise are reduced. Figure 5-39 shows the raw, non-smoothed permeability data for radially-draining CRS 1426, and Figure 5-40 shows the smoothed permeability data.

The data are again trimmed at high porosities so that permeability data are only being reported after the specimen reaches normal consolidation.

5.3.4 CRS Data Combination Procedures

Several CRS tests were performed using each set of variables – RBBC with vertical drainage, RBBC with radial drainage, RGoM-EI with vertical drainage, and RGoM-EI with radial drainage. This was done in order to differentiate testing noise from repeatable material trends. The data from each test were consequently reduced and combined, in order to quantitatively determine trends. This section describes the combination procedure used.

The analysis of a CRS test produces a compression curve, showing the porosity (n), void ratio (e), or strain (ε) – effective stress (σ'_v) relationship. Volume compressibility (m_v), permeability (k), and coefficient of consolidation (c_v) curves can also be produced as functions of porosity, void ratio, or vertical effective stress.

The volume compressibility, permeability, and coeffiecient of consolidation are binned in terms of porosity, with n=0.005 resolution. In other words, all the measured values for the parameter of interest corresponding to a porosity within a 0.005 porosity window are collected, and the averaged parameter value is assigned as the reduced value corresponding to the central porosity of that window. To reduce the compression curve, the void ratio is binned in terms of vertical effective stress, with 0.05 MPa resolution from 0.1 to 1 MPa, 0.1 MPa precision from 1 to 10 MPa, and 0.5 MPa precision from 10 to 40 MPa. An example of how the data binning process works can be seen by comparing zoomed-in RGoM-EI permeability data straight from the transducers in Figure 5-42 to the same data binned, as explained, in Figure 5-43. The spreadsheet "cataloging spreadsheet.xlsm" can be used to perform this binning operation, and the VBA code it uses is shown in Appendix C.

With the binning process complete, the parameters measured from the separate tests are ready to be quantatively compared. For the compression parameters (void ratio binned by effective stress and volume compressibility binned by porosity), the average and standard deviation parameters are calculated at each binned value from both the vertically-draining and radially-draining tests. Both types of tests are averaged together because they both exhibit 1-D consolidation, and compression behavior (not including time effects) is independent of flow direction. For the permeability and coefficient of consolidation parameters, the average and standard deviation values within each porosity bin are calculated for the tests with radial drainage separately from the tests with vertical drainage. Figure 5-44 plots the average permeability values, along with the standard deviations away from the average, calculated from the binned test data shown in Figure 5-43.

Permeabiliy anisotropy, r_k, can then be quantified for each binned porosity value using Equation 5-87:

$$r_k = \frac{k_r}{k_v} \tag{5-87}$$

where:
k_r = radial (horizontal) permeability
k_v = vertical permeability

Coefficient of consolidation anisotropy, r_{cv}, which should theoretically be identical to permeability anisotropy, can be quantified the exact same way, using Equation 5-88:

$$r_{cv} = \frac{c_{vr}}{c_v} \tag{5-88}$$

where:
c_{vr} = *coefficient of vertical consolidation with radial drainage*
c_v = *coefficient of vertical consolidation with vertical drainage*

The standard deviation, σ, for either of these parameters is calculated using Equation 5-89:

$$\sigma = r_x * \sqrt{\left(\frac{\sigma_r}{x_r}\right)^2 + \left(\frac{\sigma_v}{x_v}\right)^2} \tag{5-89}$$

where:
r_x = *anisotropy of the parameter*
σ_r = *radial standard deviation of the parameter*
x_r = *radial parameter average*
σ_v = *vertical standard deviation of the parameter*
x_v = *vertical parameter average*

Figure 5-45 shows the average permeability anisotropy values and standard deviation values away from the average calculated from the average and standard deviation permeability values shown in Figure 5-44.

This procedure fosters a quantitative representation of parameter trends and spread. All regression analyses are performed on raw data, except for the regressions for RGoM-EI coefficient of consolidaton, as the raw data include too much noise for accurate regression. These regressions are performed on the binned average data.

5.3.5 Cubic Specimen Constant Head Permeability and Resistivity Analysis

The calculation of permeability and resistivity from the cubic specimen constant head tests is based on Darcy's law and Ohm's law, respectively.

The hydraulic conductivity is calculated for each gradient applied to each flow direction of each specimen using Darcy's law, shown as Equation 5-90:

$$q = K\frac{\Delta h}{L}\mathrm{A} \tag{5-90}$$

where:
q=volumetric flow rate
K=hydraulic conductivity
Δh = change in total head
L = flow length
A = flow area

The head differential is induced on the specimen by lowering top pressure and raising the bottom pressure by the same amount. The length and area of the specimen is measured using calipers, and the volumetric flow rate is calculated as the average volume water extruded from the base PVA and the volume of water taken in by the top PVA over a chosen time period. The volumetric flow is corrected for leaks, by measuring the volumetric flow with time in each PVA when a zero gradient in the specimen is applied. The flow rate is only calculated after a steady state of flow is achieved. Steady state occurs only after specimen swelling and contracting, a consequence of an induced effective stress gradient throughout the specimen, is complete. Permeability is then calculated from the hydraulic conductivity and the water density and viscosity using Equation 5-91:

$$k = \frac{K\mu}{\rho g} \tag{5-91}$$

where:
k = permeability
K = hydraulic conductivity
μ = dynamic viscosity of fluid
ρ = density of fluid
g = acceleration due to gravity

The cubic specimens experience significant disturbance during the take down and setup procedures between each measurement direction, creating a sequencing bias. In order to account for this, the bias created in each specimen is estimated individually. The permeabilities calculated from each gradient are averaged within each flow direction setup, and these averaged values are plotted against setup number (see Figure 5-46). Since the resedimented mudrocks are cross anisotropic, the horizontal directions should theoretically produce the same permeabilities, which should differ from the vertical permeability. There is a characteristic drop in permeability, however, with each sequential measurement: vertical, horizontal 1, and horizontal 2. Assuming the drop in permeability with each measurement is linear, the theoretical horizontal permeability that would be measured were the horizontal permeability to be measured first is calculated, as shown in Figure 5-46. This permeability is the one reported.

The permeability anisotropy is reported as the ratio of horizontal to vertical permeability.

The electrical resistivity is calculated for each electrical gradient for each setup direction using Ohm's law, as shown in Equation 5-92:

$$i = \left(\frac{1}{\rho}\right)\frac{V}{L}\mathrm{A} \tag{5-92}$$

where:
i = current
ρ = resistivity
V = voltage drop
L = measured electrical field length
A = measured electrical field area

The electrical current is measured using a reference circuit with a known resistance. The voltage drop between two pin probes is measured using a voltmeter. The length of the measured electrical field is calculated by subtracting the length of the two pin probes from the length of the specimen, and the area of the electrical field is simply the measured area of the cube. Each of the electrical gradients measured for each directional setup is averaged. A measurement sequencing bias correction is performed, just as it is for permeability, to report final vertical and horizontal resistivity values.

Electrical conductivity is calculated as the inverse of resistivity, and conductivity anisotropy is calculated as the ratio of horizontal to vertical conductivity.

Figure 5-1: The vertically-draining CRS apparatus is disassembled and prepared prior to specimen trimming.

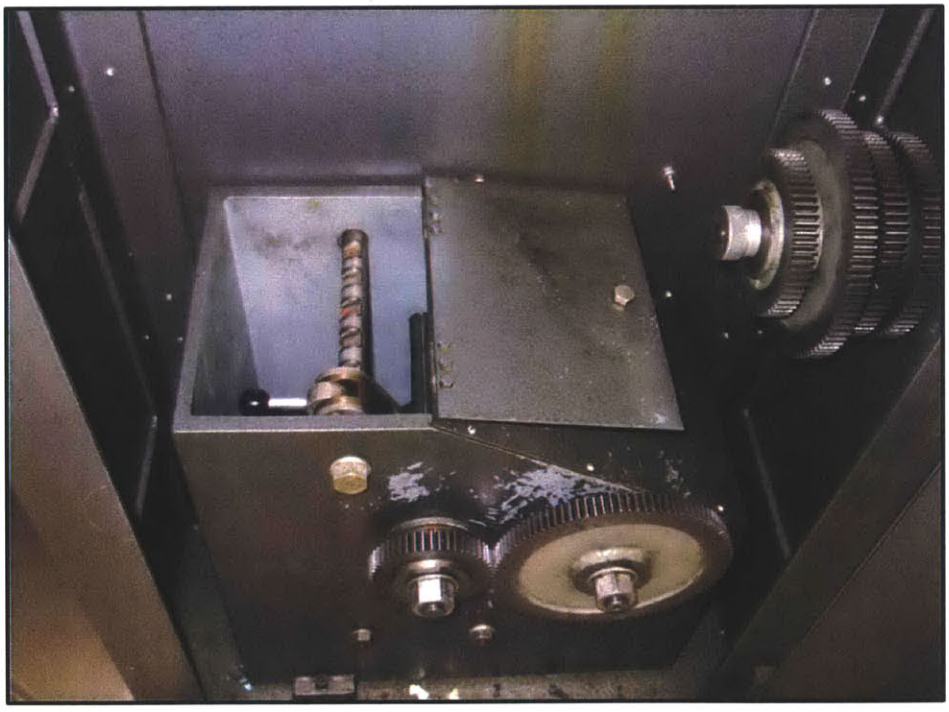

Figure 5-2: The strain rate on the Wykeham Farrance load frames is set by adjusting the cog combination.

Figure 5-3: The trimming and vertically-draining CRS set-up equipment is laid out and prepared prior to sample extrusion.

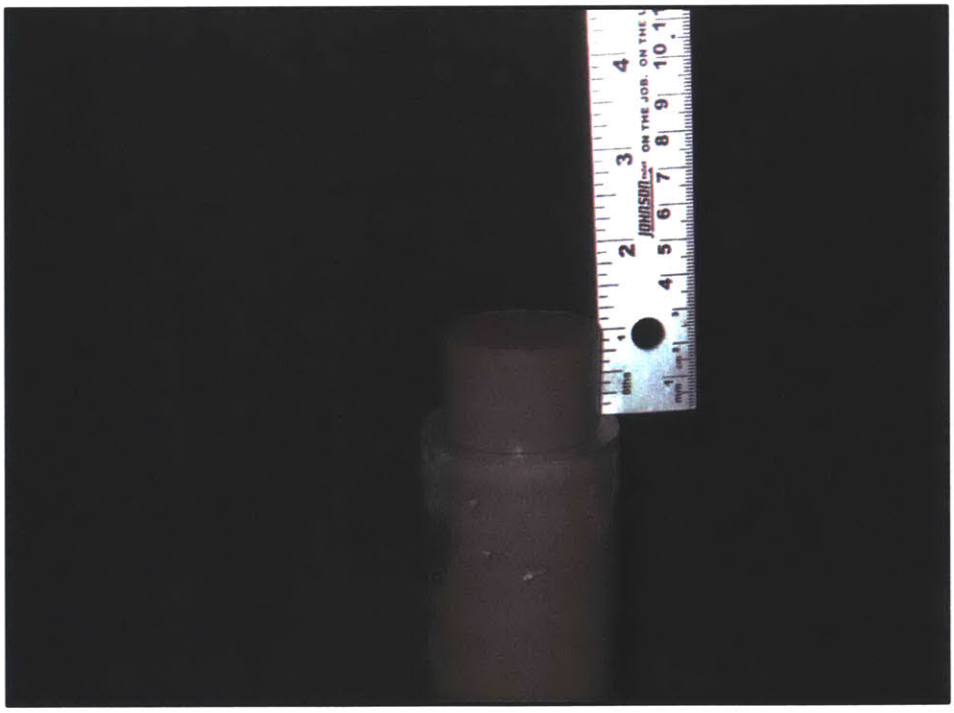

Figure 5-4: Approximately 1" of resedimented mudrock is extruded from the 1.7" resedimentation tube for trimming into either CRS device.

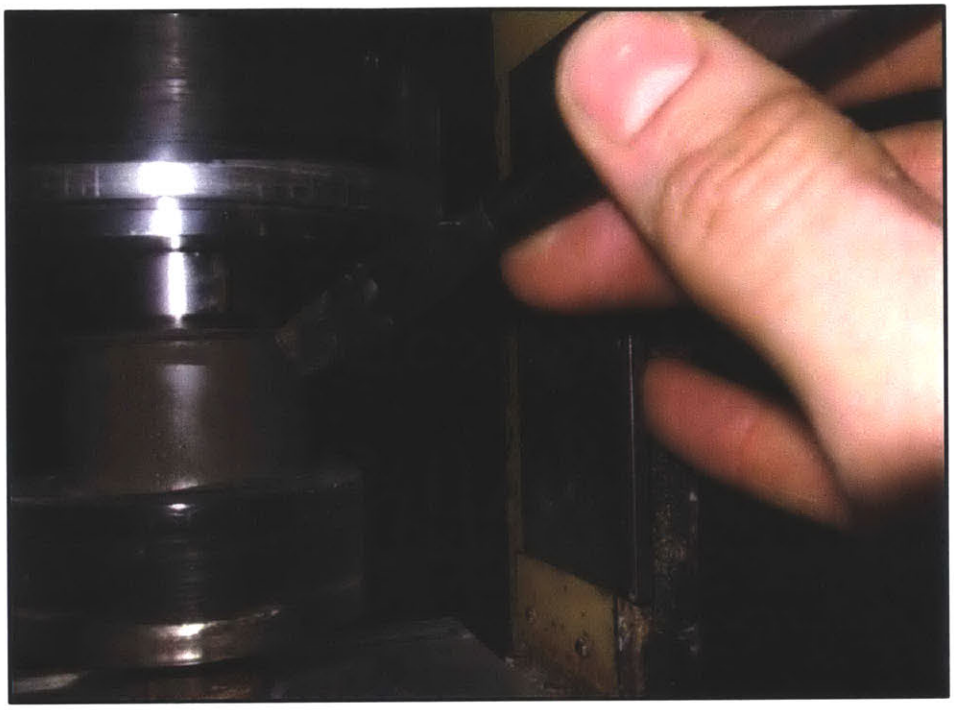

Figure 5-5: The mudrock is trimmed by alternately beveling the top of the specimen and advancing the cutting shoe/confinement ring downwards on a trimming turntable.

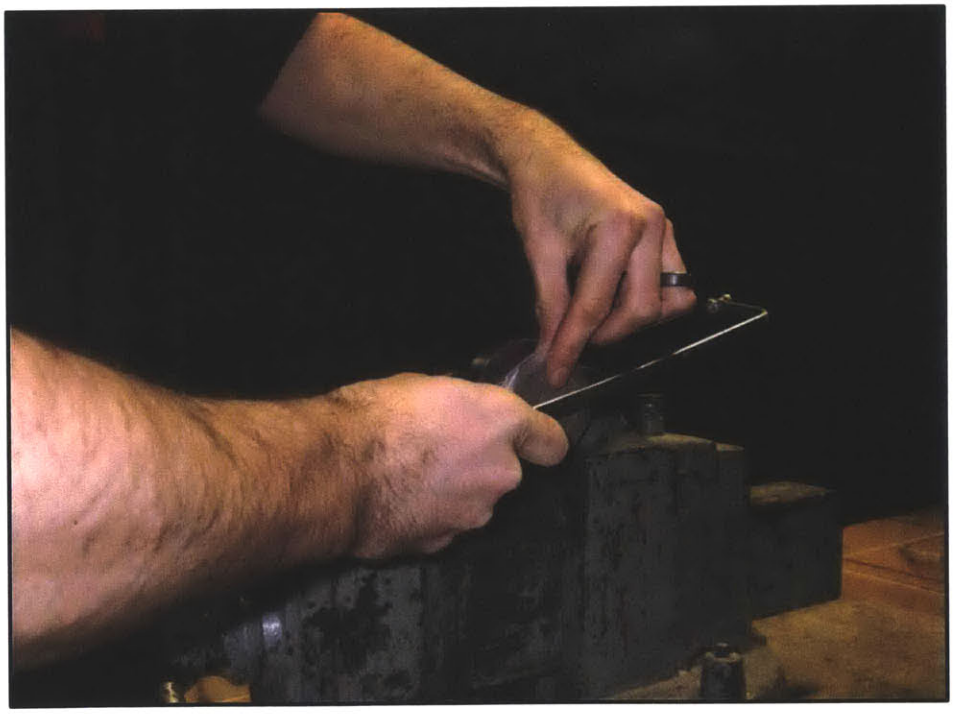

Figure 5-6: The top of the specimen is trimmed by placing the confinement ring in a bench-mounted vice. The wax paper aids in removing the trimmed soil.

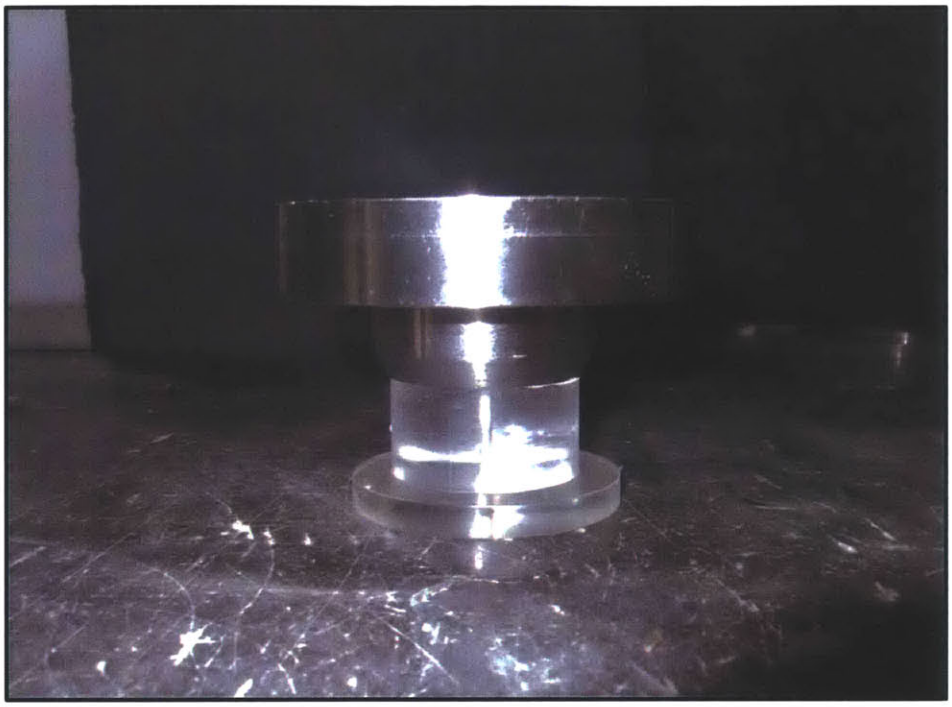

Figure 5-7: The confinement ring is aligned with the acrylic spacer to set the specimen height.

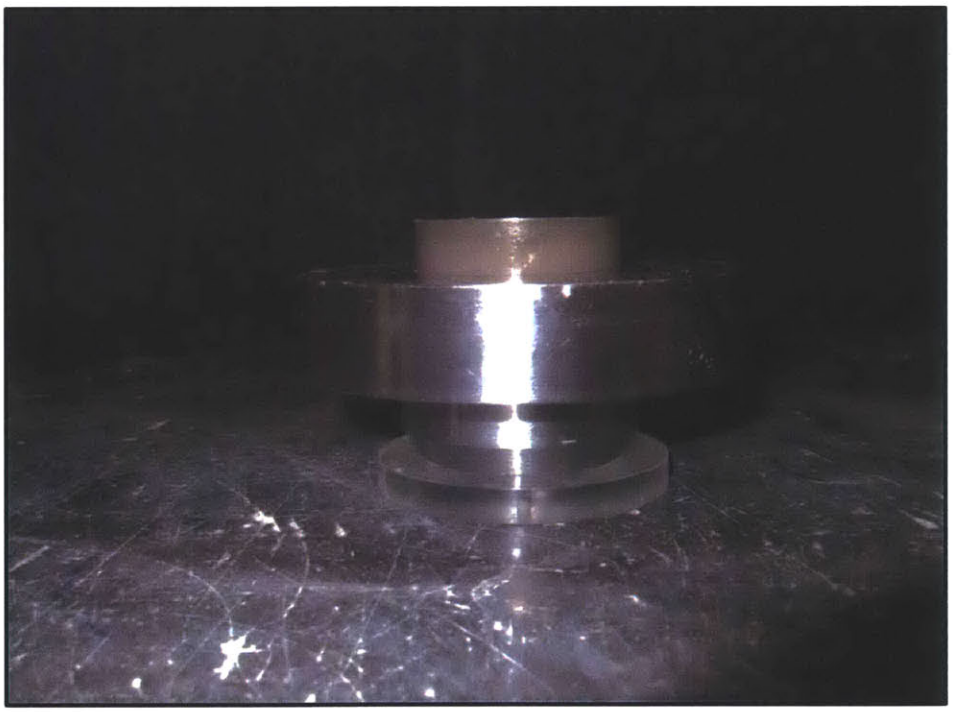

Figure 5-8: The confinement ring is advanced to meet the shoulder of the acrylic spacer to set the specimen height.

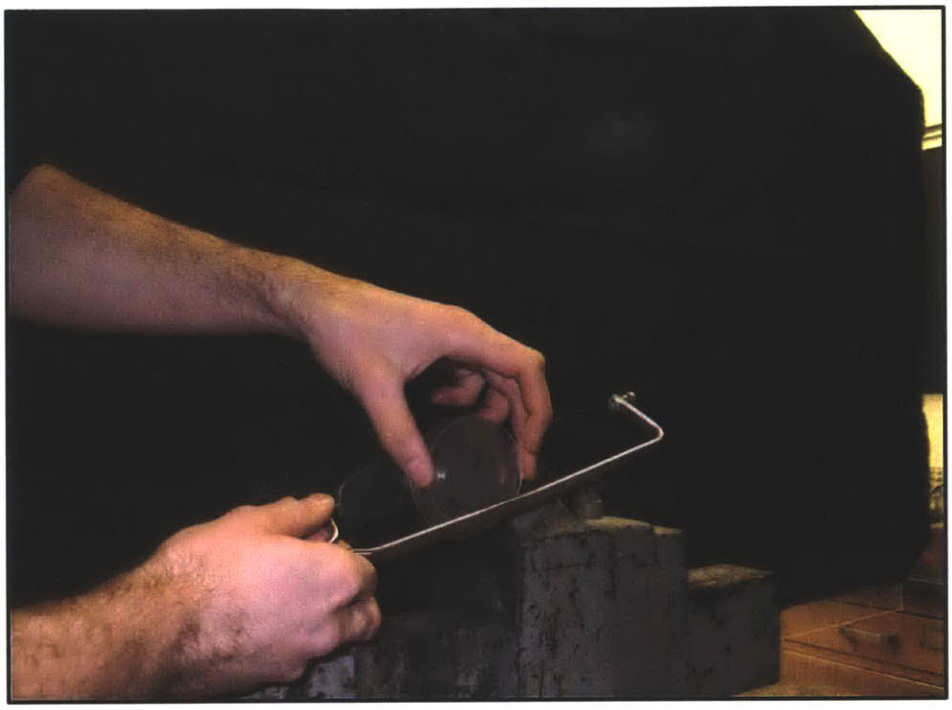

Figure 5-9: The bottom of the specimen is trimmed by placing the confinement ring in a bench-mounted vice. The plastic disc aids in removing the trimmed soil.

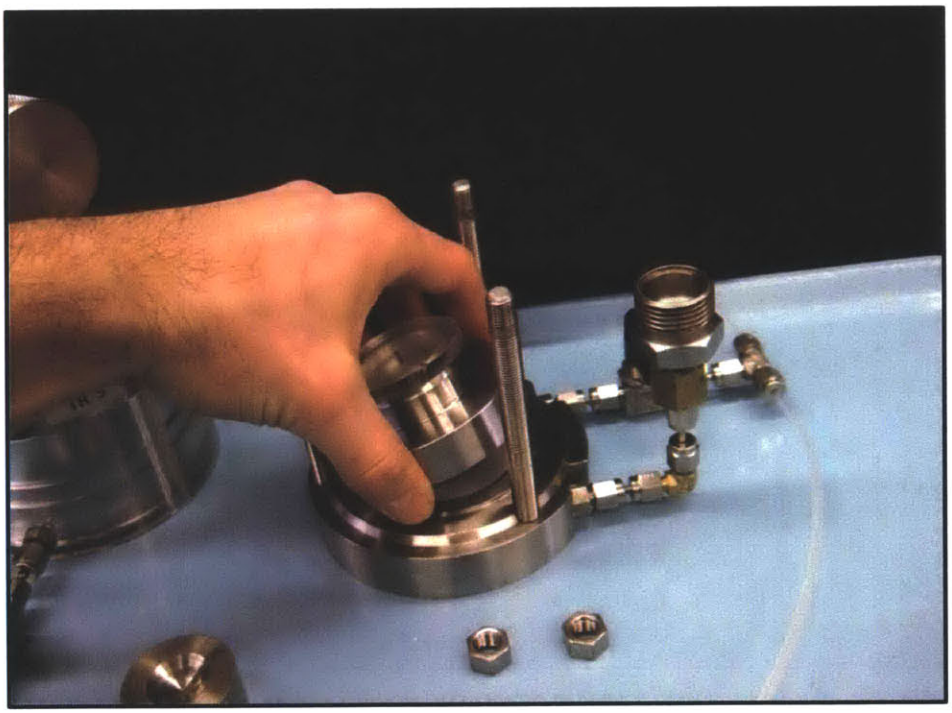

Figure 5-10: With the bottom porous stone and filter paper in place (SSD), the confinement ring containing the specimen is placed concentrically on the cell base.

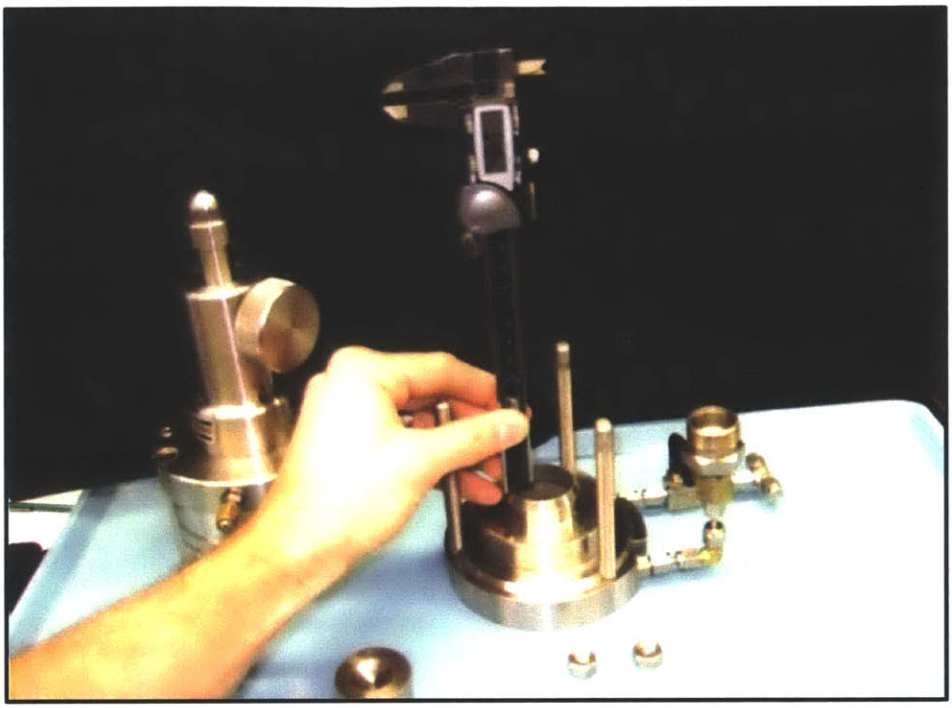

Figure 5-11: After replacing the acrylic spacer with the top porous stone (SSD), the depth of the porous stone within the confinement ring is measured using calipers.

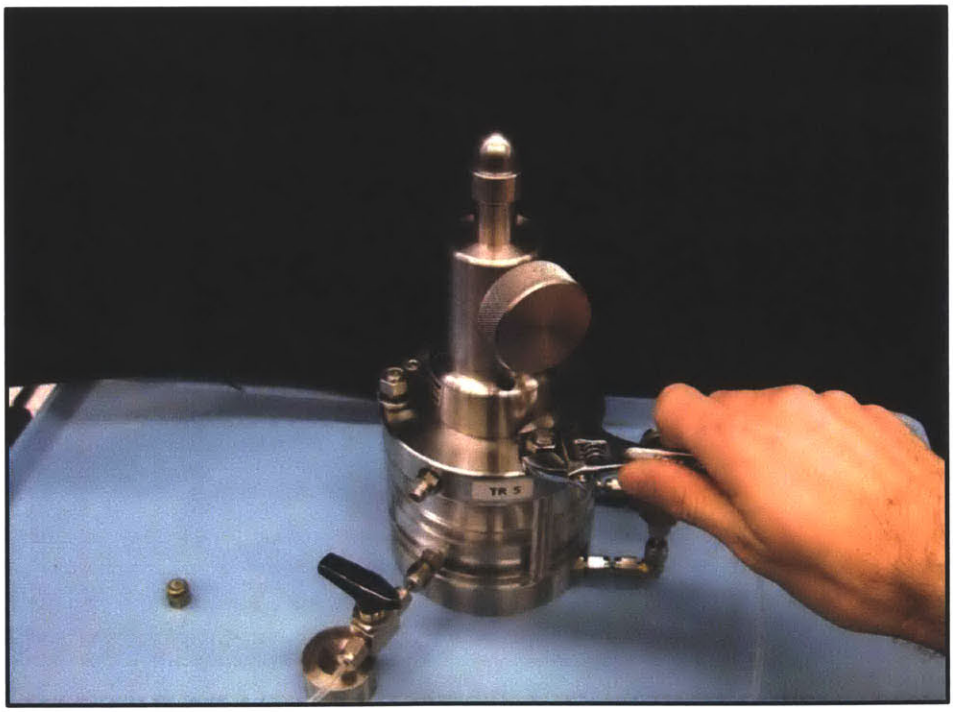

Figure 5-12: The cell is fastened onto the base by alternately tightening the bolts.

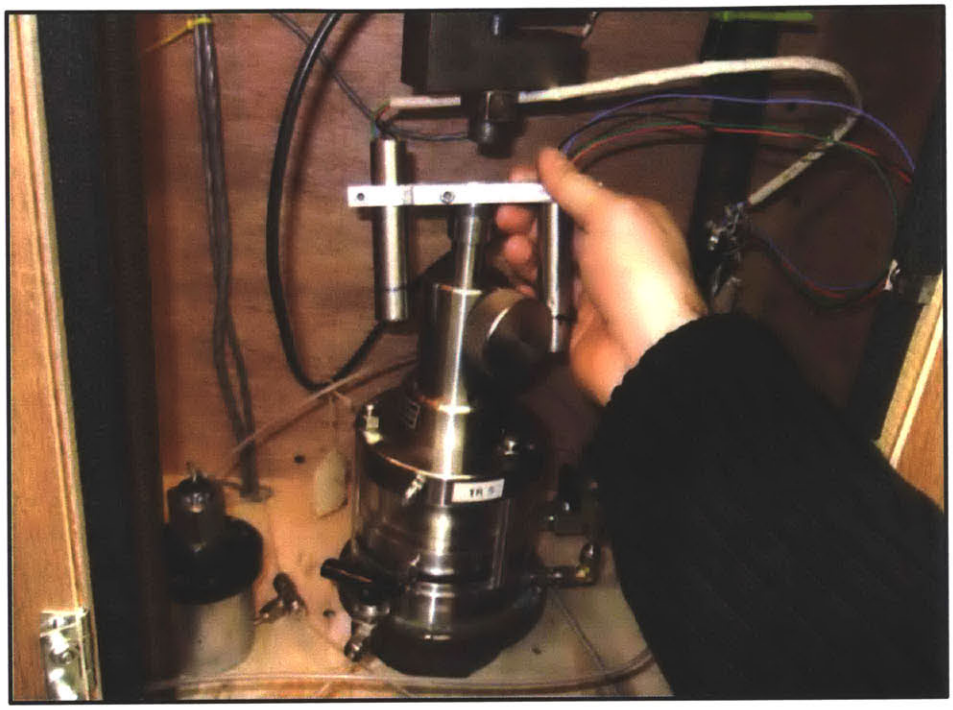

Figure 5-13: The LVDT hanger (attached to the LVDTs) is fastened onto the piston.

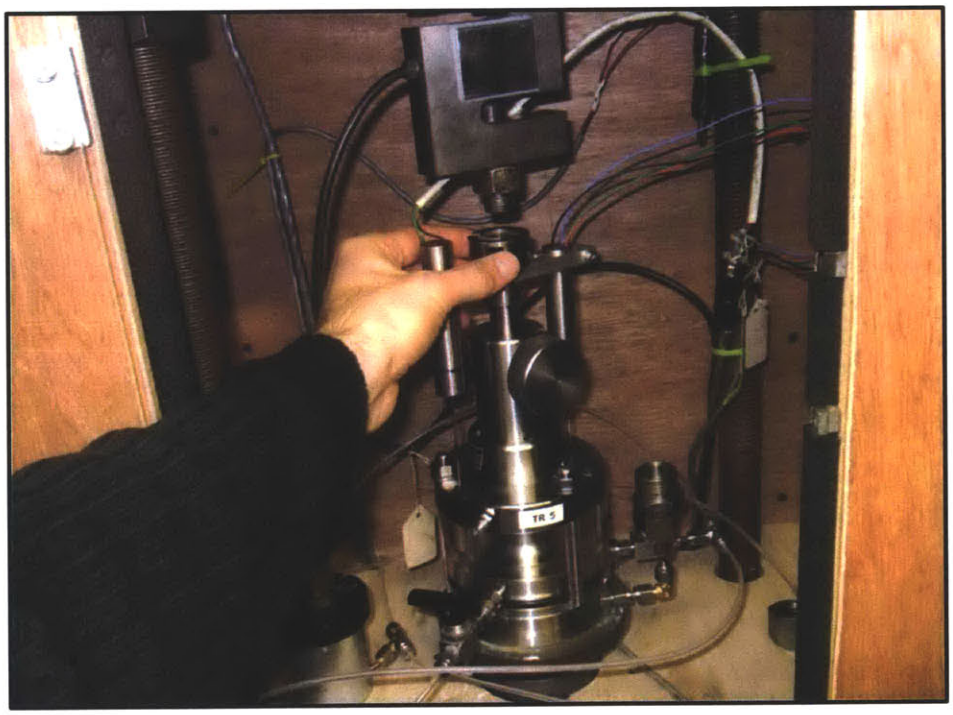

Figure 5-14: A moment/shear break is placed in-between the cell piston and the load cell on the load frame.

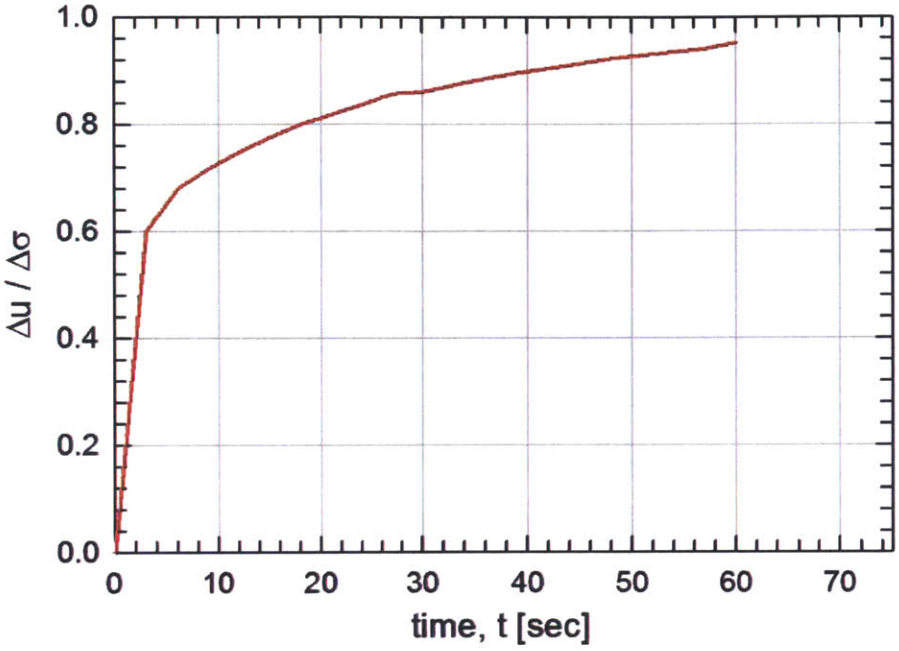

Figure 5-15: An example saturation check from vertically-draining CRS 1429 shows the base pore pressure response over time to an increase in cell pressure.

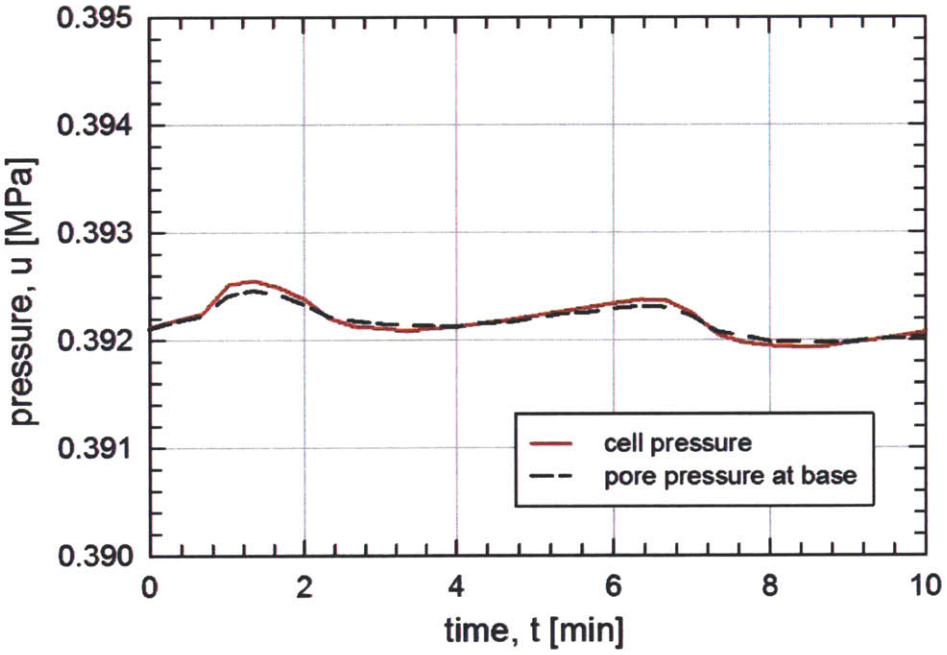

Figure 5-16: A leak check is performed on each test before loading. This leak check for vertically-draining CRS 1429 shows no significant leak up to 10 minutes when the cell pressure is hydraulically shut off from the cell pressure and PVA.

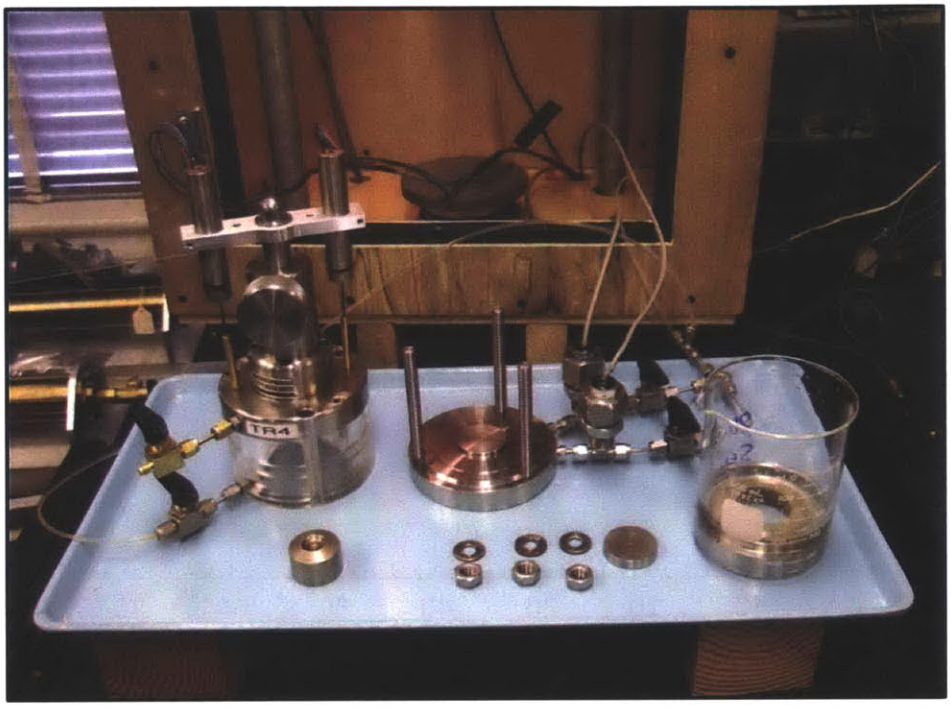

Figure 5-17: The radially-draining CRS apparatus is disassembled and prepared prior to specimen trimming.

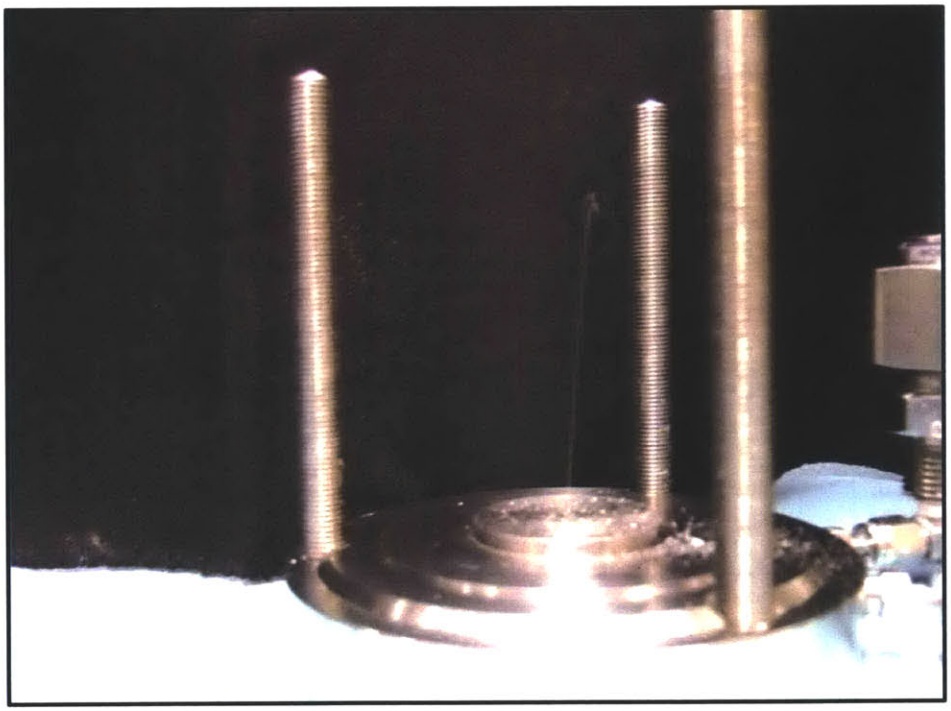

Figure 5-18: Running water through the pore pressure pinholes of the radially-draining CRS apparatus prior to test setup can detect and prevent clogs.

Figure 5-19: The trimming and radially-draining CRS set-up equipment is laid out and prepared prior to sample extrusion.

Figure 5-20: The cutting shoe is placed on top of the confinement ring to prepare for specimen transfer.

Figure 5-21: The confinement ring, cutting shoe, and specimen assembly is aligned with the top cap and acrylic spacer to transfer the specimen into the confinement ring.

Figure 5-22: The cutting shoe and confinement ring are advanced to meet the shoulder of the acrylic spacer to transfer the specimen into the confinement ring and to set its height.

Figure 5-23: The bottom of the specimen is trimmed by placing the confinement ring, cutting shoe, specimen, top cap, and acrylic spacer assembly in a bench-mounted vice. The plastic disc aids in removing the trimmed soil.

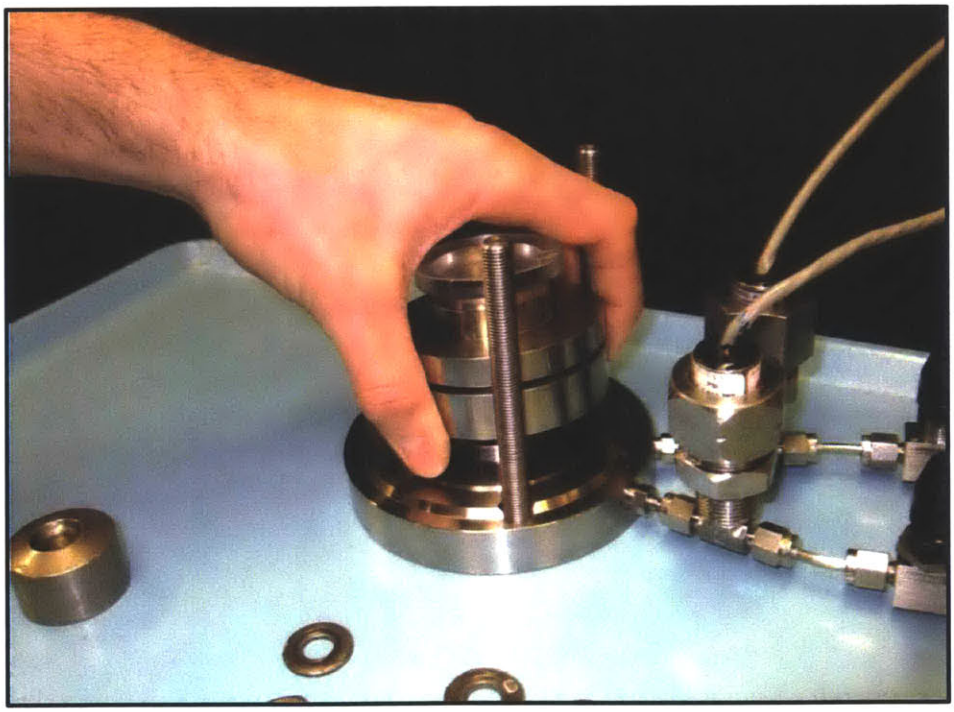

Figure 5-24: The confinement ring, cutting shoe, specimen, top cap, and acrylic spacer assembly is placed concentrically on the cell base.

Figure 5-25: The acrylic spacer and cutting shoe are removed and the confinement ring, specimen, and top cap are left on the base for the duration of the CRS test.

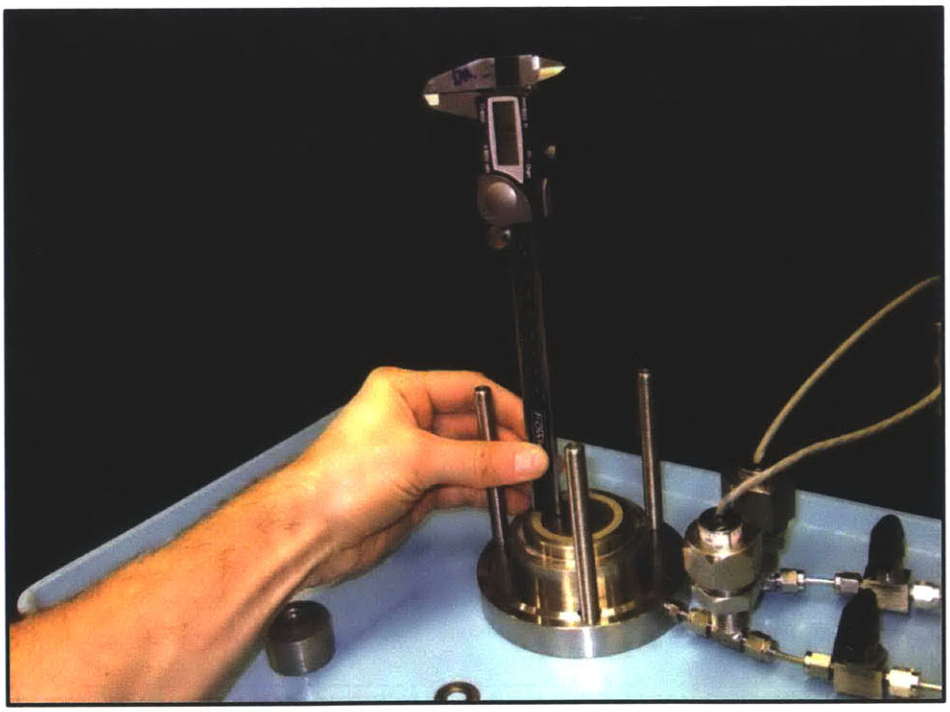

Figure 5-26: The depth of the top cap within the confinement ring is measured using calipers.

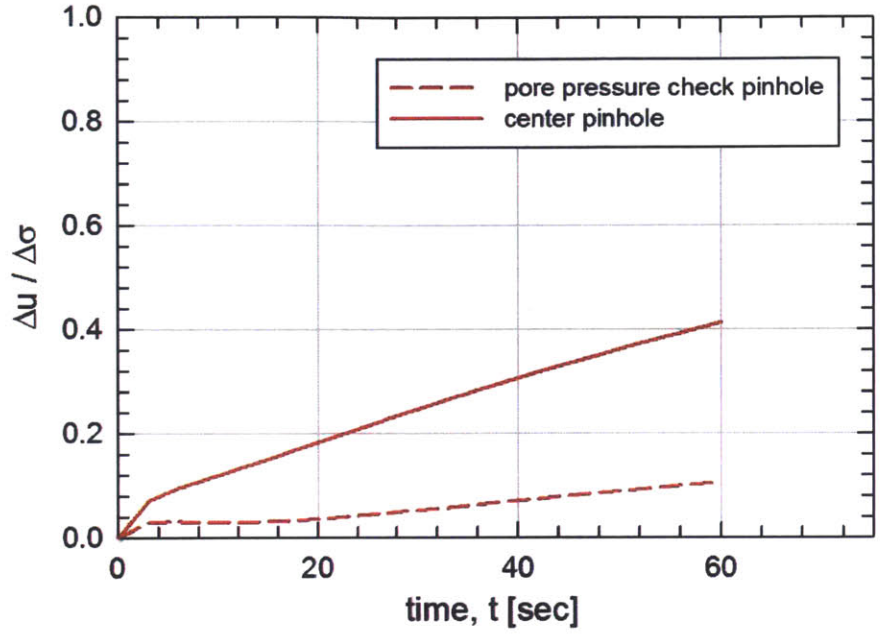

Figure 5-27: An example saturation check from radially-draining CRS 1426 shows the base pore pressure response over time to an increase in cell pressure.

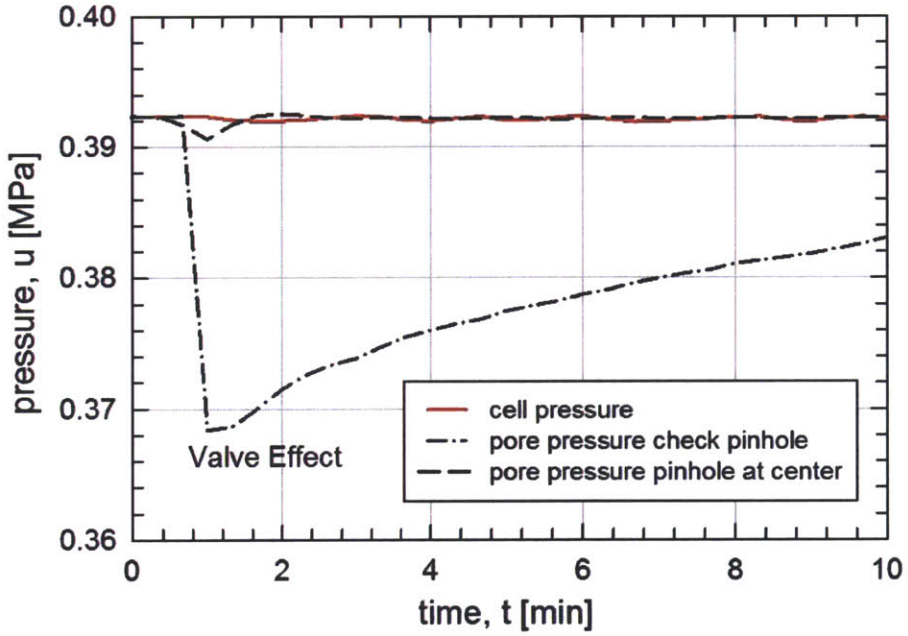

Figure 5-28: A leak check is performed on each test before loading. This leak check for radially-draining CRS 1426 shows a pressure drop in the pore pressure check pinhole due to shutting the valve. The slow recovery is likely due to a partially-clogged condition typical of the pore pressure check pinhole. The pore pressure at the center shows an acceptable no-leak condition.

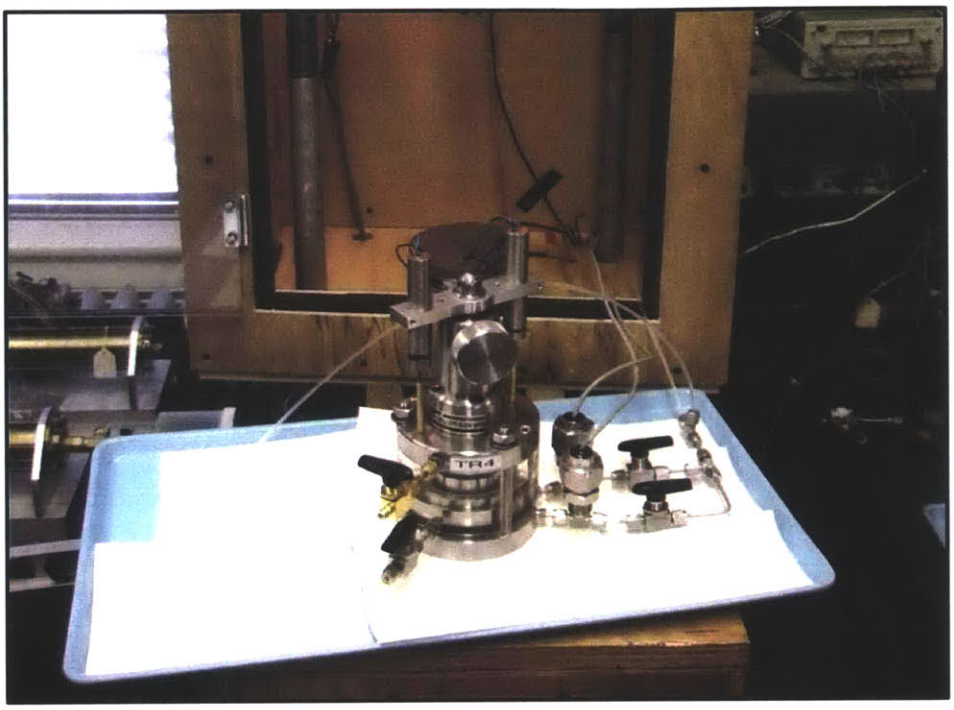

Figure 5-29: The CRS cell is placed on a paper-towel-covered tray prior to disassembly.

Figure 5-30: Paper towels can be used to absorb cell water when the cell is disassembled and to absorb water from above the specimen. Quick water absorption reduces specimen swelling.

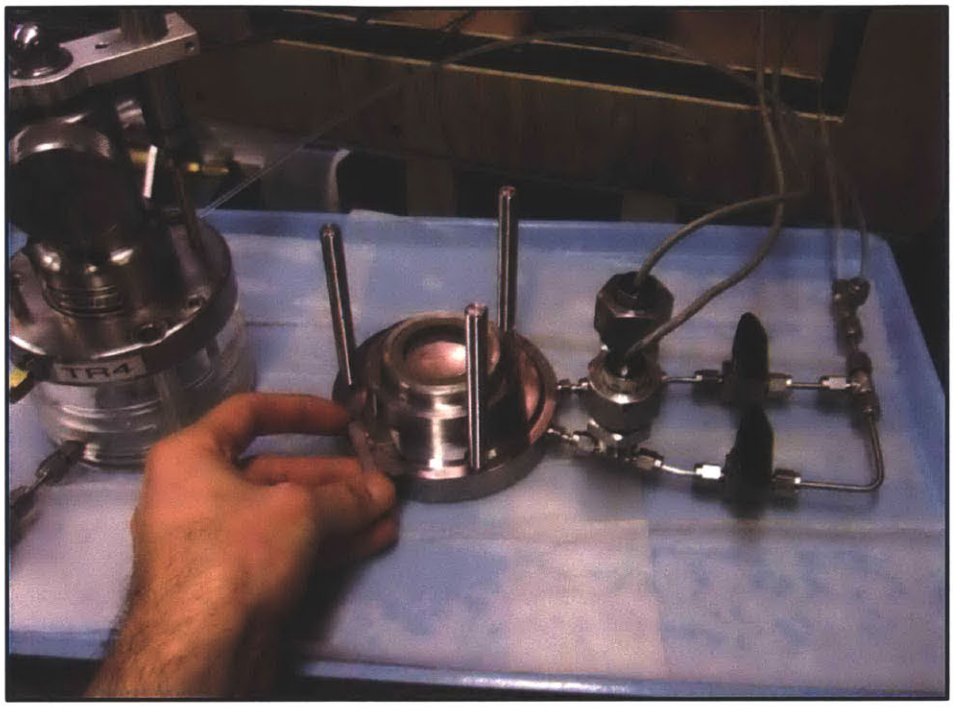

Figure 5-31: The use of a blade can help remove the confinement ring, specimen, and top cap from the base.

Figure 5-32: A hydraulic jack can be used to extrude the specimen and top cap from the confinement ring.

Figure 5-33: Extraneous soil should be collected from the confinement ring, top cap, and base pedestal after extrusion for a correct dry mass measurement.

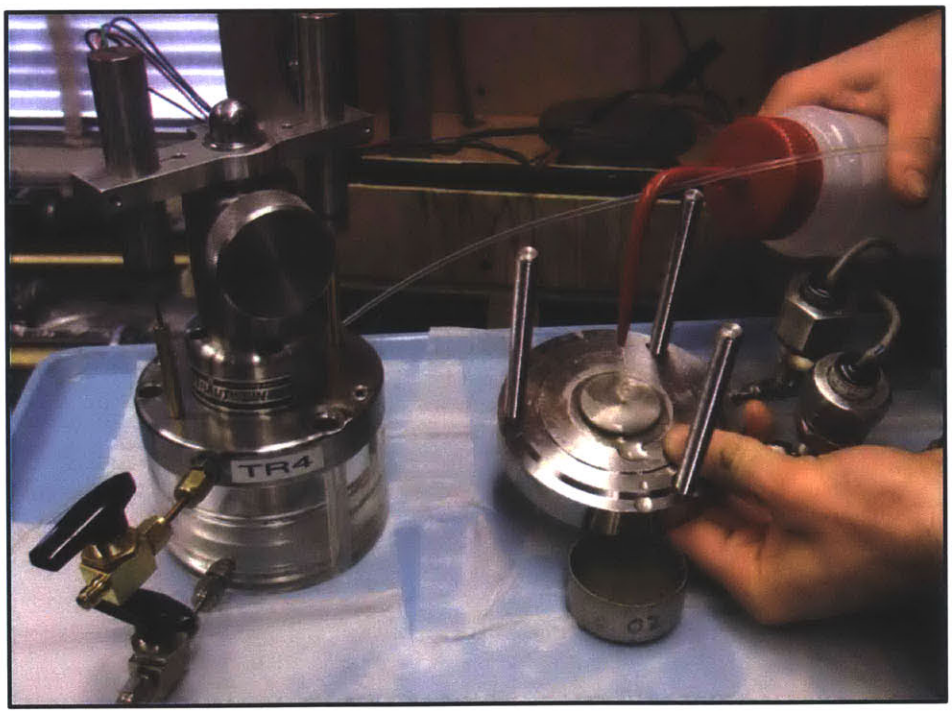

Figure 5-34: Surface agitation and a water bottle can be used to collect extraneous soil from the base pedestal.

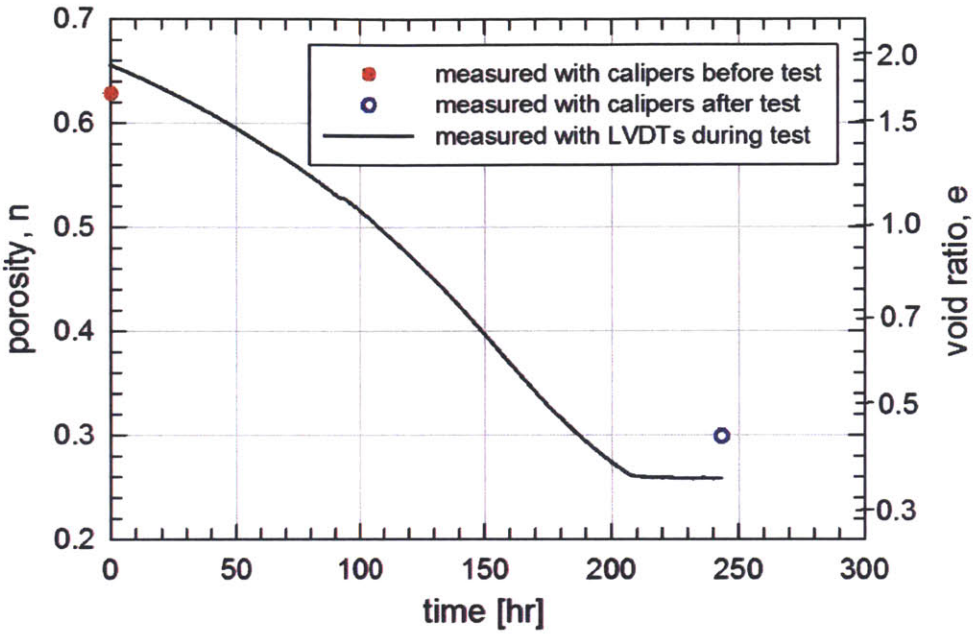

Figure 5-35: Plotting porosity measured before saturating the sample within the CRS cell, during CRS loading, and after removing from the saturated cell shows the swelling that occurs when the specimen has free access to water before and after loading. This example is from vertically-draining CRS 1429.

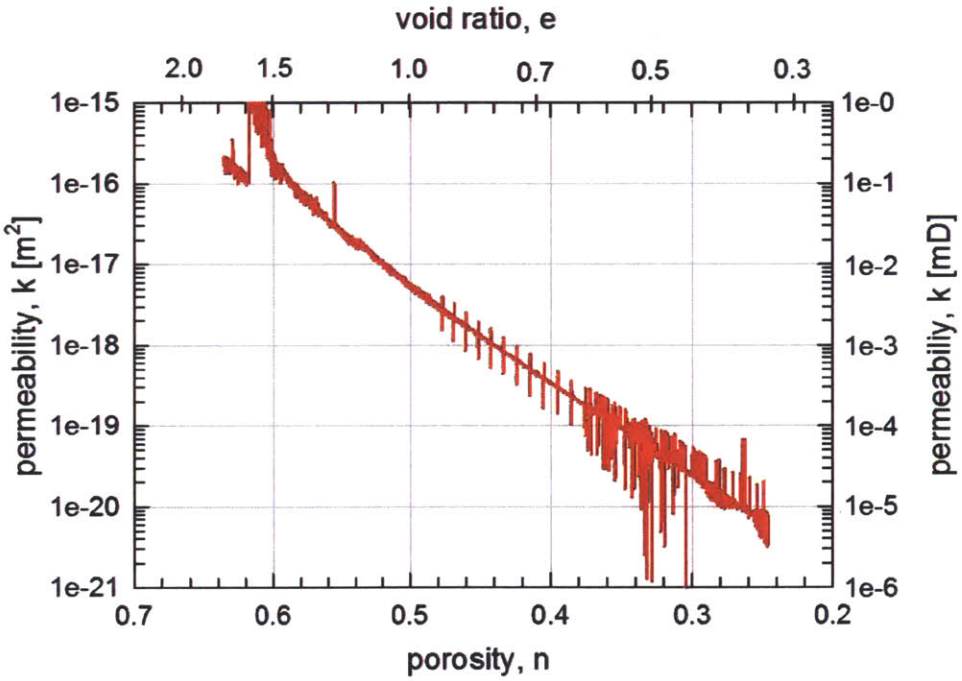

Figure 5-36: Raw permeability results from vertically-draining CRS 1429 show a substantial amount of testing and electronic noise.

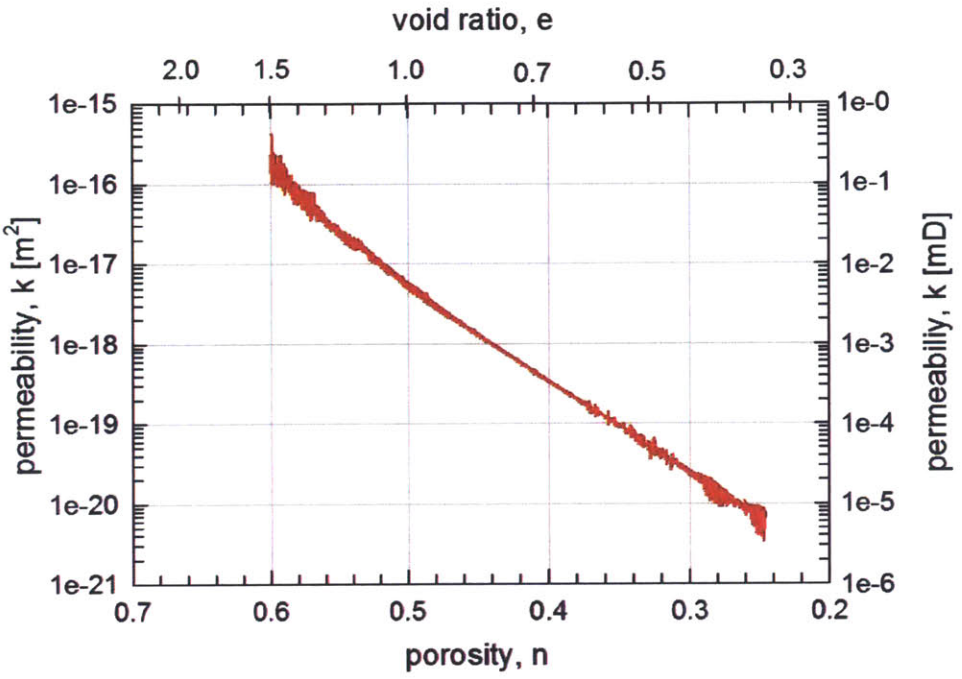

Figure 5-37: Permeability data from each test are smoothed using 5-point smoothing and a manual extreme-noise reduction technique. Data are only reported during the normally-consolidated range of the test. This example is from vertically-draining CRS 1429.

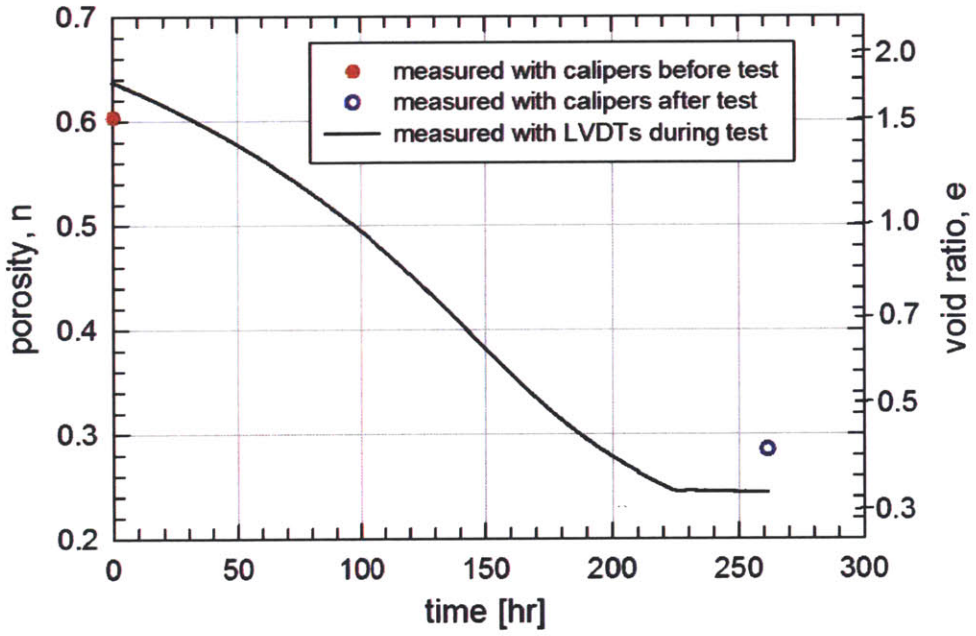

Figure 5-38: Plotting porosity measured before saturating the sample within the CRS cell, during CRS loading, and after removing from the saturated cell shows the swelling that occurs when the specimen has free access to water before and after loading. This example is from radially-draining CRS 1426.

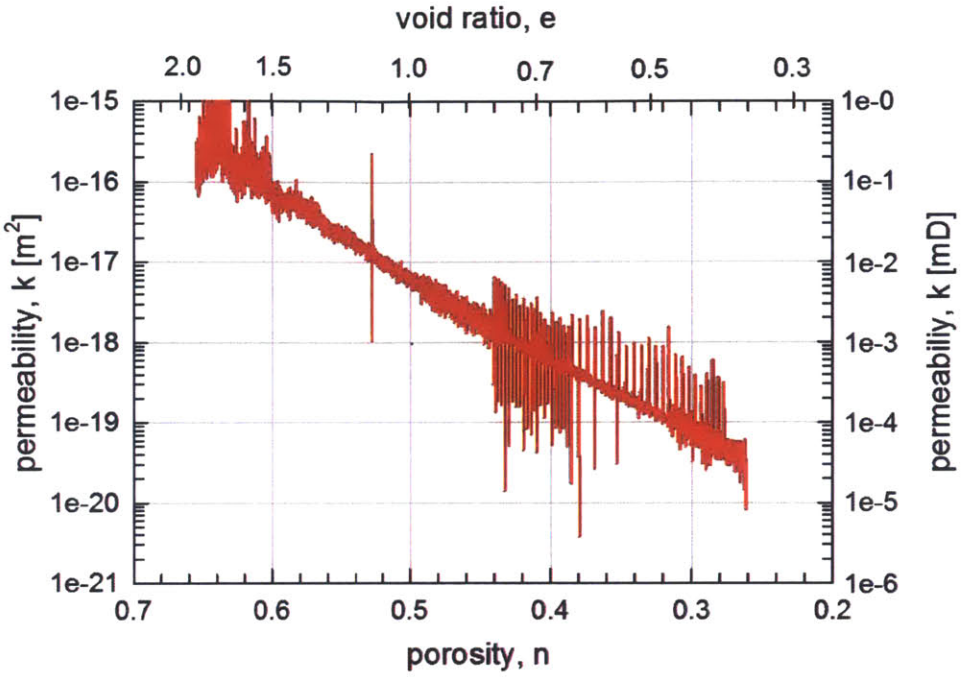

Figure 5-39: Raw permeability results from radially-draining CRS 1426 show a substantial amount of testing and electronic noise.

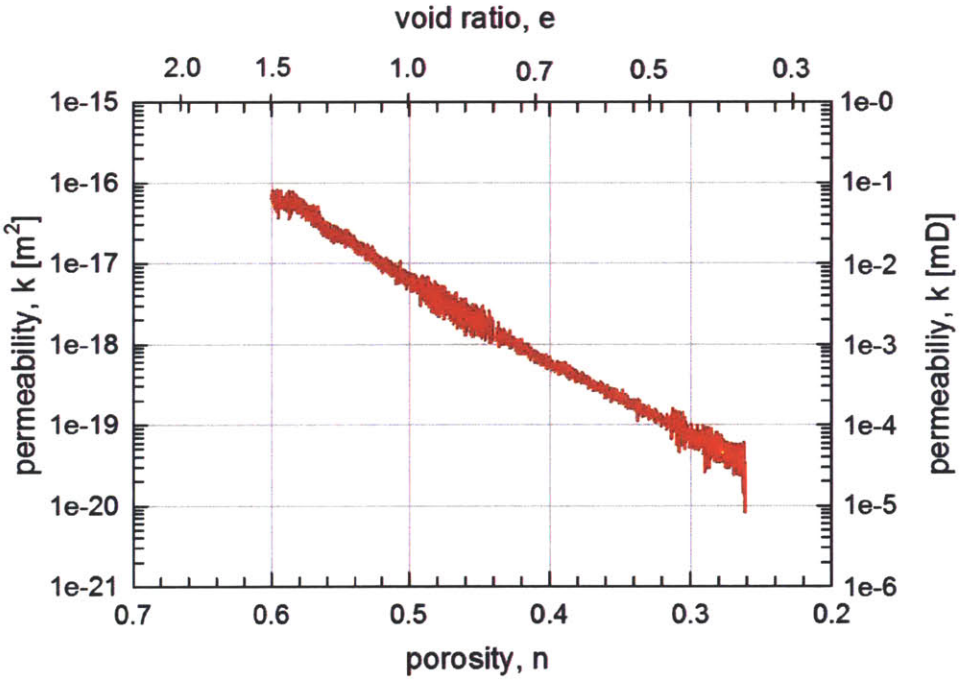

Figure 5-40: Permeability data from each test are smoothed using 5-point smoothing and a manual extreme-noise reduction technique. Data are only reported during the normally-consolidated range of the test. This example is from radially-draining CRS 1426.

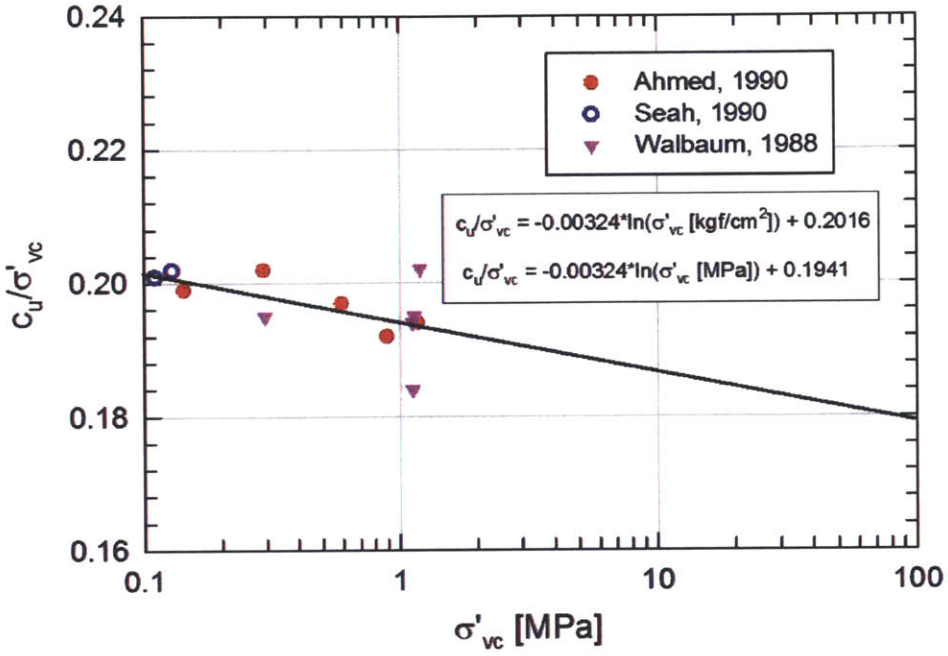

Figure 5-41: An RBBC undrained strength ratio to consolidation stress from Ahmed (1990) was extrapolated and used to estimate sidewall friction around the perimeter of the radially-draining CRS specimens.

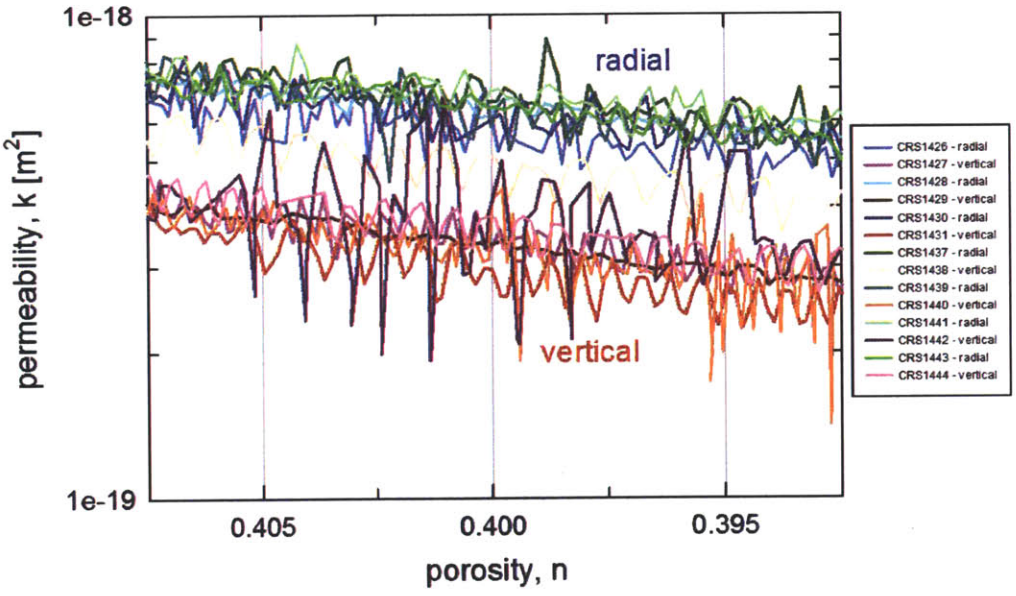

Figure 5-42: A zoomed-in view of RGoM-EI permeability data shows clear permeability trends that can't be directly quantified due to data noise.

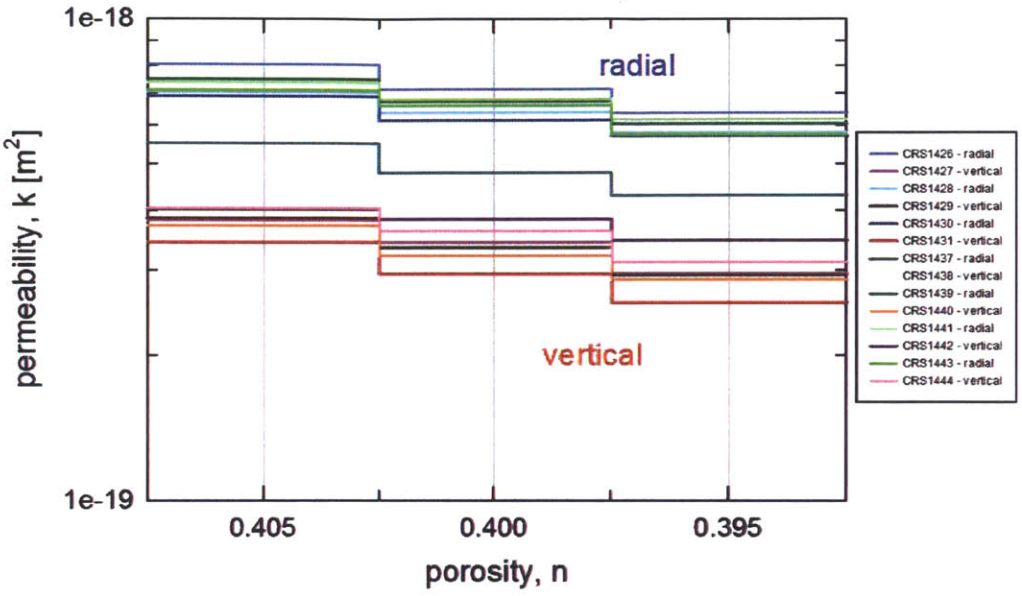

Figure 5-43: The permeability data for each test are individually binned into 0.005 porosity precision by calculating the average permeability value within +/- 0.0025 porosity of binned porosity value.

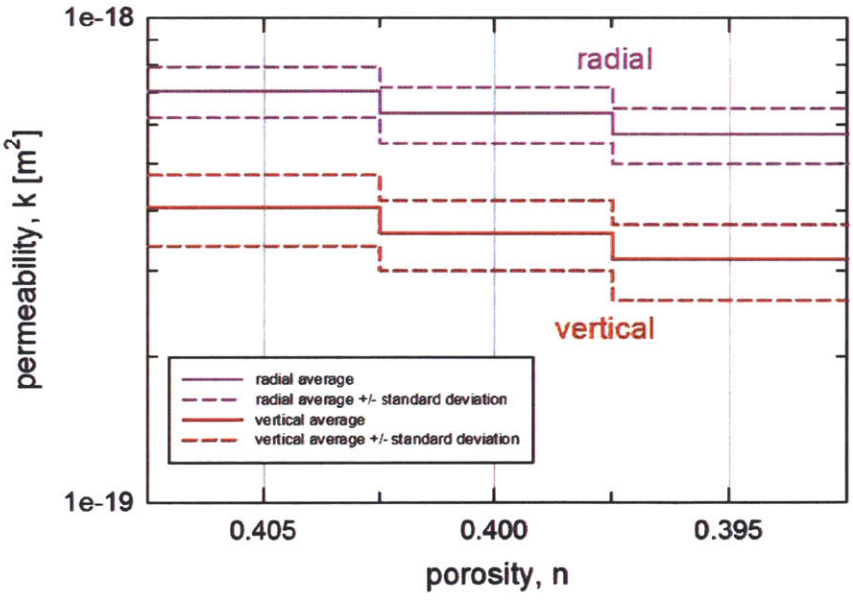

Figure 5-44: Average and standard deviation values are calculated for each flow direction at each binned porosity value.

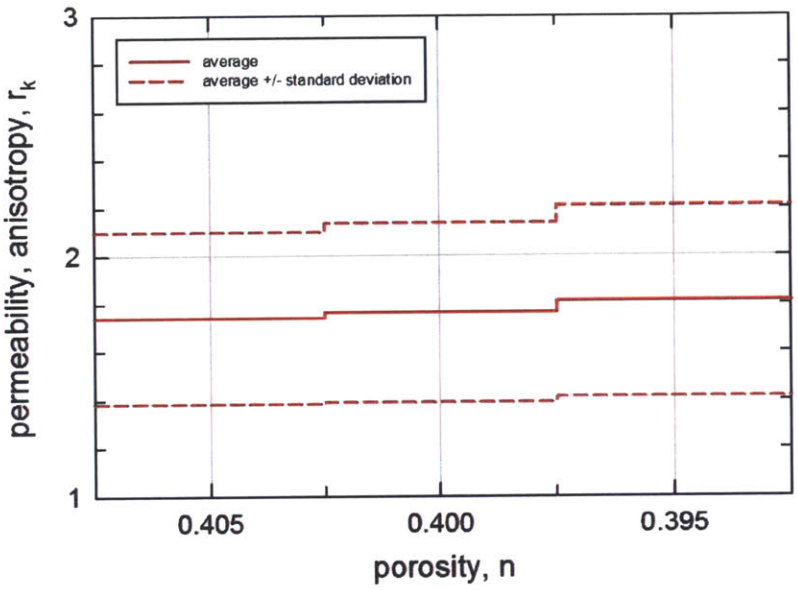

Figure 5-45: Permeability anisotropy is calculated by dividing the average radial permeability value by the average vertical permeability value at each binned porosity. Standard deviation is carried through the calculation.

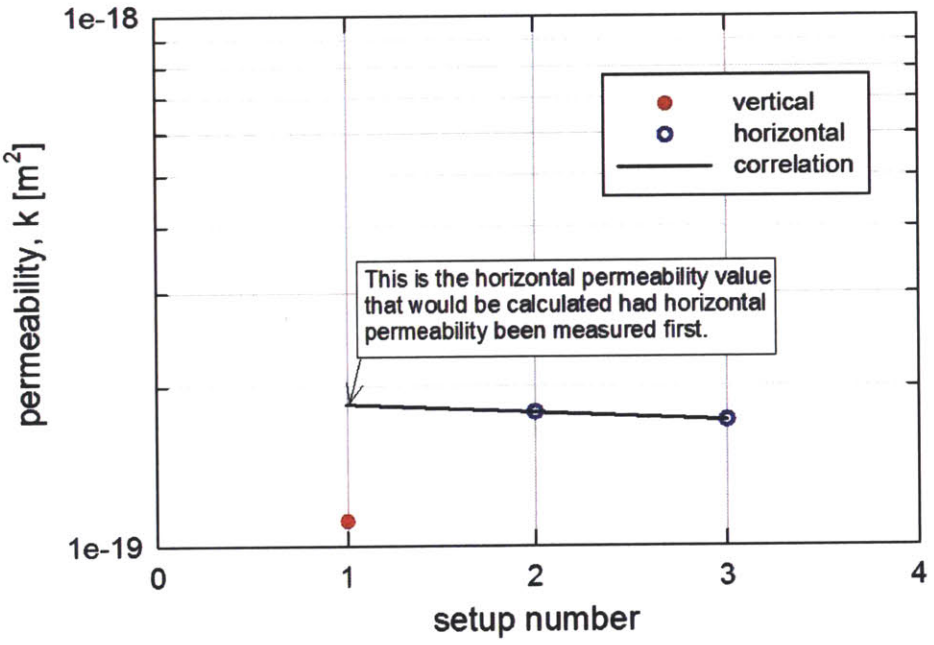

Figure 5-46: The permeability values calculated for each cubic setup direction are sequentially plotted to determine the correction to be applied to the secondary measurement direction to account for take down / set up disturbance. This example shows HC 059.

CHAPTER 6 - RESULTS AND DISCUSSION

6.1 INTRODUCTION

This chapter presents compression and permeability results from tests performed by the author, discusses them, and compares them with similar results in the literature. The data are collected from constant rate of strain consolidation (CRS) testing with both radial and vertical drainage, as well as cubic specimen constant head testing within a triaxial cell. The cubic specimen testing program also provides resistivity anisotropy data. We perform tests on resedimented Boston Blue Clay (RBBC), resedimented Gulf of Mexico – Eugene Island mudrock (RGoM-EI), and a resedimented mixture composed of 91% Boston Blue Clay and 9% Montmorillonite (RBBC + 9% Mont.). Data are also shown from Adams (2014), whose research at MIT was the impetus for our research. She tested RBBC, RGoM-EI, resedimented San Fransisco Bay Mud (RSFBM), leached RBBC, leached RSFBM, and a resedimented mixture composed of 68% Boston Blue Clay and 32% silt (39% Clay RBBC).

Table 6-1 lists the mudrocks that have been tested and sorts them by either Adams or the author with the type of testing performed. A summary of the CRS tests performed is shown in Table 6-2, and a

summary of the cubic specimen constant head tests performed by the author is shown in Table 6-3. The pore fluid salinity measurements are shown in Table 3-4 and 3-5.

The first section of this chapter gives compression results. The second section shows permeability results, which make up the majority of the research. The final section shows resistivity results.

6.2 COMPRESSION RESULTS

This section shows the compression behavior of the mudrocks tested both in the CRS and the cubic specimen constant head devices. In general, the compression results show similar vertical compression behavior independent of drainage direction during compression.

Compression curves are plotted as a fabric density parameter versus vertical effective stress. The density of the fabric can be represented either as strain, void ratio (e), or porosity (n). Void ratio is defined as the volumetric ratio of voids to soil solids, while porosity is defined as the fraction of void volume to total volume. Either parameter is used for plotting and regression, depending on the degree of linearity shown by the mudrocks when plotted in each space. Specifically, RBBC is plotted using porosity, while RGoM-EI is plotted using void ratio.

6.2.1 RBBC

Resedimented Boston Blue Clay (RBBC) is tested in the vertically-draining and radially-draining CRS devices. Six tests are performed with radial drainage, and three tests are performed with vertical drainage. The initial and final stresses and porosities are tabulated in Table 6-4, and the compression curves are shown in Figure 6-1.

The compression curves show very nice repeatability between each test. This repeatability is seen in spite of the fact that the radially-draining CRS procedure uses a sidewall friction correction factor, as the tubular-shaped porous stone is far from frictionless, while the vertically-draining CRS assumes no sidewall friction. A correlation is fit using data from the nine tests with vertical effective stresses between 0.1 and 40 MPa, with an r-squared value of 0.9989 (see Figure 6-1). Not only is there similarity between each individual test, but there is great similarity between data from the vertically-draining and the radially-draining devices. This shows that compression behavior, without considering time, is independent of the pore water drainage direction. It also creates a nice platform for comparing permeability in orthogonal directions, as compressibility is unaltered.

Most of the scatter in the compression curves occurs in the recompression portion at low stresses. While all the resedimented samples are compressed to 0.1 MPa prior to placement in the CRS cell, the actual preconsolidation pressures and accompanying initial porosities vary due to sidewall friction in the resedimentation tube. The variation in these parameters can be seen in Table 6-4. Variations in consolidometer roughness, amount of silicon oil applied, height of resedimentaton column, and location within the column can all affect preconsolidation pressures and initial porosities. Consequently, the compression and permeability parameters reported in regression are taken only beyond stresses of 0.1 MPa, in the mudrocks' normally-consolidated regions.

The volume compressibility of the 0.1 to 40 MPa vertical effective stress region is shown as Figure 6-2. Repeatability is also seen in this parameter, as an equation is fit through the data with an r-squared value of 0.98.

6.2.2 RBBC + 9% Montmorillonite

Four specimens are resedimented from a mixture of 91% BBC and 9% montmorillonite by weight (RBBC + 9% Mont.), and tested as cubic specimens in the triaxial cell permeameter. They are tested in order to compare results with RBBC results, in an attempt to determine the effect that smectite has on permeability anisotropy. In order to obtain data for various porosities, each specimen is resedimented to different vertical effective stresses, then unloaded to an OCR of four. The preconsolidation vertical effective stress to porosity relationship is shown as Figure 6-3.

6.2.3 RGoM-EI

Resedimented Gulf of Mexico – Eugene Island mudrock (RGoM-EI) is tested in both the CRS devices and the cubic specimen constant head device.

CRS

RGoM-EI is tested in the vertically-draining and radially-draining CRS devices. Seven tests are performed with both vertical and the radial drainage. The initial and final stresses and porosities are tabulated in Table 6-5, and the compression curves are shown in Figure 6-4.

The compression curves show very nice repeatability between each test. A correlation is fit using data from the fourteen tests with vertical effective stresses between 0.1 and 40 MPa, achieving an r-squared value of 0.997 (see Figure 6-4). The radially-draining and vertically-draining test data again show similar results, however, the radially-draining tests show slightly lower stresses at high porosities. This is likely due to the application of a sidewall friction correction factor in the radially-draining test, which lowers

the reported effective stress in comparison to the vertically-draining test, in which sidewall friction is assumed to be zero. Sidewall friction is never zero in a consolidometer, but it can't be more than the undrained strength, so the slight difference between the flow-direction compression curves is likely to be a result of measurement limitations. It is unlikely that the difference is material behavior, and we can conclude that the vertical compression behavior of RGoM-EI is independent of pore water drainage direction. For details on how the sidewall friction is calculated, see Section 5.3.3.

Most of the scatter in the compression curves occurs in the recompression portion at low stresses. While all the resedimented samples are compressed to 0.1 MPa prior to placement in the CRS cell, the actual preconsolidation pressures and accompanying initial porosities vary due to sidewall friction. The amount of variation can be seen in Table 6-5. Variations in consolidometer roughness, amount of silicon oil applied, height of resedimentaton column, and location within the column can all affect preconsolidation pressures and initial porosities. Consequently, the compression and permeability parameters reported in regression are taken only beyond stresses of 0.1 MPa, in the mudrocks' normally-consolidated regions.

The volume compressibility of RGoM-EI in the 0.1 to 40 MPa vertical effective stress region is shown as Figure 6-5. While similarity between the pore water drainage conditions is shown, a large amount of noise is present, especially at low stresses. The noise is likely due to a slow (0.3 %/hour) strain rate combined with frequent (4 minute) data acquisition over a week-long test. Frequent acquisition is highly susceptible to small, alternating fluctuations in pressure gradients. A log-linear regression is fit to the data with an r-squared value of 0.53.

Cubic Specimen Constant Head

Three RGoM-EI specimens are tested for permeability and resistivity in orthogonal directions within a triaxial cell. In order to obtain data for various porosities, each specimen is resedimented to different vertical effective stresses, then unloaded to an OCR of four. The vertical effective preconsolidation stress to porosity relationship is shown against the average RGoM-EI CRS virgin compression curve in Figure 6-6.

The scatter in the compression behavior of the cubic specimens lies beyond the standard deviation from the average CRS compression curve. Two possible reasons for this scatter would systematically move the cubic specimen measurements above the average CRS compression curve, but do not explain measurements below it. While the CRS curve is showing virgin compression, the cubic specimens are plotted using porosities obtained after drained unloading to an OCR of four and undrained complete

unloading. The unloading causes the specimens to swell slightly, moving the cubic specimen compression measurements up to higher porosities. The effect of sidewall friction in the resedimentation columns can also move the cubic specimen data points away from the CRS virgin compression curve. While zero sidewall friction is assumed, its inevitable presence transfers some of the load intended for the mudrock to the resedimentation column, decreasing the amount of preconsolidation stress in the sample. This moves the specimen stress measurements right to higher stresses than they have actually felt, again moving them above the virgin compression curve.

6.2.4 Discussion of Compression Results

When comparing the author's CRS compression curves with compression curves measured from other researchers, RBBC shows good repeatability, while RGoM-EI shows an offset. Figure 6-7 shows the author's RBBC compression curves plotted with CRS 1291, an RBBC compression curve measured by Aiden Horan at MIT (Horan, 2012). All the tests represented were performed on mudrocks batched to 16 g/L salinity. Horan's curve fits well within the limited scatter of the author's data set. Figure 6-8 shows the author's RGoM-EI compression curves plotted with three other tests on RGoM-EI. CRS 109-UT was measured by Will Betts at the University of Texas at Austin (Betts, 2014), and CRS 1364 and 1366 were measured by Brian Fahy at MIT (Fahy, 2014). The author's data set, while in fair agreement within itself, is offset from the tests from Betts and Fahy, which are in fair agreement with themselves. The discrepancy is not likely due to salinity, as we resedimented our specimens to 80 g/L pore fluid salinity (the same that Betts used), while Fahy's data used resedimented specimens batched to salinities both higher and lower than the rest of the data, 64 g/L and 128 g/L respectively. The discrepancy in the RGoM-EI compression curves could be due to improper mixing of the GoM-EI powder, small differences in the resedimentation batching, or unpredictable material behavior.

RGoM-EI is a more compressible mudrock than RBBC, as can be seen in Figure 6-9. This is most likely due to the large amount of smectite present in RGoM-EI, where large double layers hold a lot of water volume at low stresses. RBBC is represented most linearly in void ratio – log stress space, while RGoM-EI is represented most linearly in porosity – log stress space.

The compression behavior of the resedimented specimens tested for permeability as cubic specimens is shown in Figure 6-10. The porosities are calculated from caliper-measured dimensions taken after the specimens are unloaded in a drained condition to an OCR of 4, then completely unloaded in an undrained condition. The preconsolidation stress is plotted as the vertical effective stress. It is the maximum stress applied to the sample during resedimentation. It is harder to see material trends when

plotting the compression behavior from the cubic specimens than it is using CRS data, as the trends must be interpolated between data from different specimens. However, the 39% Clay RBBC displays a lower porosity at all stresses than the other mudrocks, indicating that clay content has a significant effect on compressibility.

6.3 PERMEABILITY RESULTS

Permeability is calculated for RBBC and RGoM-EI in both the vertical and radial horizontal directions using CRS testing. This method uses the buildup of excess pore pressure during mudrock compression to infer permeability, producing a continuous set of permeability data as a function of compression. Permeability is calculated using cubic specimen constant head testing on RBBC + 9% Mont. and RGoM-EI (in addition to CRS testing). This method induces flow through overconsolidated mudrock cubes isotropically compressed to an OCR of 4 in a triaxial cell to calculate permeability. Results from both types of test are presented in this section, compared with each other, and compared with data from Adams (2014).

6.3.1 RBBC

The permeability of resedimented Boston Blue Clay (RBBC) is measured in the vertical and radial horizontal directions using CRS testing. Six tests are performed using the radially-draining CRS device, and three are performed using the vertically-draining CRS device (see Table 6-4). Multiple tests are performed using the same material and drainage direction in order to separate testing noise from material behavior. Each RBBC specimen is compressed at a strain rate, $\dot{\varepsilon}$, of 1.4 %/hour.

Permeability, k

Figure 6-11 shows the permeability results within the normally-consolidated region for the RBBC CRS tests. The test results show a clear distinction in permeability data between the radially-draining and the vertically-draining tests, and considerable repeatability within each flow regime. This repeatability is in large part a consequence of using homogenous resedimented material. While the mudrocks compress and porosity decreases, permeability decreases in a roughly log-linear pattern for both flow directions. However, there is a slight curvature to the data. The radial horizontal permeability is slightly larger at all porosities, and the two permeability trends diverge slightly with compression. These results agree well with the current theories of flowpath tortuosity around plate-shaped clay particles creating greater horizontal permeability than vertical.

Log-linear permeability equations are fit through the test data in the format used by Casey (2014). The equation, shown below as Equation 6-1, uses two parameters: the permeability value at a porosity of 0.5, $k_{0.5}$, and the log-linear slope of the permeability trend, γ.

$$log_{10}(\mathrm{k}) = \gamma(\mathrm{n} - 0.5) + log_{10}(k_{0.5}) \tag{6-1}$$

The γ and $k_{0.5}$ parameters are fit for RBBC for both radial and vertical permeability, and can be seen in Figure 6-11. The radial and vertical log-linear regressions achieve r-squared values of 0.989 and 0.996, respectively.

Figure 6-12 and Figure 6-13 show the permeability anisotropy results within the normally-consolidated region for the RBBC CRS tests. The average and standard deviations away from the average are plotted, as determined using the binning procedure described in Section 5.3.4. The average permeability anisotropy of RBBC is seen to increase from about 1.4 to 3, as the mudrock in compressed from 0.1 to 40 MPa, corresponding to porosities changing from 0.56 to 0.26. These results agree well with current theories of increasing particle orientation with compression creating increasing permeability anisotropy.

A simple regression should not be performed on the permeability anisotropy data developed using the binning procedure, as the binned data represent twice averaged data. Therefore, permeability anisotropy equations are developed algebraically from the equations fit to permeability in both directions. Figure 6-12 shows the predicted permeability anisotropy using Equation 6-2, which is derived by taking the ratio of the radial permeability to vertical permeability forms of Equation 6-1.

$$log_{10}(r_k) = (\gamma_r - \gamma_v)(n - 0.5) + log_{10}\left(\frac{k_{r,0.5}}{k_{v,0.5}}\right) \tag{6-2}$$

Permeability anisotropy is represented as r_k, γ_r and γ_v are the radial and vertical slope factors, and $k_{r,0.5}$ and $k_{v,0.5}$ are the radial and vertical permeabilities at a porosity of 0.5. These parameters are the same parameters used in the individual permeability log-linear equation, Equation 6-1, and are shown in Figure 6-11. This equation stays within the standard deviation of the data; however, it underpredicts anisotropy at high porosities.

Representing the permeability – porosity trends log-linearly is an artificial way of representing natural mudrock behavior. While these linear trends are representative and user-friendly, they do not catch small nuances within the trends. When permeability values are divided with each other to calculate anisotropy, these nuances can be amplified. In an attempt to make a more precise regression of permeability anisotropy, quadratic functions are fit to both radial and vertical permeability test data in log-linear space. The radial and vertical permeability quadratic regressions produce r-squared values of 0.98 and 0.990, respectively. A quadratic permeability anisotropy equation is then derived for RBBC by taking the ratio of the two functions. The result of this process is shown as Equation 6-3, and is plotted with the binned permeability anisotropy data in Figure 6-13.

$$log_{10}(r_k) = 2.11(n - 0.5)^2 - 0.77(\mathrm{n} - 0.5) + log_{10}(1.56) \qquad (6\text{-}3)$$

Permeability anisotropy is represented as r_k, and 1.56 is the anisotropy value corresponding to a porosity of 0.5. This quadratic equation in log-linear space better captures the concavity of the permeability anisotropy trend at high porosities. At lower porosities, however, the trendline is still offset from the average values.

Coefficient of Vertical Consolidation, c_v

The coefficient of vertical consolidation, c_v, is measured from both the vertically- and radially-draining CRS tests. Figure 6-14 plots the coefficient of vertical consolidation with radial drainage, $c_{v,r}$, and vertical drainage, $c_{v,v}$, against porosity from the normally-consolidated portions of the tests on RBBC. For both drainage conditions, the coefficient of vertical consolidation increases gradually at the beginning of compression, then levels off around a porosity of 0.35 (~ 10 MPa effective stress). The coefficient of vertical consolidation with radial drainage increases at a slightly greater rate than that of vertical drainage, creating a slight divergence.

A log-linear quadratic equation is fit to the data for each drainage condition, using the same format that is used for the permeability equations. The equation, shown below as Equation 6-4, uses a parameter representing the coefficient of vertical consolidation with radial or vertical drainage at a porosity of 0.5, $c_{v,r,0.5}$ or $c_{v,v,0.5}$, along with two other parameters representing the curvature of the trends, α and β.

$$log_{10}(c_v) = \alpha(n - 0.5)^2 + \beta(\mathrm{n} - 0.5) + log_{10}(c_{v,0.5}) \qquad (6\text{-}4)$$

The α, β, and $c_{v0.5}$ parameters are fit for RBBC for both radial and vertical drainage conditions, and can be seen in Figure 6-14. The radial and vertical log-linear quadratic regressions achieve r-squared values of 0.86 and 0.90, respectively. These parameters can also be computed directly from hydraulic conductivity and the coefficient of volume compressibility.

Figure 6-15 shows the coefficient of consolidation anisotropy results within the normally-consolidated region for the RBBC CRS tests. The average and standard deviations away from the average are plotted, as determined using the binning procedure described in Section 5.3.4.

A quadratic coefficient of vertical consolidation anisotropy equation is derived for RBBC by mathematically dividing the log-linear quadratic regressions, the same way the permeability anisotropy equation is derived. Radial and vertical r-squared values of 0.86 and 0.90, respectively, are achieved. The final coefficient of vertical consolidation anisotropy for RBBC equation is shown as Equation 6-5, and is presented with the binned coefficient of vertical consolidation anisotropy data in Figure 6-15.

$$log_{10}(r_{cv}) = -1.4(n-0.5)^2 - 1.5(\mathrm{n}-0.5) + log_{10}(1.55) \qquad (6\text{-}5)$$

Permeability anisotropy and coefficient of vertical consolidation anisotropy are theoretically equal. This research shows that they are mostly equal in practice as well. The coefficient of consolidation is a product of both the permeability and the compressibility of the mudrock. Since the compressibility of the mudrock is independent of pore water drainage direction, the difference in the coefficient of vertical consolidation with radial and vertical drainage is dependent only on permeability. The relationship between the two anisotropy parameters is shown graphically with RBBC data in Figure 6-16 and algebraically in Equation 6-6:

$$r_{cv} = \frac{c_{v,r}}{c_{v,v}} = \frac{\left(\frac{k_r}{m_v \gamma_w}\right)}{\left(\frac{k_v}{m_v \gamma_w}\right)} = \frac{k_r}{k_v} = r_k \qquad (6\text{-}6)$$

where:
m_v = volume compressibility
γ_w = unit weight of water

6.3.2 RBBC + 9% Montmorillonite

A 91% BBC and 9% montmorillonite (by weight) mixture is made (RBBC + 9% Mont.) and resedimented to various stresses to test permeability anisotropy inside the cubic specimen constant head permeameter. Four specimens are resedimented (see Table 6-6) and tested in order to see the effect of smectite content on permeability anisotropy. The permeability results are shown in Figure 6-17 and the permeability anisotropy results are shown in Figure 6-18. The addition of smectite pushes RBBC permeability anisotropy to a value just over two, while that of RBBC alone never reaches a value of two (Adams, 2014).

6.3.3 RGoM-EI

The permeability of resedimented Gulf of Mexico – Eugene Island mudrock (RGoM-EI) is measured in the vertical and radial horizontal directons using CRS testing, as well as cubic specimen constant head testing. Nine tests are performed using the radially-draining CRS device, nine are performed using the vertically-draining CRS device (see Table 6-5), and three are measured in the cubic specimen permeameter (see Table 6-6). Multiple CRS tests are performed using the same material and drainage direction, only with differing resolution pressure transducers, in order to separate testing noise from material behavior. Most of the specimens are compressed at a strain rate, $\dot{\varepsilon}$, of 0.3 %/hour, while one pair of specimens is compressed at 0.8 %/hour. Two specimens are tested after they are sheared to 29.5% horizontal shear strain at 0.14 MPa in a direct simple shear (DSS) device.

Permeability, k

Permeability is measured in orthagonal directions for RGoM-EI using both CRS and cubic specimen constant head testing.

CRS

Figure 6-19 shows the permeability results within the normally-consolidated region for the RGoM-EI CRS tests loaded at 0.3% per hour. The results for radially-draining and vertically-draining CRS tests follow more or less the same log-linear trend down to a porosity of about 0.45. At lower porosities, however, the radial and vertical permeability trends diverge. Significant repeatability is found within the RGoM-Ei permeability tests, just as is found in RBBC. Again, this is a consequence of the homogenization and control of specimen stress history that is possible through resedimentation. The results agree well with current theories of permeability anisotropy, where anisotropy is believed to be created through flowpath tortuosity due to increasing particle alignment with compression.

Log-linear permeability equations are fit through the test data in the same format used for RBBC (Equation 6-1), taken from Casey (2014). The γ and $k_{0.5}$ parameters are fit for RGoM-EI for both radial and vertical permeability, and can be seen in Figure 6-19. The radial and vertical log-linear regressions achieved r-squared values of 0.98 and 0.993, respectively.

Figure 6-20 and Figure 6-21 show the permeability anisotropy results within the normally-consolidated region for the RGoM-EI CRS tests. The average and standard deviations away from the average are plotted, as determined using the binning procedure described in Section 5.3.4. The average permeability anisotropy of RGoM-EI is seen to increase from about 1 to 5, as the mudrock is compressed from 0.1 to 40 MPa, corresponding to porosities transitioning from 0.6 to 0.25. These results not only show increasing permeability anisotropy due to particle alignment, but an increasing rate of increase in anisotropy, or upward concavity.

Figure 6-20 shows the permeability anisotropy equation derived from dividing the log-linear permeability equations, which is the same as Equation 6-2 for RBBC. In the figure, however, a new list of parameters is presented that are fit to the RGoM-EI CRS data. This log-linear permeability anisotropy equation fails to represent the data's upward concavity, and underpredicts permeability anisotropy at porosities below 0.38, corresponding to effective stresses greater than 4 MPa. While the log-linear permeability fits look accurate in Figure 6-19 and show good r-squared values, their locked-in linearity cannot capture the nonlinear nuances in the curves. These non-linear nuances can greatly affect permeability anisotropy, and ignoring them can amplify errors.

In order to make a more precise regression of permeability anisotropy, quadratic functions are fit to both radial and vertical permeability test data in log-linear space. The radial and vertical permeability quadratic regressions produce r-squared values of 0.98 and 0.994, respectively. A permeability anisotropy equation is derived by dividing the radial permeability equation by the vertical permeability equation. The resulting permeability anisotropy equation for RGoM-EI is shown in Figure 6-21 and below as Equation 6-7:

$$log_{10}(r_k) = 4.81(n - 0.5)^2 - 1.2(\mathrm{n} - 0.5) + log_{10}(1.18) \qquad (6\text{-}7)$$

Permeability anisotropy is represented as r_k, and 1.18 is the anisotropy value corresponding to a porosity of 0.5. This quadratic RGoM-EI permeability anisotropy equation, shown in Figure 6-21 overlaying the averaged binned permeability anisotropy data, is a better representation than the log-

linear permeability anisotropy equation. The concavity of the regression is more representative of observed material behavior at both high and low porosities.

Cubic Specimen Constant Head

Three cubic RGoM-EI specimens are tested in the cubic constant head permeameter, in order to expand the database for the material, and check the agreeability of cubic specimen permeability anisotropy data with that of the CRS testing program. The permeability results for both the horizontal and vertical flow directions are shown in Figure 6-22. The tests show isotropic conditions at high porosities, and higher horizontal than vertical permeability measurements at low porosities. Figure 6-23 shows the development of permeability anisotropy with compression, as measured from the cubic specimens. The permeability anisotropy trend measured from the cubic specimens increases with a decrease in porosity, just like the CRS trend for RGoM-EI. However, permeability anisotropy does not exceed 2, when compressed to a porosity of 0.34.

Coefficient of Vertical Consolidation, c_v

The coefficient of vertical consolidation, c_v, is measured from both the vertically and radially-draining CRS tests. Figure 6-24 plots the coefficient of vertical consolidation with radial drainage, $c_{v,r}$, and with vertical drainage, $c_{v,v}$, against porosity from the normally-consolidated portions of the tests on RGoM-EI. Excessive experimental noise is present at high porosities, making the high-porosity trend impossible to visualize. Attempts to fit equations to the data are unsuccessful, due to the large amount of noise. This is likely due in part to frequent data collection for a slow-straining test, and could be avoided in the future by taking readings every 10 minutes or so instead of every 3 minutes, as is done in this research.

In order to visualize the coefficient of vertical consolidation trends for RGoM-EI, the binned average and standard deviation from average values, as determined in Section 5.3.4, are shown in Figure 6-25. While the coefficient of vertical consolidaton with vertical drainage, $c_{v,v}$, steadily decreases with compression, the coefficient of vertical consolidation with radial drainage, $c_{v,r}$, remains more or less constant around 3 to 4 x 10^{-7} cm^2/sec. A great amount of divergence is seen at low porosities in-between the data sets. Regressions are performed on the binned average data, as they are unsuccessful on the raw data. Polynomial functions of the third order are used, in the form of Equation 6-8, to capture the curvature of the trend, especially in the coefficient of vertical consolidation with radial drainage.

$$log_{10}(c_v) = \alpha(\mathrm{n} - 0.5)^3 + \beta(n - 0.5)^2 + \chi(\mathrm{n} - 0.5) + log_{10}(c_{v,0.5}) \quad (6\text{-}8)$$

The parameters α, β, and χ describe the curvature of the trend, while $c_{v,0.5}$ represents the coefficient of vertical consolidation at a porosity of 0.5. These parameters are presented in Figure 6-25 for both the vertically- and radially-draining coefficients of vertical consolidation.

Figure 6-26 shows the coefficient of consolidation anisotropy results within the normally-consolidated region for the RGoM-EI CRS tests. The average and standard deviation away from the average are plotted. Equation 6-9 describes the anisotropy behavior, using the same parameters that are used in Equation 6-8.

$$log_{10}(r_{cv}) = (\alpha_r - \alpha_v)(n-0.5)^3 + (\beta_r - \beta_v)(n-0.5)^2 + (\chi_r - \chi_v)(\mathrm{n}-0.5) + log_{10}\left(\frac{c_{v,r,0.5}}{c_{v,v,0.5}}\right) \qquad (6\text{-}9)$$

To show the relationship between permeability anisotropy and coefficient of vertical consolidation anisotropy for RGoM-EI, the two anisotropies are plotted together in Figure 6-27. While the coefficient of vertical consolidation anisotropy does not reach quite as high as the permeability anisotropy at low porosities, the general concave-upward trends for both parameters agree quite well. The parameters are theoretically equal, as is shown in Equation 6-6.

6.3.4 Discussion of Permeability Results

The permeability results are analyzed and compared with each other and with results from Adams (2014) in this section. First, the RBBC and RGoM-EI CRS data are compared, primarily to see the effect of smectite (or high plasticity) on permeability anisotropy. The RGoM-EI and RBBC CRS data are then compared to the cubic specimen constant head data, and the applicability of both methods is discussed. We then present a compilation of cubic specimen constant head permeability tests, combining the author's data with the data from Adams (2014).

Finally, we present data for two sets of CRS permeability anisotropy tests which are run using different testing variables. The following tests are run to see how each variable affects permeability anisotropy results: one set of tests on RGoM-EI loaded at a rate of 0.8%/hour, and one set of tests on RGoM-EI specimens horizontally sheared in a direct simple shear (DSS) device prior to CRS loading.

All of these results are measured from homogeneous mudrocks. When scaled to *in-situ* formations, the presence of layering should be taken into account (see Secton 2.5.1).

Comparison of RBBC and RGoM-EI CRS Data

Figure 6-28 shows vertical and radial permeabilities for both RBBC and RGoM-EI as determined through CRS testing. Plotting the two mudrocks together shows (a) the lower permeability of RGoM-EI in general and (b) the larger change in anisotropy with compression of RGoM-EI material. Both of these phenomena are likely caused by the high amount of smectite in RGoM-EI mudrock, compared to illitic RBBC. Smectite particles have aspect ratios approximately an order of magnitude greater than illite particles (Lambe and Whitman, 1969). Thus, they are likely to form more anisotropic tortuosity in general.

While greater anisotropy in smectitic mudrocks can be explained by aspect ratios and tortuosity, the mechanism for higher anisotropy in RBBC than RGoM-EI at early stages of compression is not fully understood. It could be a result of relatively large illite particles becoming horizontally organized earlier in the compression process than small smectite particles, due to gravitational forces having slightly more impact, when compared to surfacial forces, on illite than smectite.

The same CRS permeability data are shown in the form of permeability anisotropy in Figure 6-29. The binned average permeability anisotropies of RBBC and RGoM-EI are shown in color, while the quadratic equations fit to the data are represented by the smooth black lines. The smectitic RGoM-EI anisotropy curve has a strong upward concavity to it, transitioning from isotropy to an anisotropy value of five, in an exponential manner. The RBBC anisotropy curve also increases with compression, with only a slight upward concavity, starting at about 1 ½ and increasing to 3.

Figure 6-30 shows the coefficient of vertical consolidation with vertical and radial drainage for both RBBC and RGoM-EI as determined through CRS testing. Plotting data from the two mudrocks together gives new insight on the impact of permeability anisotropy on the coefficient of consolidation. When drainage occurs vertically, the illitic RBBC coefficient of vertical consolidation remains nearly constant while the smectitic RGoM-EI coefficient of vertical consolidation decreases log-linearly during compression. When drainage occurs radially outward, the smectitic RGoM-EI coefficient of vertical consolidation remains nearly constant while the illitic RBBC coefficient of vertical consolidation increases during compression. The shift up of the radially-draining coefficient of vertical consolidation curves for both mudrocks is reflective of the shift up in radial permeability during compression when compared to

vertical. In general, the RGoM-EI coefficient of vertical consolidation is lower than that of RBBC, as it is a less permeable material.

The same CRS coefficient of consolidation data are shown in terms of coefficient of consolidation anisotropy in Figure 6-31. The coefficient of consolidation anisotropy trends are almost identical to the permeability anisotropy trends. This should be expected, since volume compressibility is independent of drainage direction (see Equation 6-6). The binned average coefficient of consolidation anisotropies of are shown in color, while the polynomial equations fit to the data are represented by smooth black lines.

To visualize how permeability anisotropy develops with burial depth, the permeability equations fit to the CRS data for RGoM-EI and RBBC are plotted against burial depth in Figure 6-32 and Figure 6-33. Assuming a homogenous, normally-consolidated sedimentation system beneath the seafloor with hydrostatic pore pressures, the porosity with depth of a mudrock can be characterized using its compression curve. The radial and vertical permeability equations are plotted for RBBC and RGoM-EI, using the calculated porosities, and are shown in Figure 6-32. Looking at the permeability trends on a linear depth scale illustrates that most of the decrease in permeability occurs at shallow depths, and less change in permeability is seen at depths beyond 1,000 meters. Figure 6-33 shows the trend in permeability anisotropy with depth, where the quadratic anisotropy equations are used to plot the curves for RBBC and RGoM-EI. For RBBC, permeability anisotropy increases significantly at shallow depths, then increases only slightly at depths below 1,000 meters. The RGoM-EI data show an almost linear increase in permeability anisotropy with depth.

Comparison of CRS Data to Cubic Specimen Constant Head Data

CRS permeability anisotropy testing is performed on the same materials that were tested by the author and Adams (2014) using cubic specimen constant head testing, in part to investigate comparability between the two measurement methods. All the RBBC cubic specimen tests presented were performed by Adams (2014), and the RGoM-EI cubic specimen tests are performed by Adams (2014) and the author (see Table 6-1).

Permeability anisotropy is a very sensitive measurement, as it seeks to determine a simple ratio of permeability, a parameter which varies over orders of magnitude during compression. The ratios also have to be matched up with porosity, a state parameter which is challenging to precisely identify. This is likely why we see a slight offset between cubic specimen constant head and CRS testing permeability values in both the vertical and horizontal directions for RBBC, as can be seen in Figure 6-34. Despite the

offset in permeability trends, the general behavior is similar. A big difference between the data sets, however, is the decrease in anisotropy at low porosities which is seen in the cubic specimen data but not in the CRS data. The decrease in RBBC anisotropy at low porosities appears to result more from lower horizontal permeability values than increasing vertical permeability values, if linear trends are extrapolated from the cubic specimen permeability data. This shift in trend can be seen more clearly in Figure 6-35, which plots RBBC permeability anisotropy as a function of porosity for both the cubic specimen constant head and CRS test methods.

Figure 6-36 plots vertical and horizontal RGoM-EI permeability data measured using cubic specimen constant head testing compared to vertical and radial horizontal data measured using CRS testing. With RGoM-EI, the vertical cubic specimen data line up nearly perfectly with the vertical CRS data. However, the radial permeability measured using cubic specimens is much lower than that measured using CRS testing. The difference in resulting permeability anisotropy can be seen in Figure 6-37, where the CRS-measured anisotropy is up to two times that from cubic specimen testing.

While cubic specimen constant head and CRS permeability anisotropy measuring techniques give similar trends for RBBC and RGoM-EI mudrocks, the differences in measurements should be discussed. The following hypotheses, among others, could be causing the measurement discrepancies:

- The cubic specimen constant head method tests permeability at an over-consolidation ratio (OCR) of four while CRS testing is performed during virgin compression. The cubic specimen data points' porosities are measured using calipers when the specimens are unloaded in a drained condition to one-fourth of their maximum load, then completely unloaded in an undrained condition. In contrast, the CRS porosities are measured using LVDTs while the specimen is under virgin compression within the CRS cell. Reloading the cubic specimens within the triaxial cell after porosity determination under atmospheric pressure could lower the measured permeabilities when related to their corresponding unloaded porosities. This effect is minimized due to the overconsolidated state of the mudrocks, but cannot be neglected.
- Cubic specimens go through an extensive trimming on all six sides before being put into the permeameter. This trimming causes isotropic disturbance, which could lead to more isotropic permeability measurements.
- The cubic specimen permeability procedure requires a lot of take down and set up within the permeameter. Although water is introduced under vacuum in the permeameter setup, pockets of air are more likely to enter the soil matrix, reducing permeability, in the cubic specimen

procedure than in the CRS procedure. The CRS procedure only has one set up, and the water is only flowed out of the specimen, greatly reducing the possibility of air pockets within the soil matrix.

- It should be noted that the cubic-specimen-measured permeability anisotropy for both RBBC and RGoM-EI mudrocks at low porosities drops significantly from the trend established at high porosities. This could be caused by pore water cavitation due to the large amount of negative pore pressure induced on these highly-compressed specimens during unloading. Pore water cavitation would disturb fabric and create more isotropy within it.
- CRS testing calculates an upper bound on permeability anisotropy. The permeability is measured using the pressure differential between the base and the top of the specimen in the vertically-draining device and the center and the circumference of the specimen in the radially-draining device. In order for the maximum excess pore pressure to be measured by the pore pressure transducer, a small amount of expansion must occur in the pore pressure lines and transducer housing, in the form of water compressibility, steel tubing expansion, transducer engagement, and O-ring expansion. The amount of expansion is reduced due to the back-pressuring procedure, but it cannot be eliminated. It will slightly lower the measured maximum excess pore pressure compared to the pressure that would develop in the sample due to a no-flow boundary alone. Although the pore pressure line is checked for leaks prior to loading, any small leak would lower the maximum excess pore pressure as well. A lower maximum excess pore pressure would cause an artificially high permeability to be calculated. This artificially high permeability is likely most pronounced in the radially-draining device, as the pore pressure line is fed by a 0.005" pinhole. When compared to the vertically-draining device, where the pore pressure line is fed by the entire base of the sample, any expansion or leak in the radially-draining system's pore pressure line would greatly affect the maximum pore pressure, thus the permeability, reading. With an artificially high radial permeability measured compared to an accurate vertical permeability measurement, artificially high permeability anisotropy could be produced.

Considering the sensitivity of permeability anisotropy measurement and the universal possibilities for measurement error (some of which are included above), the general increase in permeability anisotropy trend with compression is evident.

CRS permeability anisotropy testing is considered by the author to be a more reliable measurement of permeability anisotropy than cubic specimen constant head testing. Along with the reasons mentioned above, measuring the permeability during virgin compression essentially eliminates sampling disturbance, creating more accurate permeability measurements. The CRS permeability anisotropy measurement technique produces reproducible data with low scatter in a relatively short amount of time.

Compilation of Cubic Specimen Permeability Results

In order to get a better understanding of anisotropy behavior from the cubic specimen permeability tests, the author's tests on RGoM-EI and RBBC + 9% Mont are plotted with Adams (2014) tests. The permeability and permeability anisotropy data are combined with the vast amount of data collected by Adams (2014) in Figure 6-38 and Figure 6-39.

Figure 6-38 shows that permeability generally decreases with smectite content, or plasticity, with 39% clay RBBC being the most permeable and RGoM-EI being the least permeable. Figure 6-39 shows that permeability anisotropy generally increases with compression, and the rate of increase increases with plasticity. RSFBM and RGoM-EI are outliers in this trend, where one would expect anisotropies similar to or greater than of RBBC at low porosities, due to their higher plasticities

Effect of strain rate

CRS testing can be affected by the strain rate used, depending on the material being tested. The compression curve can shift up, shift down, or stay constant when the strain rate is changed (Gonzalez, 2000). Similarly, permeability behavior can change depending on strain rate.

All of the CRS tests on RBBC are strained at 1.4 %/hour, and all the tests on RGoM-EI are strained at 0.3 %/hour, except for CRS 1432 and 1433 (see Table 6-2). These two tests are strained at 0.8 %/hour, to investigate how strain rate affects permeability and permeability anisotropy. Figure 6-40 compares the permeabilities of the CRS tests strained at 0.8%/hour with the binned average and standard deviation permeabilities of the RGoM-EI tests strained at 0.3%/hour. The faster strain rate results in higher vertical and radial permeabilities at low porosities, and similar permeabilities at high porosities. Figure 6-41 compares the permeability anisotropy of the CRS tests strained at 0.8%/hour with the binned average and standard deviation permeablities of the RGoM-EI tests strained at 0.3%/hour. While the faster strain rate increases both the vertical and radial permeabilities at low porosities, it increases them a similar amount, resulting in similar permeability anisotropy measurements up to 10 MPa, as shown in Figure 6-41. The 0.8%/hour strain rate anisotropy value plateaus at 2.5 after 10 MPa effective stress,

however, due to even greater increase in measured vertical permeability at this point. The reason for this is unknown.

To investigate this further, the maximum excess pore pressures of the 0.8 %/hour RGoM-EI tests are plotted against a set of 0.3 %/hour tests in Figure 6-42. The faster strain rate produces high excess pore pressures earlier on in compression. Figure 6-43 shows the same data in the form of pore pressure ratios, or the ratio of maximum excess pore pressure to the total vertical stress. The higher strain rate tests create higher pore pressure ratios; however, the pore pressure ratios stay below the recommended maximum of 15% (ASTM D4186). The RBBC excess pore pressures and pore pressure ratios follow similar trends.

Two tests are insufficient to draw conclusions about the effect of strain rate on CRS permeability anisotropy measurement. More testing is merited in this area, as the discrepancies between permeability measurements using different strain rates could be indicative of a lag effect in the pore pressure lines.

Effect of shearing

While vertical compression causes soil fabric anisotropy, and is the primary mechanism considered in this research, shearing is also capable of affecting fabric anisotropy (Dewhurst et al, 1996; Terzaghi et al, 1996). Shearing can occur in nature due to phenomena such as landslides and tectonics. In order to begin exploring the effect of mudrock shearing on permeability anisotropy, a pair of specimens are sheared in a direct simple shear (DSS) device prior to testing for permeability anisotropy in the CRS consolidometers.

Two 2.6" diameter specimens are consolidated to 0.14 MPa vertical effective stress in a DSS device. The specimens are then sheared to 29.5% shear strain in an undrained condition. No visbile shear bands are observed when the specimens are removed from the apparatus. The central portion of the specimens are then cored into the 1.9" diameter CRS rings, and CRS testing for permeability anisotropy is then performed.

Figure 6-44 shows the measured vertical and radial permeability values from the tests on DSS-sheared specimens, and compares them with the binned average and standard deviation values from the non-sheared specimens. No change in permeability behavior is observed. Figure 6-45 shows the measured permeability anisotropy values from the tests on DSS-sheared specimens compared with the binned

average and standard deviation values from the non-sheared specimens. Again, no change in permeability anisotropy behavior is observed.

There are several schools of thought on shear-induced permeability anisotropy. Horizontal shearing could cause increased horizontal particle alignment and/or anisotropic micro-cracking, increasing permeability anisotropy (Daigle and Dugan, 2011; Dewhurst et al, 1996; Arch and Maltman, 1990). With the particle alignment mechanism, increased permeability anisotropy during loading beyond shearing would be observed. With anisotropic micro-cracking, permeability anisotropy would be expected initially, but the effect would be erased as compression ensues and micro-cracks are closed. The results in Figure 6-44 and Figure 6-45 show no visible effect of shearing on permeability anisotropy due to ether mechanism. More research should be done, shearing samples to greater shear strains, under higher and lower stresses, and using different mudrocks, in order to determine if and how shearing affects permeability anisotropy.

6.4 RESISTIVITY RESULTS

The flowability, or permeability, of a fluid through a soil fabric in a mudrock can be correlated to the flowability, or electrical conductivity, of an electrical current through that fabric. This is helpful because electrical resistivity is routinely measured in exploratory boreholes. Electrical conductivity itself cannot be directly correlated to permeability due to the differences in the mechanisms governing electrical currents versus those governing fluid flow (Archie, 1942). In addition, differences in salinity and mineralogy can greatly affect electrical conductivity while making little to no difference in the permeability of a fluid. Electrical conductivity anisotropy, however, can be correlated to permeability anisotropy, as the anisotropy of both parameters is governed by flowpath tortuosity.

6.4.1 Conductivity Anisotropy

The cubic specimen constant head endcaps are equipped with 4-probe resistivity measurement technology. A plate electrode on each endcap induces an electrical current through the cubic specimens, while a pin electrode, which penetrates the specimen slightly, measures the voltage drop within the cubic specimen. The resistivity is calculated from the current and voltage using Ohm's law. This is all done within the pressurized triaxial cell immediately following the permeability measurements. Resistivity anisotropy is calculated as the ratio of horizontal to vertical resistivity. Conductivity anisotropy, which is analogous to permeability anisotropy, is calculated as the inverse of resistivity anisotropy. Figure 6-44 plots the electrical conductivity anisotropy results for RGoM-EI and

RBBC + 9% Mont., tested by the author, and the results are tabulated in Table 6-6. These results are combined with Adams' (2014) results in Figure 6-45.

In Figure 6-45, conductivity anisotropy increases with compression. It follows a similar trend as permeability anisotropy, and can be explained by flowpath tortuosity anisotropy created from particle orientation due to compression. Counterintuitively, there is no definitive trend of greater conductivity anisotropy in smectitic mudrocks when compared to illitic mudrocks. This would be expected due to the larger aspect ratio of smectite particles than illite particles.

Resistivity Anisotropy, the inverse of conductivity anisotropy, can be measured *in-situ* using a down-hole triaxial resistivity tool, where a 3-dimensional electrical current is induced in the formation surrounding a borehole.

6.4.2 Correlation between Conductivity Anisotropy and Permeability Anisotropy

While the cubic specimen constant head tests produce lower permeability and conductivity anisotropies than expected for smectitic mudrocks, they produce good correlation between permeability and conductivity anisotropy. Figure 6-48 plots the two parameters against each other, using RBBC, leached RBBC, RBBC + 9% Mont., RGoM-EI, and leached RSFBM data measured by Adams (2014) and the author. A good one-to-one correlation is found between electrical conductivity anisotropy and permeability anisotropy. This suggests that, within a uniform mudrocks, *in-situ* resistivity anisotropy measurements can be used to directly infer permeability anisotropy values. It also suggests that the cubic specimen permeability measurements correctly characterize the specimens, as do the resistivity measurements.

While the one-to-one correlation is applicable to uniform mudrocks, it does not extend to layered systems. Mudrock layering greatly affects formation permeability anisotropy. While layering also affects resistivity anisotropy, the effect isn't as great as it is with permeability anisotropy. This is because permeability varies over orders of magnitude, while resistivity does not (Adams, 2014). *In-situ* resistivity anisotropy can be an indicator for permeability anisotropy in localized, homogenous, areas, but it is not applicable in a layered system.

Table 6-1: Overview of permeability and resistivity testing programs performed by Adams (2014) and Nordquist (author)

		Cubic Specimen Constant Head Permeability and Resistivity Anisotropy	CRS Permeability Anisotropy
Adams, 2014	RBBC	✓	
	RBBC leached	✓	
	39% Clay RBBC	✓	
	RSFBM	✓	
	RSFBM leached	✓	
	RGoM-EI	✓	
Nordquist	RBBC		✓
	RBBC + 9% Mont.	✓	
	RGoM-EI	✓	✓

Table 6-2: Summary of CRS tests performed

Test ID	Resedimentation ID	Mudrock	Drainage Direction	Device ID	Strain Rate, $\dot{\varepsilon}$ [%/hr]	Resedimented σ'_{max} [MPa]
CRS 1412†	RS 422-A	RBBC	radial	TR2 - radial base	1.4	0.1
CRS 1413†	RS 422-B	RBBC	radial	TR2 - radial base	1.4	0.1
CRS 1414†	RS 422-C	RBBC	radial	TR2 - radial base	1.4	0.1
CRS 1415†	RS 421-A	RBBC	radial	TR2 - radial base	1.4	0.1
CRS 1416	RS 421-B	RBBC	radial	TR4 - radial base	1.4	0.1
CRS 1417	RS 421-C	RBBC	radial	TR4 - radial base	1.4	0.1
CRS 1418	RS 426-A	RBBC	radial	TR4 - radial base	1.4	0.1
CRS 1419‡	RS 426-B	RBBC	vertical	TR5	1.4	0.1
CRS 1420	RS 426-C	RBBC	radial	TR4 - radial base	1.4	0.1
CRS 1421	RS 426-D	RBBC	vertical	TR5	1.4	0.1
CRS 1422	RS 425-A	RBBC	radial	TR4 - radial base	1.4	0.1
CRS 1423	RS 425-B	RBBC	vertical	TR5	1.4	0.1
CRS 1424	RS 425-C	RBBC	radial	TR4 - radial base	1.4	0.1
CRS 1425	RS 425-D	RBBC	vertical	TR5	1.4	0.1
CRS 1426	RS 431-A	RGoM-EI	radial	TR4 - radial base	0.3	0.1
CRS 1427	RS 431-B	RGoM-EI	vertical	TR5	0.3	0.1
CRS 1428	RS 431-C	RGoM-EI	radial	TR4 - radial base	0.3	0.1
CRS 1429	RS 431-D	RGoM-EI	vertical	TR5	0.3	0.1
CRS 1430	RS 432-A	RGoM-EI	radial	TR4 - radial base	0.3	0.1
CRS 1431	RS 432-B	RGoM-EI	vertical	TR5	0.3	0.1
CRS 1432	RS 432-C	RGoM-EI	radial	TR4 - radial base	0.8	0.1
CRS 1433	RS 432-D	RGoM-EI	vertical	TR5	0.8	0.1
CRS 1435	RS 436-A	RGoM-EI	radial	TR4 - radial base	0.3	0.14*
CRS 1436	RS 436-B	RGoM-EI	vertical	TR5	0.3	0.14*
CRS 1437	RS 433-A	RGoM-EI	radial	TR4 - radial base	0.3	0.1
CRS 1438	RS 433-B	RGoM-EI	vertical	TR5	0.3	0.1
CRS 1439	RS 433-C	RGoM-EI	radial	TR4 - radial base	0.3	0.1
CRS 1440	RS 433-D	RGoM-EI	vertical	TR5	0.3	0.1
CRS 1441	RS 434-A	RGoM-EI	radial	TR4 - radial base	0.3	0.1
CRS 1442	RS 434-B	RGoM-EI	vertical	TR5	0.3	0.1
CRS 1443	RS 434-C	RGoM-EI	radial	TR4 - radial base	0.3	0.1
CRS 1444	RS 434-D	RGoM-EI	vertical	TR5	0.3	0.1

*These tests were sheared in direct simple shear prior to testing.

†These tests were performed as part of the radially-draining CRS cell development

‡This tests ha d an apparatus compressibility error

Table 6-3: Summary of cubic specimen constant head tests performed

Test ID	Resedimentation ID	Mudrock	Resedimented σ'_{max} [Mpa]	Porosity, n
HC 054	RS 371	RBBC + 9% Mont.	9.51	0.370
HC 055	RS 384	RBBC + 9% Mont.	3.19	0.416
HC 056	RS 417	RBBC + 9% Mont.	6.27	0.391
HC 057	RS 416	RBBC + 9% Mont.	0.78	0.480
HC 058	RS 307	RGoM_EI	0.10	0.560
HC 059	RS 418	RGoM_EI	9.68	0.355
HC 060	RS 419	RGoM_EI	6.27	0.379

Table 6-4: The RBBC compression data show specimen swelling from initial caliper porosity measurement to initial LVDT measurement within the CRS cell and from final LVDT measurement to final caliper measurement. LVDT-calculated porosities are used for plotting, due to direct applicability.

Test ID	Drainage Direction	Resedimented σ'_{max} [MPa]	CRS Curve from Compression σ'_p [Mpa]	CRS During Testing σ'_{max} [Mpa]	Porosity, n			
					Initial (calipers)	Initial (LVDTs)	Final (LVDTs)	Final (calipers)
CRS 1416	radial	0.1	0.042	34.9	0.584	0.587	0.267	0.319
CRS 1417	radial	0.1	0.061	37.0	0.544	0.544	0.208	0.270
CRS 1418	radial	0.1	0.042	35.0	0.575	0.585	0.269	0.313
CRS 1419*	vertical	0.1	0.088	9.0	0.569	0.582	0.356	0.392
CRS 1420	radial	0.1	0.063	36.0	0.565	0.576	0.268	0.312
CRS 1421	vertical	0.1	0.095	50.6	0.552	0.557	0.245	0.320
CRS 1422	radial	0.1	0.041	35.0	0.578	0.588	0.273	0.313
CRS 1423	vertical	0.1	0.068	45.2	0.569	0.575	0.255	0.324
CRS 1424	radial	0.1	0.057	35.9	0.567	0.575	0.269	0.315
CRS 1425	vertical	0.1	0.083	45.0	0.561	0.609	0.250	0.320

*rolling diaphragm seal was used (lower stress capacity than U-shaped O-ring seal)

Table 6-5: The RGoM-EI compression data show specimen swelling from initial caliper porosity measurement to initial LVDT measurement within the CRS cell and from final LVDT measurement to final caliper measurement. LVDT-calculated porosities are used for plotting, due to direct applicability.

Test ID	Drainage Direction	Resedimented σ'_{max} [MPa]	CRS Curve σ'_p from Compression [Mpa]	CRS σ'_{max} During Testing [Mpa]	Porosity, n			
					Initial (calipers)	Initial (LVDTs)	Final (LVDTs)	Final (calipers)
CRS 1426	radial	0.1	0.026	33.0	0.628	0.656	0.258	0.299
CRS 1427	vertical	0.1	0.046	22.6	0.628	0.654	0.282	0.320
CRS 1428	radial	0.1	0.042	20.9	0.616	0.647	0.279	0.303
CRS 1429	vertical	0.1	0.054	43.4	0.603	0.637	0.246	0.285
CRS 1430	radial	0.1	0.036	36.7	0.629	0.654	0.246	0.269
CRS 1431	vertical	0.1	0.039	46.7	0.625	0.656	0.236	0.280
CRS 1432	radial	0.1	0.044	24.2	0.633	0.643	0.276	0.294
CRS 1433	vertical	0.1	0.058	17.1	0.617	0.634	0.283	0.323
CRS 1435*	radial	0.14	0.117	37.2	0.574	0.590	0.251	0.284
CRS 1436*	vertical	0.14	0.132	37.2	0.567	0.588	0.254	0.306
CRS 1437	radial	0.1	0.039	3.4	0.634	0.646	0.384	0.399
CRS 1438	vertical	0.1	0.050	3.4	0.623	0.636	0.380	0.397
CRS 1439	radial	0.1	0.045	4.7	0.618	0.631	0.369	0.388
CRS 1440	vertical	0.1	0.080	5.8	0.600	0.621	0.364	0.388
CRS 1441	radial	0.1	0.037	3.6	0.638	0.648	0.381	0.395
CRS 1442	vertical	0.1	0.046	3.9	0.626	0.640	0.382	0.412
CRS 1443	radial	0.1	0.056	4.5	0.609	0.627	0.369	0.379
CRS 1444	vertical	0.1	0.079	4.9	0.592	0.615	0.369	0.394

*sheared in direct simple shear prior to loading

Table 6-6: Results of permeability and conductivity anisotropy data measured using the cubic specimen constant head technique.

Test ID	Material	Resedimented σ'_{max} [MPa]	Porosity, n	Permeability, k [m^2]		Permeability anisotropy, r_k	Electrical Resistivity, ρ [Ωm]		Resistivity Anisotropy, r_ρ	Conductivity Anisotropy, r_σ
				Horizontal	Radial		Horizontal	Radial		
HC054	RBBC + 9% Mont.	9.51	0.370	1.93E-18	9.07E-19	2.13	1.45	2.82	0.51	1.95
HC055	RBBC + 9% Mont.	3.19	0.416	5.58E-18	2.68E-18	2.08	1.38	2.58	0.54	1.87
HC056	RBBC + 9% Mont.	6.27	0.391	3.09E-18	1.45E-18	2.14	1.63	3.39	0.48	2.07
HC057	RBBC + 9% Mont.	0.78	0.480	1.65E-17	9.66E-18	1.71	1.12	1.80	0.62	1.61
HC058	RGoM_EI	0.1	0.560	3.59E-17	3.60E-17	1.00	0.40	0.43	0.92	1.09
HC059	RGoM_EI	9.68	0.355	1.85E-19	1.11E-19	1.66	0.60	0.96	0.63	1.60
HC060	RGoM_EI	6.27	0.379	2.84E-19	2.02E-19	1.40	0.64	0.98	0.66	1.52

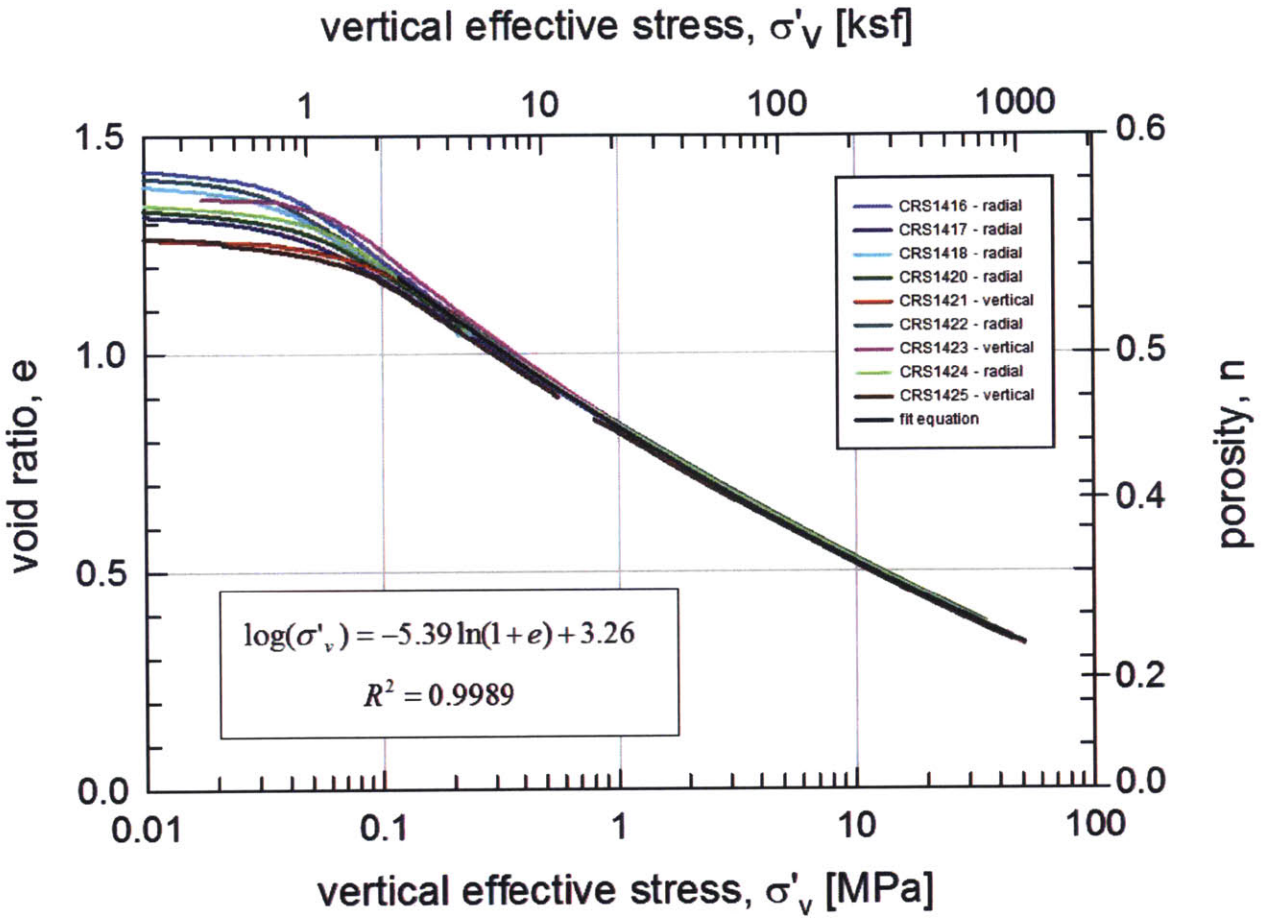

Figure 6-1: The CRS-derived compression curves for RBBC with both radial and vertical drainage show similarity and repeatability. The equation is fit for the data between 0.1 and 40 MPa of vertical effective stress.

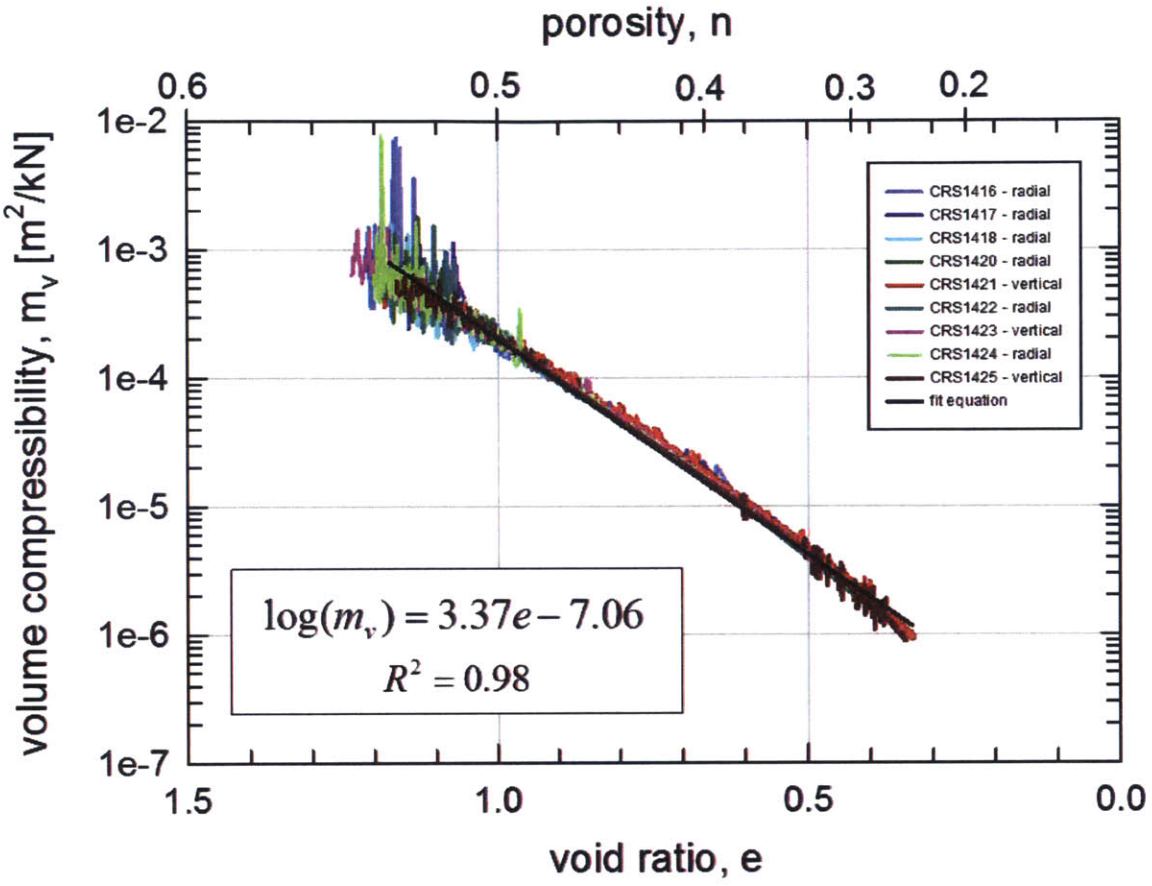

Figure 6-2: The CRS-derived volume compressibility for RBBC with both radial and vertical drainage show similarity and repeatability. The log-linear equation is fit for the semi-log-linear data between 0.1 and 40 MPa of vertical effective stress.

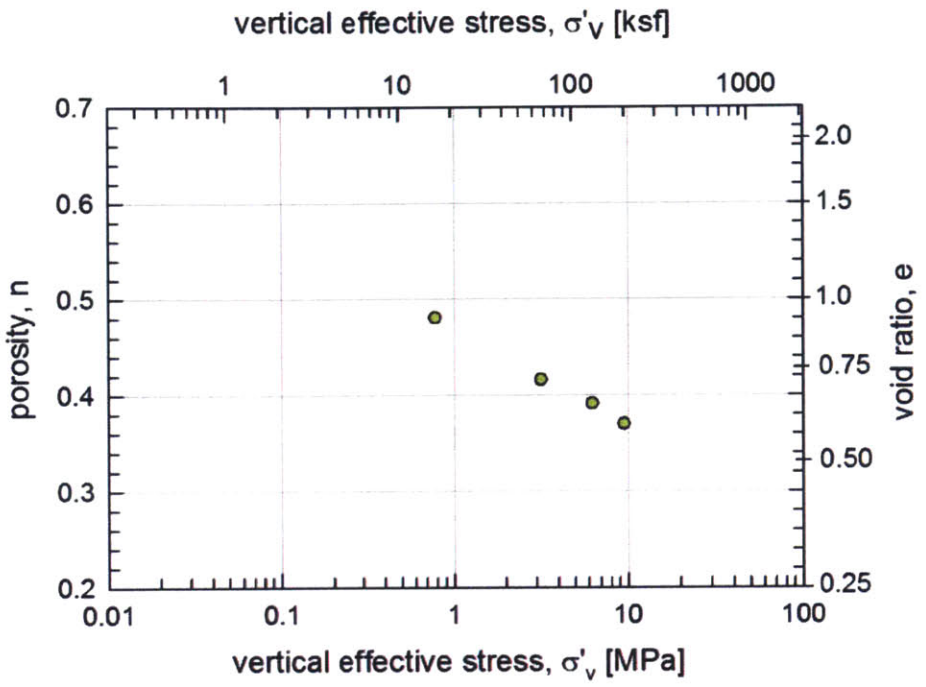

Figure 6-3: The preconsolidation stress plotted against OCR =4 porosity of RBBC + 9% Mont. cubic specimens shows a monotonic compression trend.

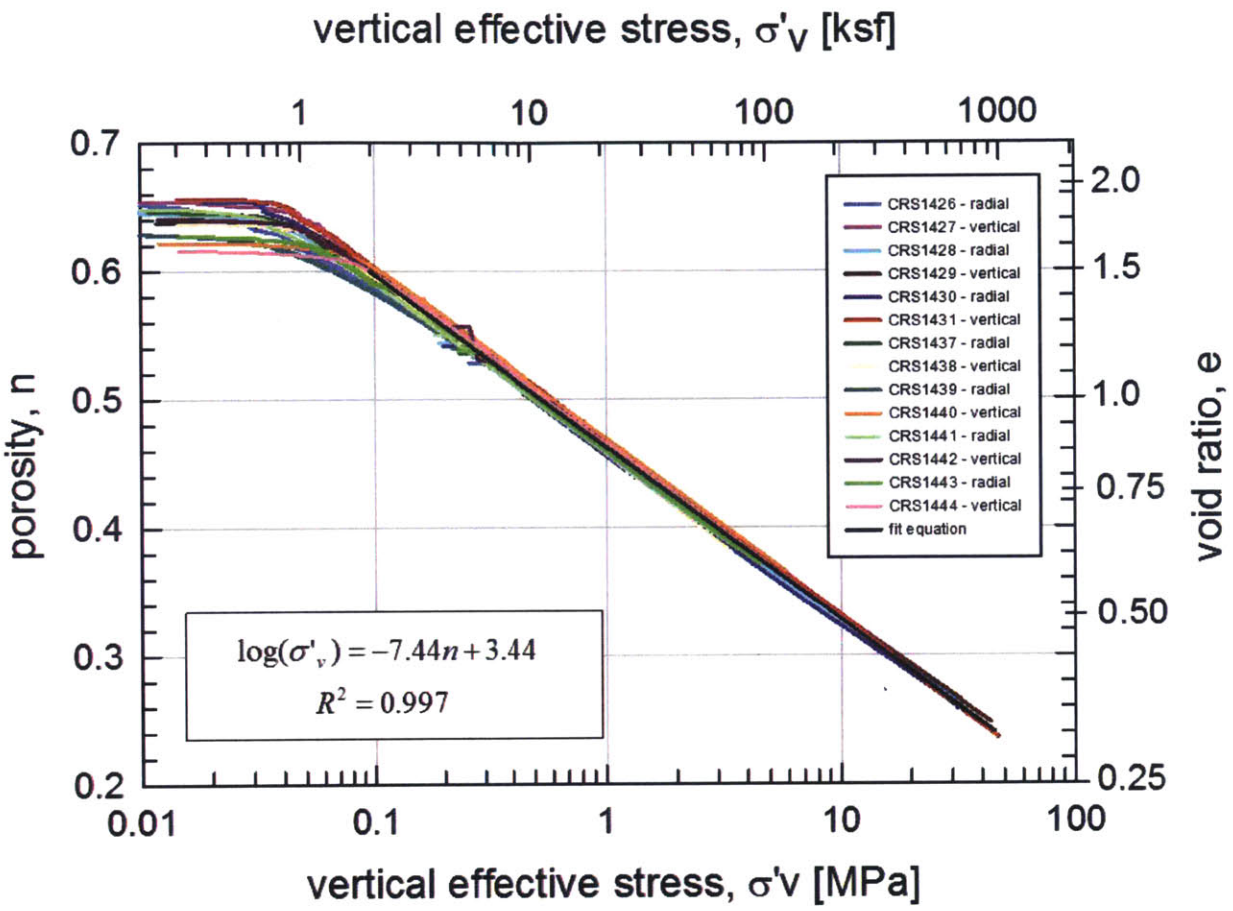

Figure 6-4: The CRS-derived compression curves for RGoM-EI with both radial and vertical drainage show similarity and repeatability. The equation is fit for the data between 0.1 and 40 MPa of vertical effective stress.

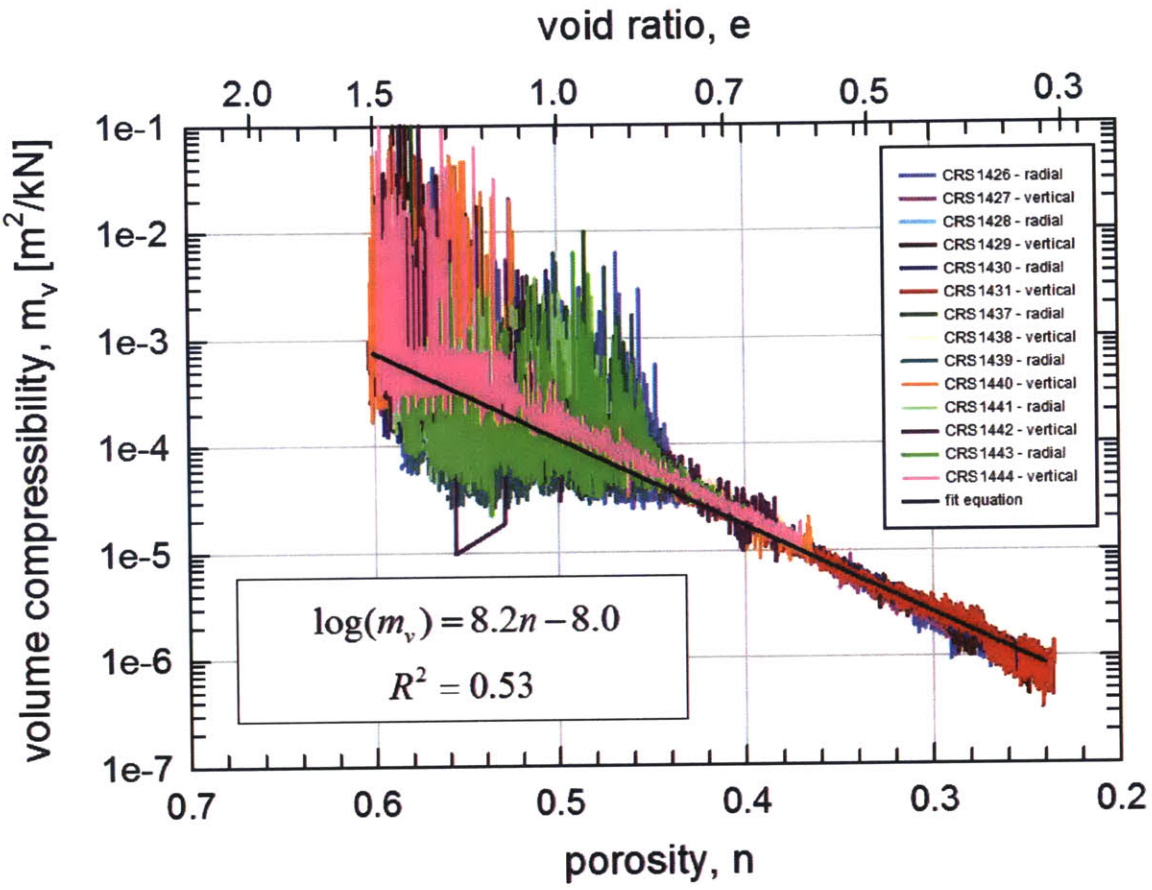

Figure 6-5: The CRS-derived volume compressibility for RGoM-EI with both radial and vertical drainage show similarity but a lot of noise. The equation is fit for the data between 0.1 and 40 MPa of vertical effective stress.

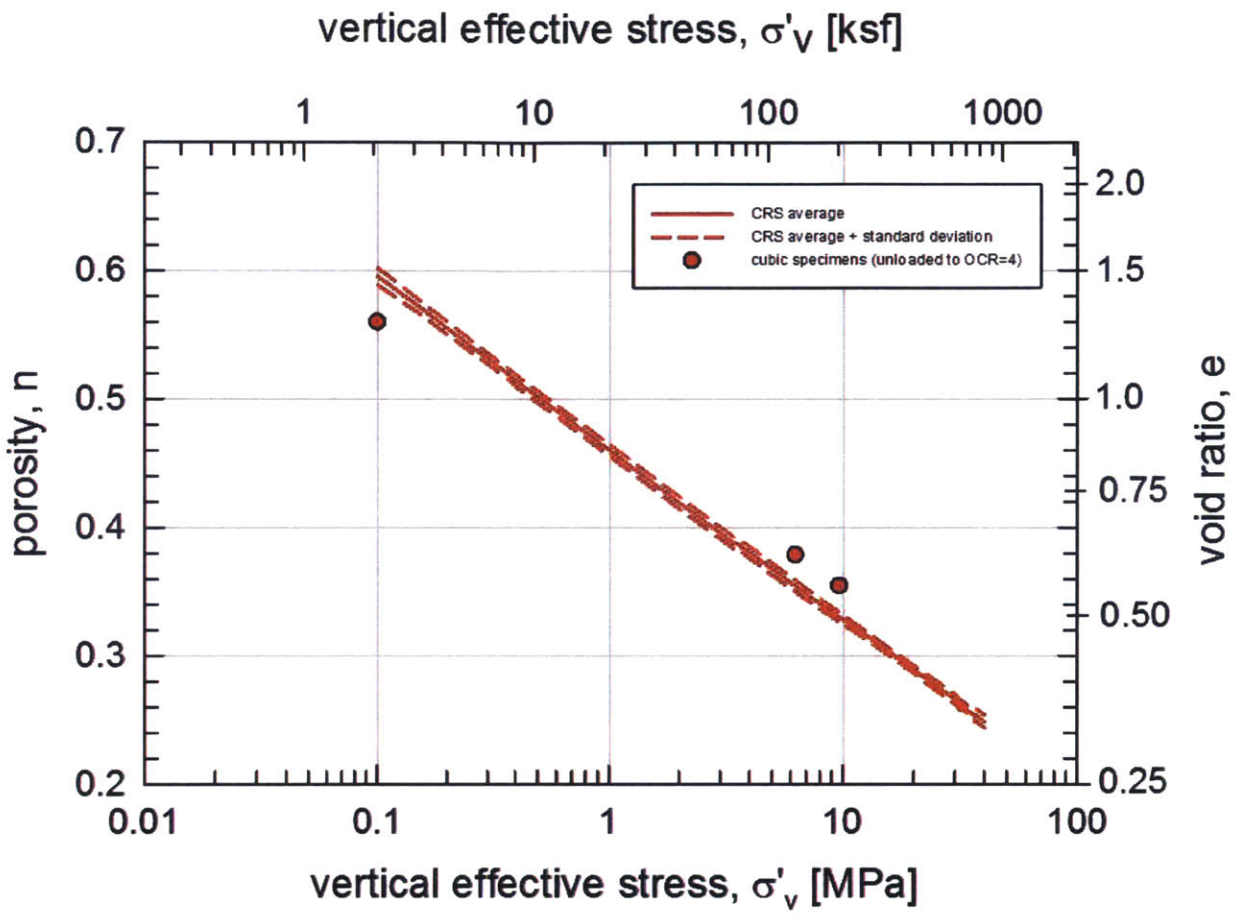

Figure 6-6: The RGoM-EI cubic specimens, unloaded to an OCR of 4, should result in slightly higher porosities than the virgin compression line when plotting preconsolidation stress against measured porosity.

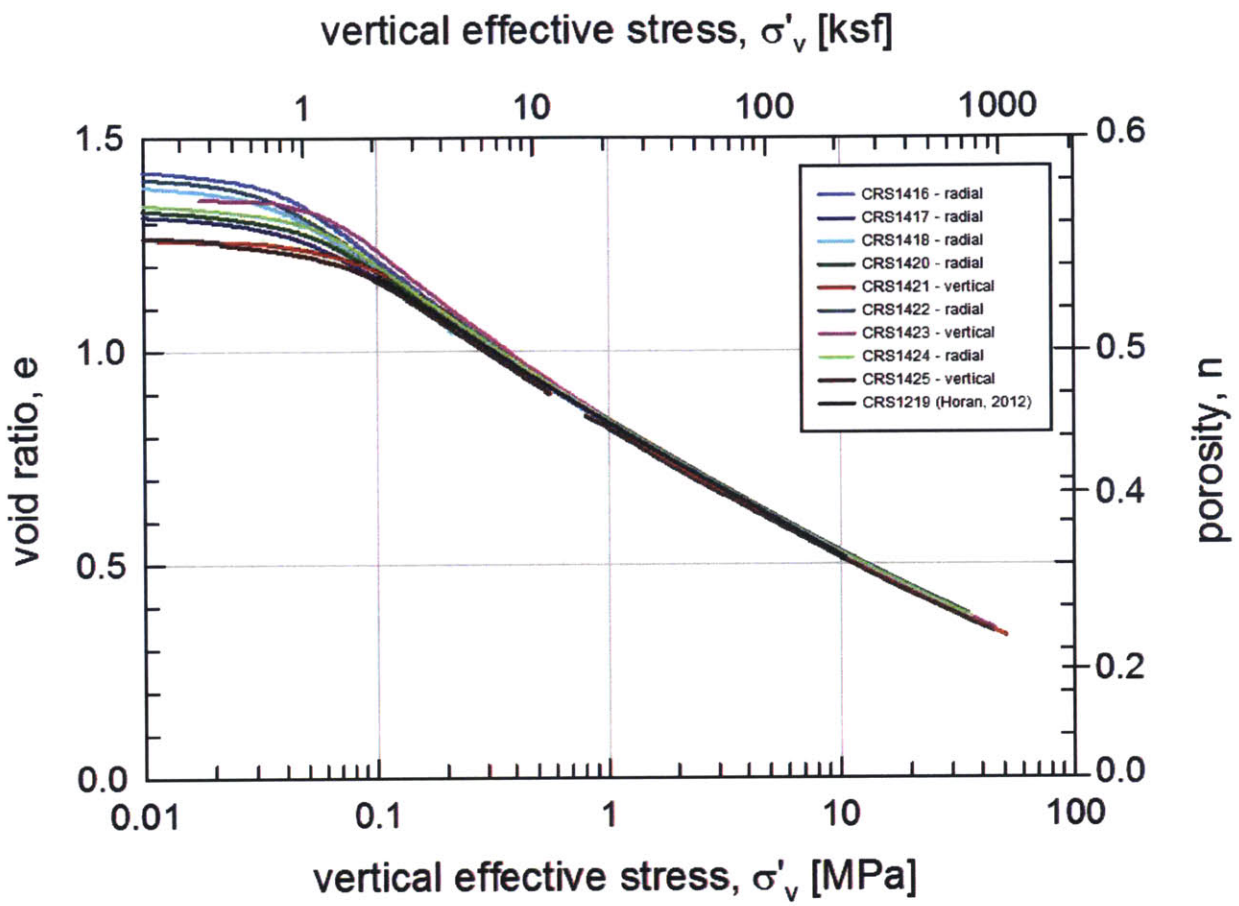

Figure 6-7: The author's CRS compression data for RBBC agrees well with Horan's (2012) compression curve for the same material.

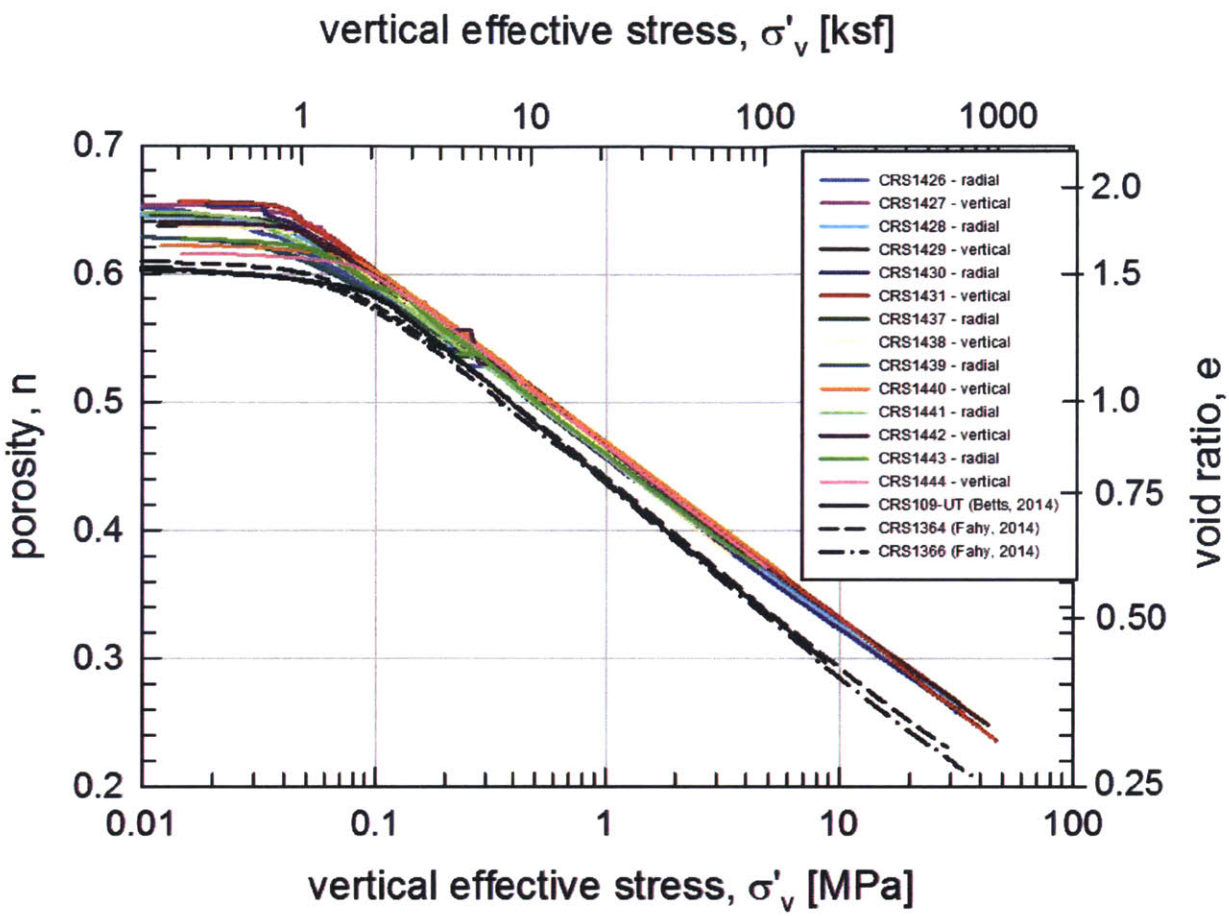

Figure 6-8: The author's CRS compression data for RGoM-EI is slightly offset from compression curves for the same material measured by Betts (2012) and Fahy (2014).

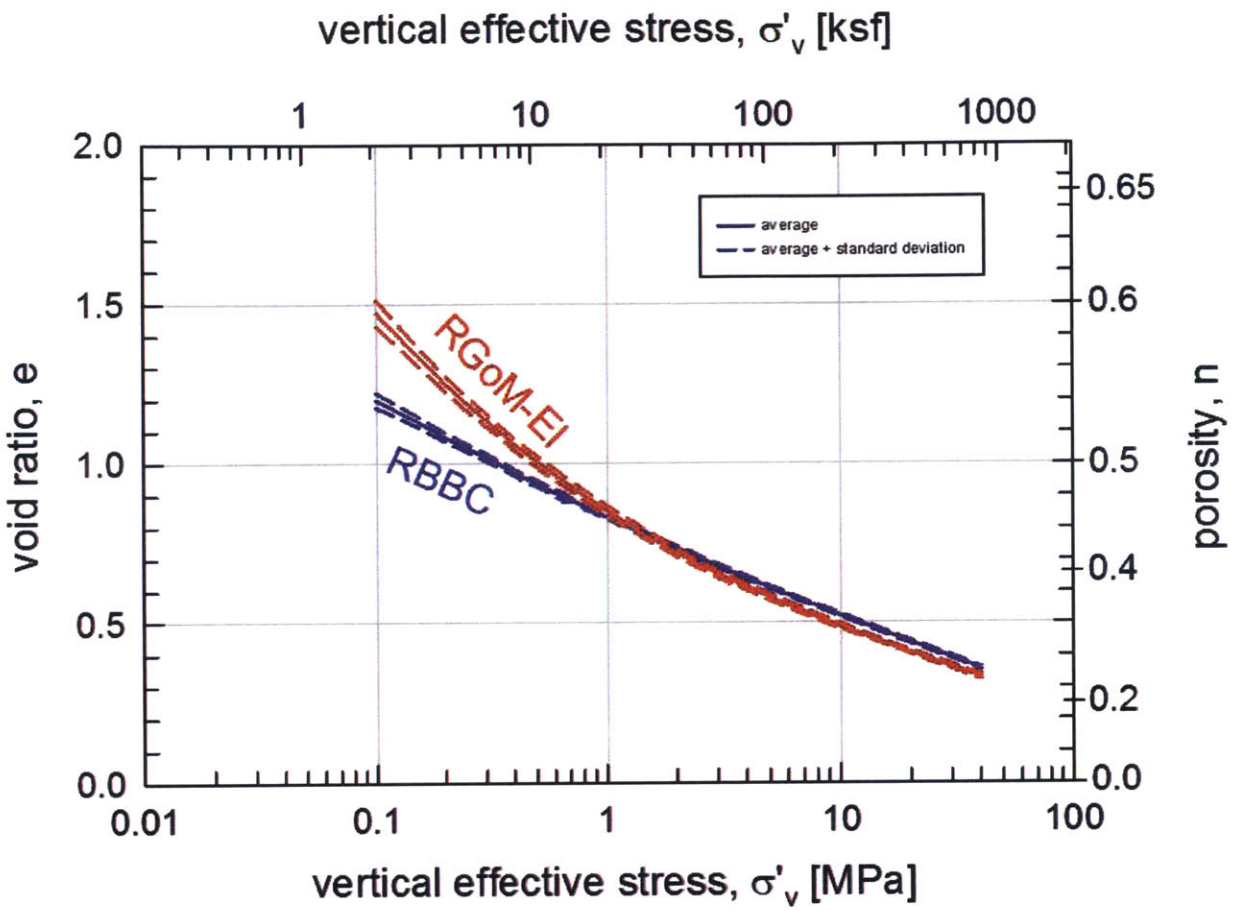

Figure 6-9: Comparing the averaged CRS compression curves shows that RGoM-EI is a more compressible mudrock than RBBC, which is due to its high smectite content. RBBC compresses nearly linearly in e – log(σ) space, while RGoM-EI compresses nearly linearly in n – log(σ) space.

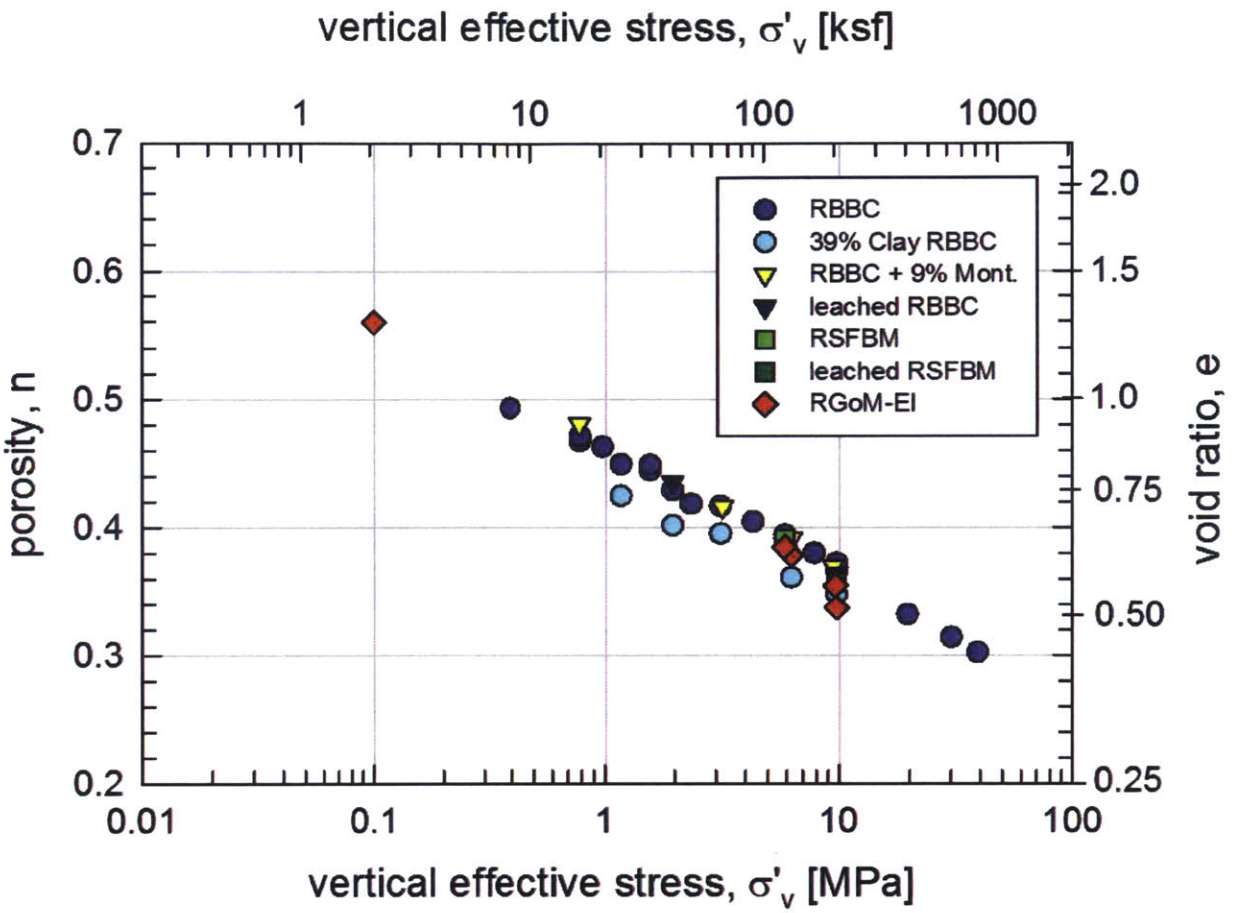

Figure 6-10: Plotting caliper-measured porosities at an OCR = 4 with preconsolidation stresses for cubic specimen constant head tests performed by the author and Adams (2014) shows nearly linear compression curves for the mudrocks tested.

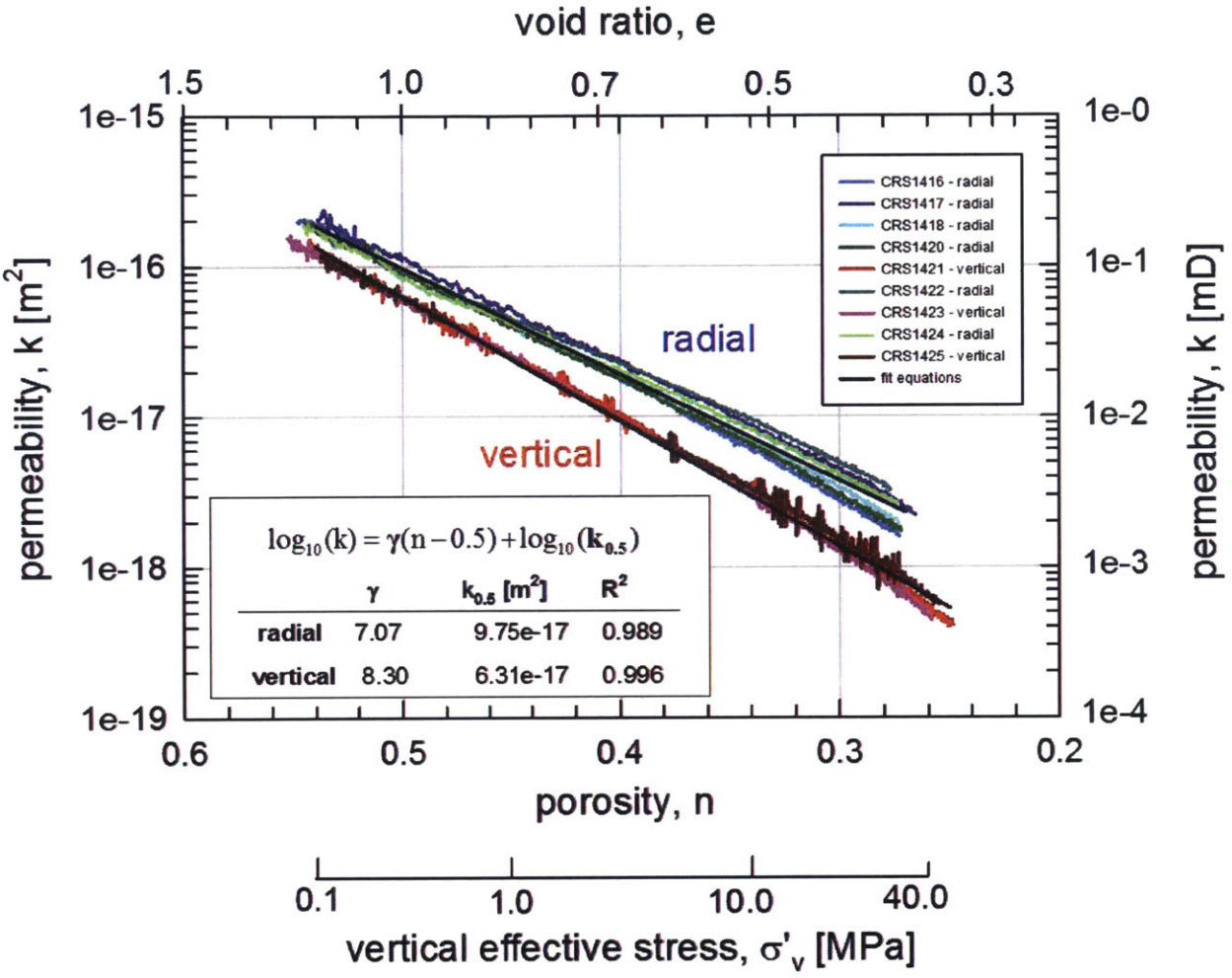

Figure 6-11: RBBC vertical and radial permeability, measured using CRS testing, decrease and diverge with compression. The results from nine tests show significant repeatability.

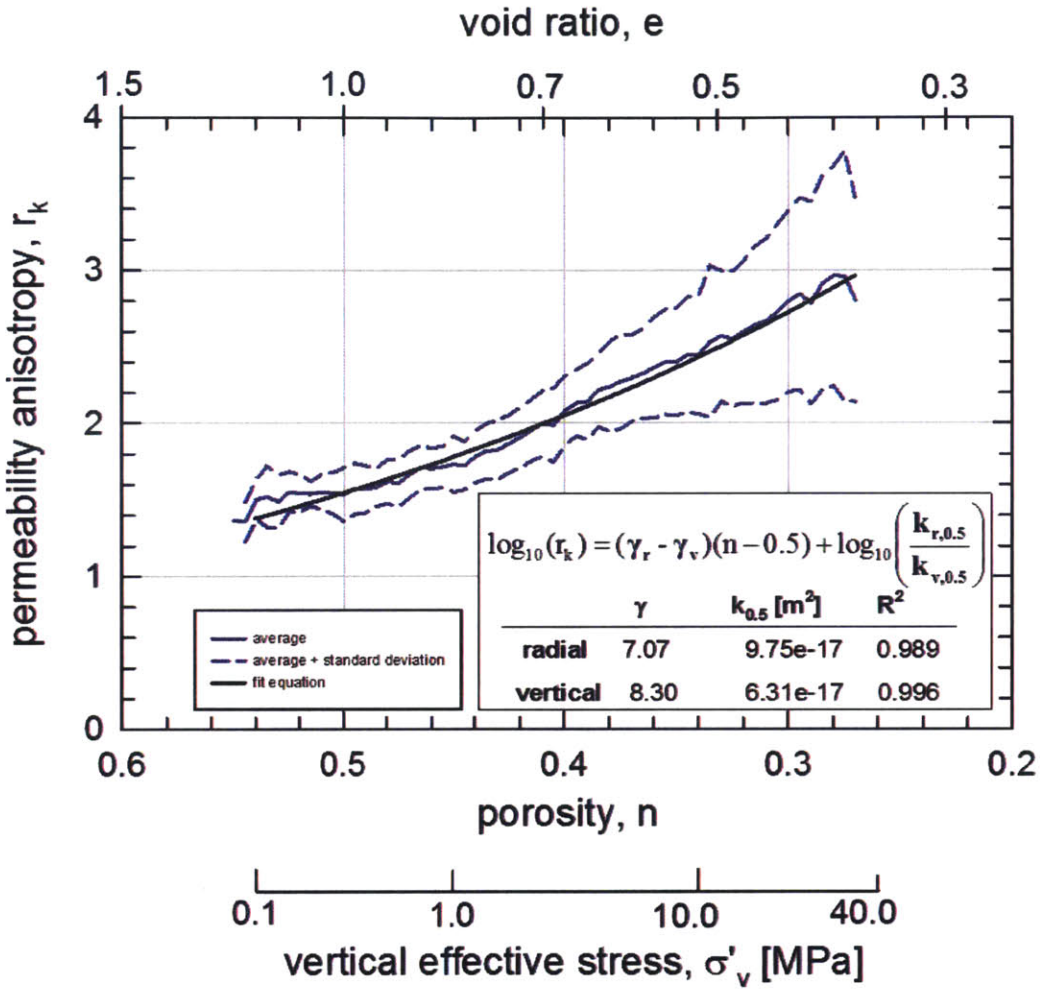

Figure 6-12: RBBC permeability anisotropy, measured using CRS testing, increases from ~1.5 to ~3 during compression. The regression equation for permeability anisotropy is derived from the log-linear permeability regression equations.

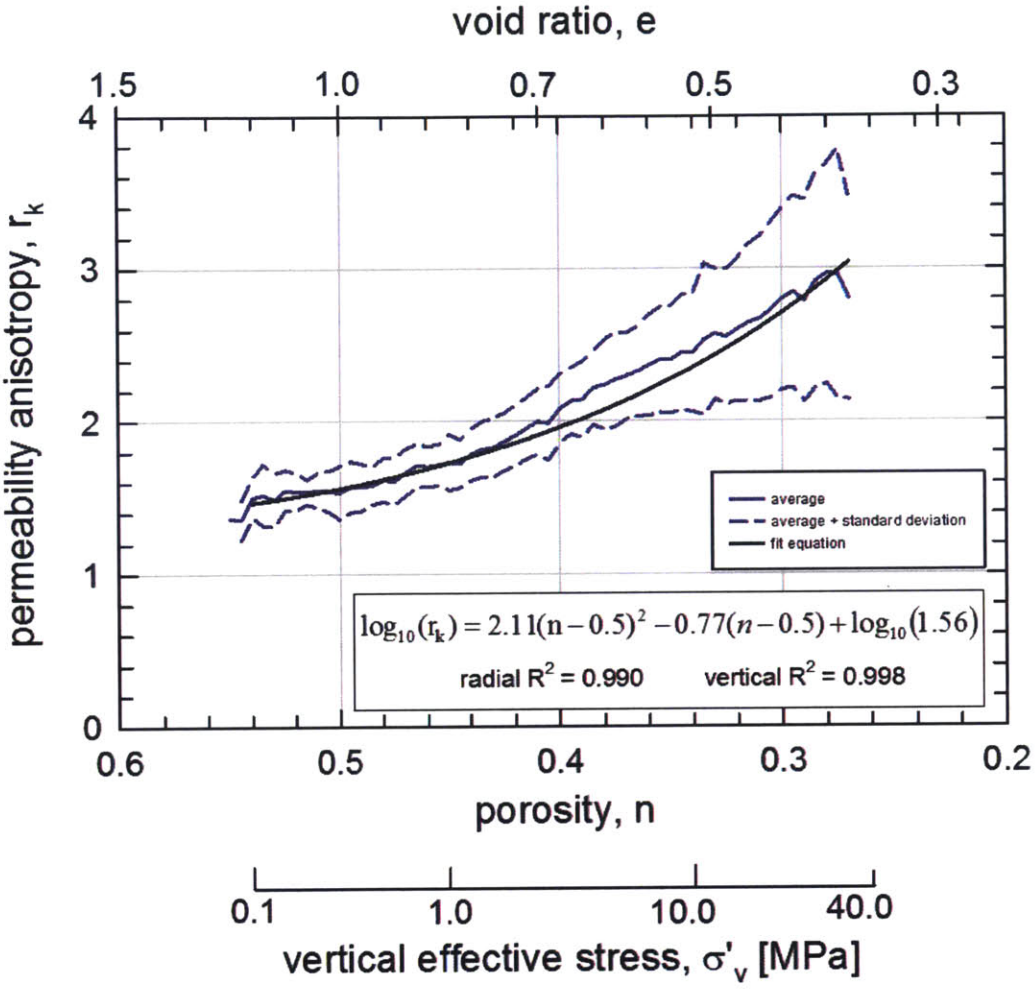

Figure 6-13: RBBC permeability anisotropy, measured using CRS testing, increases from ~1.5 to ~3 during compression. The regression equation for permeability anisotropy is derived from log-linear quadratic permeability regression equations.

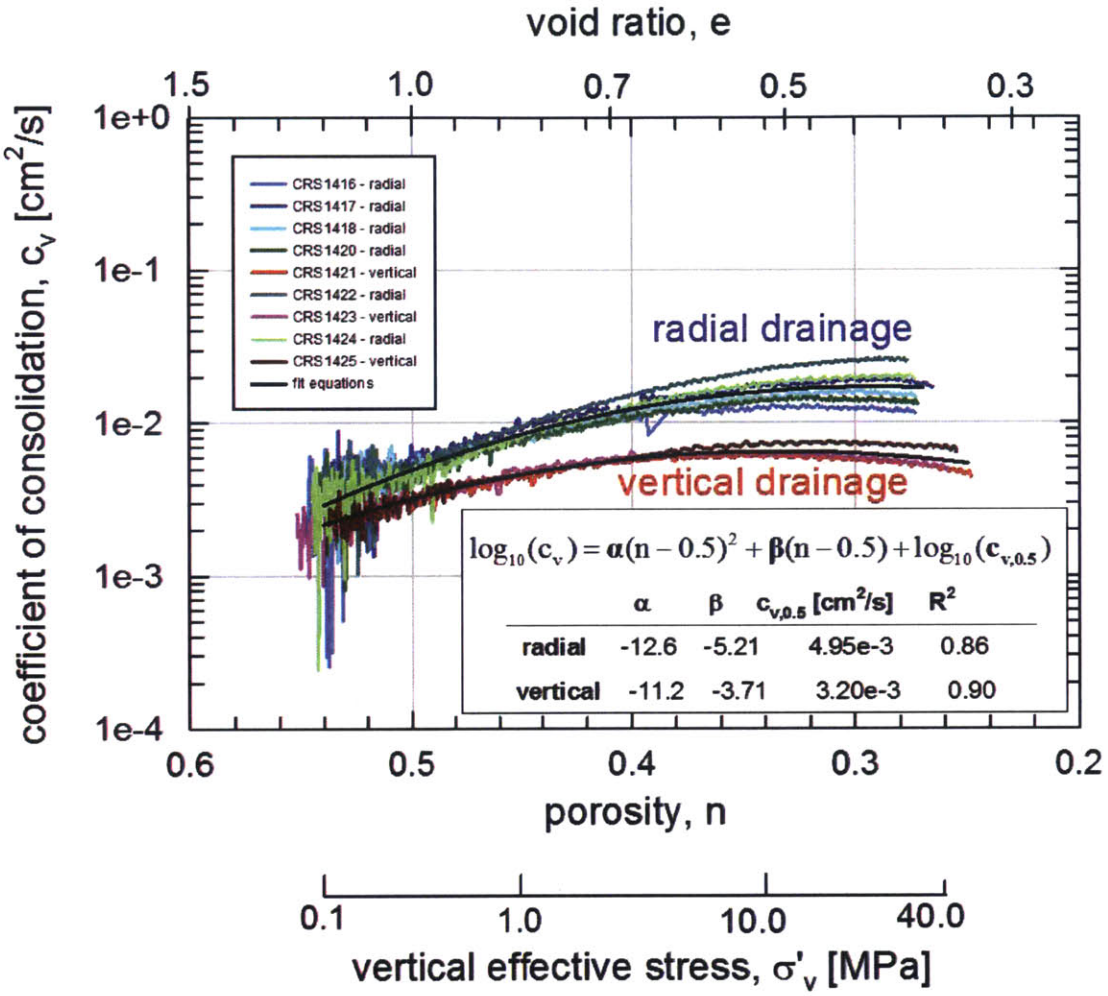

Figure 6-14: RBBC coefficient of vertical consolidation with vertical and radial drainage, measured using CRS testing, stays roughly constant but diverges with compression.

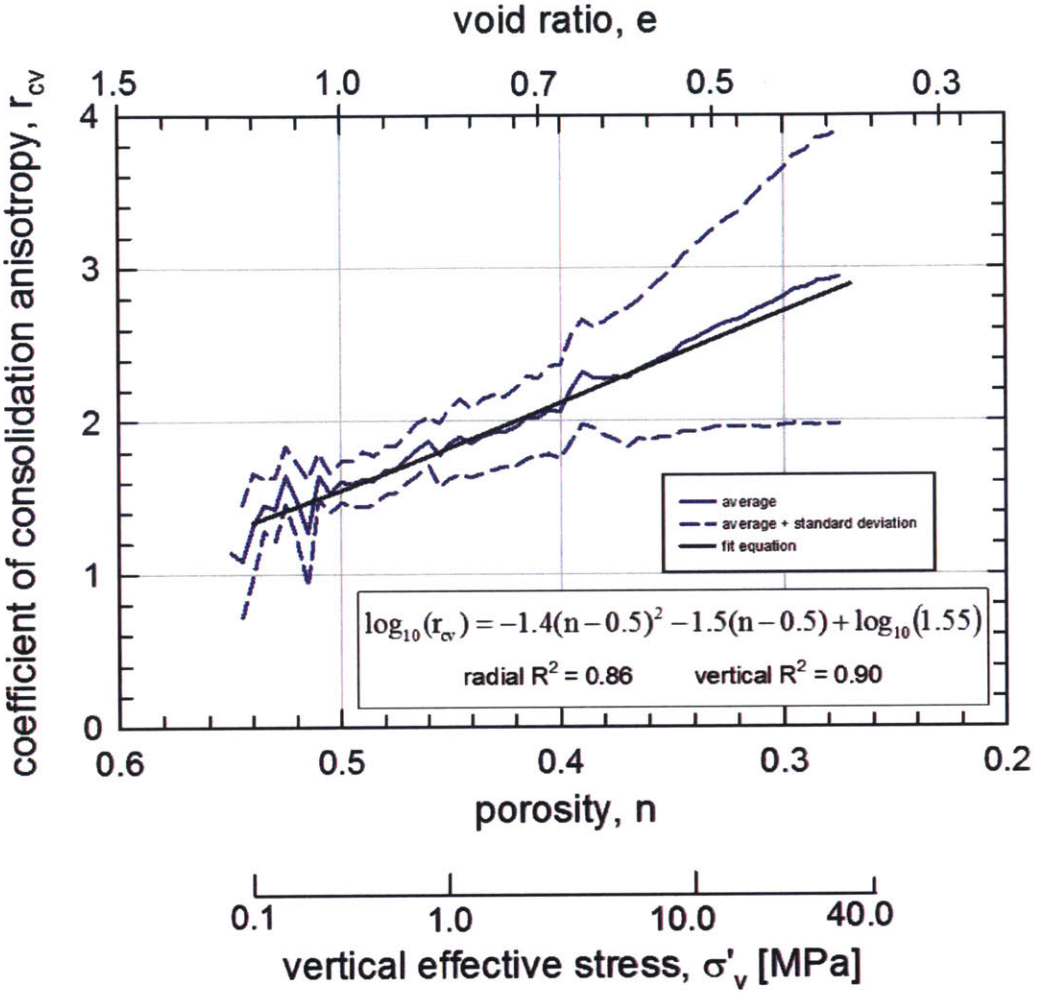

Figure 6-15: RBBC coefficient of consolidation anisotropy, measured using CRS testing, increases from ~1.5 to ~3 during compression. The regression equation for permeability anisotropy is derived from log-quadratic permeability regression equations.

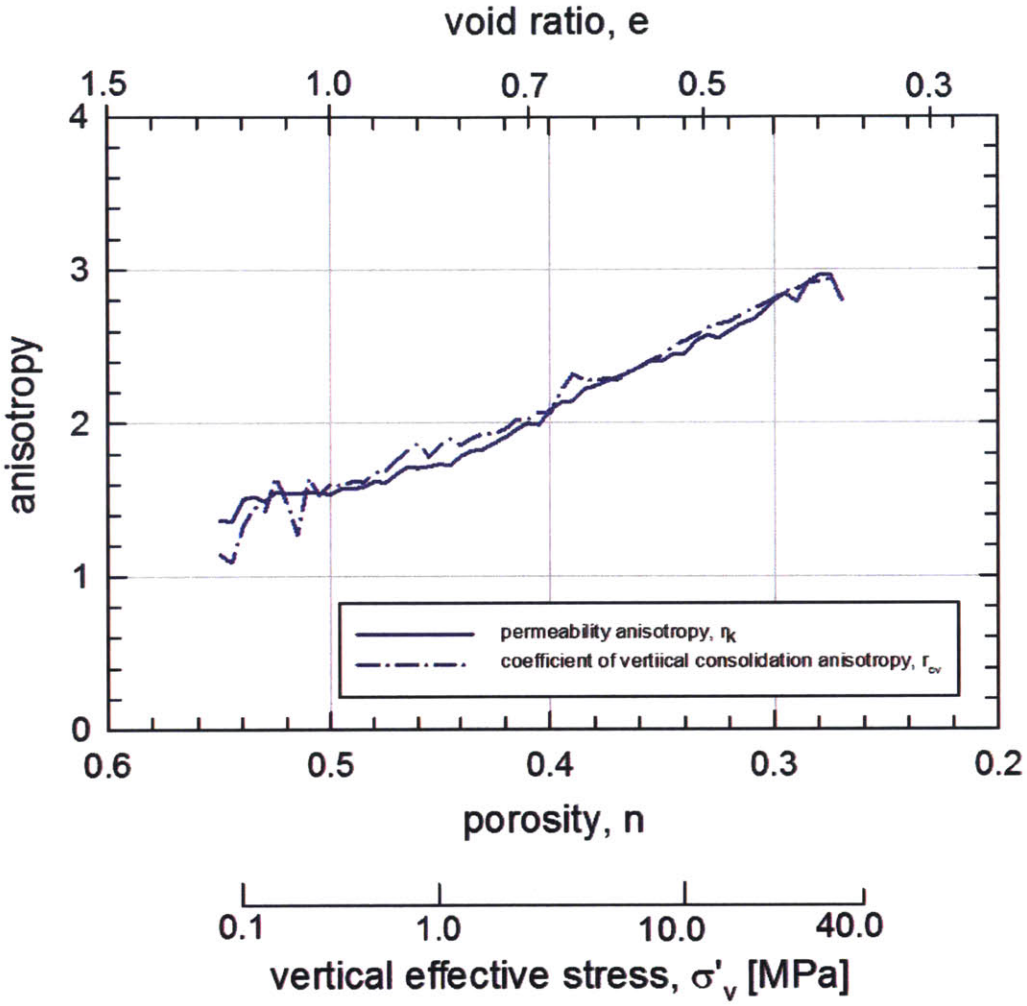

Figure 6-16: Comparing RBBC's CRS-measured permeability anisotropy to coefficient of vertical consolidation anisotropy shows that the parameters are the same.

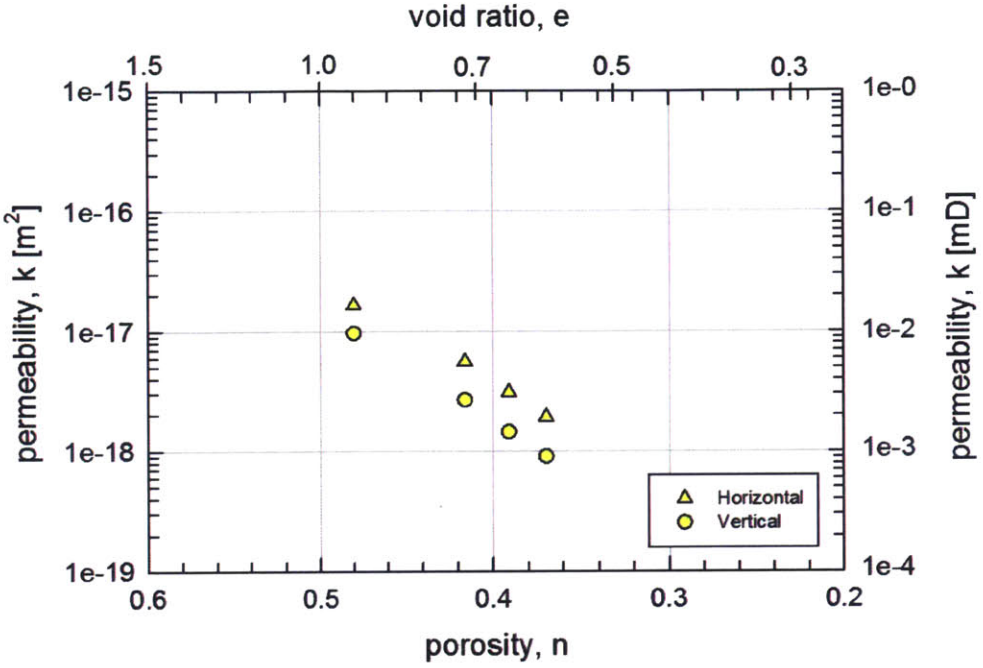

Figure 6-17: RBBC + 9% Mont. produced fairly anisotropic permeability results using cubic specimen constant head testing.

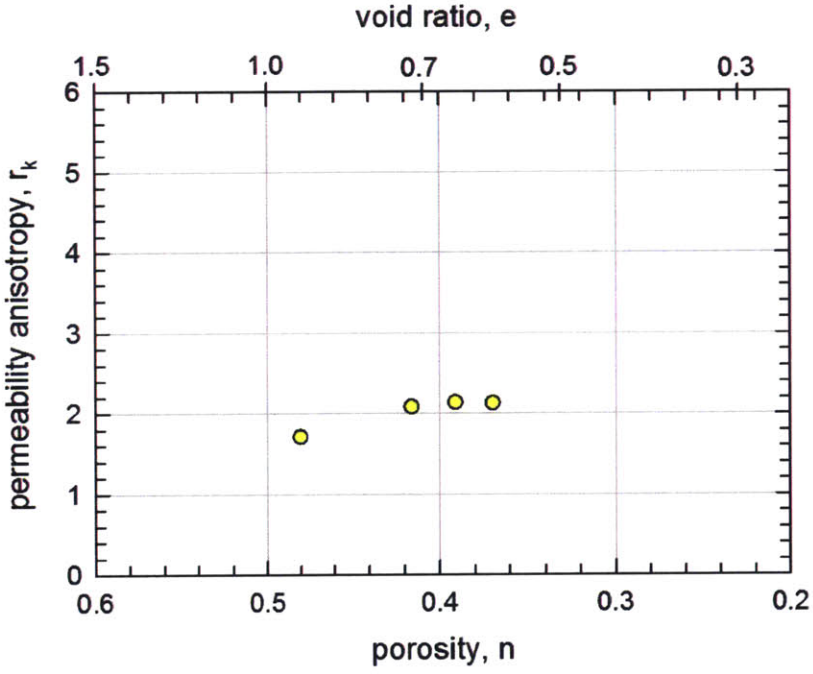

Figure 6-18: RBBC + 9% Mont. tested in the cubic specimen permeameter show permeability anisotropy reaching greater than 2.

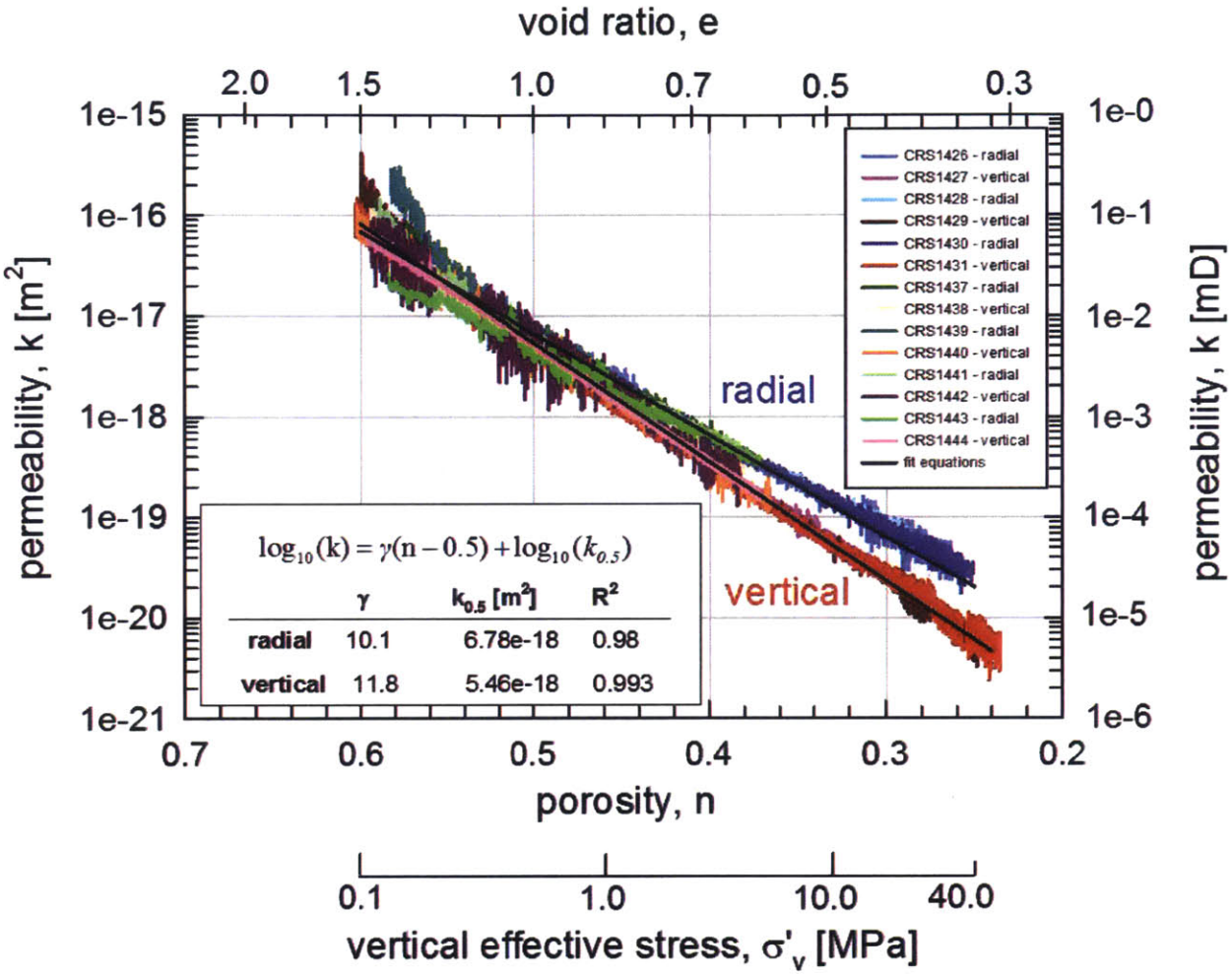

Figure 6-19: RGoM-EI vertical and radial permeability, measured using CRS testing, decrease and diverge with compression. The results from fourteen tests show significant repeatability.

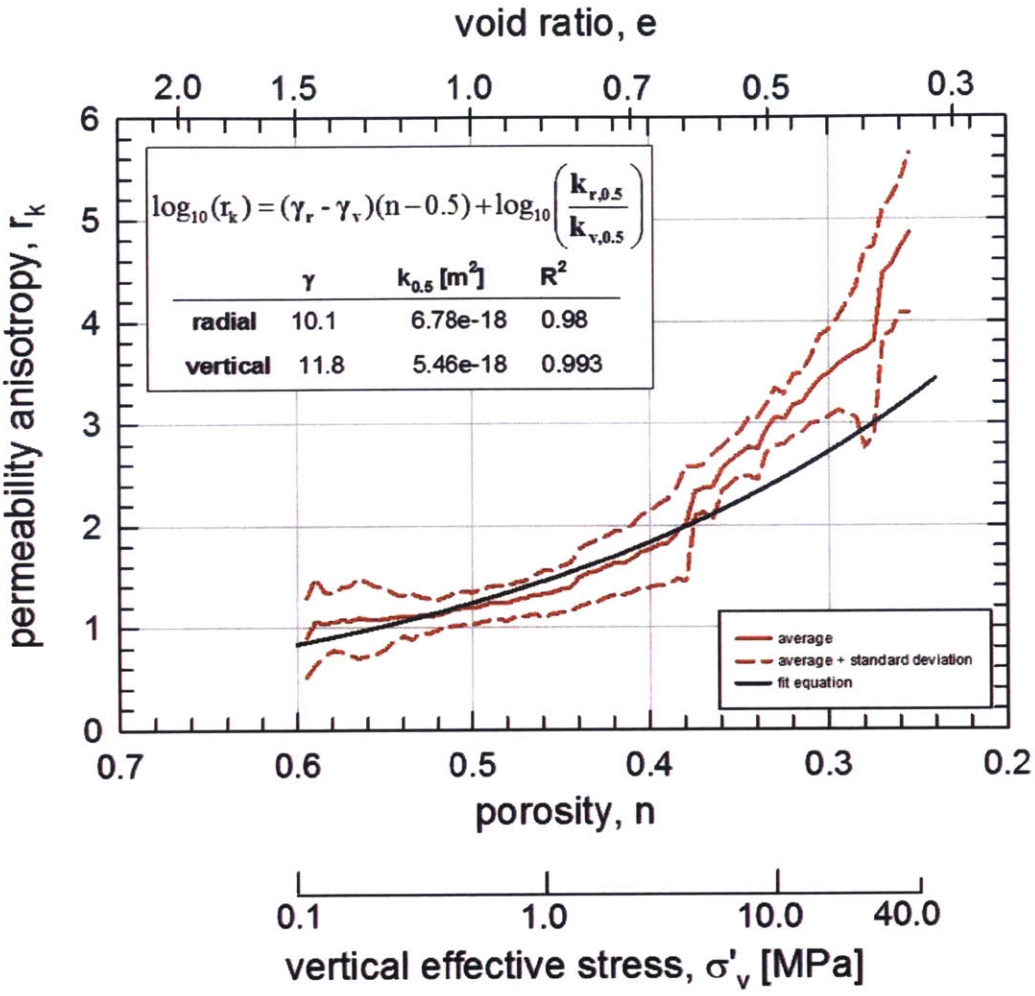

Figure 6-20: RGoM-EI permeability anisotropy, measured using CRS testing, increases from ~1 to ~5 during compression. The regression equation for permeability anisotropy is derived from the log-linear permeability regression equations, and underpredicts anisotropy at low porosities

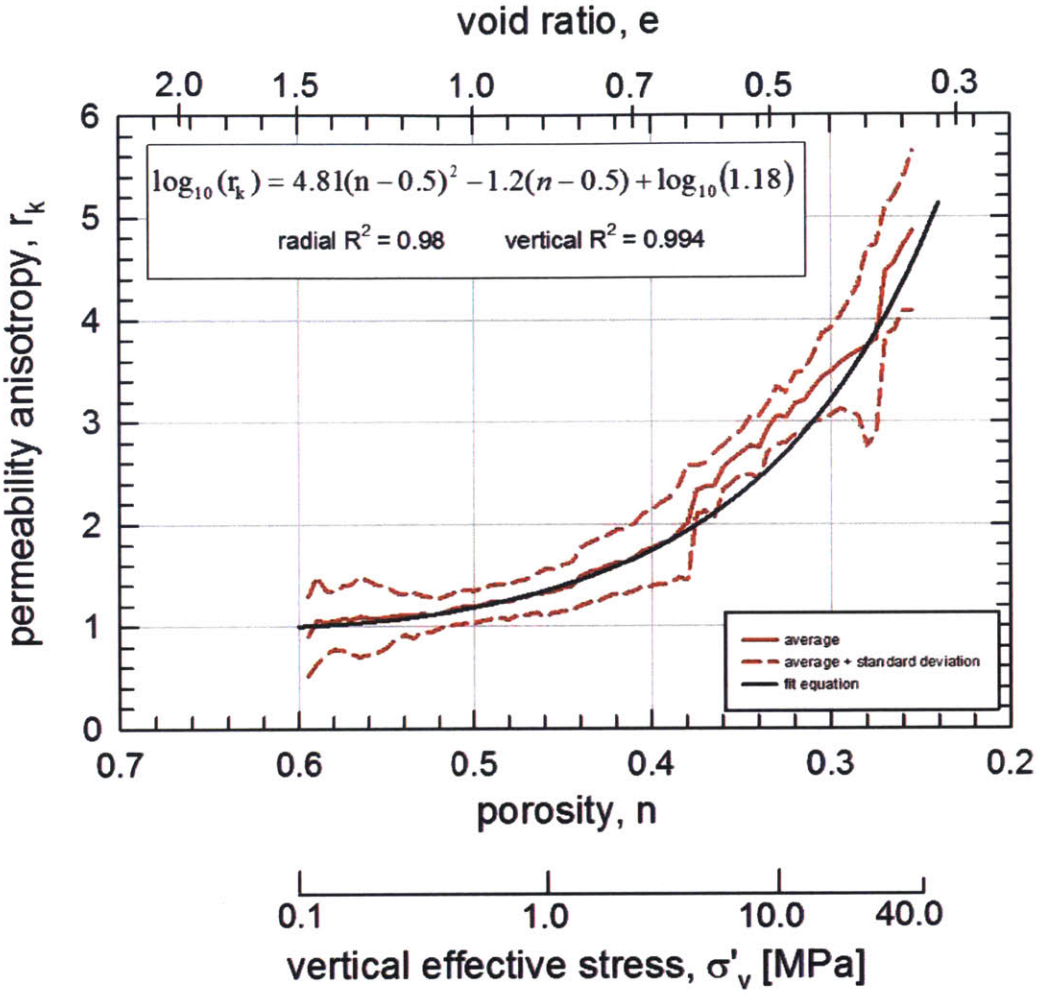

Figure 6-21: RGoM-EI permeability anisotropy, measured using CRS testing, increases from ~1 to ~5 during compression. The regression equation for permeability anisotropy is derived from log-linear quadratic permeability regression equations, and predicts anisotropy more correctly than the log-linear equation for RGoM-EI.

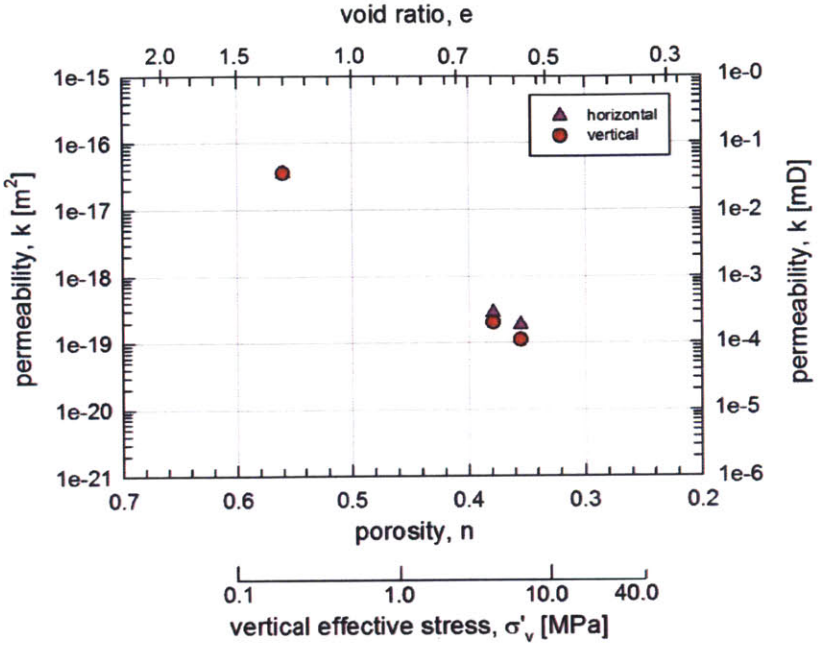

Figure 6-22: Permeability measured for RGoM-EI using cubic specimen constant head testing shows anisotropic development with decreasing porosity.

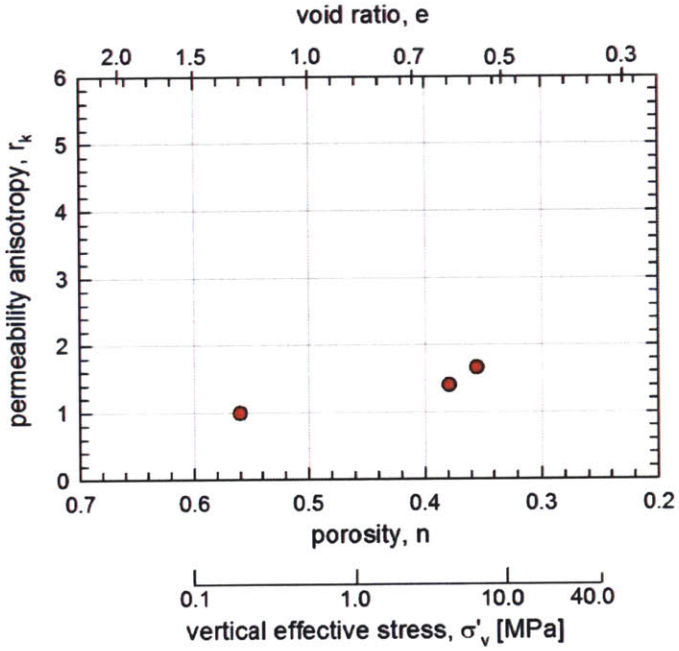

Figure 6-23: The permeability anisotropy of RGoM-EI reaches just under 2 using cubic specimen constant head testing.

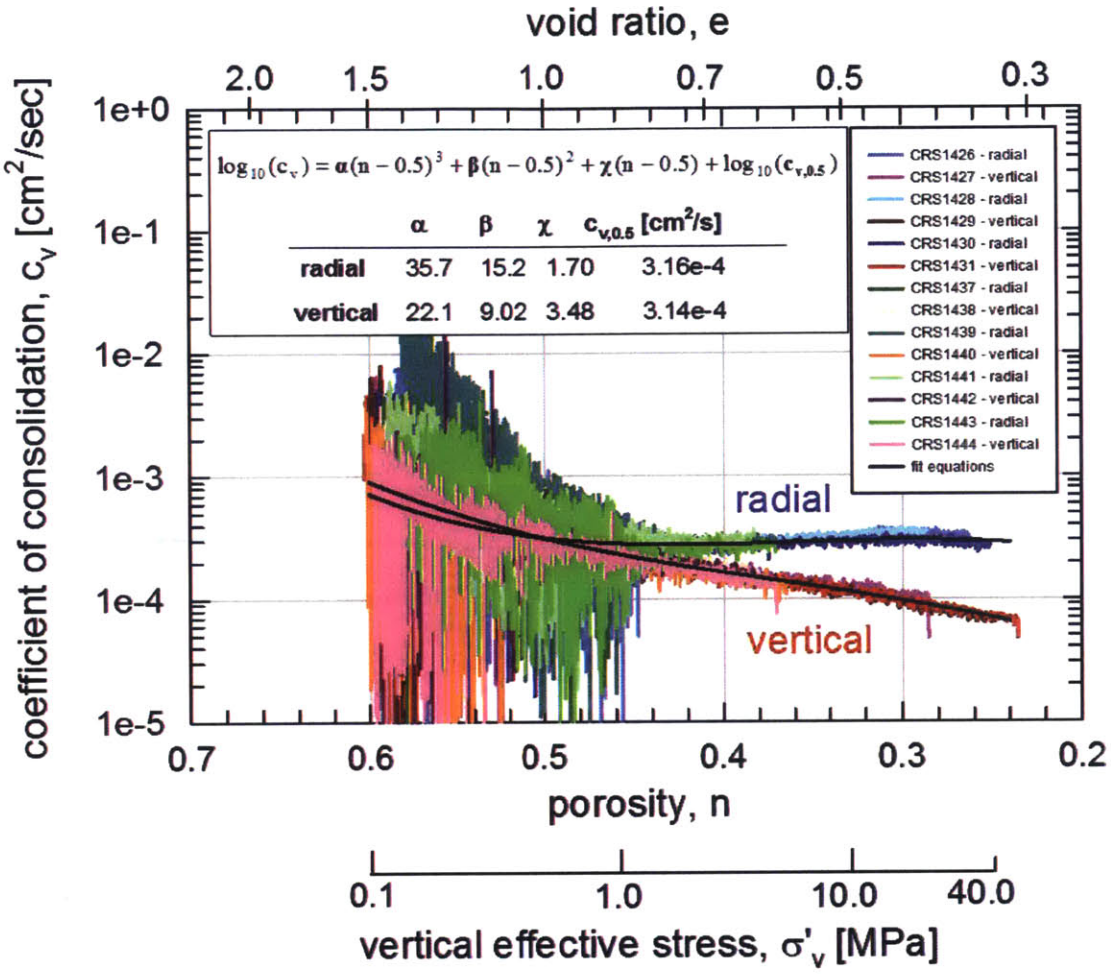

Figure 6-24: RGoM-EI coefficient of vertical consolidation with vertical and radial drainage, measured using CRS testing, stays roughly constant but diverges with compression. Significant noise in the data hides trends at high porosities. Polynomial regressions are fit to averaged binned data.

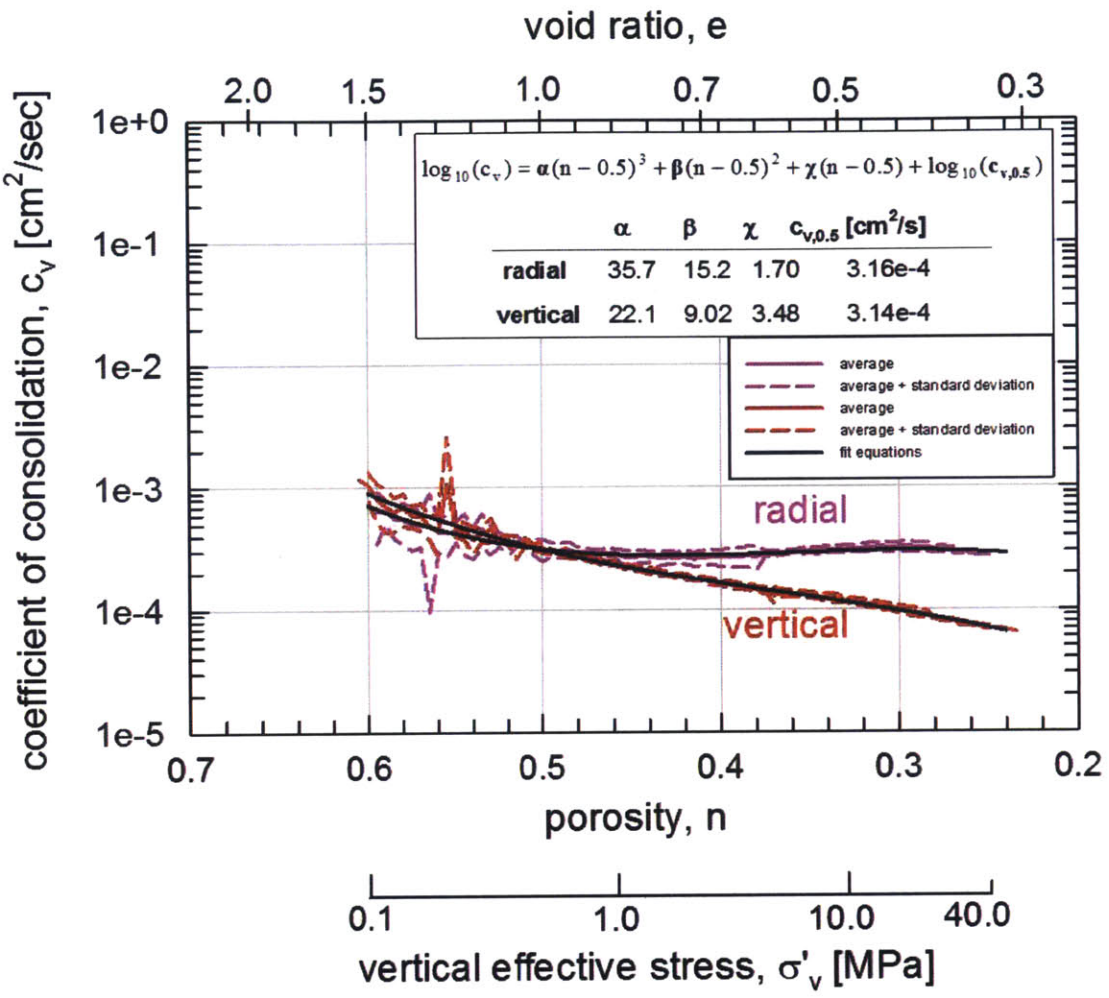

Figure 6-25: RGoM-EI coefficient of vertical consolidation with vertical and radial drainage data are more discernable when averages and standard deviations are taken from raw data and plotted. The coefficient of vertical consolidation with radial drainage stays roughly constant, while the coefficient of vertical consolidation with vertical drainage decreases linearly with compression. Polynomial regressions are fit to the averaged binned data.

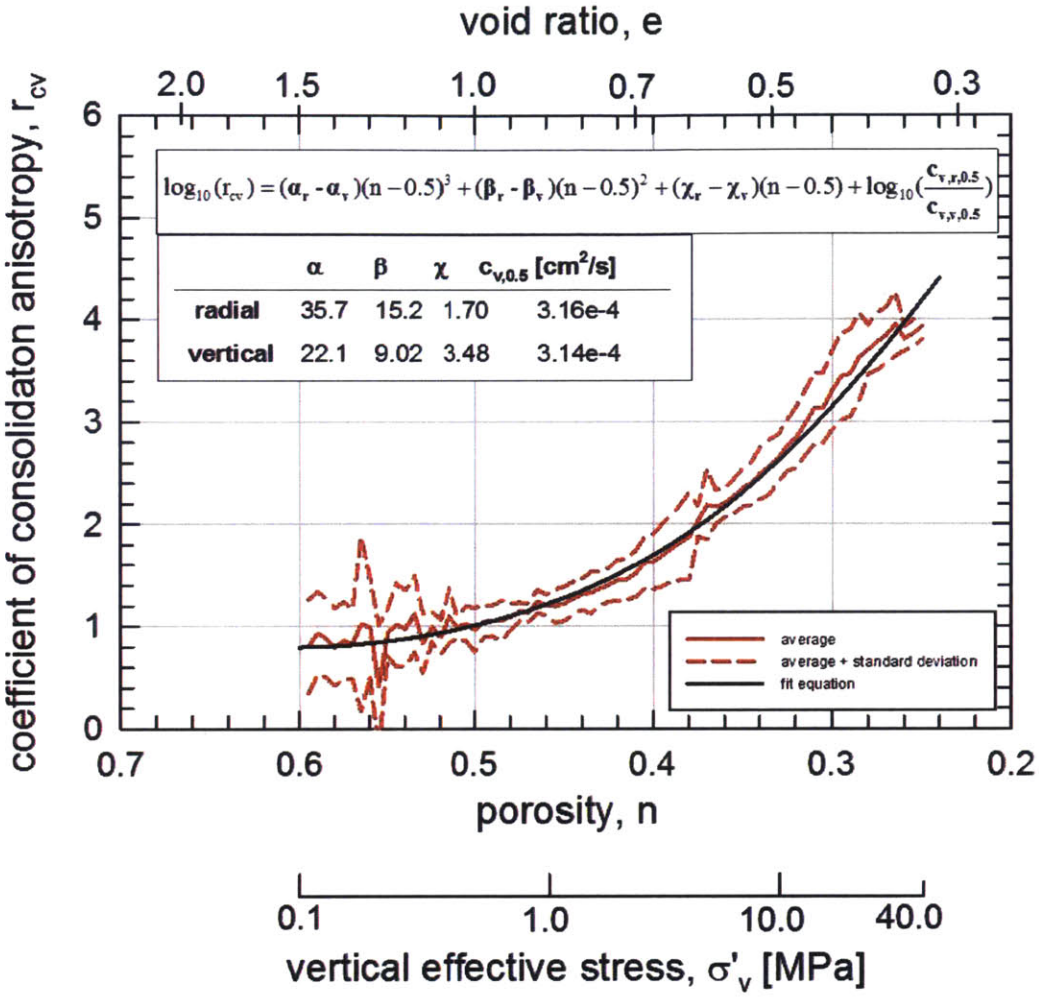

Figure 6-26: RGoM-EI coefficient of consolidation anisotropy, measured using CRS testing, increases from ~1 to ~4 during compression. The polynomial regression equation is derived from the polynomial coefficient of consolidation equations.

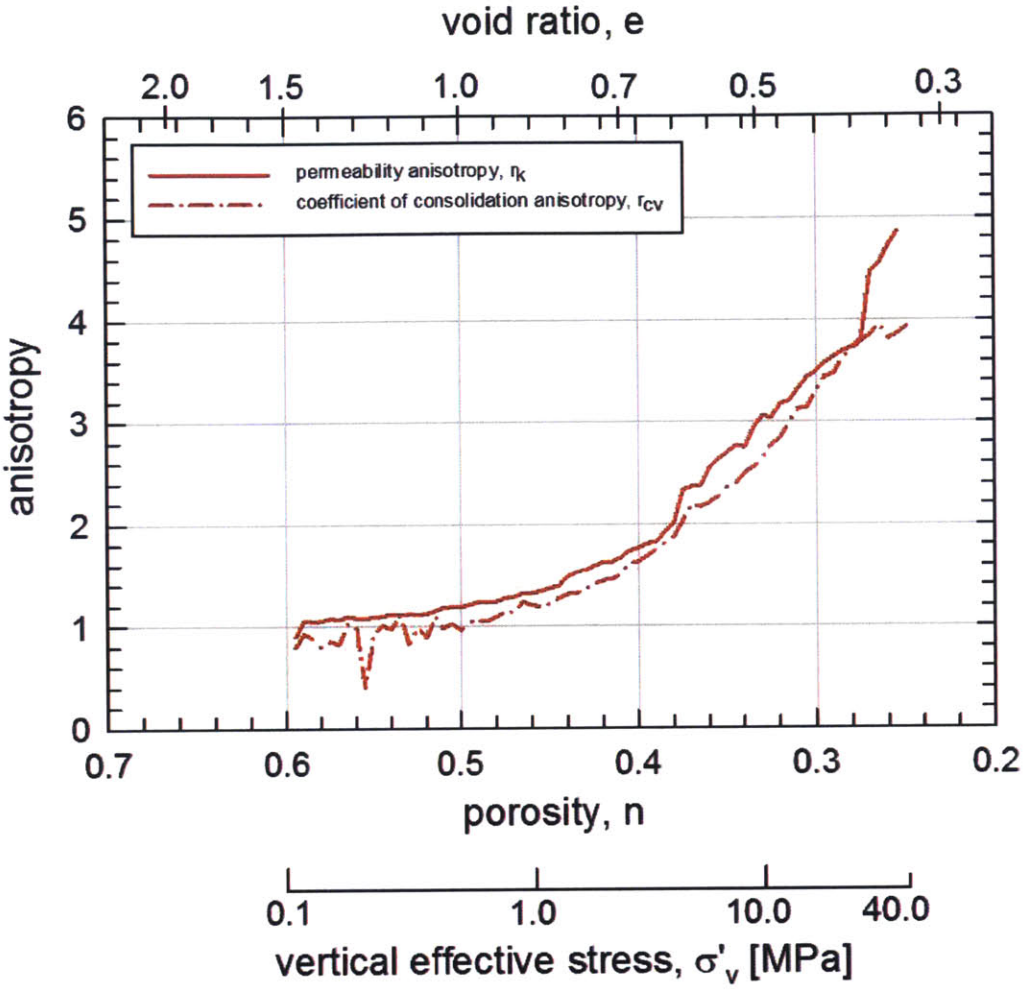

Figure 6-27: Comparing RGoM-EI's CRS-measured permeability anisotropy to coefficient of vertical consolidation anisotropy shows that the parameters are the same.

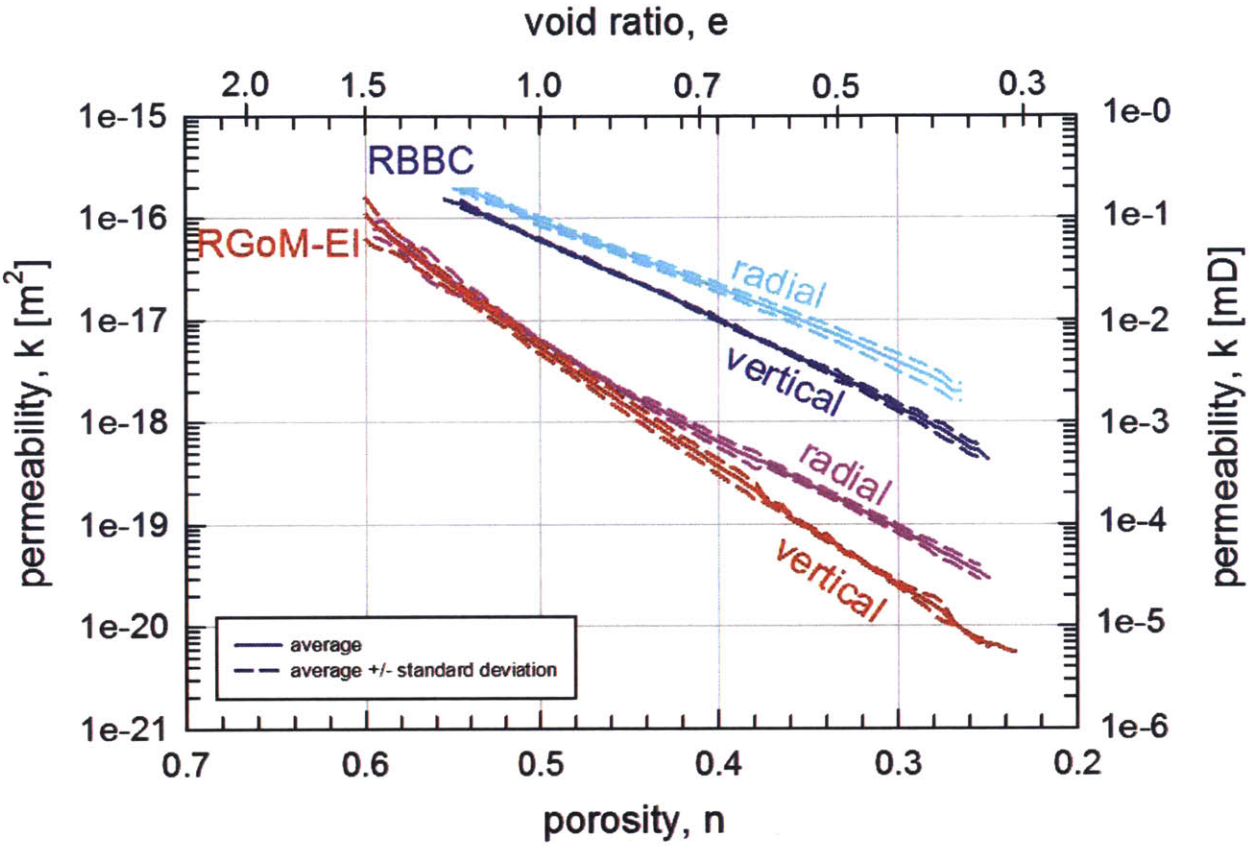

Figure 6-28: Comparing both radial and vertical CRS-measured permeabilties of RBBC and RGoM-EI illustrates differences in permeability.

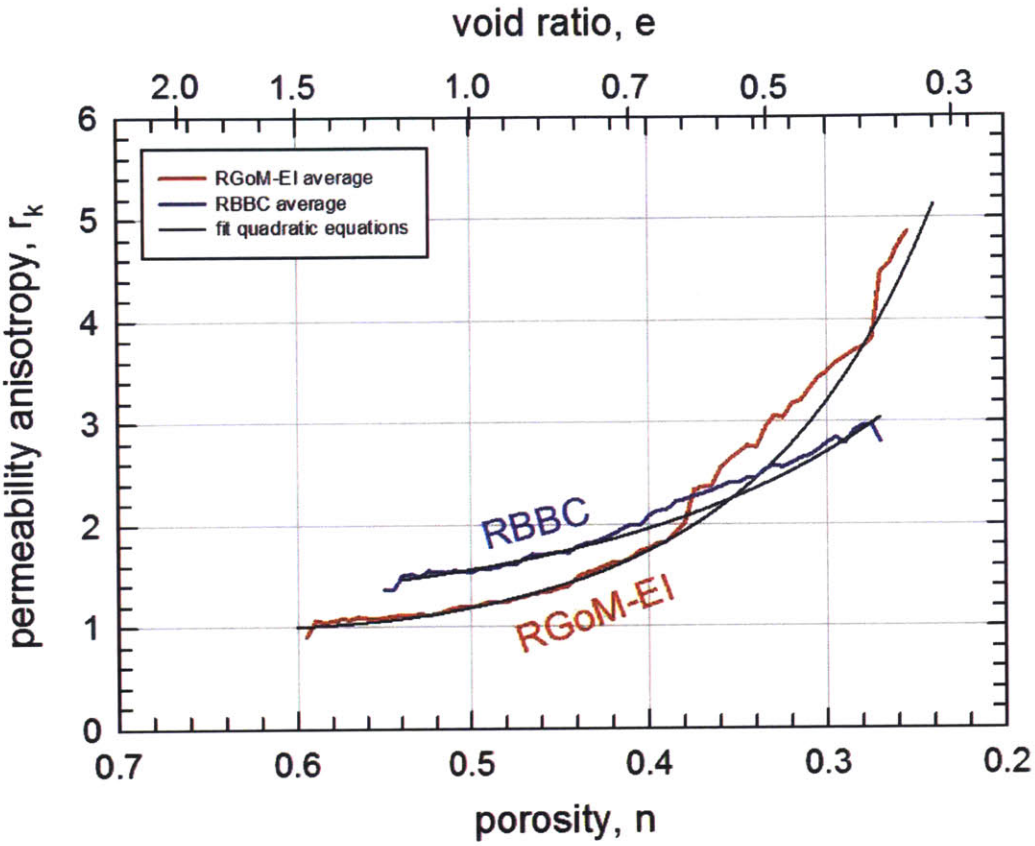

Figure 6-29: CRS-measured permeability anisotropy values show a steady increase with compression for RBBC, while RGoM-EI has a more exponential trajectory.

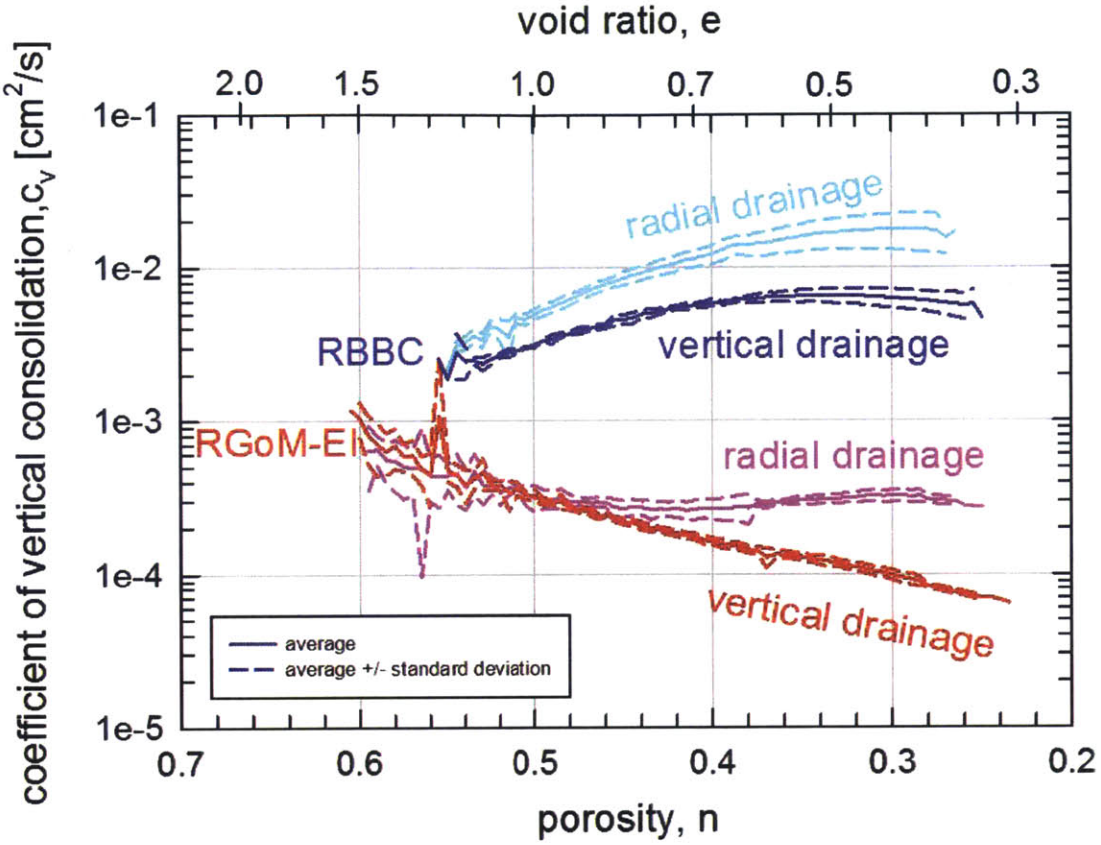

Figure 6-30: Plotting coefficients of vertical consolidation with both vertical and radial drainage for both RBBC and RGoM-EI shows how drainage direction and smectite content will affect the time for settlement.

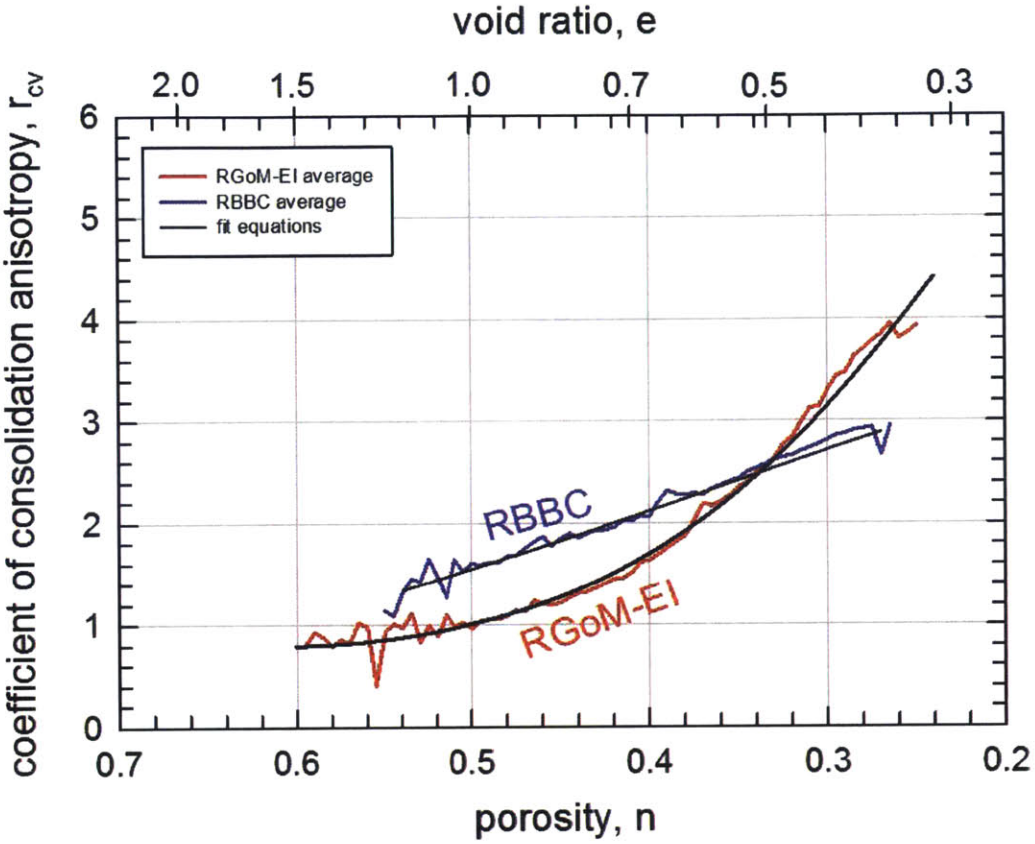

Figure 6-31: CRS-measured coefficient of vertical consolidation anisotropy values show a steady increase with compression for RBBC, while RGoM-Ei has a more exponential trajectory. The permeability anisotropy and coefficient of consolidaton anisotropy are theorectially equivalent.

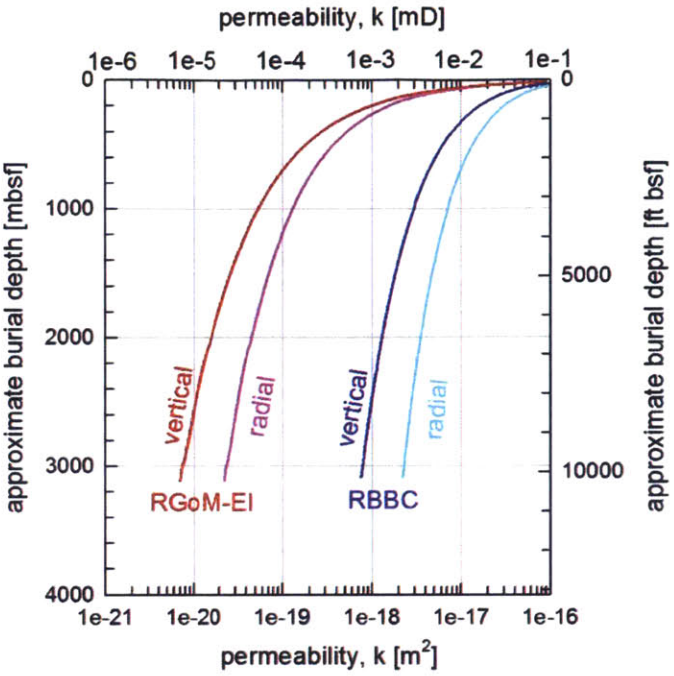

Figure 6-32: Plotting permeability with depth below the sea floor (bsf) gives an intuitive view of subgrade permeability. Normally-consolidated conditions, hydrostatic water pressures, and no layering are assumed.

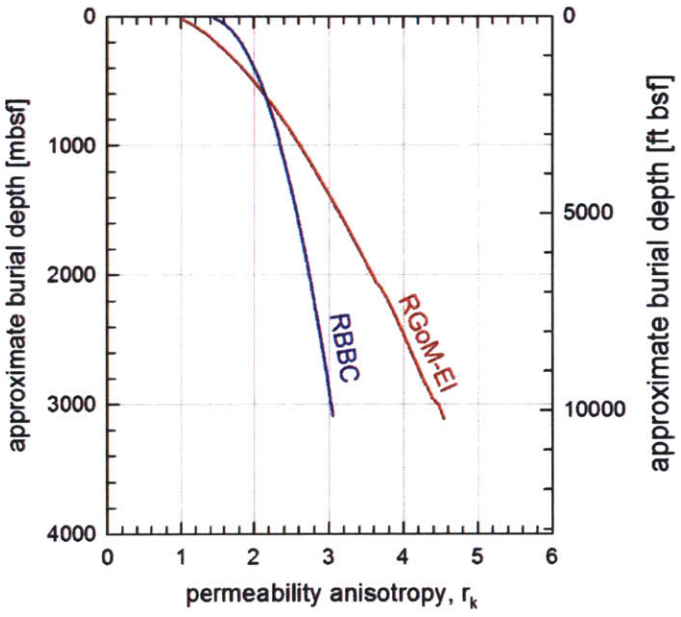

Figure 6-33: Plotting permeability anisotropy with depth below the sea floor (bsf) gives an intuitive view of subgrade permeability anisotropy development. Normally-consolidated conditions, hydrostatic water pressures, and no layering are assumed.

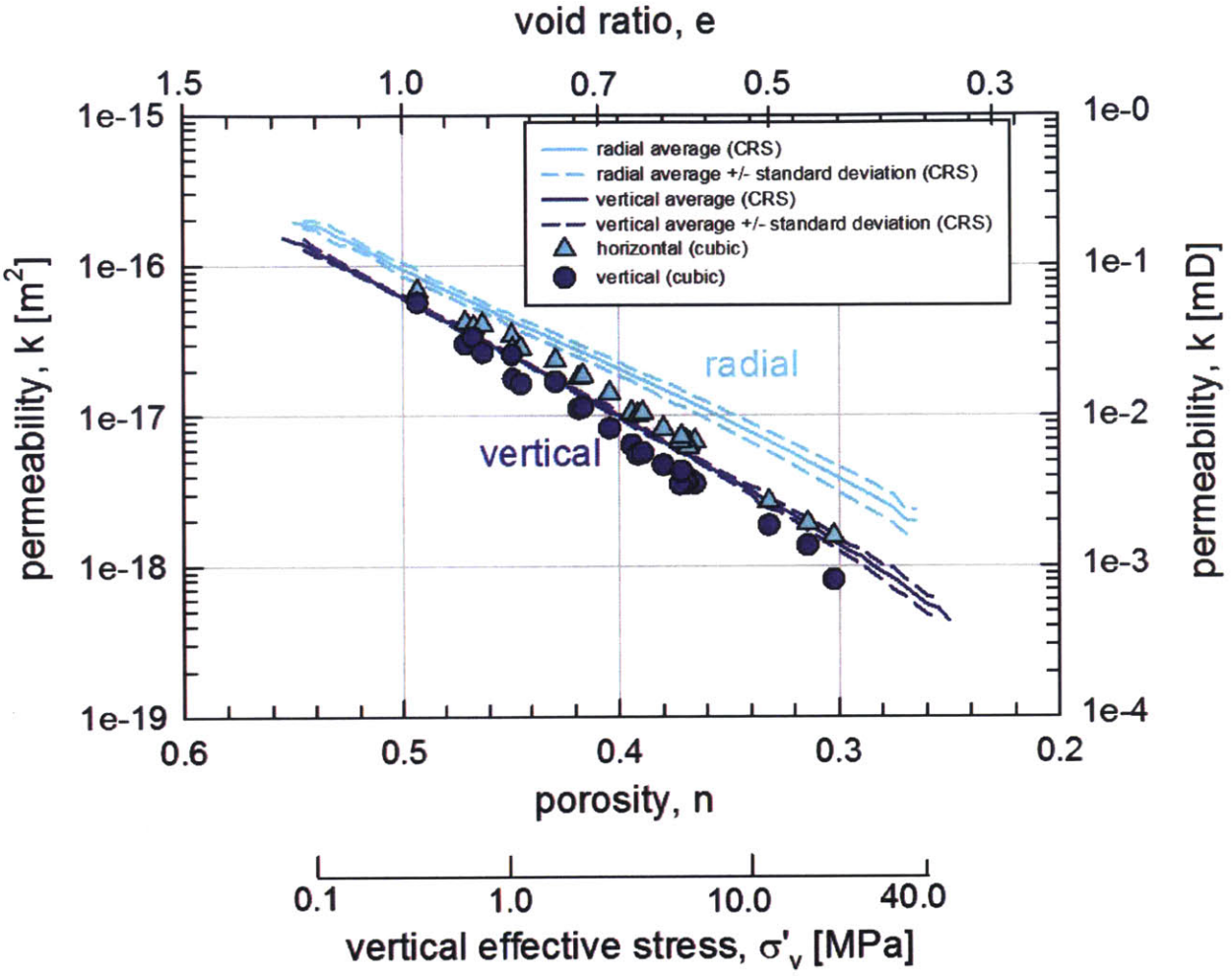

Figure 6-34: The CRS-measured RBBC permeability data compared with the cubic-specimen-measured data (Adams, 2014) show a similar trend; however, there is a slight offset between the two methods.

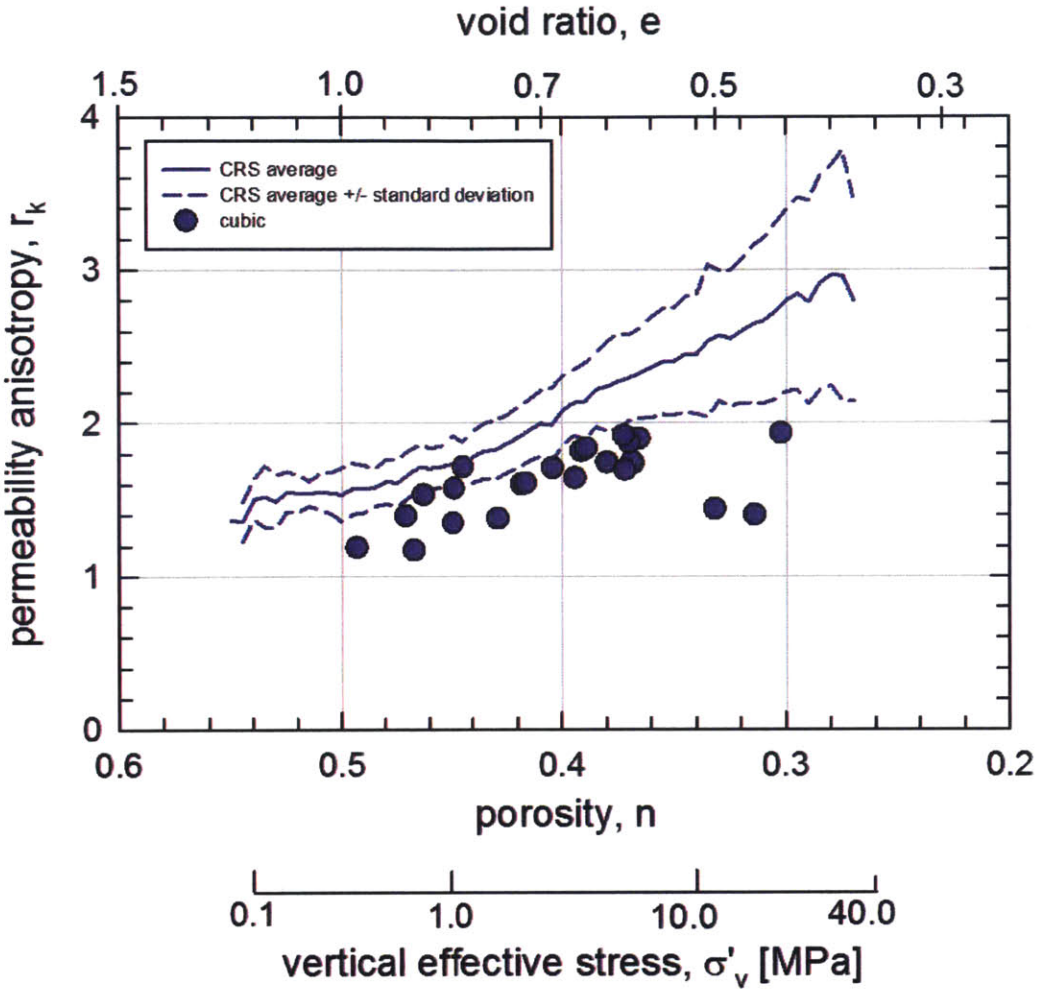

Figure 6-35: The CRS-measured RBBC permeability anisotropy data compared with the cubic-specimen-measured data (Adams, 2014) show a similar trend; however, there is consistently less anisotropy exhibited by the cubic specimens.

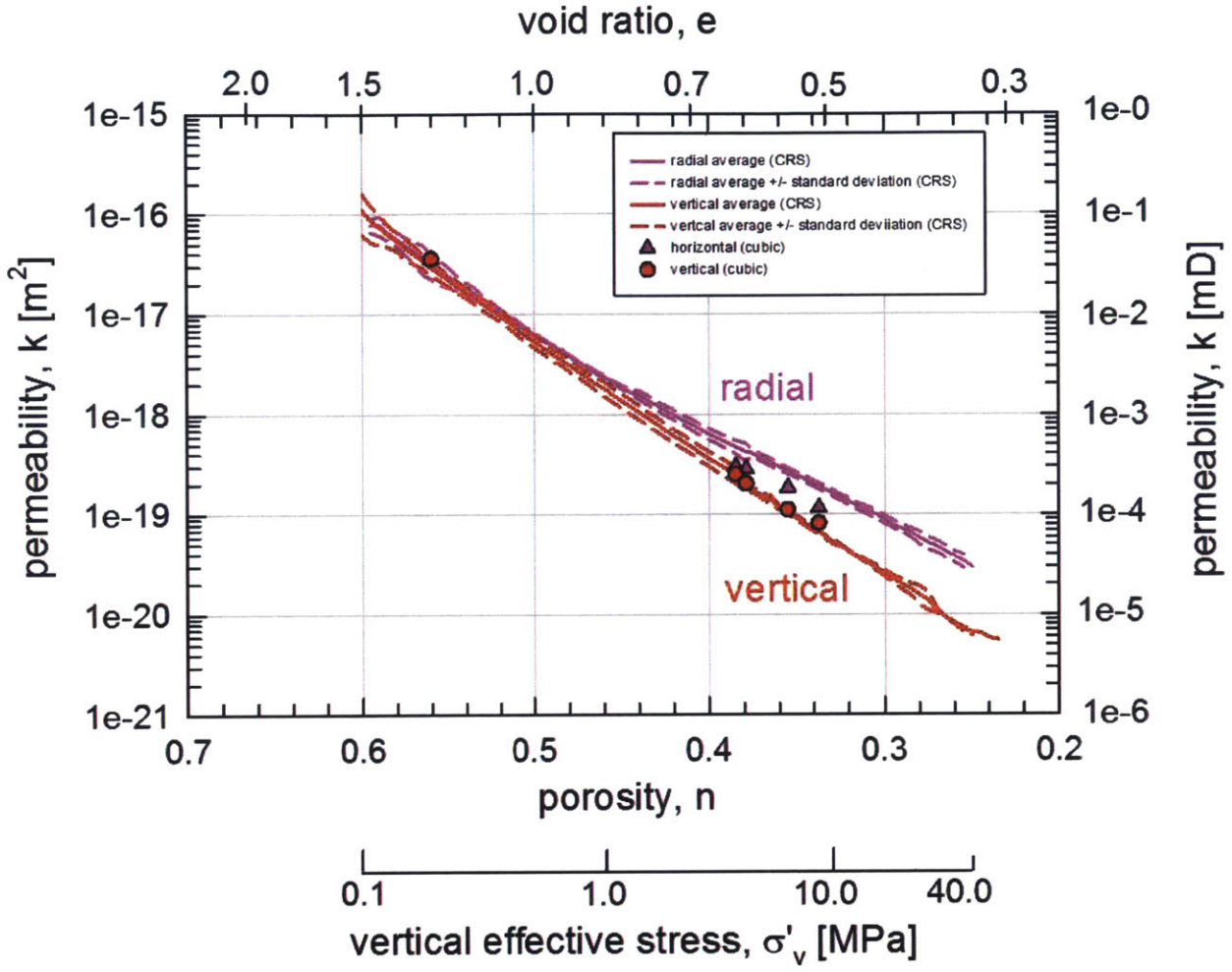

Figure 6-36: The CRS-measured RGoM-EI permeability data compared with the cubic-specimen-measured data (author and Adams, 2014) show a similar trend. The vertical permeability values measured in the cubic specimen fit within the standard deviations of the average CRS curve, while the horizontal permeabilities measured sighly lower in the cubic specimens than the CRS tests.

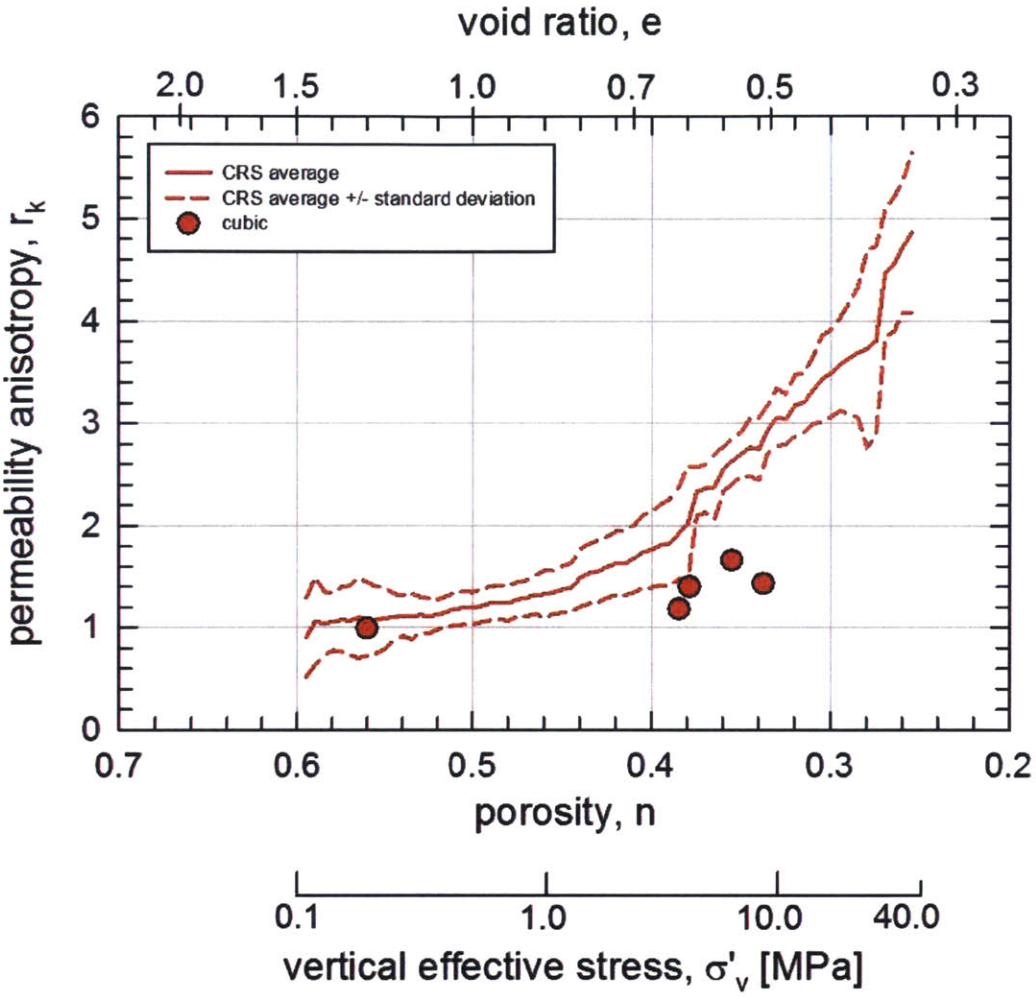

Figure 6-37: The CRS-measured RGoM-EI permeability anisotropy data compared with the cubic-specimen-measured data (author and Adams, 2014) show a similar trend; however, there is consistently less anisotropy exhibited by the cubic specimens.

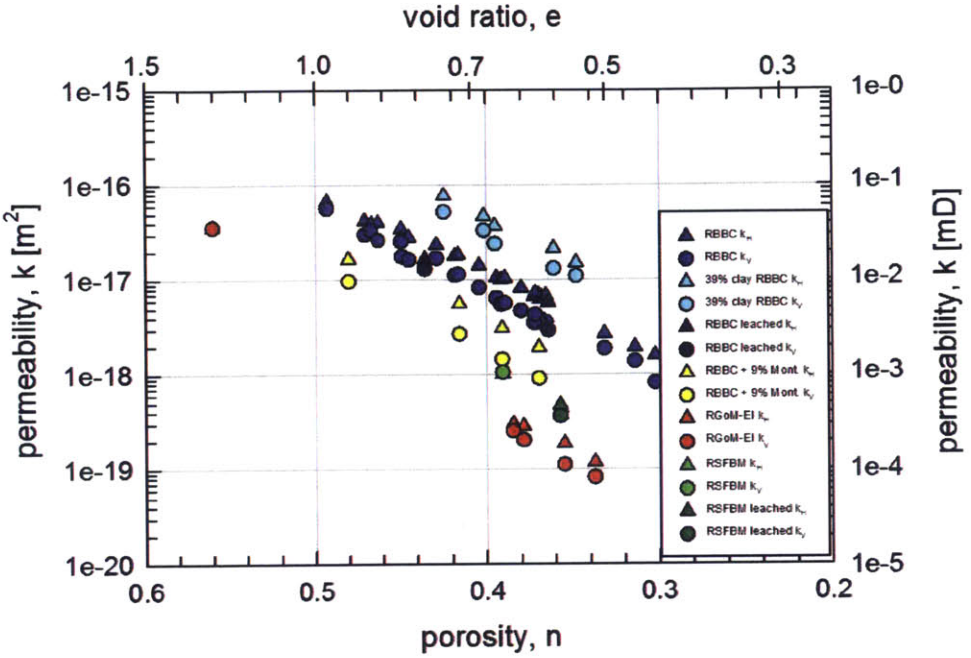

Figure 6-38: All the materials tested in the cubic specimens by the author and Adams (2014) show linear but offset permeability trends with compression. The more smectitic materials have lower permeabilities.

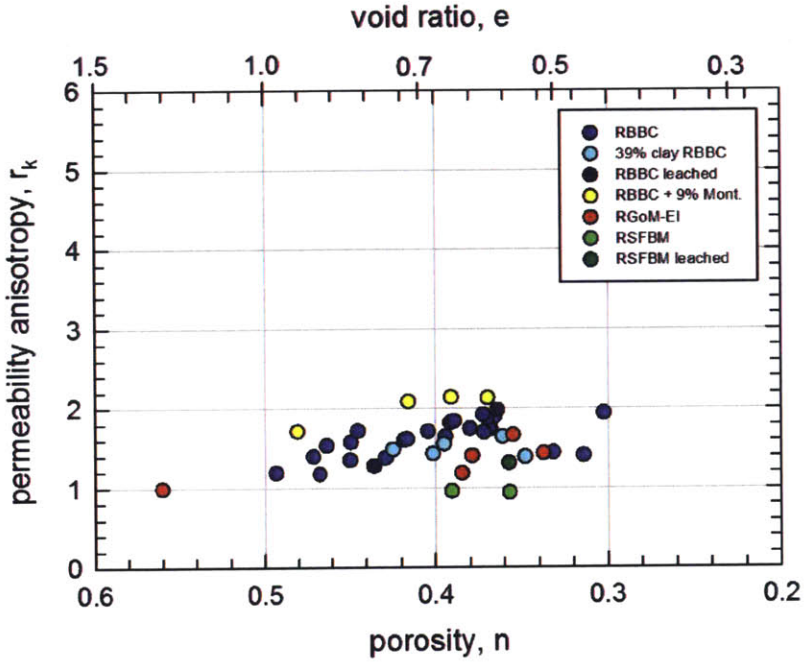

Figure 6-39: The materials tested in the cubic specimens by the author and Adams (2014) show increasing permeability anisotropy with increasing smectite content. RGoM-EI and RSFBM do not follow the same trend.

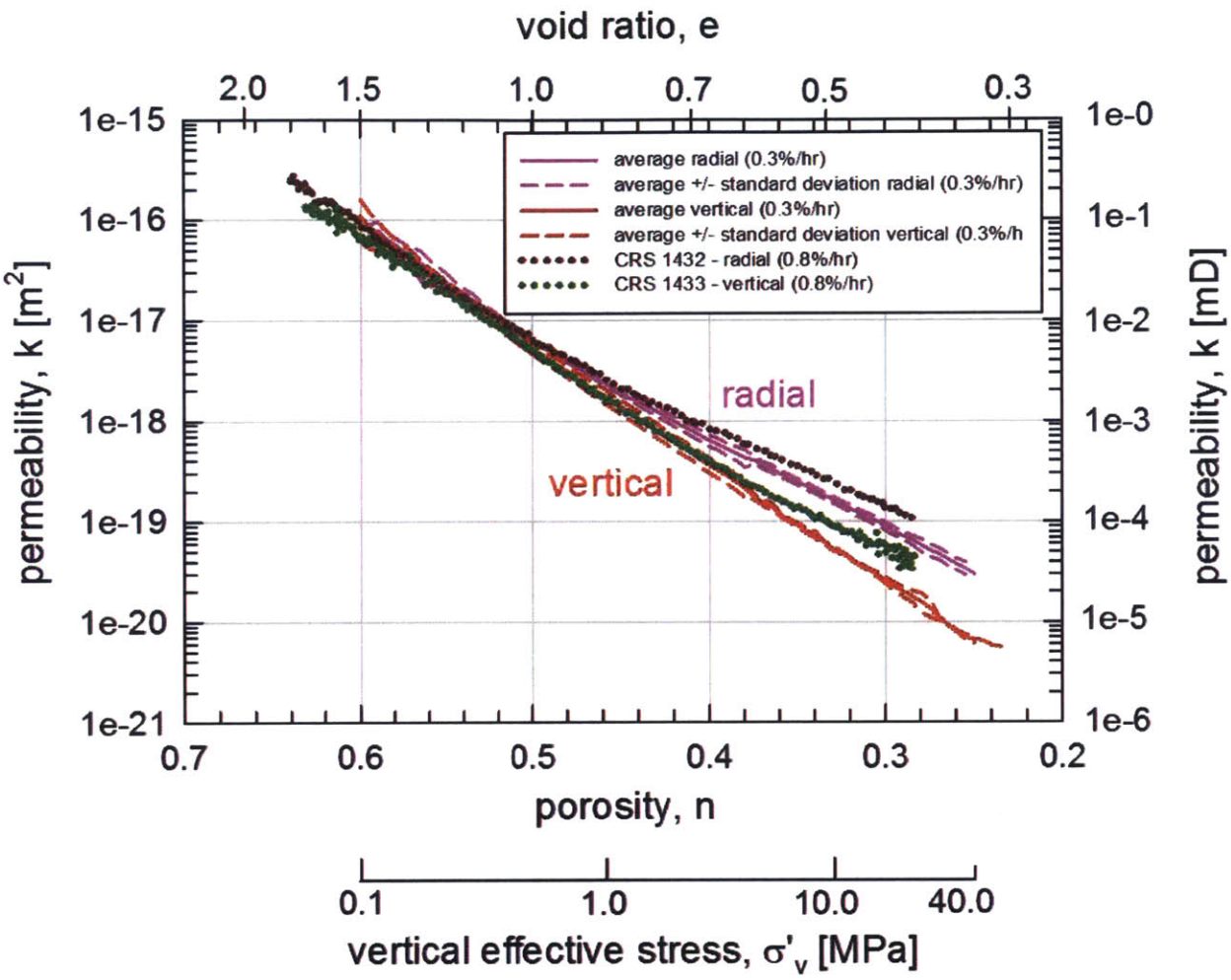

Figure 6-40: A pair of CRS tests is performed on RGoM-EI mudrock using a 0.8 %/hour strain rate. Higher permeability values are measured at low porosities for both drainage directions when compared to the database which is compressed at 0.3 %/hour.

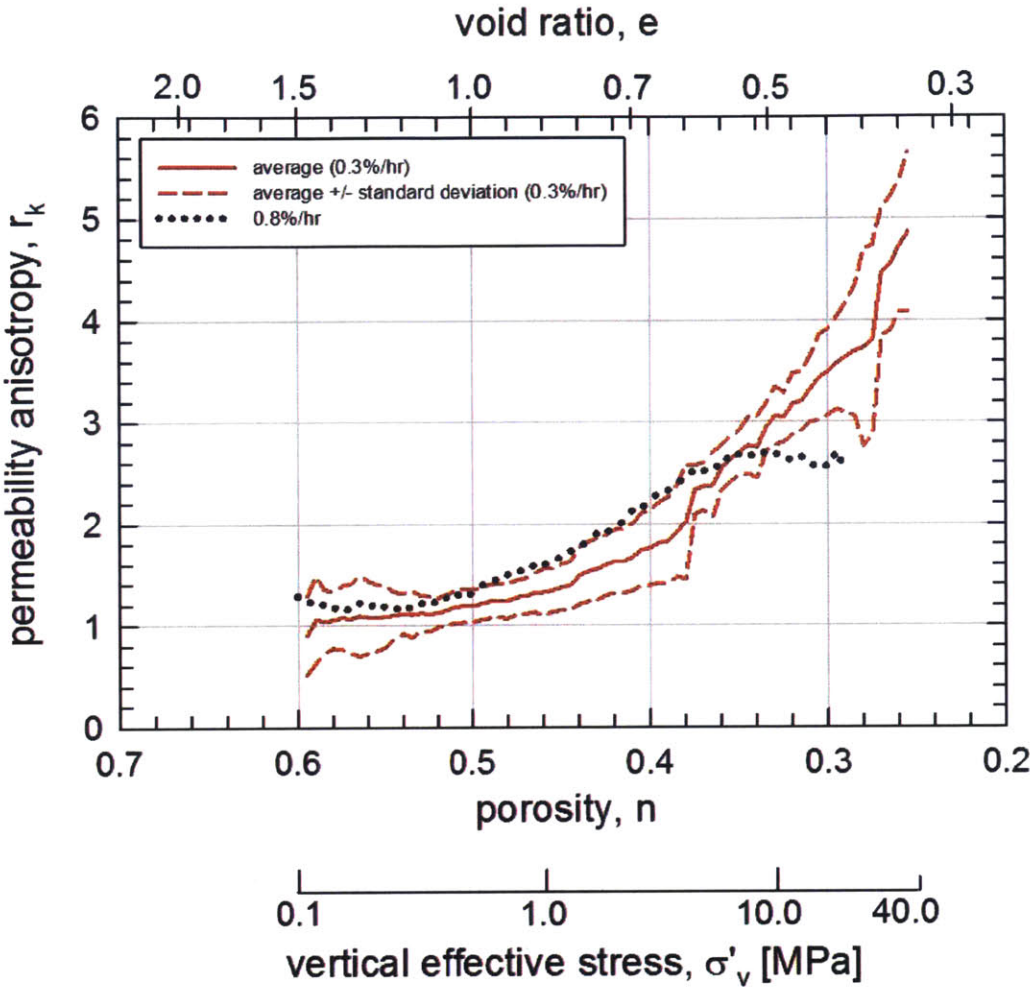

Figure 6-41: A pair of CRS tests is performed on RGoM-EI mudruck using a 0.8 %/hour strain rate. Permeability anisotropy data measured from these tests mostly matches the database which is compressed at 0.3 %/hour.

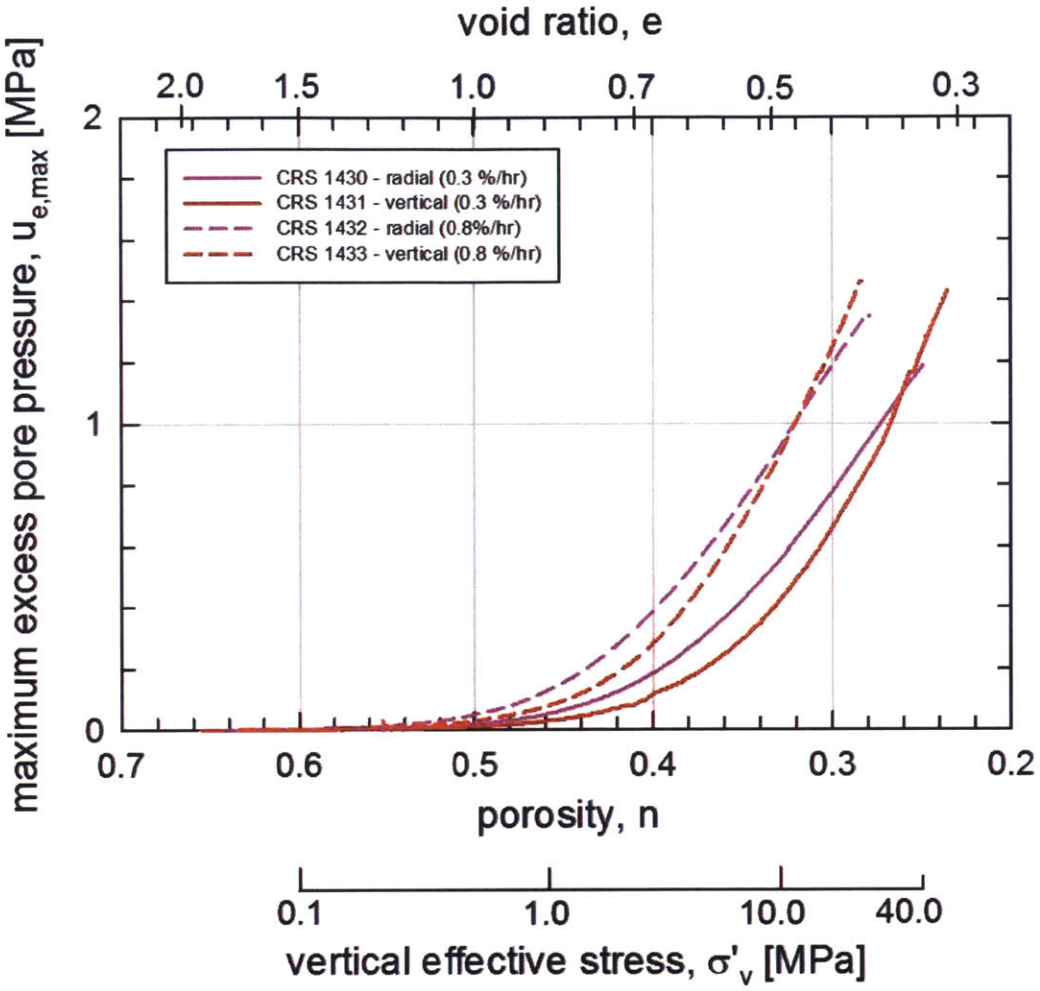

Figure 6-42: The maximum excess pore pressure buildup during RGoM-EI tests strained at 0.8 %/hour is significantly greater than the buildup during the tests strained 0.3 %/hour.

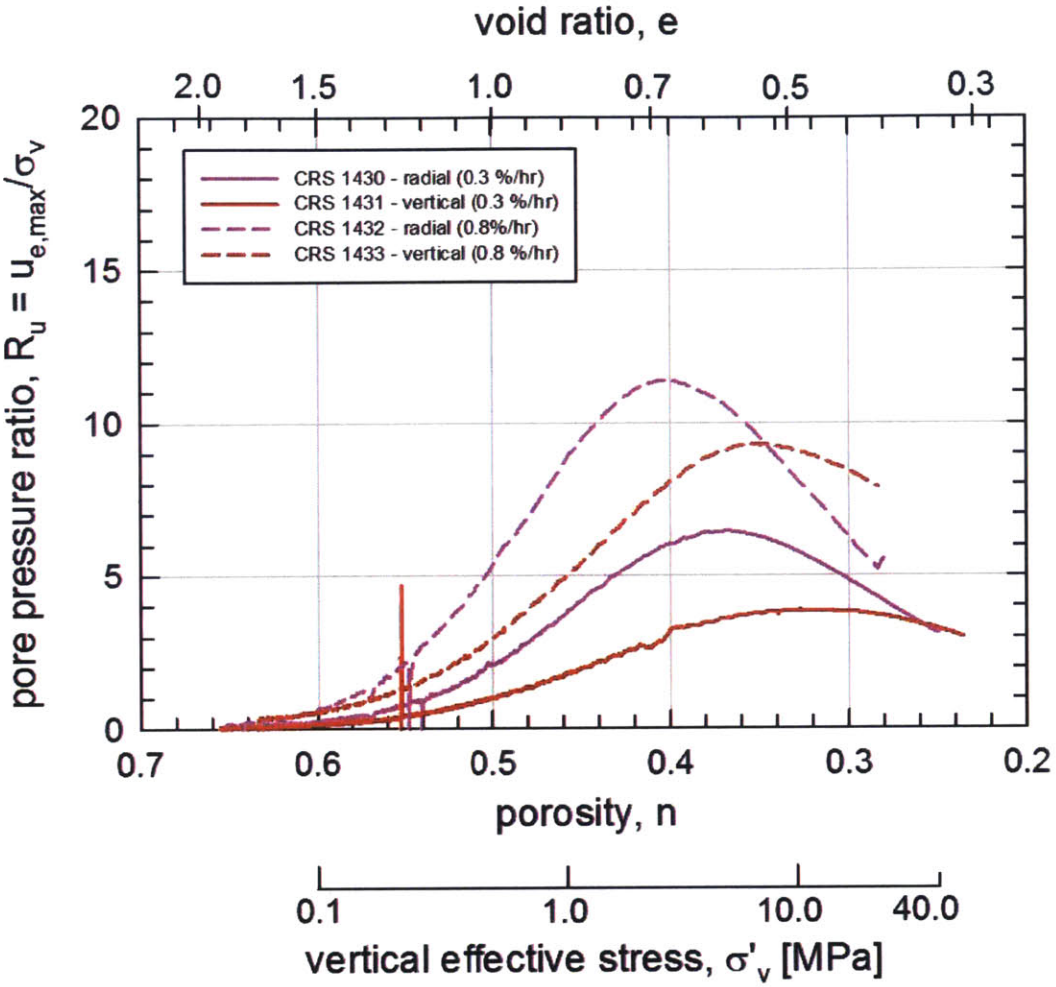

Figure 6-43: The pore pressure ratios developed in the RGoM-EI tests strained at 0.8 %/hour are significantly greater than the ratios for the tests strained 0.3 %/hour, but stay below the ASTM-recommended maximum of 15% (ASTM D4186).

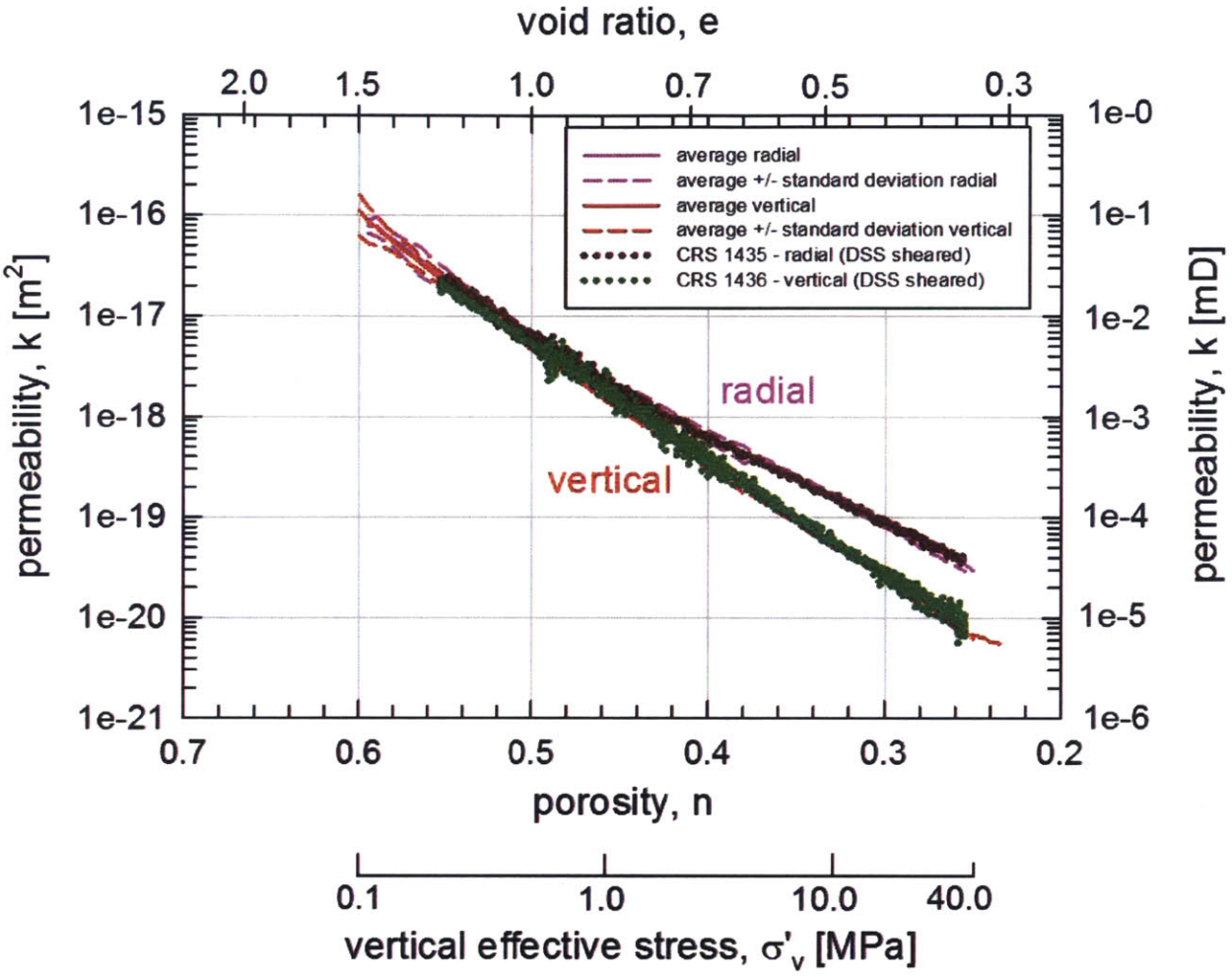

Figure 6-44: A pair of CRS tests is performed on RGoM-EI mudrocks that have been sheared to 29.5% shear strain at a vertical effective stress of 0.14 MPa within a DSS device. No change in permeability is observed.

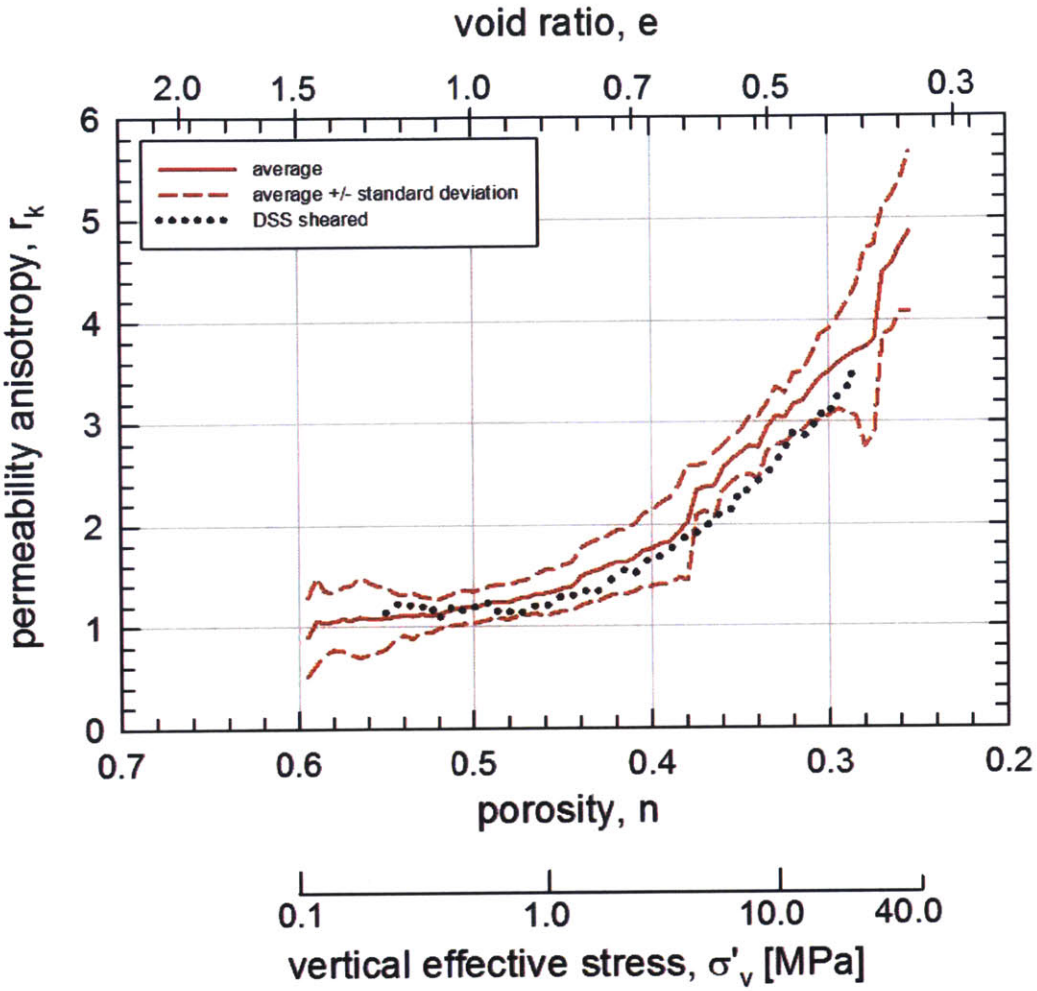

Figure 6-45: A pair of CRS tests is performed on RGoM-EI mudrocks that have been sheared to 29.5% shear strain at a vertical effective stress of 0.14 MPa within a DSS device. No change in permeability anisotropy is observed.

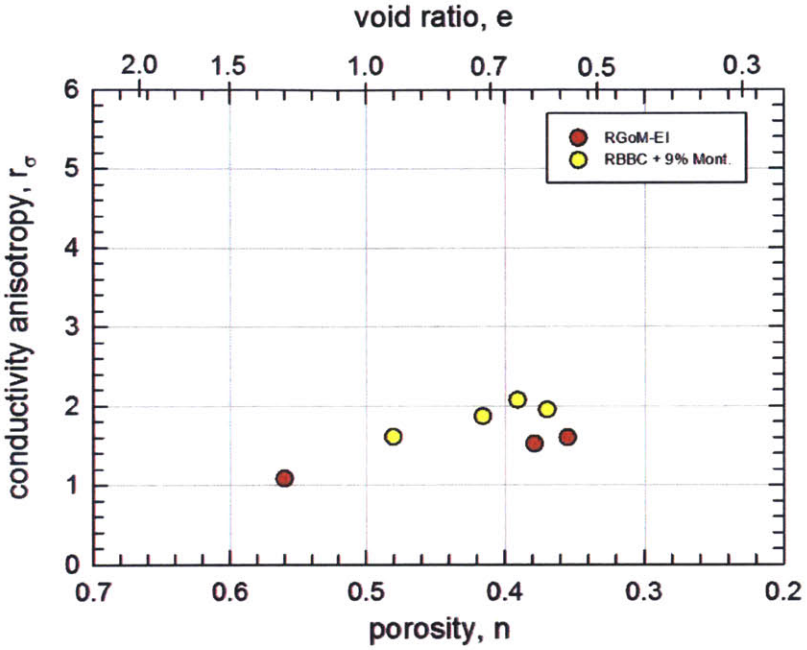

Figure 6-46: Electrical conductivity anisotropy, the inverse of electrical resistivity anisotropy, is measured within a triaxial cell during cubic specimen constant head testing. RGoM-EI and RBBC + 9% Mont. are measured by the author.

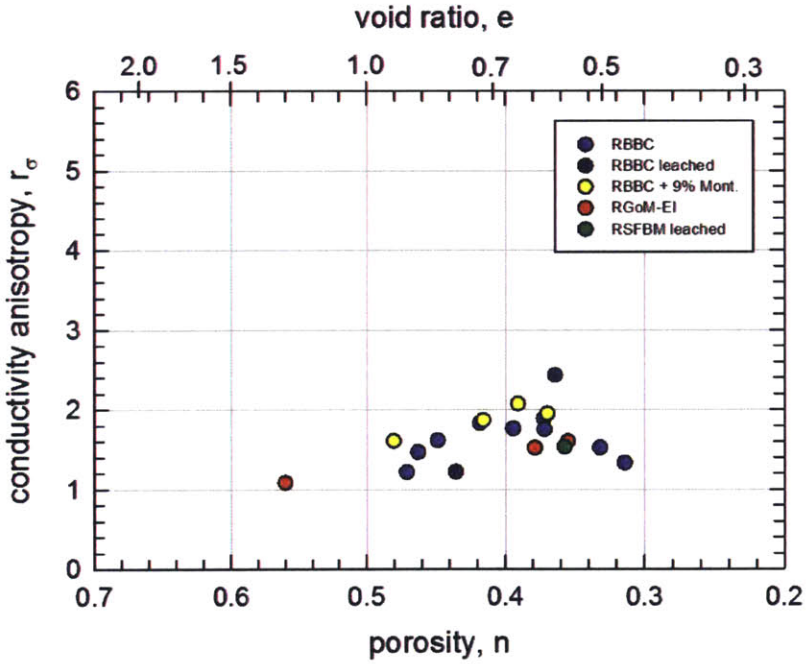

Figure 6-47: Electrical conductivity anisotropy, the inverse of electrical resistivity anisotropy, as measured by Adams (2014) and the author shows an increasing trend with decreasing porosity, similar to permeability anisotropy.

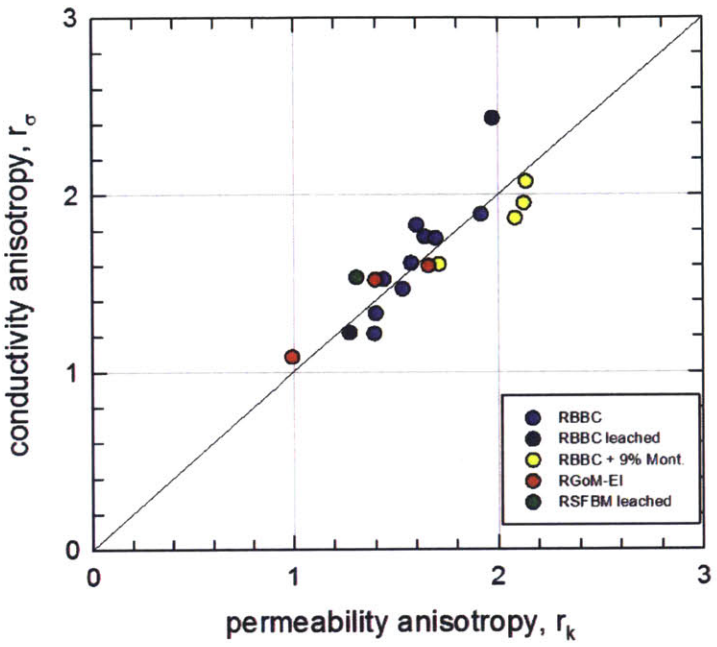

Figure 6-48: Permeability and resistivity anisotropy, measured on cubic specimens within a triaxial cell, show a direct correlation (Author and Adams, 2014).

CHAPTER 7 – CONCLUSIONS

7.1 INTRODUCTION

The major themes and ideas from this experimental research are presented in this chapter, along with recommendations for future areas of research. The development of a new radially-draining CRS consolidometer through adapting a traditional device is first recapitulated. This is followed by the testing results from the new equipment, combined with results from the traditional vertically-draining CRS. The cubic specimen constant head testing results are then summarized. Finally, recommendations for further research and development are given.

7.2 RADIALLY-DRAINING CRS DEVICE

Modifications are made to the Trautwein® CRS cell to change it from vertically-draining to radially-draining. The base is modified to include a no-flow boundary and pore pressure pinholes to monitor internal excess pore pressures. The confinement ring is modified to become a drainage boundary, through the use of a high-strength tubular-shaped porous stone that is thermally press-fit into a steel confinement ring. The top of the specimen is also confined by a nonporous stainless steel top cap. These modifications create a radially-outward drainage regime within a vertically-compressing cylindrical specimen. The equipment has the strength to load specimens to at least 40 MPa of vertical stress. The equipment drawings are shown in Appendix A.

The radially-draining device creates an excess pore pressure gradient between the center and the perimeter of the specimen, allowing for the measurement of radial permeability. A solution proposed by Yune and Chung (2005) uses the strain rate and radial pore pressure gradient to calculate radial-horizontal permeability.

7.3 CRS TESTING

The development of a radially-draining CRS consolidometer allows for permeability to be measured in the radial-horizontal direction on relatively undisturbed, normally-consolidating mudrocks. It is a low scatter, low time testing method. By measuring vertical permeability with a traditional vertically-draining CRS consolidometer on a similar specimen at the same time, the permeability anisotropy of a homogenous mudrock can be characterized. Permeability anisotropy is characterized for resedimented Boston Blue Clay (RBBC) and resedimented Gulf of Mexico – Eugene Island mudrock (RGoM-EI). Nine tests are run on RBBC and 16 are performed on RGoM-EI, to average out the effect of specimen variability (see Table 6-2). Each specimen is consolidated to 0.1 MPa vertical effective stress through resedimentation prior to CRS testing. Repetition is necessary, because vertical and radial permeability are not measured on the same specimen, while they are in the cubic specimen constant head tests (Adams, 2014). Very little variability is observed (see Figure 6-11 and Figure 6-19), showing that resedimentation is a successful method for creating separate specimens that are comparable with each other.

Both of these materials show permeability anisotropy due to vertical consolidation that increases as porosity decreases (see Figure 6-29). RGoM-EI, a smectitic, high-plasticity mudrock, shows permeability anisotropy values that are highly dependent on porosity. At a porosity of 0.6, corresponding to 0.1 MPa of vertical effective stress, it exhibits isotropic permeability. The isotropy turns to anisotropy at an increasing rate, reaching a value of 5 at a porosity of 0.25, corresponding to 40 MPa of vertical effective stress. This is a much steeper trend than the permeability anisotropy trend for RBBC, where anisotropy increases from 1.5 at a porosity of 0.55 (corresponding to 0.1 MPa of vertical effective stress) to 3 at a porosity of 0.26 (corresponding to 40 MPa of vertical effective stress). The RBBC trend shows more of a linear, slightly concave-up trend, while RGoM-EI shows a curve with great upward concavity, suggesting dramatic anisotropy increase at low porosities. These results confirm trends found in the literature, where smectite content plays a large role in mudrock permeability anisotropy, due to flowpath tortuosity caused by clay particle alignment (Scholes et al, 2007; Meegoda, 1989).

The CRS results are believed to be more representative of soil behavior than the cubic specimen constant head results from Adams (2014) and the author. The cubic specimen results show a dropoff in anisotropy values for RBBC at stresses beyond 10 MPa (see Figure 6-35) and lower anisotropy in RGoM-EI than RBBC (see Figure 6-39). Both of these trends are counter-intuitive and do not agree with the literature (Scholes et al, 2007; Olsen, 1962; Lambe, 1958; Mitchell, 1956). RGoM-EI cubic specimens

also display cracking along the bedding planes during trimming, suggesting sample disturbance as a possible explanation.

The compression characteristics from the CRS tests remain unaltered by pore fluid drainage direction, including e - log stress compression behavior (see Figure 6-1 and Figure 6-4) and volume compressibility (see Figure 6-2 and Figure 6-5). The coefficient of vertical consolidation is shown to increase with radial drainage when compared to vertical drainage (see Figure 6-14 and Figure 6-24). The relationship between the coefficient of vertical consolidation with radial drainage to that with vertical drainage is the same as the relationship between radial permeability and vertical permeability.

RGoM-EI mudrocks sheared to 29.5% horizontal shear strain while under 0.14 MPa of vertical effective stress do not exhibit any change in permeability anisotropy when compared to intact RGoM-EI mudrocks (see Figure 6-43). Shear-induced permeability anisotropy is hypothesized to be caused by shear bands parallel to shearing direction and/or increased particle alignment (Dewhurst et al, 1996; Terzaghi et al, 1996; Arch and Maltman, 1990). Several possible explanations for why no increased permeability is seen in the DSS-sheared specimens are that (1) shear bands are immediately closed from ensuing compression, (2) not enough shear strain was induced, and/or (3) individual particles need to be compressed to a lower porosity prior to shearing to engage shear-induced particle rotation.

Permeability measurements made from CRS testing are dependent on strain rate for RGoM-EI. Even though the pore pressure ratios are kept below 15% (see Figure 6-42 and Figure 6-43), as recommended by ASTM D4186, different permeability and permeability anisotropy measurements are collected when a different strain rate is used (see Figure 6-40 and Figure 6-41).

7.4 CUBIC SPECIMEN CONSTANT HEAD TESTING

Seven cubic specimen constant head tests are performed: 3 on RGoM-EI and 4 on RBBC + 9% Mont. The permeability anisotropy and conductivity anisotropy (inverse of electrical resistivity anisotropy) values are calculated and combined with the test results from Adams (2014). The results show anisotropy in RBBC + 9% Mont. of over 2, more than any of the other cubic specimen results. RGoM-EI anisotropy was lower than expected, similar to the measurements made by Adams (2014) (see Figure 6-39).

Cubic specimen constant head testing is a time-consuming permeability anisotropy measurement technique that induces a lot of handling disturbance on the mudrocks being tested. The testing results are believed to be less reliable than the CRS-measured permeability anisotropy results. However, the

cubic specimen constant head testing method gives valuable insight to the relationship between permeability anisotropy and conductivity anisotropy. This method is also applicable to the measurement of permeability anisotropy of intact samples, as multiple flow directions can be imposed on the same specimen.

Permeability anisotropy shows a one-to-one correlation with electrical conductivity anisotropy. This trend is seen in all the tests where the permeability and electrical resistivity are both measured within the pressurized triaxial cell (see Figure 6-46). These tests include RBBC, RBBC + 9% Mont., RGoM-EI, and RSFBM mudrocks. While this trend is useful for uniform mudrocks, it does not extend to layered systems (Adams, 2014).

7.5 RECOMMENDATIONS FOR FUTURE WORK

This section presents a few questions and recommendations for how this research can be continued. Recommendations for design improvements for the radially-draining CRS cell are given first, followed by ideas for future CRS permeability anisotropy testing.

7.5.1 Radially-Draining CRS Device Improvements

While the radially-draining CRS equipment works well, there are a few improvements that could be implemented to increase its performance. The suggested improvements are shown below:

- The 0.005" pinholes at the base of the specimen, where the excess pore pressures are measured, tend to clog frequently, especially when high-concentration salt water is used. The 0.005" diameter pinholes extend 0.040" into the steel base, before they open up to 0.063" diameter holes. When clogs occur, they can be cleared by flowing water through the holes and penetrating the bottom of the 0.005" diameter hole through the 0.063" diameter hole with a small drill bit (see Section 5.2.2); however, this unclogging process can be time consuming. Shortening the length of the 0.005" pinholes would decrease the propensity of the holes to clog, without increasing the diameter of the pinholes.
- Along with the maximum excess pore pressure monitor pinhole connected to the center of the specimen, an excess pore pressure check monitor is connected to a pinhole located at a radius of 0.685" from the center of the specimen. This monitor was created in order to investigate the effectiveness of the radial drainage system. Since the monitor's pinhole is located near the edge of the specimen (at a radius of 0.750"), little difference is found between the excess pore pressure check pressure and the cell pressure. Moving the location of the pore pressure check

pinhole closer to the center of the specimen would provide better insight into the radial pore pressure distribution. A 0.500" radius location for the excess pore pressure check pinhole should theoretically measure approximately 50% of the maximum excess pore pressure, according to the finite difference model described in Section 4.2.1.

- The permeability results are upper-bound values, due to a necessary lowering of maximum excess pore pressures in order to engage the maximum excess pore pressure lines. This lowering of pressures is a result of the necessary expansion of the pore pressure lines, transducer housings, and pore pressure transducers themselves. It would be worthwhile, therefore, to investigate for potential bias in radial permeability measurement due to pore pressure line compressibility. A minor amount of experimentation was performed on this topic by varying the pore pressure line volume, as described in Section 4.2.3.
- With the permeability anisotropy and resistivity anisotropy one-to-one relationship, it would be good to investigate that relationship in CRS permeability anisotropy testing. Electrodes could be included in the CRS cell, similar to how they are in the triaxial cell with the cubic specimens. Resistivity measurements could be taken at different points during compression. McCarter et al (2005) provides a method for measuring electrical anisotropy in an oedometer, which could likely be applied to a CRS consolidometer.

7.5.2 CRS Testing

This research provides a foundation of permeability anisotropy data for two mudrocks within the medium to high plasticity range, caused by a big difference in smectite content. A greater understanding of permeability anisotropy and the mechanisms behind it can be developed through the following recommendations:

- Test the pore pressure response in the radially-draining CRS device. The change in permeability values with respect to strain rate could be indicative of a lag in the pore pressure measurement system. To test this, CRS tests can be performed where the tests are stopped during loading, the excess pore pressures are allowed to dissipate, then started again. If the excess pore pressures quickly return to their former values before loading was stopped, the system has good pore pressure response and the data are reliable. Theoretically, the excess pore pressures built up in a CRS test should be linked to the stress state in virgin compression of the material, and those pressures should be fairly independent of loading history.

- More resedimented mudrock types can be tested, to quantify the hypothesized trend of greater permeability anisotropy with greater plasticity, or smectite content. By testing multiple mudrock types, one could separately characterize the effect of smectite content with that of clay fraction on permeability anisotropy. Testing a silt would provide a meaningful test on the null hypothesis of isotropic flow with compression.
- The effect of mudrock pore fluid salinity on permeability anisotropy could be researched. Salinity has a large impact on the size of clay particles' double layers, which are highly responsible for their behavior. Resedimenting a leached mudrock, simulating a lacustrine sedimentation environment, would give it a dispersed structure initially, due to the large double layers. How the dispersed structure develops into a soil fabric could potentially have a large impact on permeability anisotropy.
- Given the near exponential increase in the permeability anisotropy of RGoM-EI when plotted against porosity, it would be of interest to test permeability anisotropy to greater stresses and see if the "exponential" trend continues. If it does, very large anisotropy values would be found, matching the high anisotropies predicted by Daigle and Dugan's (2011) analytical model. This would require the design of a new high-stress radially-draining CRS consolidometer.
- As all of these results are from homogenous resedimented mudrocks, and consequently characterize permeability anisotropy only due to particle rotation, it would be interesting to resediment and test layered mudrocks. While being difficult to quantify, this could at least give experimental insight to test the effect of layering on permeability anisotropy. The results could be checked with the layering model proposed by Adams (2014).
- Only one set of CRS tests is performed on sheared specimens. More testing is needed to determine how shearing affects anisotropy. DSS shearing can be performed at different consolidation stresses and using different materials. Shearing samples to greater shear strains would also be prudent; however, the Geonor® DSS device can only shear samples up to about 30% shear strain, so a new undrained horizontal shearing technique that can strain to high shear strains would be needed. These tests can be performed in an attempt to characterize permeability anisotropy caused by submarine mass transfer complexes, where tectonics or landslides have sheared the mudrocks.

REFERENCES

Abdulhadi, N. O. (2009). "An Experimental Investigation into the Stress-Dependent Mechanical Behavior of Cohesive Soil with Application to Wellbore Instability." Ph.D. Thesis, MIT, Cambridge, MA.

Adams, A. L. (2011). "Laboratory Evaluation of the Constant Rate of Strain and Constant Head Techniques for Measurement of the Hydraulic Conductivity of Fine Grained Soils." S.M. Thesis, MIT, Cambridge, MA

Adams, A. L. (2014). "Permeability Anisotropy and Resistivity Anisotropy of Mechanically Compressed Mudrocks." Ph.D. Thesis, MT, Cambridge, MA

Adams, A. L., Germaine, J. T., Flemings, P. B., and Day-Stirrat, R. J. (2013). "Stress induced permeability anisotropy of Resedimented Boston Blue Clay." *Water Resources Research*, 49, 6561-6571.

Ahmed, I. (1990). "Investigation of Normalized Behaviour of Resedimented Boston Blue Clay using Geonor Direct Simple Shear." S.M. Thesis, Massachusetts Institute of Technology

Arch, J. and Maltman, A. (1990). "Anisotropic Permeability and Tortuosity in Deformed Wet Sediments." *Journal of Geophysical Research*, 95(B6), 9035-9045.

Archie, G. E. (1942). "The Electrical Resistivity Log as an Aid in Determining Some Reservoir Characterisitics." *Transactions of the American Institute of Mining and Metallurgical Engineers*, 146, 54-62.

ASTM Standard D2435/D2435M. (2011). "Standard Test Method for One-Dimensional Consolidation Properties of Soils Using Incremental Loading." ASTM International, West Conshohocken, PA, 2011, DOI: 10.1520/D2435_D2435M-11. <www.astm.org>

ASTM Standard D4186/D4186M. (2012). "Standard Test Method for One-Dimensional Consolidation Properties of Saturated Cohesive Soils Using Controlled-Strain Loading." ASTM International, West Conshohocken, PA, 2012, DOI: 10.1520/D4186_D4186M-12, <www.astm.org>

ASTM Standard D5084. (2010). "Standard Test Methods for Measurement of Hydraulic Conductivity of Saturated Porous Materials Using a Flexible Wall Permeameter." ASTM International, West Conshocken, PA, 2012, DOI: 10.1520/D5084-10, <www.astm.org>

ASTM Standard D854. (2010). "Standard Test Methods for Specific Gravity of Soil Solids by Water Pycnometer." ASTM International, West Coonshohocken, PA, 2010, DOI: 10.1520/D0854-10, <www.astm.org>

Bailey, W. W. (1961). "Effects of Salt on the Shear Strength of Boston Blue Clay." S.B. Thesis, MIT, Cambridge, MA.

Barosh, P. J. and Woodhouse, D. (2012). "A City Upon a Hill: The Geology of the City of Boston & Surrounding Region." *Journal of the Boston Society of Civil Engineers Section / ASCE* (26 & 27).

Betts, W. S. (2014). "Compressibilty and Permeability of Gulf of Mexico Mudrocks, Resedimented and In-Situ." M.S. Thesis, University of Texas at Austin.

Boggs, S. (2006). *Principles of Sedimentology and Stratigraphy*. Pearson Prentice Hall, Upper Saddle River, NJ.

Bolton, A. J., Maltman, A. J., and Fisher, Q. (2000). "Anisotropic permeability and bimodal pore-size distributions of fine-grained marine sediments" *Marine and Petroleum Geology,* 17, 657-672.

Brewer, R. and Sleeman, J. R. (1960). "Soil Structure and Fabric." *Journal of Soil Science*, 11(1). 172-185.

Carman, P. C. (1937). "Fluid flow through a granular bed." *Transactions of the Institution of Chemical Engineers,* 15, 150-156.

Casey, B. (2014). "The Consolidation and Strength Behavior of Mechanically Compressed Fine-Grained Sediments." Ph.D. Thesis, Massachusetts Institute of Technology.

Cauble, D. F. (1997). "An Experimental Investigation of the Behavior of a Model Suction Caisson in a Cohesive Soil." Ph.D. Thesis, MIT, Cambridge, MA.

Chapuis, R. P. and Gill, D. E. (1989). "Hydraulic Anisotropy of Homogeneous Soil and Rocks: Influence of the Densification Process." *Bulletin of the International Association of Engineering Geology, 39, 75-86.*

Clennell, M. B., Dewhurst, D. N., Brown, K. M, and Westbrook, G. K. (1999). "Permeablity anisotropy of consolidated clays." *Muds and Mudstones: Physical and Fluid Flow Properties.* Geological Society, London, Special Publications. 79-96

Daigle, H. and Dugan, B. (2011). "Permeability anisotropy and fabric development: A mechanistic explanation." *Water Resources Research.* 47. W12517.

Darcy, H. (1856). "Les Fontaines Publiques de la ville de Dijon." Paris.

Day-Stirrat, R. J., Dutton, S. P., Milliken, K. L., Loucks, R. B., Aplin, A. C., Hillier, S., and van der Plujim, B. A. (2010). "Fabric anisotropy induced by primary depositional variations in the silt: clay ratio in two fine-grained slope fan complexes: Texas Gulf coast and northern North Sea." *Sedimentary Geology*, 226, 42-53.

Delage, P. and Lefebvre, G. (1984). "Study of the structure of a sensitive Champlain clay and of its evolution during consolidation." *Canadian Geotechnical Journal,* 21, 21-35.

Dewhurst, D. N. and Aplin, A. C. (1999). "Influence of clay fraction on pore-scale properties and hydraulic conductivity of experimentally compacted mudstones." *Journal of Geophysical Research.* 104(B12). 29,261-29,274.

Dewhurst, D. N., Aplin, A. C., Sarda, J. P. and Yang, Y. L. (1998). "Compaction-driven evolution of porosity and permeability in natural mudstones: An experimental study." *Journal of Geophysical Research – Solid Earth*, 103(B1), 651-661

Dewhurst, D. N., Brown, K., Clennell, M. B., and Westbrook, G. K. (1996). "A comparison of the fabric and permeability anisotropy of consolidated and sheared silty clay." *Engineering Geology,* 42, 253-267.

Emmanuel, S. and Day-Stirrat, R. J. (2012). "A framework for quantifying size dependent deformation of nano-scale pores in mudrocks." *Journal of Applied Geophysics, 86,29-35.*

Fahy, B. P. (2014). "The Influence of Salinity on the Mechanical Behavior of High Plasticity Soils." S.M. Thesis, MIT, Cambridge, MA.

Gere, J.M. and Goodno, B.J. (2009). Mechanics of Materials, 7th Ed., Cengage Learning, Toronto.

Germaine, J. T. (1982). "Development of the Directional Shear Cell for Measuring Cross-Anisotropic Clay Properties." Sc.D. Thesis, MIT, Cambridge, MA.

Germaine, J. T. and Germaine, A. V. (2009). *Geotechnical Laboratory Measurements for Engineers.* John Wiley & Sons, Inc. Hoboken, NJ.

Gluyas, J. and Swarbrick, R. (2004). *Petroleum Geoscience.* Blackwell Publishing, Malden, MA.

Gonzalez, J.H. (2000). "Experimental and Theoretical Investigation of Constant Rate of Strain Consolidation." SM Thesis, MIT, Cambridge, MA.

Horan, A. J. (2012). "The mechanical behavior of normally consolidated soils as a function of pore fluid salinity." S.M. Thesis, Cambridge, MA.

Ladd, C. C. (1996). "1.361 Advanced Soil Mechanics Notes." Massachusetts Institute of Technology.

Ladd, C. C. and Edgers, L. (1972). "Consolidated-Undrained Direct-Simple Shear Tests on Saturated Clays." Research in Earth Physics Phase Report # 16. Soil Mechanics Division, Department of Civil Engineering, MIT, Cambridge, MA.

Ladd, C. C. and Varallyay, J. (1965). "The Influence of Stress System on the Behavior of Saturated Clays During Undrained Shear." *Research Report R65-11, Soils Publication No. 177.* Department of Civil Engineering, MIT, Cambridge, MA.

Lambe, T. W. and Whitman, R. V. (1969). *Soil Mechanics.* John Wiley & Sons, New York.

Leroueil S., Bouclin G., Tavenas R., Bergeron L., and La Rochell P. (1990). "Permeability anisotropy of natural clays as a function of strain." *Canadian Geotechnical Journal.* 27, 568-579.

McCarter, W. J., Blewett, J., Chrisp, T. M., and Starrs, G. (2005). "Electrical property measurements using a modified hydraulic oedometer." *Canadian Geotechnical Journal*. 42, 655-662.

Meegoda, N. J., King, I.P., and Arulanandan, K. (1989). "An Expression for the Permeability of Anisotropic Granular Media." *International Journal for Numerical and Analytical Methods in Geomechanics.* 13(6), 575-598.

Mitchel, J. K. and Soga, K. (2005). *Fundamentals of Soil Behavior, 3rd Edition*. John Wiley & Sons, New Dehli.

Mousseau, R. J. and Trump, R. P. (1967). "Measurement of Electrical Anisotropy of Claylike Materials." *Journal of Applied Physics*, 38(11), 4375.

Neuzil, C. E. (1994). "How permeable are clays and shales?" *Water Resources Research.* 30(2). 145-150.

Olsen, H. W. (1962). "Hydraulic flow through saturated clays." *Clays and Clay Minerals,* 9(2), 131-161.

Potter, P. E., Maynard, J. B., Pryor, W. A. (1980). *Sedimentology of Shale: Study Guide and Reference Source.* Springer-Verlag, New York.

Santagata, M. C. (1994). "Simulation of Sampling Disturbance in Soft Clays using Triaxial Element Tests." S.M. Thesis, MIT, Cambridge, MA.

Scholes, O. N., Clayton, S. A., Hoadley, A. F. A., and Tiu, C. (2007). "Permeability anisotropy due to consolidation of compressible porous media." *Transport of Porous Media, 68, 365-387.*

Seah, H.S. and Juirnarongrit, T. (2003). "Constant Rate of Strain Consolidation with Radial Drainiage." Geotechnical Testing Journal, 26(4).

Seah, T. H. (1990). "Anisotropy of Resedimented Boston Blue Clay." Sc.D. Thesis, MIT, Cambridge, MA.

Sharqawy, M.H., Lienhard, J.H., and Zubair, S.M. (2012). "Thermophysical Properties of Seawater." < http://web.mit.edu/seawater/> (Aug. 26 2014)

Stow, D. A. V. (1981). "Fine-grained sediments: Terminology." *Quarterly Journal of Engineering Geology and Hydrogeology.* 14(4), 243-244

Taylor, D. W. (1948). *Fundamentals of Soil Mechanics*. John Wiley & Sons. New York

Terzaghi, K., Peck, R. B., and Mesri, G. (1996). *Soil Mechanics in Engineering Practice, 3rd Edition*. John Wiley & Sons, New York.

Ting, N. H. (1990). "Effects of Disturbance on Consolidation with Vertical Drains." S.M. Thesis, MIT, Cambridge, MA.

Walbaum, M. (1988). "Procedure for Investigaton of Sample Disturbance Using the Direct Simple Shear Apparatus." S.M. Thesis, Massachusetts Institute of Technology.

Wissa, A.E.Z., Christian, J.T., Davis, E.H., Heiberg, S. (1971). "Consolidation at Constant Rate of Strain." ASCE Journal of the Soil Mechanics and Foundations Division, 97(10).

Witt, K. J., and Brauns, J. (1984). "Permeability-anisotropy due to particle shape." *Journal of Geotechnical Engineering.* 109, 1181-1187.

Yang, Y., and Aplin, A. (1998). "Influence of lithology and compaction on the pore size distribution and modelled permeability of some mudstones from the Norwegian margin." *Marine and Petroleum Geology, 15, 163-175*

Yune, C.Y., and Chung, C.K. (2005). "Consolidation Test at Constant Rate of Strain for Radial Drainage." Geotechnical Testing Journal, 28(1).

Yune, C.Y., and Jung, Y.H. (2012). "Application of Multi-Directional Flow Consolidometer for a Constant Rate of Strain Consolidation Test under Various Drainage Conditions." Geotechnical Testing Journal, 35(2).

APPENDIX A – EQUIPMENT DRAWINGS

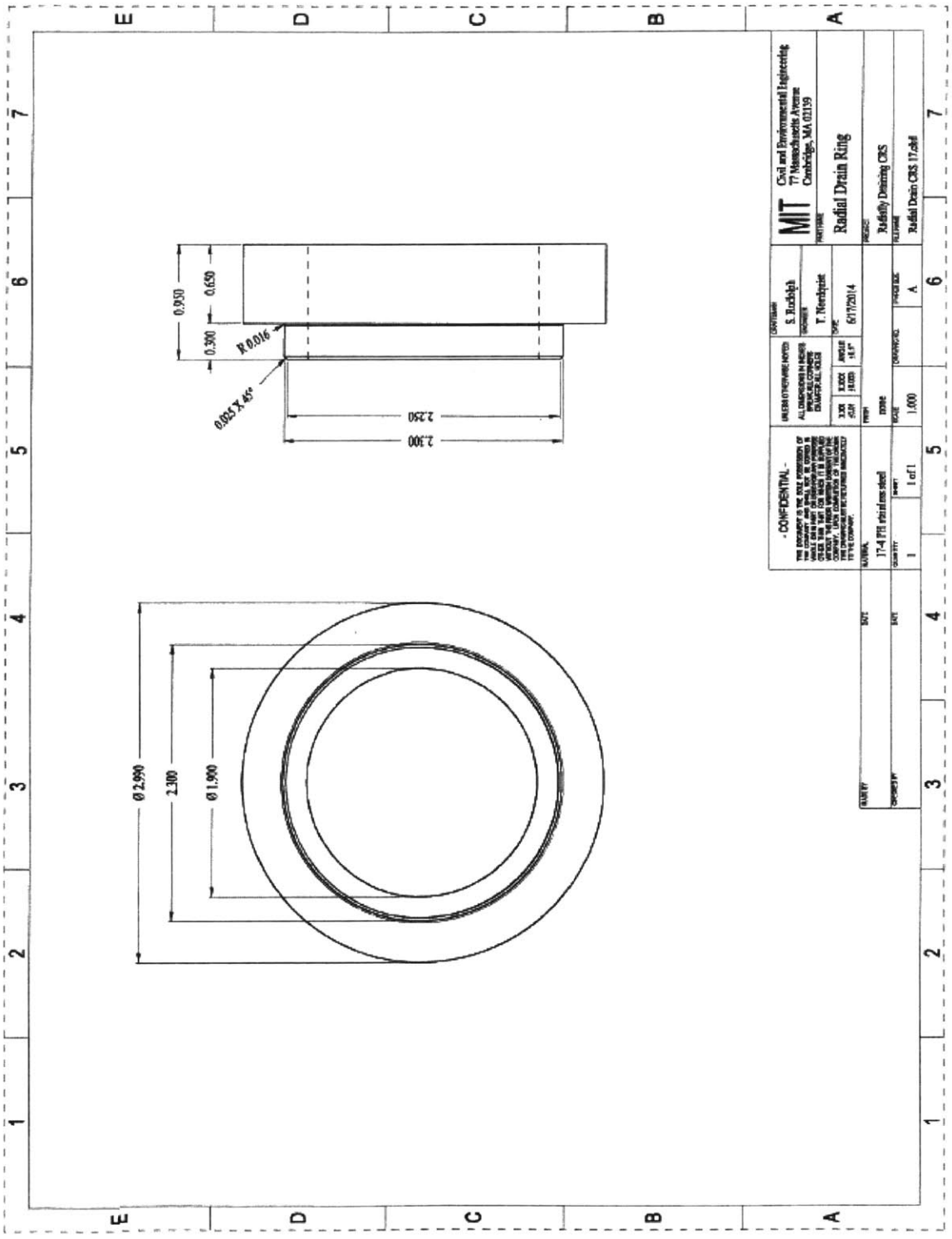

Figure A-49: CAD drawing for radially-draining CRS steel confining ring. The tubular porous stone is placed inside it.

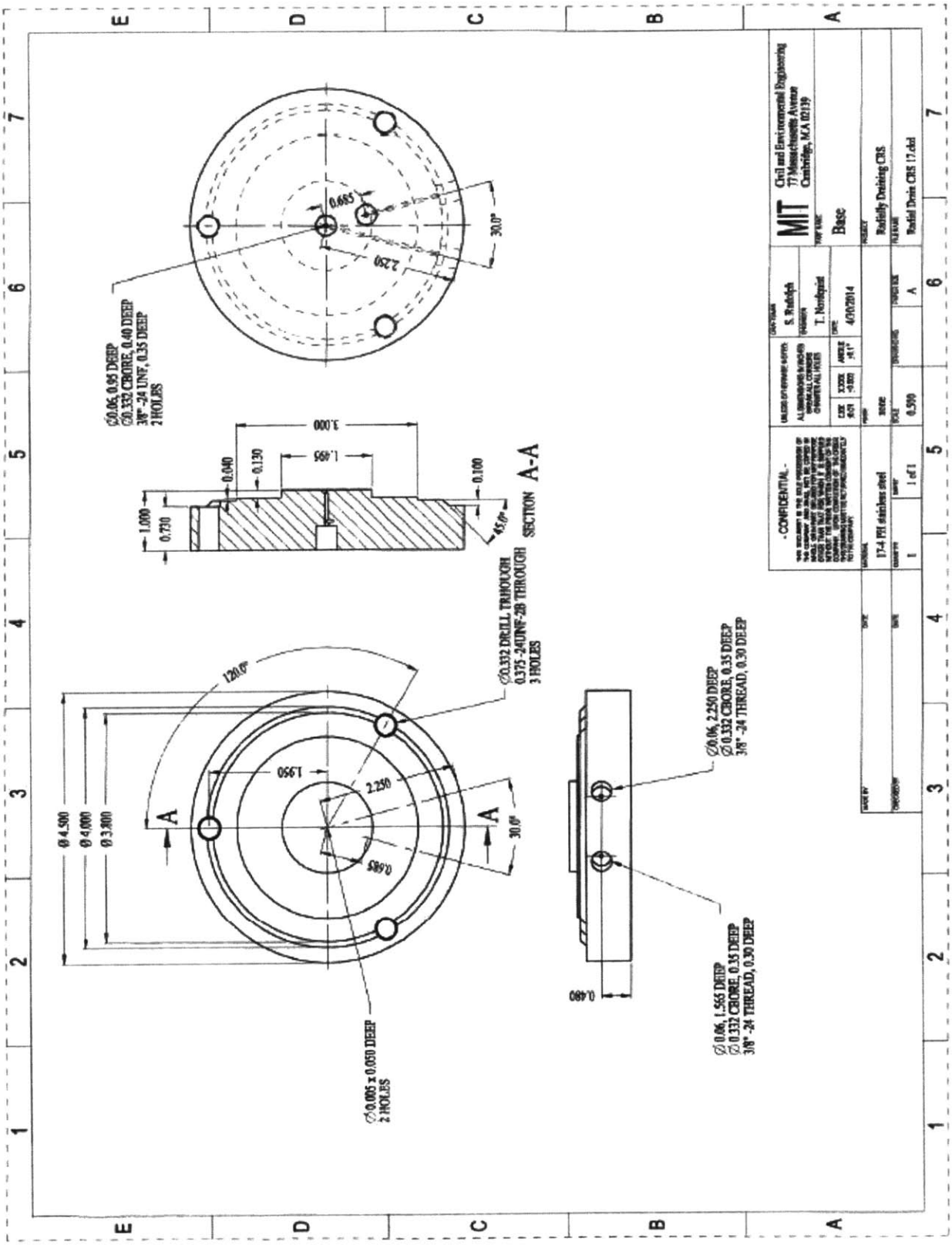

Figure A-2: CAD drawing for radially-draining CRS base

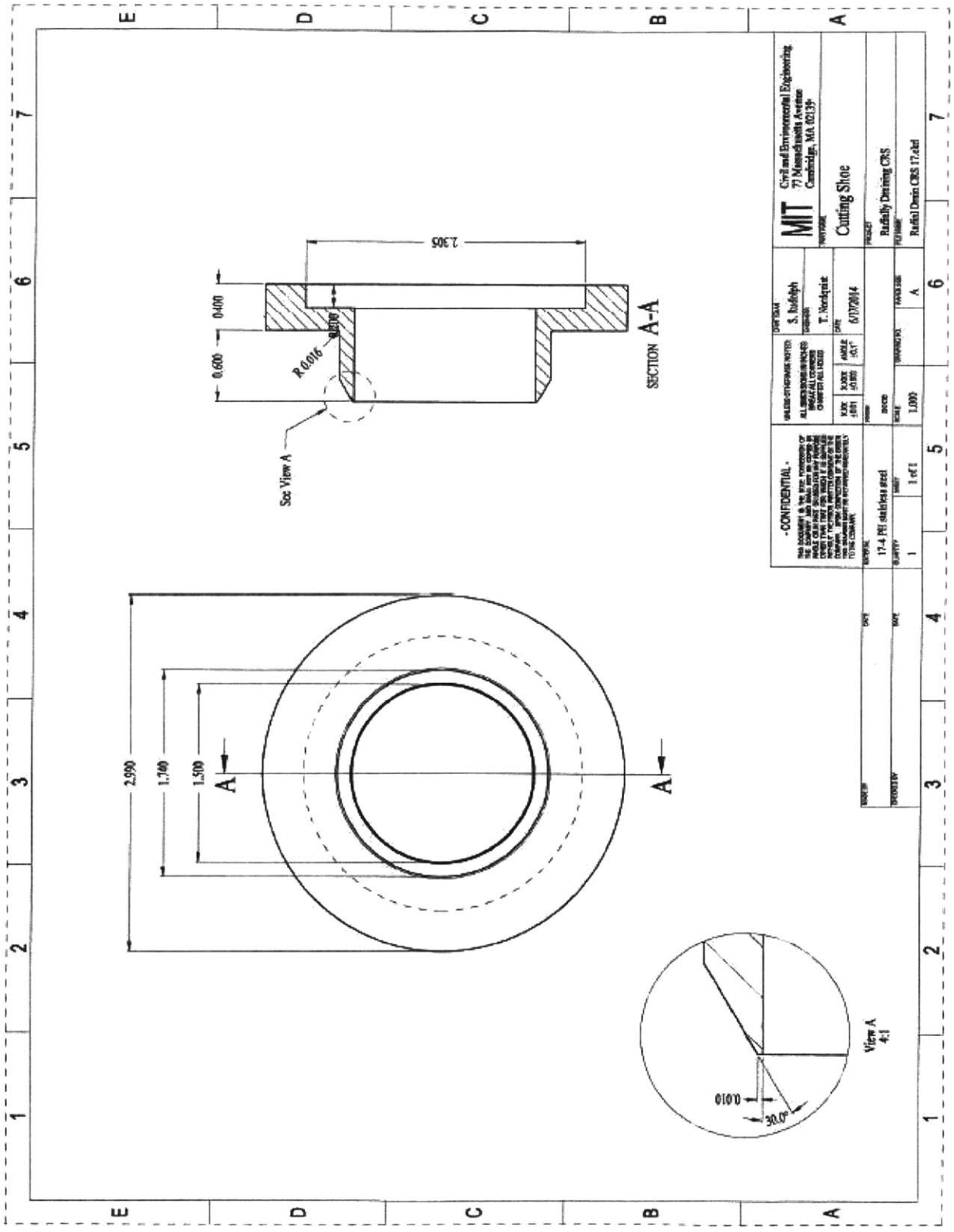

Figure A-3: CAD drawing for radially-draining CRS cutting shoe

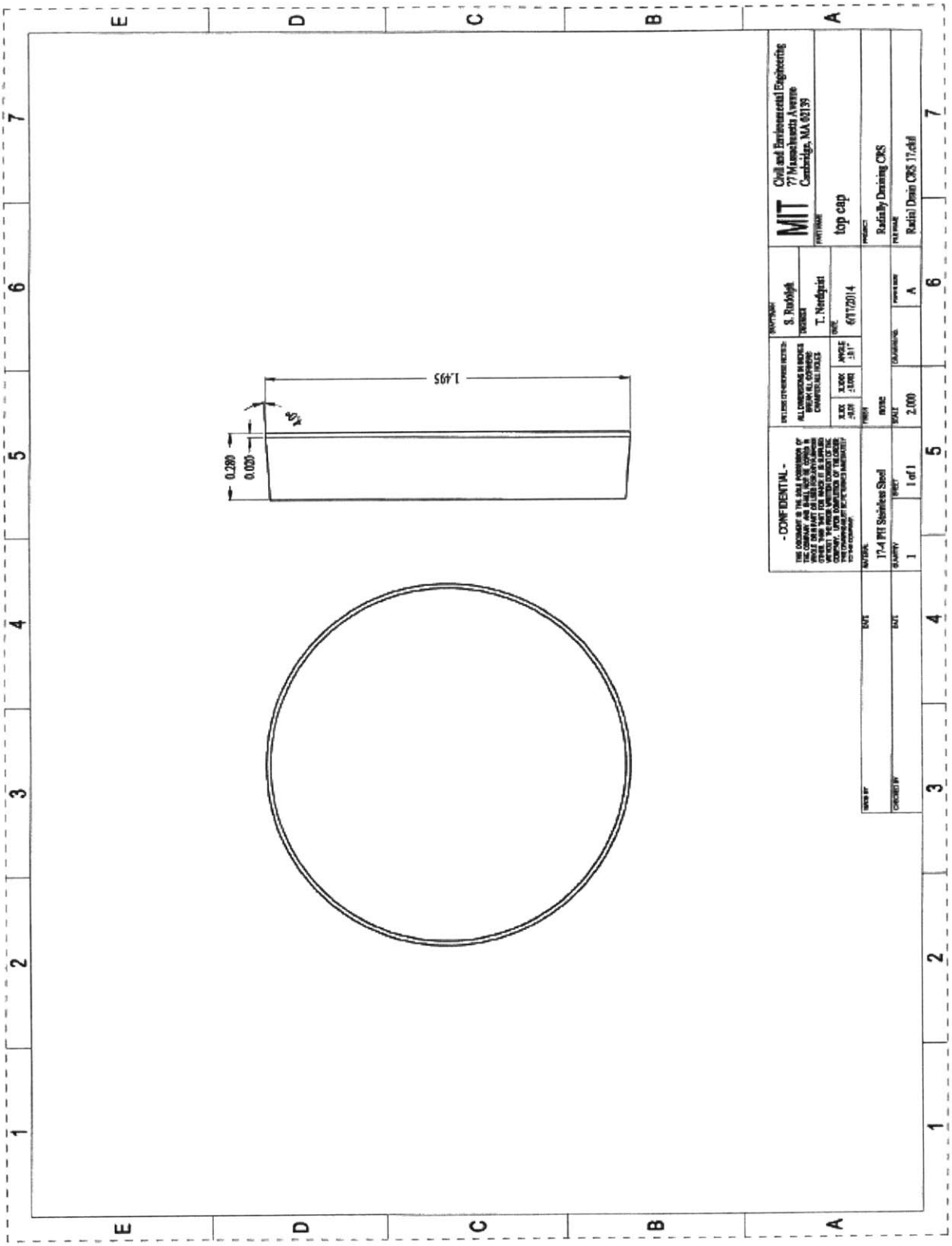

Figure A-4: CAD drawing for radially-draining CRS top cap

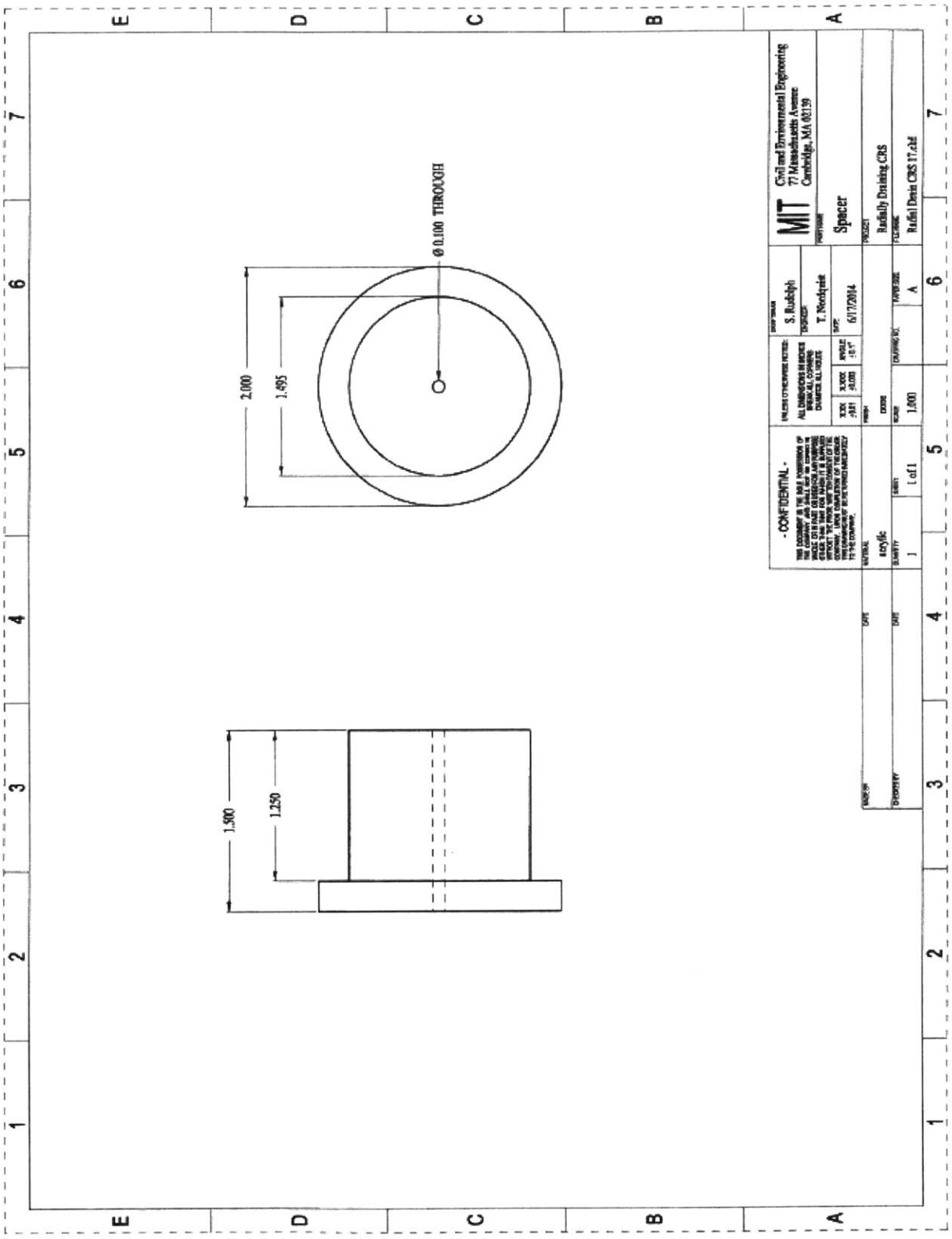

Figure A-50: CAD drawing for radially-draining CRS acrylic spacer

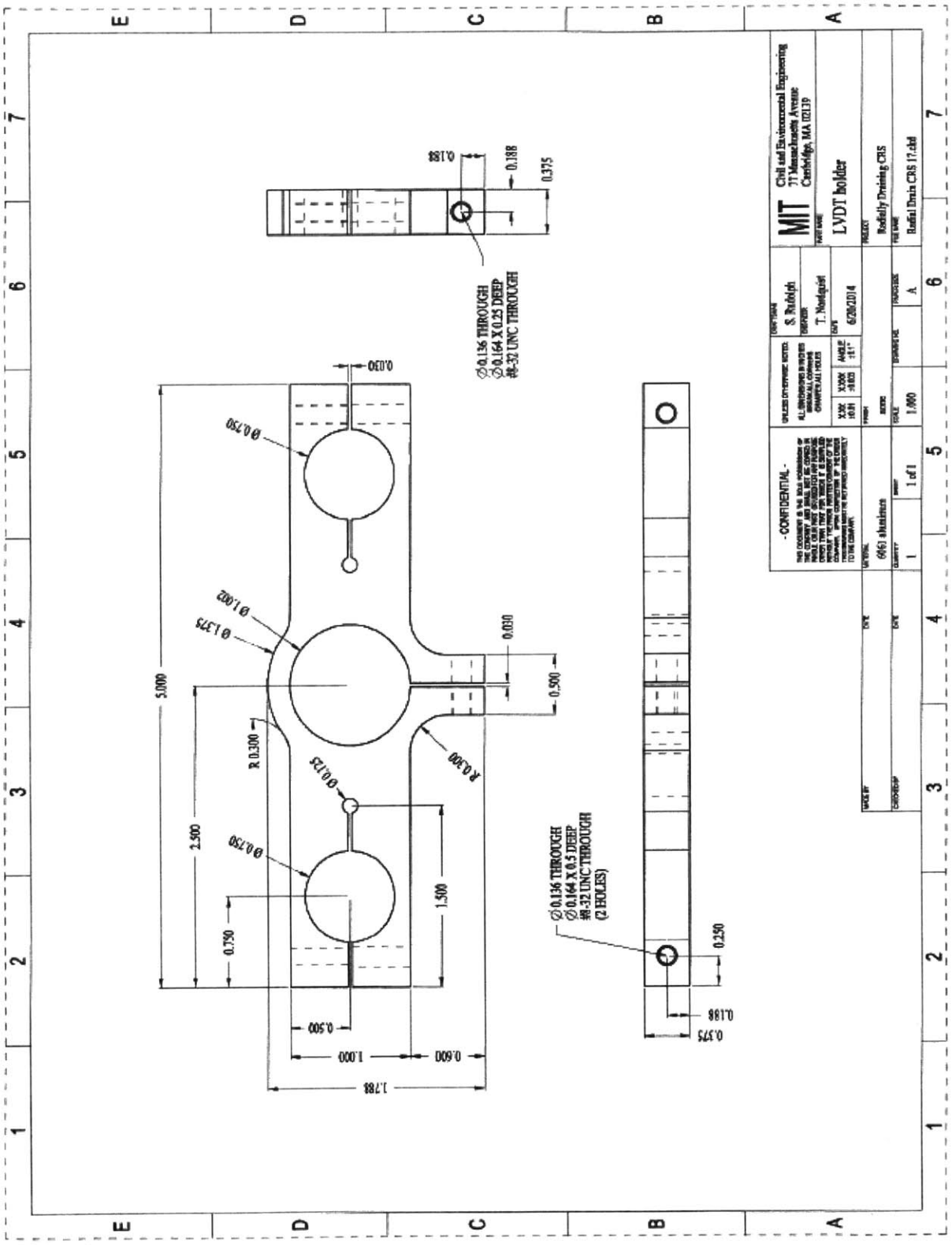

Figure A-6: CAD drawing for radially-draining CRS dual LVDT holder

APPENDIX B – TESTING WORKSHEETS

MIT GEOTECHNICAL LABORATORY
CONSTANT RATE OF STRAIN CONSOLIDATION - VERTICAL PERMEABILITY TEST

Test No: _____ Specimen ID: _____ Date Start: _____
Project: _____ Material Type: _____ Date End: _____
Apparatus: _____ Depth: _____ Tested by: _____

Preparations

- ☐ LVDTs previously zeroed
- ☐ Disassemble apparatus
- ☐ Set gears & transmission to desired ε
- ☐ mass 3 tares
- ☐ mass ring, spacer, top porous stone, top filter paper
- ☐ calipers
- ☐ ziploc bag for 3 tares
- ☐ turntable, trimming tool
- ☐ wire saw, plastic disc
- ☐ wax paper on bottom of turntable
- ☐ grease ring

Trimming

- ☐ Extrude ~1" of specimen
- ☐ place on turntable, centered
- ☐ insert ring into turntable
- ☐ trim specimen
- ☐ remove ring/specimen and place in vice
- ☐ trim top of specimen, pulling off soil w/ wax paper
- ☐ place spacer on table w/ filter paper
- ☐ press ring/specimen onto spacer
- ☐ place setup on its side in vice
- ☐ trim bottom of spec. w/ disk
- ☐ clean bottom of ring
- ☐ mass setup
- ☐ mass cuttings for w.c.

1.0 Specimen Properties

Water Contents

Location							
Tare ID							
Tare [g]							
Tare + Wet [g]							
Tare + Dry [g]							
WC [%]							

Dimensions

top of ring to stone [mm]							

Diameter [mm]	35.57
ring height [mm]	31.62
top stone/paper height [mm]	6.28
bottom stone/paper (inside ring) [mm]	none

Mass	
Ring [g]	
Acrylic Spacer [g]	
Top Porous Stone (SSD) [g]	
Top Filter Paper (SSD) [g]	
Specimen, Ring, Acrylic Spacer [g]	

Setup

- ☐ thoroughly clean base
- ☐ place bottom stone & filter paper (SSD)
- ☐ concentrically place setup on base
- ☐ remove spacer
- ☐ place top porous stone
- ☐ measure ΔH between top stone & ring
- ☐ place greased square O-ring arnd ring
- ☐ place cell on base, avoiding contact between piston and stone
- ☐ tightly bolt cell to base (alternating bolts)
- ☐ place cell in load frame
- ☐ secure LVDTs & holder onto piston
- ☐ unlock piston, rest on top porous stone (don't relock)
- ☐ record load zero
- ☐ insert moment/shear break
- ☐ lower frame to ~Δ .01 mV
- ☐ record seated load zero
- ☐ fill cell with water
- ☐ connect PP transducer
- ☐ fill (lower) CP PVA
- ☐ hydraulically connect CP, PP lines to atmosphere
- ☐ record LVDT,PP,CP zeros

2.0 Transducer Data

					DAQ	Computer	
Component	ID	Channel	CF	Units	Zero [V]	Zero [V]	Normalized [V/V]
LVDT black (axial)	D-94	126	-1.572132	cm/V/V			
CP	D10342	127	-703.35876	ksc/V/V			
Load Cell	AE13295	128	1508993.93	kg/V/V			
Load Cell - seated							
PP	D10343	130	-700.821961	ksc/V/V			
LVDT blue (vol)	G-90	131	2.521938	cm/V/V			
Input		132	-	-			-

Figure B-1: Vertically-draining CRS test data sheet, page 1

3.0 Backpressuring Filename: _____

	CP						
	target	actual				End CP	End Load
[ksc]	[mV]	[mV]	Duration	Date	Time	[mV]	[mV]
0							
0.03							
0.06							
0.12							
0.24							
0.5							
1.0							
2.0							
3.0							
4.0							

Backpressure

- ☐ input zeros into spreadsheet & computer & computer
- ☐ start 4 min. data file
- ☐ backpressure to 4 ksc w/ 10-20 min. intervals
- ☐ allow ≥ 8 hrs. for equilibration

4.0 Check Saturation Filename: _____

	CP	
	target	actual
[ksc]	[mV]	[mV]
5.0		
4.0		

15 s "B" value	60 s "B" value

Check Saturation

- ☐ start 3 s. data file
- ☐ close valve to isolate PP line
- ☐ increase PVA pressure to 5 ksc
- ☐ run for 60 s.
- ☐ bring pressure back to 4 ksc
- ☐ hydraulically connect cell to PP lines

5.0 Re-Zero Transducers

	DAQ		Computer		
	$[V_{out}]$	$[V_{in}]$	$[V_{out}]$	$[V_{in}]$	[V/V]
Cell Pressure					-
PP - old					-
PP - new	-	-	-	-	

Re-Zero Transducers

- ☐ realign pressure to 4 ksc
- ☐ record mV readings for CP & PP lines
- ☐ input values into spreadsheet

6.0 Leak Check Filename: _____

		CP	PP
Date	Time	[mV]	[mV]

Leak Check

- ☐ start 20 s. data file
- ☐ close valves to isolate PP line
- ☐ check for leaks after 10 min.

Figure B-2: Vertically-draining CRS test data sheet, page 2

7.0 Loading

Filename: _____

strain rate: _____ [in/min]

_____ [%/hr]

loading direction: forward / reverse

Monitoring:

Date	Time	Blue LVDT [V]	Black LVDT [V]	Load [mV]	PP [mV]	Comments
						Start loading - ENGAGE TRANSMISSION!

Loading

- ☐ check gears, transmission, & switch direction
- ☐ start 3 or 4 min. data file
- ☐ engage transmission
- ☐ turn on motor
- ☐ wait to see changing voltages
- ☐ load to the greatest of:
  - +16.5 mV on load cell
  - -100 mV on PP_{bot} transducer
- ☐ shut off motor
- ☐ allow u_a to dissipate

8.0 Check Transducers

					DAQ	Computer	
Component	ID	Channel	CF	Units	Zero [V]	Zero [V]	Normalized [V/V]
LVDT black (axial)	D-94	126	-2.572132	cm/V/V			
CP	D10342	127	-703.15876	ksc/V/V			
Load Cell	AE13295	128	1508993.93	kg/V/V			
Load Cell - seated							
PP	D10343	130	-700.821961	ksc/V/V			
LVDT blue (vol)	G-90	131	2.521938	cm/V/V			
Input		132	-	-	-	-	-

Take Down

- ☐ mass 2 tares
- ☐ prepare hydraulic jack
- ☐ knife
- ☐ calipers
- ☐ water
- ☐ lock piston
- ☐ hydraulically connect PP line to CP
- ☐ bring CP back to atmospheric
- ☐ record LVDT,PP,CP zeros
- ☐ unload piston
- ☐ record load cell zero
- ☐ remove LVDT hanger
- ☐ remove cell and place on tray covered with paper towels
- ☐ close PP line & cell valves
- ☐ open cell drainage valve
- ☐ unbolt cell from base
- ☐ carefully remove cell, allowing water to soak into paper towels
- ☐ drain water off of top stone
- ☐ measure ΔH between top stone & ring
- ☐ remove square O-ring
- ☐ remove ring/specimen/top stone
- ☐ mass ring/specimen/top stone
- ☐ extrude specimen using hydraulic jack
- ☐ measure H of specimen
- ☐ mass specimen

9.0 Final Properties

Mass

Specimen, Ring, Top Porous Stone [g]	
Ring [g]	
Top Porous Stone [g]	

Tare ID		Tare ID	
Tare [g]		Tare [g]	
Wet Specimen & Tare [g]			
Dry Specimen & Tare [g]		Dry Extraneous Soil & Tare [g]	

Dimensions

Depth to top cap [mm]							
Specimen Height [mm]							

Figure B-3: Vertically-draining CRS test data sheet, page 3

MIT GEOTECHNICAL LABORATORY
CONSTANT RATE OF STRAIN CONSOLIDATION - RADIAL PERMEABILITY TEST

Test No: _____ Specimen ID: _____ Date Start: _____
Project: _____ Material Type: _____ Date End: _____
Apparatus: _____ Depth: _____ Tested by: _____

Preparations

- □ LVDTs previously zeroed
- □ Disassemble apparatus
- □ Run water through PP lines
- □ Set gears & transmission to desired ε̇
- □ mass 3 tares
- □ mass cutting shoe, spacer, top cap
- □ calipers
- □ ziploc bag for 3 tares
- □ turntable, trimming tool
- □ wire saw, plastic disc
- □ wax paper on bottom of turntable

Trimming

- □ Extrude "1" of specimen
- □ place on turntable, centered
- □ insert cutting shoe into turntable
- □ trim specimen
- □ mass ring (SSD)
- □ remove cutting shoe/specimen
- □ trim top of specimen
- □ clean cutting shoe
- □ place cutting shoe on ring
- □ place top cap on top of specimen (large ∅ adjacent to specimen)
- □ place space on counter (small ∅ up)
- □ press shoe/ring/spec./top cap onto spacer
- □ advance specimen into confinement ring
- □ place setup on its side in vice
- □ trim bottom of spec. w/ disk
- □ clean bottom of ring
- □ mass setup
- □ mass cuttings for w.c.

1.0 Specimen Properties

Water Contents

Location							
Tare ID							
Tare [g]							
Tare + Wet [g]							
Tare + Dry [g]							
WC [%]							

Dimensions

Depth to top cap [mm]						

ring diameter [mm]	38.13
top cap height [mm]	7.07
ring height [mm]	24.26
pedestal height [mm]	3.34

Mass

Cutting Shoe [g]	
Acrylic Spacer [g]	
Top Cap [g]	
Ring [g]	
Specimen, Ring, Cutting Shoe, Acrylic Spacer, Top Cap [g]	

Setup

- □ run water through PP lines
- □ thoroughly clean base
- □ concentrically place setup on base
- □ remove spacer, cutting shoe
- □ measure ΔH between top cap & ring
- □ place greased square O-ring arnd ring
- □ place cell on base, maintaining a space between piston & top cap
- □ tightly bolt cell to base (alternating bolts)
- □ place cell in load frame
- □ unlock piston, rest on top cap (don't relock)
- □ record load zero
- □ insert moment/shear break
- □ lower frame to ~0 .10 mV
- □ record seated load zero
- □ fill cell with water
- □ hydraulically connect CP, PP lines to atmosphere
- □ record LVDT,PP,CP zeros

2.0 Transducer Data

Component	ID	Channel	CF	Units	Zero [V]	Vin [V]
LVDT blue	G-90	40	2.620202	cm/V/V		-
LVDT black	H-90	41	2.624379	cm/V/V		-
Pore Pressure $_{check}$	A53551	42	702.328383	ksc/V/V		-
Pore Pressure $_{max}$	A80012	43	-701.135551	ksc/V/V		-
Input 40-43	-	44	-	-	-	
Cell Pressure	?	74	-706.675163	ksc/V/V		-
Load Cell	?	75	143628.441	kg/V/V		-
Load Cell - seated	?					-
Input 74-75	-	76	-	-	-	

Figure B-4: Radially-draining CRS test data sheet, page 1

3.0 Backpressuring Filename: _____

	CP						
	target	actual				End CP	End Load
[ksc]	[mV]	[mV]	Duration	Date	Time	[mV]	[mV]
0							
0.03							
0.06							
0.12							
0.24							
0.5							
1.0							
2.0							
3.0							
4.0							

Backpressure

- ☐ input zeros into spreadsheet
- ☐ record mV for CP to backpressure
- ☐ record mV for CP to check saturation
- ☐ start 4 min. data file
- ☐ backpressure to 4 ksc w/ 10-20 min. intervals
- ☐ allow ≥ 8 hrs. for equilibration

4.0 Check Saturation Filename: _____

	CP	
	target	actual
[ksc]	[mV]	[mV]
5.0		
4.0		

	15 s "B" value	60 s "B" value
30% PP		
100% PP		

Check Saturation

- ☐ start 3 s. data file
- ☐ close valves to isolate PP lines
- ☐ close valves to isolate cell
- ☐ increase manifold pressure to 5 ksc
- ☐ open cell to manifold
- ☐ run for 60 s.
- ☐ bring pressure back to 4 ksc
- ☐ hydraulically connect cell to PP lines

5.0 Re-Zero Transducers

		$[V_{out}]$	$[V_{in}]$	$[V_{zero\ out}]$	[ksc]
current	Cell Pressure			-	
	PP_{check}			-	
	PP_{max}			-	
new	PP_{check}	-	-		
	PP_{max}	-	-		

Re-Zero Transducers

- ☐ realign pressure to 4 ksc
- ☐ record mV readings for CP & PP lines
- ☐ input values into spreadsheet

6.0 Leak Check Filename: _____

		CP	PP_{check}	CP_{max}
Date	Time	[mV]	[mV]	[mV]

Leak Check

- ☐ start 20 s. data file
- ☐ close valves to isolate PP lines
- ☐ check for leaks after 10 min.

Figure B-51: Radially-draining CRS test data sheet, page 2

7.0 Loading

Filename: _____

strain rate: _____ [in/min]

_____ [%/hr]

loading direction: forward / reverse

Monitoring:

Date	Time	Blue LVDT [V]	Black LVDT [V]	Load [mV]	100% PP [mV]	Comments
						Start loading - ENGAGE TRANSMISSION!

8.0 Check Transducers

Component	ID	Channel	CF	Units	Zero [V]	Vin [V]
LVDT blue	G-90	40	2.620202	cm/V/V		-
LVDT black	H-90	41	2.624379	cm/V/V		-
Pore Pressure $_{check}$	A53551	42	702.328383	ksc/V/V		-
Pore Pressure $_{max}$	A80012	43	-701.135551	ksc/V/V		-
Input 40-43	-	44	-	-	-	
Cell Pressure	?	74	-706.675163	ksc/V/V		-
Load Cell	?	75	143628.441	kg/V/V		-
Input 74-75	-	76	-	-	-	

9.0 Final Properties

Mass

Specimen, Ring, Top Cap [g] _____

ring after extrusion [g] _____

ring after ultrasonic [g] _____

Tare ID _____

Tare [g] _____

Wet Specimen & Tare [g] _____

Dry Specimen & Tare [g] _____

Tare ID _____

Tare [g] _____

Dry Extraneous Soil & Tare [g] _____

Dimensions

Depth to top cap [mm]							
Specimen Height [mm]							

Loading

- ☐ check gears, transmission, & switch direction
- ☐ start 3 or 4 min. data file
- ☐ engage transmission
- ☐ turn on motor
- ☐ wait to see changing voltages
- ☐ load to the greatest of:
  - +170 mV on load cell
  - +100 mV on PP_{max} transducer
  - +200 mV on PP_{drain} transducer
- ☐ shut off motor
- ☐ allow u_e to dissipate

Take Down

- ☐ mass 2 tares
- ☐ prepare hydraulic jack
- ☐ knife
- ☐ calipers
- ☐ water
- ☐ lock piston
- ☐ hydraulically connect PP lines to CP
- ☐ bring CP back to atmospheric
- ☐ record LVDT,PP,CP zeros
- ☐ unload piston
- ☐ record load cell zero
- ☐ remove cell and place on tray covered with paper towels
- ☐ close PP line & cell valves
- ☐ open cell drainage valve
- ☐ unbolt cell from base
- ☐ carefully remove cell, allowing water to soak into paper towels
- ☐ drain water off of top cap
- ☐ measure ΔH between top cap & ring
- ☐ remove square O-ring
- ☐ remove ring/specimen/top cap
- ☐ mass ring/specimen/top cap
- ☐ extrude specimen using hydraulic jack
- ☐ measure H of specimen
- ☐ mass specimen
- ☐ obtain extraneous soil from ring.

Figure B-52: Radially-draining CRS test data sheet, page 3

APPENDIX C – VBA CODE

Code for Individual Test Smoothing

```
Option Explicit

Sub smoothdata2()

Dim myrow As Integer
Dim mymax As Integer
Dim mynumber As Integer

On Error Resume Next
Worksheets("Smoothed Loading").Delete

Worksheets("Loading Input").Select
Worksheets("Loading Input").Copy After:=Worksheets("Loading Input")
Worksheets("Loading Input (2)").Select
Worksheets("Loading Input (2)").Name = "Smoothed Loading"

mynumber = Worksheets("Loading Input").Range("S5")
Worksheets("Smoothed Loading").Range("r5") = "Smoothing number used:"
Worksheets("Smoothed Loading").Range("r5").HorizontalAlignment = xlRight
Worksheets("Smoothed Loading").Range("S5") = mynumber

myrow = 14
mymax = 14

Do Until Worksheets("Loading Input").Cells(mymax + 1, 5) = ""

  mymax = mymax + 1

Loop

Worksheets("Loading Input").Range("S6") = mymax
Worksheets("smoothed loading").Range("s6") = mymax

Dim valuebelow As Double
Dim valuebelow2 As Double
Dim valueabove As Double
Dim valueabove2 As Double
Dim value As Double

If mynumber = 1 Then
```

```
ElseIf mynumber = 3 Then

   Do Until myrow = mymax - 1

      myrow = myrow + 1
      Worksheets("Smoothed Loading").Cells(myrow, 5).Clear
      Worksheets("Smoothed Loading").Cells(myrow, 6).Clear
      Worksheets("Smoothed Loading").Cells(myrow, 8).Clear

      valuebelow = Worksheets("Loading Input").Cells(myrow - 1, 5)
      value = Worksheets("Loading Input").Cells(myrow, 5)
      valueabove = Worksheets("Loading Input").Cells(myrow + 1, 5)
      value = (valuebelow + value + valueabove) / 3
      Worksheets("Smoothed Loading").Cells(myrow, 5) = value

      valuebelow = Worksheets("Loading Input").Cells(myrow - 1, 6)
      value = Worksheets("Loading Input").Cells(myrow, 6)
      valueabove = Worksheets("Loading Input").Cells(myrow + 1, 6)
      value = (valuebelow + value + valueabove) / 3
      Worksheets("Smoothed Loading").Cells(myrow, 6) = value

      valuebelow = Worksheets("Loading Input").Cells(myrow - 1, 8)
      value = Worksheets("Loading Input").Cells(myrow, 8)
      valueabove = Worksheets("Loading Input").Cells(myrow + 1, 8)
      value = (valuebelow + value + valueabove) / 3
      Worksheets("Smoothed Loading").Cells(myrow, 8) = value

   Loop

ElseIf mynumber = 5 Then

   myrow = myrow + 2

   Do Until myrow = mymax - 2

      myrow = myrow + 1
      Worksheets("Smoothed Loading").Cells(myrow, 5).Clear
      Worksheets("Smoothed Loading").Cells(myrow, 6).Clear
      Worksheets("Smoothed Loading").Cells(myrow, 8).Clear

      valuebelow2 = Worksheets("Loading Input").Cells(myrow - 2, 5)
      valuebelow = Worksheets("Loading Input").Cells(myrow - 1, 5)
      value = Worksheets("Loading Input").Cells(myrow, 5)
      valueabove = Worksheets("Loading Input").Cells(myrow + 1, 5)
      valueabove2 = Worksheets("Loading Input").Cells(myrow + 2, 5)
```

```
    value = (valuebelow2 + valuebelow + value + valueabove + valueabove2) / 5
    Worksheets("Smoothed Loading").Cells(myrow, 5) = value

    valuebelow2 = Worksheets("Loading Input").Cells(myrow - 2, 6)
    valuebelow = Worksheets("Loading Input").Cells(myrow - 1, 6)
    value = Worksheets("Loading Input").Cells(myrow, 6)
    valueabove = Worksheets("Loading Input").Cells(myrow + 1, 6)
    valueabove2 = Worksheets("Loading Input").Cells(myrow + 2, 6)
    value = (valuebelow2 + valuebelow + value + valueabove + valueabove2) / 5
    Worksheets("Smoothed Loading").Cells(myrow, 6) = value

    valuebelow2 = Worksheets("Loading Input").Cells(myrow - 2, 8)
    valuebelow = Worksheets("Loading Input").Cells(myrow - 1, 8)
    value = Worksheets("Loading Input").Cells(myrow, 8)
    valueabove = Worksheets("Loading Input").Cells(myrow + 1, 8)
    valueabove2 = Worksheets("Loading Input").Cells(myrow + 2, 8)
    value = (valuebelow2 + valuebelow + value + valueabove + valueabove2) / 5
    Worksheets("Smoothed Loading").Cells(myrow, 8) = value

  Loop

End If

End Sub
```

Cataloging Code for Permeability (k), Coefficient of Consolidation(C_v), and Coefficient of Compressibility (m_v)

```
Sub reduce_my_data()

Dim myrow As Integer
Dim myresult As Integer
Dim mycolumn As Integer
Dim increment As Double

myrow = 3
myresult = 3
mycolumn = 10
increment = 0.005

Range("j3:ZZ1000").ClearContents

Do Until Cells(myresult, 8) = ""
  Do Until Cells(myrow, 2) = ""
    If Cells(myrow, 2) > (Cells(myresult, 8) - increment / 2) And Cells(myrow, 2) < (Cells(myresult, 8) +
increment / 2) Then
      Cells(myresult, mycolumn) = Cells(myrow, 4)
      Cells(myresult + 105, mycolumn) = Cells(myrow, 5)
      Cells(myresult + 210, mycolumn) = Cells(myrow, 6)
      mycolumn = mycolumn + 1
    End If
    myrow = myrow + 1
  Loop
  myresult = myresult + 1
  myrow = 3
  mycolumn = 10
Loop

Range("A3:f10000").ClearContents

End Sub
```

Cataloging Code for Compression Curve

```
Sub reduce_my_data()

Dim myrow As Integer
Dim myresult As Integer
Dim mycolumn As Integer
Dim increment As Double

myrow = 3
myresult = 3
mycolumn = 8
increment = 0.05

Range("h3:ZZ1000").ClearContents

Do Until Cells(myresult, 6) = ""
  If Cells(myresult, 6) > 1 And Cells(myresult, 6) < 10 Then
    increment = 0.1
  ElseIf Cells(myresult, 6) > 10 Then
    increment = 0.5
  End If
  Do Until Cells(myrow, 4) = ""
    If Cells(myrow, 4) > (Cells(myresult, 6) - increment / 2) And Cells(myrow, 4) < (Cells(myresult, 6) +
increment / 2) Then
      Cells(myresult, mycolumn) = Cells(myrow, 1)
      mycolumn = mycolumn + 1
    End If
    myrow = myrow + 1
  Loop
  myresult = myresult + 1
  myrow = 3
  mycolumn = 8
Loop

Range("A3:D10000").ClearContents

End Sub
```